PACIFIC EARTHQUAKE ENGINEERING RESEARCH CENTER

Behavior and Failure Analysis of a Multiple-Frame Highway Bridge in the 1994 Northridge Earthquake

Gregory L. Fenves
Michael Ellery
University of California, Berkeley

A report on research sponsored by the California Department of Transportation
under contract RTA-59X517

PEER 1998/08
DEC. 1998

Behavior And Failure Analysis Of A Multiple-Frame Highway Bridge In The 1994 Northridge Earthquake

by

Gregory L. Fenves
Department of Civil and Environmental Engineering, University of California, Berkeley

Michael Ellery
Department of Civil and Environmental Engineering, University of California, Berkeley

A report on research sponsored by the California Department of Transportation under Contract RTA-59X517

Report No. PEER 98/08
Pacific Earthquake Engineering Research Center
College of Engineering
University of California
Berkeley, California

December 1998

ABSTRACT

The Route 14/Interstate 5 Separation and Overhead bridge, a curved ten-span structural concrete structure, partially collapsed in the 1994 Northridge earthquake. The primary objective of this study is to ascertain the cause of failure by comparing estimates of the capacities and demands of various components in the bridge. A secondary objective is to examine earthquake modeling and analysis recommendations for highway bridges. As part of the examination, nonlinear static analysis (push-over analysis) is used to determine the capacity of a frame. Linearized analyses are compared with nonlinear dynamic analysis results to evaluate the capability of simpler models to predict maximum earthquake displacement demands.

To simulate the earthquake response of the bridge, a three-dimensional nonlinear model was developed using the DRAIN-3DX computer program. A suite of four recorded and two simulated ground motion records were used for the time history analysis, assuming uniform free-field ground motion. The earthquake analysis provided estimates of the force and deformation demands of components. The demands were compared to the capacity of the piers, superstructure, and intermediate hinges to determine which component initiated the partial collapse of the bridge.

The demand-capacity comparison shows that shear failure of pier 2 in a brittle-ductile mode was the most likely cause of the collapse. Based on the analysis, pier 3 reached its shear capacity shortly after the time at which pier 2 reached capacity. The analysis indicated that there may have been minor yielding in the pier shafts below ground., The negative bending moment in the box girder over pier 3 nearly reached the flexural capacity or had started to yield at the time piers 2 and 3 reached their shear capacity. The displacement at intermediate hinge 4 was much less than the hinge seat width; it is unlikely that hinge unseating precipitated the collapse. The conclusions about the cause of the partial collapse of the bridge are consistent with the observed damage after the earthquake.

The three-dimensional model of the bridge was used to investigate the expected behavior of the bridge assuming seismic retrofit. For the model of the hypothetically retrofitted bridge, the maximum drift angle demands were 4% for piers 2 and 3 and approximately 2% for the other piers. The maximum curvature ductility demand, occurring at pier 2, is approximately 10. Had the bridge been retrofit, it would have experienced minor to moderate damage in plastic hinge zones of several piers. The analyses indicate the bridge would have been functional after the earthquake. These analyses also show that the vertical component of certain near-source ground motions can have a large effect on some of the structural response quantities, particularly column axial load and superstructure bending moments. The displacement response of the nonlinear model is compared with three-dimensional linear “compression” and “tension” models typically used in seismic design of bridges. The comparison indicates that the compression model adequately represents the displacement demands on the bridge.

ACKNOWLEDGMENTS

This study was sponsored by the California Department of Transportation under Research contract RTA 59X17. The support of James Roberts, Chief, Caltrans Engineering Service Center is appreciated. Caltrans engineering staff, including Ray Zelinski, Pat Hipley, and Brian Maroney provided valuable advice.

The Federal Highway Administration was instrumental in providing funding for post-Northridge earthquake investigations of bridges, including support for this project. James Cooper,, Phillip Yen, and Nancy Bobb of FHWA supported this study.

At the University of California, Berkeley, the following individuals assisted in aspects of the study: Jack Moehle, Phillip Meymand, Reginald DesRoches, and Frank McKenna. Janine Hannel of the Pacific Earhquake Engineering Research Center helped with the editing and in producing the final report. Larry Hutchings of the Lawrence Livermore National laboratory and Andrei Reinhorn of the State University of New York at Buffalo provided the simulated ground motion records used in the study.

The conclusions presented in this report are the views of the authors and do not necessarily reflect the views of the California Department of Transportation or the Federal Highway Administration.

Contents

List of Tables

List of Figures

Chapter 1

Introduction

A thorough evaluation of bridges that experience a large earthquake is important for improving understanding of the seismic performance of bridges. The January 17, 1994 Northridge, California earthquake caused the partial or complete collapse of five bridges, and it damaged approximately 200 others (EERI, 1995). The damage to structural concrete bridges included ductile-brittle shear failure or brittle shear failure of columns, unseating of superstructure at intermediate hinges, column spalling, and damage to abutments. Most of the damage to bridges in the Northridge earthquake was not surprising based on known deficiencies in bridges constructed prior to 1975. The minimal transverse reinforcement in columns designed prior to the 1971 San Fernando earthquake is a well-known deficiency that can lead to brittle or ductile-brittle shear failure of columns. Design provisions adopted by the California Department of Transportation beginning in 1975, and continually improved since then, have addressed the deficiencies in pre-1971 bridge construction. An extensive bridge retrofit program is providing a dramatic increase in seismic performance of older bridges in California. In fact, many of the bridges severely damaged in the 1994 Northridge earthquake had been scheduled for retrofit. Evaluation of the bridges damaged in the Northridge earthquake can assist engineers in understanding whether the current and proposed seismic design procedures are adequate and pointing the way towards improvements in seismic-resistant design.

This study examines the earthquake response of one of the most severely damaged bridges in the Northridge earthquake. The primary objective is to determine the cause of failure by comparing estimates of the capacities and demands of important components in the bridge. A secondary objective is to examine earthquake modeling and analysis recommendations for highway bridges (ATC-32, 1996). The models are also used to estimate the hypothetical behavior of the bridge if it had been seismically retrofit prior to the earthquake. As part of the examination, linearized analysis models are compared with nonlinear analysis to evaluate the capability of simpler models to predict maximum earthquake displacement demands.

1.1 Description of the Separation and Overhead Bridge

At the time of the 1994 Northridge earthquake the Route 14/Interstate 5 interchange consisted of four curved multiple-frame bridges and a number of shorter bridges. The interchange site is at the confluence of two narrow valleys. The site is located approximately 12 km north

of the Northridge earthquake epicenter. During the earthquake two spans of a sharply curved connector bridge from westbound Route 14 to northbound Interstate 5 collapsed completely. One frame (three spans) of the connector bridge from westbound Route 14 to southbound Interstate 5 collapsed. The latter bridge was designated the Route 14/Interstate 5 Separation and Overhead (Bridge No. 53-1960F), and it is the subject of this report. The other bridges in the interchange exhibited local damage due to spalling of concrete columns, pounding at the intermediate hinges, failed restrainer cables, and movement of the abutments.

The Separation and Overhead is a structural concrete ten-span bridge consisting of five frames as shown in Figure 2.1. The total length of the bridge is 482 m (1582 ft) and the box girder width is 16 m (53 ft). The bridge plan subtends an arc of 41° at a constant radius of 676 m (2220 ft). The superstructure is a multi-cell box girder with the frames alternatively conventionally reinforced and prestressed. The piers are single column bents with rectangular cross-section, tapering near the top, ranging in height from 9 m (28 ft) to 36 m (120 ft). The footings are drilled shafts embedded 12 to 18 m (40-60 ft) below grade into firm sandy soil. The abutments are seat-type with external shear keys, supported by spread footings.

At the time of the 1971 San Fernando earthquake, the interchange was under construction (Jennings, 1971) and the Separation and Overhead bridge was partially complete. All of the columns were constructed, as was the end frame from hinge 9 to abutment 11, although it had not been post-tensioned. The bottom slab and web stems from abutment 1 to pier 3 had been placed. The 1971 earthquake caused cracking in the soffit and web from abutment 1 to pier 3. The cracked concrete was removed and replaced. Abutment 1 required repair of the shear keys and wingwalls. The hinges were modified to the final 360 mm (14 in.) seat length and cable restrainers were added.

1.2 1994 Northridge Earthquake

The M_w=6.7 Northridge earthquake occurred on a reverse thrust fault below the northern part of the San Fernando Valley. The fault is part of a complex network of faults along the southern base of the Santa Susanna mountains. It is just west of the Sierra Madre fault system, the source of the 1971 San Fernando earthquake. The Route 14/Interstate 5 interchange is located about 12 km north of the Northridge epicenter and is within the surface projection of the fault rupture zone.

A large number of strong motion accelerographs were deployed in the Los Angeles area at the time of the earthquake and they recorded some of the largest accelerations and velocities ever obtained in an earthquake. Notable peak accelerations near the interchange include the Jensen Filtration Plant, Generator Building, PGA=0.98 g (292° component); Sylmar Converter Station, free-field, with PGA=0.90 g (142° component); Sylmar County Hospital, free-field, with PGA=0.91 g (360° component). The ground motion records from the earthquake clearly showed that areas north of the epicenter, which includes the Route 14/Interstate 5 interchange, experienced a large velocity pulse associated with the forward directivity of the updip rupture (Wald and Heaton, 1994). The stations north of the epicenter had peak ground velocities of up to 0.170 m/sec recorded at the Rinaldi Station.

Near-source forward directivity ground motion can be very damaging to bridges, and current design procedures do not directly recognize such effects.

After the earthquake there was discussion about the vertical ground motions and large peak accelerations in the epicentral region. In general, but with a few exceptions, the peak accelerations fit the pattern of previous earthquakes in which peak vertical accelerations are about two-thirds of the peak horizontal acceleration (Moehle, 1994). However, near-source instruments recorded peak vertical acceleration close to or exceeding the peak horizontal acceleration. The near-source records led to speculation that unusually large vertical accelerations was the cause of damage in bridges and buildings (Saadeghvaziri, 1996; Papazoglou and Elnashai, 1996). The effect of vertical ground motion on the Separation and Overhead will be examined in this study.

1.3 Damage to the Separation and Overhead Bridge

The 1994 Northridge earthquake caused the collapse of the first frame between abutment 1 and hinge 4 of the Separation and Overhead bridge. Damage to the bridge is described in a Caltrans (1994) post-earthquake report. The box girder unseated from abutment 1, moving north approximately 1.5 m (5 ft). There was no evidence that the box girder impacted the backwall of the abutment, but the external shear key on the east-side failed as the box girder slipped off the seat. The column at pier 2 was crushed underneath the fallen box girder. A post-earthquake photograph indicates a northerly longitudinal displacement of pier 2, which is consistent with the final position of the box girder north of abutment 1 (Priestley et al., 1994a). The box girder over pier 2 had flexural cracks in the bottom portion of the web, indicating flexural yielding due to positive bending moments. Pier 3 remained standing with the box girder having dropped on both sides of the pier. The bent cap was severely damaged at the top. At the next span, the box girder unseated at hinge 4 ending up on the ground slightly north of the original position under the seat at hinge 4.

Based on the field observation, a team from the Earthquake Engineering Research Center at the University of California, Berkeley, postulated that the failure of the frame was precipitated by shear failure of pier 2 (Moehle, 1994). A report from the National Center for Earthquake Engineering Research (Buckle, 1994) postulated that failure either started with brittle shear failure of pier 2, or possibly by unseating of the span at hinge 4 due to the spatial variation of ground motion in the narrow valley.

A team from the University of California, San Diego (Priestley et al., 1994a) investigated the failure of the bridge using the information available shortly after the earthquake. They determined that the post-tensioning tendons in the collapsed frame were ungrouted in galvanized steel ducts and only balanced 62% of the dead load. Priestley et al. (1994a) also observed that the ground level had been significantly excavated by up to 18 m (60 ft) in the vicinity of pier 2, whereas there was little or no excavation near pier 3. The constitutive properties of the soil and hence the behavior of the pier shaft can be significantly affected by the state of the soil. Based on their examination, Priestley et al. (1994a) inferred the following sequence of failure:

1. The pier 2 column failed in brittle shear mode, most likely in the longitudinal direction.

2. Failure of pier 2 caused excessive positive bending moment in the box girder over pier 2 and a plastic hinge formed in the box girder.

3. The negative bending moment over pier 3 suddenly increased with the loss of support from pier 2, and a plastic hinge began to form in the box girder above pier 3.

4. The prestressing tendons reached their ultimate strain as the plastic hinge formed in the negative bending region over pier 3. The sudden fracture of the tendons released explosive forces at the top of the pier 3 cap beam.

5. Spans 1-3 then collapsed. The cantilever from pier 3 to hinge 4 dropped at pier 3, pulling the box girder off the hinge seat.

Although Priestley et al. (1994a) show it was unlikely that the frame collapsed by a punching shear failure of the box girder at pier 3 and that vertical ground motion could not have caused the failure, another study (Saadeghvaziri, 1996) argues for this scenario. Both Priestley et al. (1994a) and Saadeghvaziri (1996) estimate that a peak vertical ground acceleration of 0.40 to 0.46 g in the downward direction would have initiated failure of the superstructure. However, Priestley et al. (1994a) argues that superstructure failure would have been associated with unrealistically large flexural ductility demand and displacement because the shear capacity of the box girder is adequate. In contrast, Saadeghvaziri (1996) states that the shear capacity of the box girder at pier 3 was less than the shear force required to develop a plastic hinge in the box girder, and the failure was precipitated by brittle shear failure. Saadeghvaziri (1996) concludes that pier 2 failed when the lateral force was suddenly transferred from pier 3 to pier 2 after shear failure of the superstructure.

A recent study of the Separation and Overhead bridge by Mylonakis et al. (1997) examined the role of spatial variation in the ground motion as a factor in the damage and collapse of the frame. They developed an inelastic model of the bridge, and studied the response as determined from nonlinear dynamic analysis with the IDARC-Bridge computer program (Reichman and Reinhorn, 1995). The foundation was modeled as frequency-independent springs below the ground surface, so model did not allow yielding of the shaft below the ground. The non-uniform ground motion at the site was developed by Horton and Barstow (1995), which will be discussed in Section 2.3 of this report. The results of the study show that the effects of the spatial variation of ground motion are less than 15% on column displacements when compared with the response due to uniform ground motion. The analyses show that the vertical component of ground motion had an even smaller effect. The vertical accelerations are not sufficiently large that they would have an influence on the inelastic shear and flexural behavior of the columns. The demands in the columns did not exceed the capacities, except for piers 3, 4, and 5 in the transverse direction, so the study was inconclusive as to the cause of failure. However, Mylonakis et al. (1997) discount hinge unseating and vertical ground motion as the precipitate cause of collapse. A range of cases with different modeling assumptions showed the sensitivity of the earthquake response to the assumed boundary conditions. The elastic time history analysis overestimated column displacements by a large margin compared with the nolinear dynamic analysis.

1.4 Scope of the Report

The primary objective of this study is explain the damage to the Separation and Overhead bridge in the 1994 Northridge earthquake. This is accomplished by a thorough evaluation of the capacities of the components, estimate of the motion at the interchange site, and a demand analysis of the bridge using nonlinear dynamic analysis. Chapter 2 describes the bridge and the ground motion in the 1994 Northridge earthquake. Chapter 3 presents the modeling of the bridge, which is used for the static and dynamic analyses. The capacity of the columns, box girders, and hinges are determined in Chapter 4. In addition a nonlinear static analysis ("pushover analysis") of the first frame is performed to examine the longitudinal force-displacement relationship and the onset of various limit states. Chapter 5 presents the results of the dynamic analysis for the postulated ground motions at the site. The likely sequence of failure in the earthquake is identified. The effect of the vertical ground motion on the failure mechanism is examined, as is the uncertainty of the ground elevation at pier 2. Chapter 6 presents the response analysis of the bridge assuming the columns had been retrofit to have sufficient shear strength. Comments about the system and component behavior for strong near-source ground motion are made. The capacity of the bridge is examined and other potential failure modes identified. The modeling and earthquake analysis guidelines in the ATC-32 report (ATC-32, 1996) are examined. Finally, Chapter 7 presents the conclusions of the study.

Chapter 2

Description of Site, Bridge, and Earthquake

2.1 Site Description

The Route 14/Interstate 5 interchange is located at the juncture of two valleys bordered by hills forming a topographic basin. The geology is generally "soft rock" consisting of weathered and fractured sandstone (Hutchings and Jarpe, 1996). Laboratory tests of the sandstone at four sites showed a variation of small strain shear modulus by over a factor of two. Near piers 2, 3, and 6 to 9 the sandstone is overlayed by stiff alluvial deposits of unconsolidated silts and sands with a small strain shear wave velocity of about 300 m/sec (980 ft/sec). The alluvial deposits overlay a poorly consolidated layer of siltstones and sandstones to a depth of about 30 m (100 ft) (Horton and Barstow, 1995). The topographic character of the basin, varying properties of the sandstone, and surficial soil can lead to differences in earthquake ground motion over short distances.

The natural and constructed ground level of the site is of considerable importance to the earthquake response of the bridge in the 1994 Northridge earthquake. The design drawings show a cut of the natural soil from abutment 1 to north of pier 2. Priestley et al. (1994a) comment that the ground level appears to have been excavated by up to 18 m (60 ft) in the vicinity of pier 2, whereas there was little or no excavation near pier 3. As will be discussed in subsequent sections, the condition of the excavation affects the the soil properties and the free length of the pier 2 column. The effect of the ground elevation at pier 2 on the earthquake response is examined in the analyses.

2.2 Bridge Description

The Separation and Overhead is a ten-span, 483-m (1584-ft) long bridge with a cast in-place structural concrete box girder superstructure, as shown in Figure 2.1. The bridge consists of five frames with single column piers, connected at four intermediate hinges. The two end frames and the central frame have prestressed box girder superstructures, whereas the second and fourth frames are conventionally reinforced box girder superstructures. The alignment

of the bridge is in a nearly north-south direction.

Figure 2.2 shows the elevations of pier 2 as an example of the single column bents with the foundation shaft. The column heights vary considerably over the bridge, as shown in Figure 2.3. The tallest column is pier 7 at about 37 m (120 ft) tall. Pier 2 is the shortest with a nominal height of 8.7 m (28 ft), but it may be shorter because the actual ground level may be higher than that indicated in the design drawings. The pier may be as short as 7.0 m (23 ft), although an accurate survey of the site at the time of the earthquake is not available.

The nominal material strengths specified in the design drawings; material tests were not performed after the earthquake. Most piers have a specified concrete compressive strength of 28 MPa (4 ksi); the taller piers 8 and 9 have a specified concrete strength of 21 MPa (3 ksi). The concrete specified for the superstructure, both the reinforced and post-tensioned frames, has a strength of 24 MPa (3.5 ksi). For the modeling and analysis the concrete is estimated to have a realistic compressive strength of 34 MPa (5 ksi) for the piers and 30 MPa (4.4 ksi) for the superstructure. The grade 60 longitudinal reinforcement is assumed to have an actual yield stress of 460 MPa (67 ksi). The column transverse reinforcement is assumed to be grade 40 with an actual yield stress of 310 MPa (45 ksi).

The coordinate systems used in the capacity and demand analysis of the bridge are shown in Figure 2.4. The global X-axis is in the direction of the chord connecting the abutments, which is 1.7° east of magnetic north. The global Y-axis is orthogonal to the chord and the global Z-axis is vertical. The X and Y-axes are referred to as the global longitudinal and global transverse directions, respectively. For the demand analyses, the pier responses are reported in the local coordinate system aligned with the principal axes of the pier, as shown in Figure 2.4. The local longitudinal direction is tangential to the curve, and the transverse direction is radial to the curve.

2.2.1 Superstructure

The superstructure for the Separation and Overhead bridge is a five-cell box girder, 16.2 m (53 ft) wide by 2.1 m (7 ft) deep, as shown in Figure 2.5. The prestressed box girder has a deck and soffit thickness of 180 mm (7 in.) and 150 mm (6 in.), respectively, and the web thickness is 300 mm (12 in.). The prestressed sections have six prestressing tendons per web, each of which consists of ten 13 mm (0.5 in.) nominal diameter strands. Grouting of the tendons is not specified on the construction drawings and the absence of grout was confirmed by observations at the site after the 1994 Northridge earthquake (Priestley et al., 1994a). The conventionally reinforced box girder differs only slightly in dimensions with a deck and soffit thickness of 180 mm (7.25 in.) and 160 mm (6.25 in.), respectively, and a web thickness of 200 mm (8 in.).

2.2.2 Substructure

The superstructure is supported on nine single-column bents. The columns are nearly rectangular in cross section and vary from 1.2 m (4 ft) by 3.7 m (12 ft) to 1.8 m (6 ft) by 3.7 m (12 ft) with chamfers at the four corners. The upper 4.3 m (14 ft) of the columns are

tapered. The wide dimension of the column tapers from 3.7 m (12 ft) to 7.9 m (26 ft) at the soffit, and the narrow dimension is constant. Piers 6 through 9 have internal voids that extend from the soffit of the box girder to ground level. All columns continue into the ground as a 3.7-m (12-ft) diameter cast-in-place drilled shaft.

The geometric and reinforcement details of the columns are summarized in Table 2.1 and Figures 2.6 and 2.7. The longitudinal reinforcement consists of 28 or 40- #18 bars extending from the bent caps to a distance below ground that is 2/5 of the shaft length (but not to exceed 7.6 m or 25 ft). At that elevation all but eight of the longitudinal bars terminate. The longitudinal reinforcement at the top of the columns follows the shape of the taper and enters the bent cap at an angle. The transverse reinforcement consists of #5 hoops at 300 mm (12 in.). Additionally, 3- #4 bars are spaced at 300 mm (12 in.) spanning the short dimension of the column. Anchorage hook details for the transverse reinforcement are not specified on the drawings. Piers 6 through 9 have a nominal amount of shrinkage steel placed near the face of the interior voids.

Table 2.1: Column Properties

Pier Number	Length Above Ground m (ft)	Length Below Ground m (ft)	Gross Area A_g m^2 ($in.^2$)	Longitudinal Reinforcement Ratio ρ_l (%)	Approximate Axial Force Due to Dead Load P MN (kips)	Approximate Dead Load Ratio $\frac{P}{f'_c A_g}$
2	8.67 (28.4)	14.6 (48.0)	4.21 (6520)	2.45	14.4 (3240)	0.099
3	8.97 (29.4)	16.8 (55.0)	4.21 (6520)	2.45	14.3 (3210)	0.098
4	12.8 (41.9)	11.6 (38.0)	4.21 (6520)	1.72	11.0 (2480)	0.076
5	13.3 (43.6)	15.8 (52.0)	4.21 (6520)	1.72	11.0 (2470)	0.076
6	24.5 (80.3)	14.6 (48.0)	3.67 (5688)	2.81	15.2 (3420)	0.120
7	36.5 (119.8)	12.2 (40.0)	4.00 (6210)	1.80	12.0 (2690)	0.087
8	26.2 (85.8)	10.7 (35.0)	4.00 (6210)	1.80	9.39 (2110)	0.068
9	27.9 (91.4)	10.7 (35.0)	4.00 (6210)	1.80	11.5 (2590)	0.083
10	12.9 (42.2)	15.2 (50.0)	4.21 (6520)	1.72	14.6 (3290)	0.100

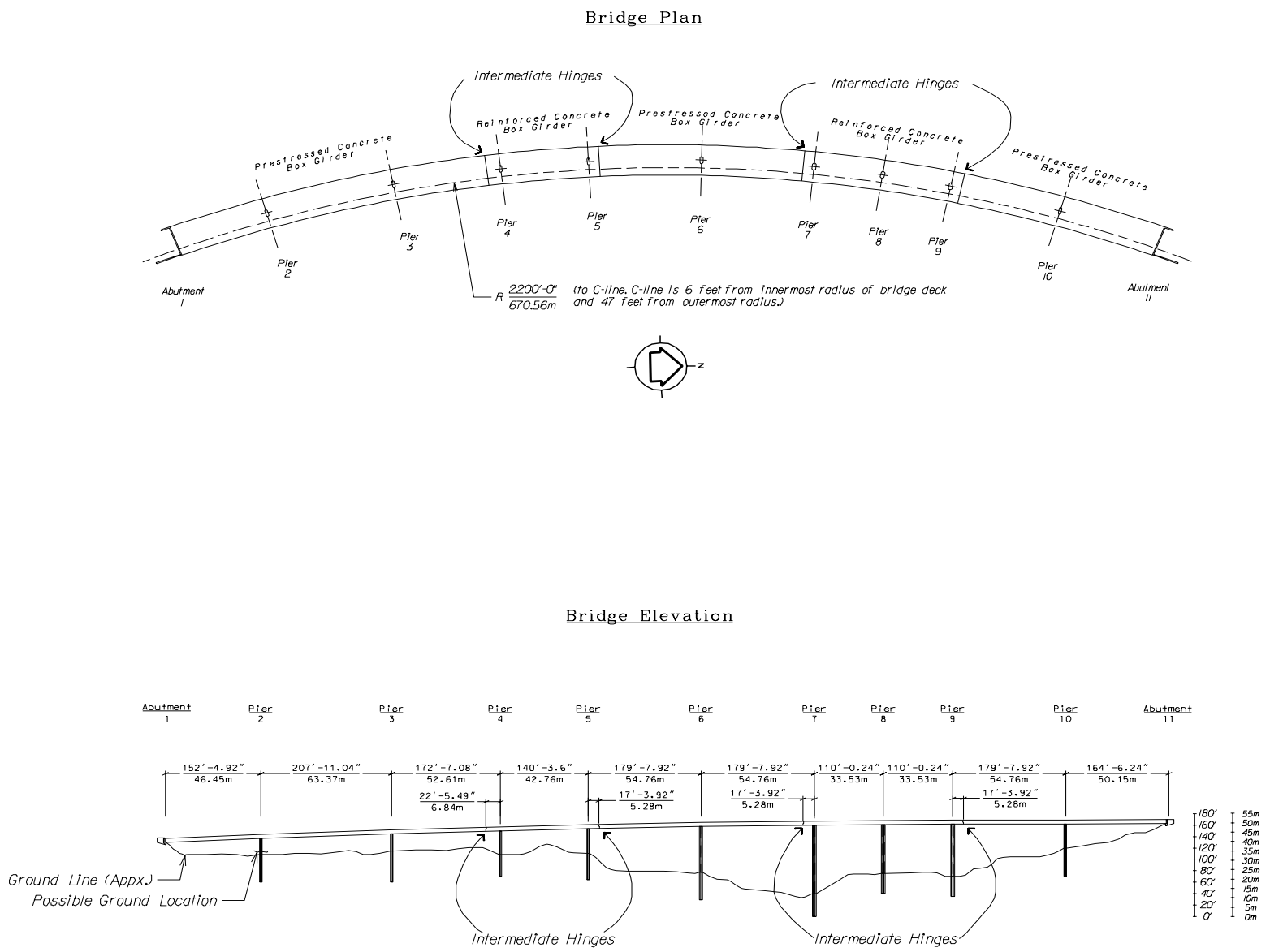

Figure 2.1: General Elevation and Plan for Route 14/Interstate 5 Separation and Overhead Bridge

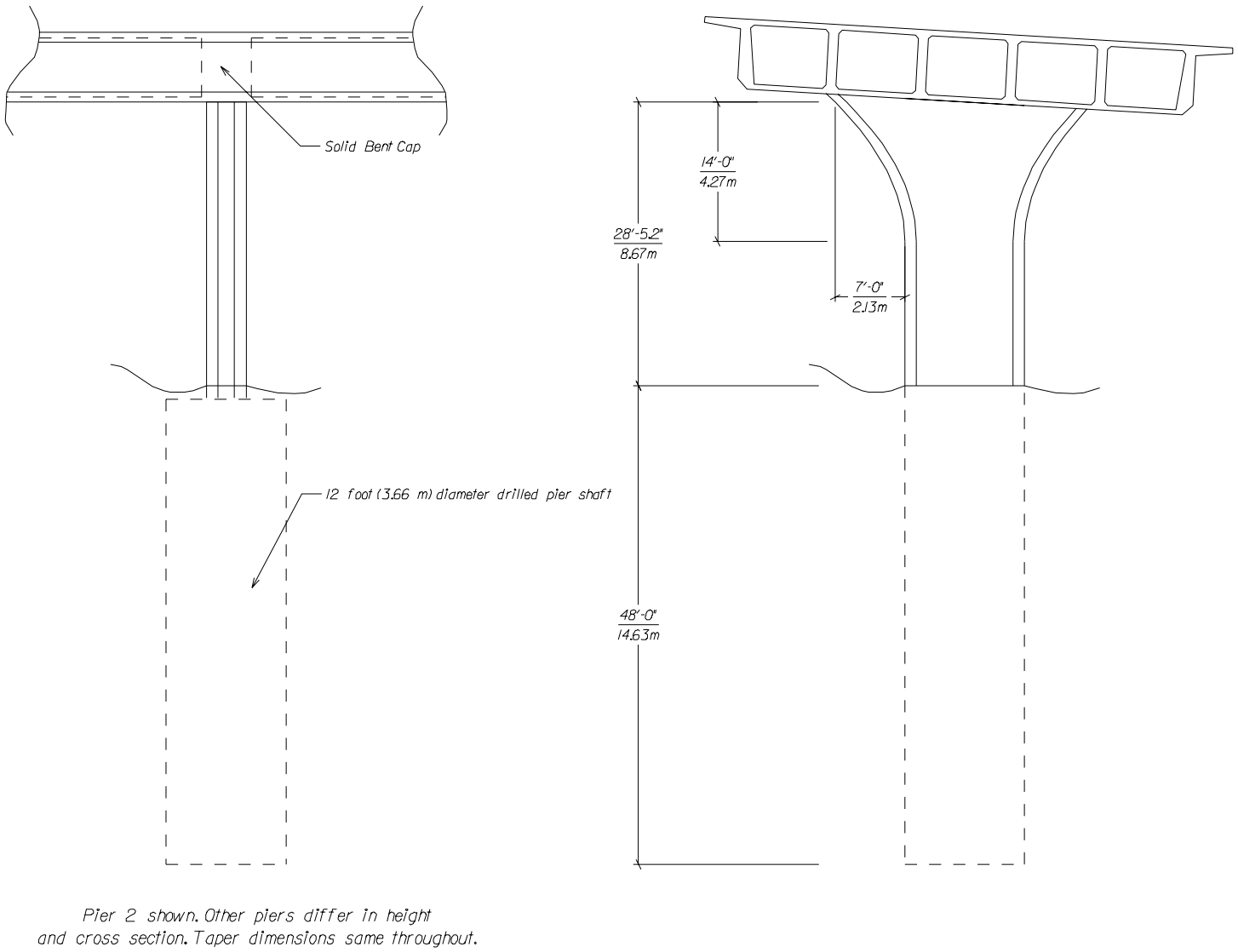

Figure 2.2: Typical Bent Elevations

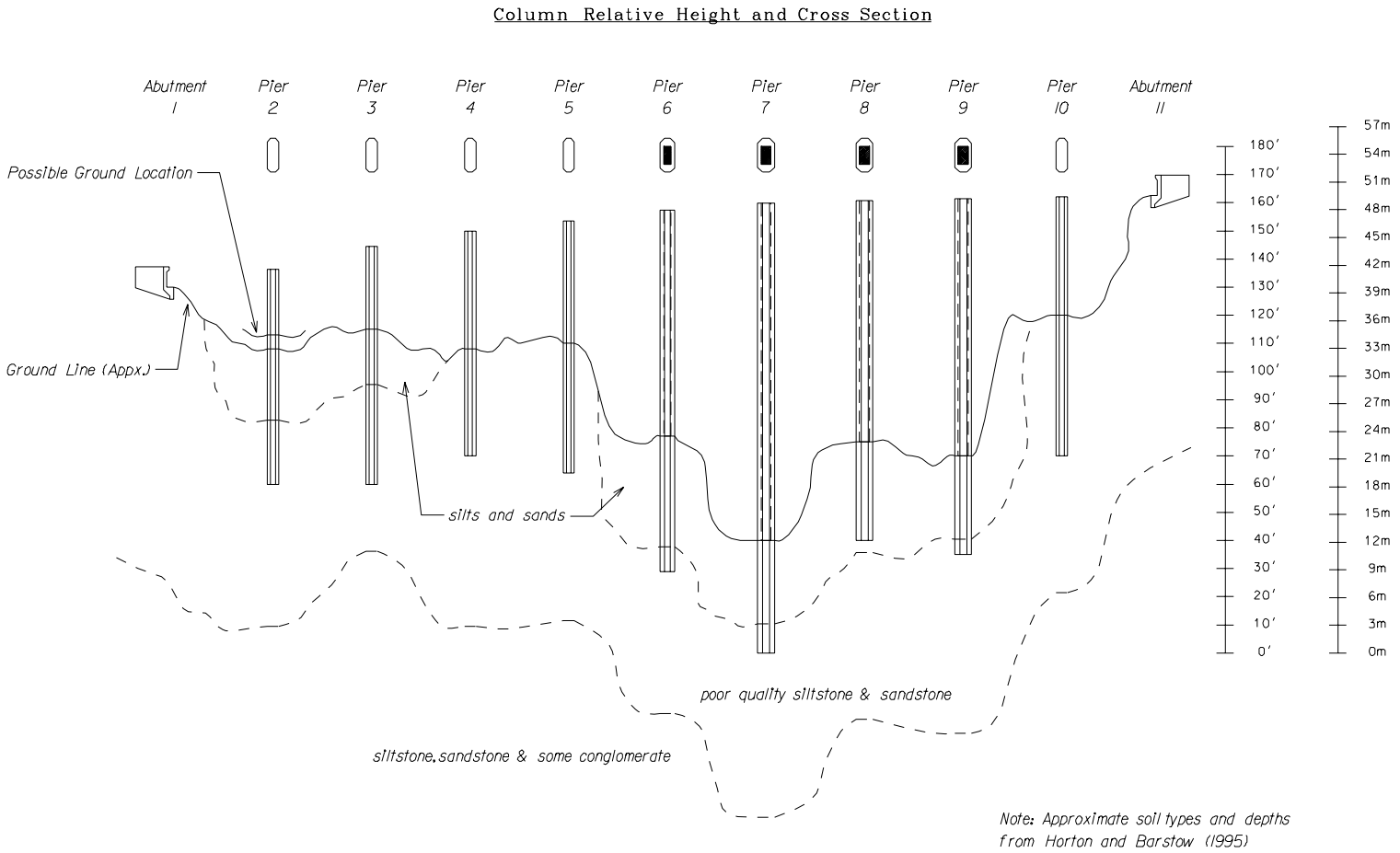

Figure 2.3: Column Heights, Cross Section, and Soil Layers

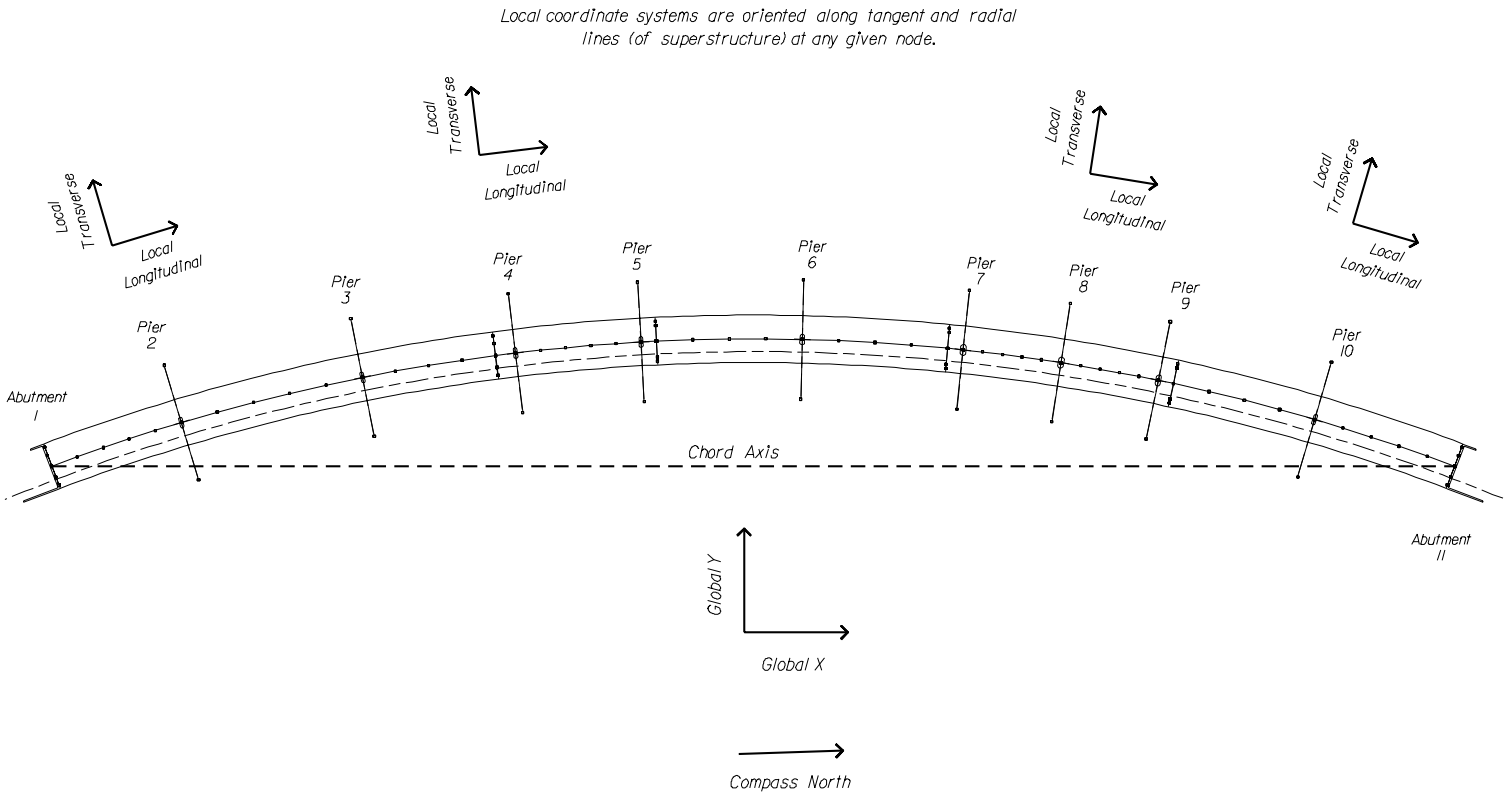

Figure 2.4: Coordinate System for the Bridge

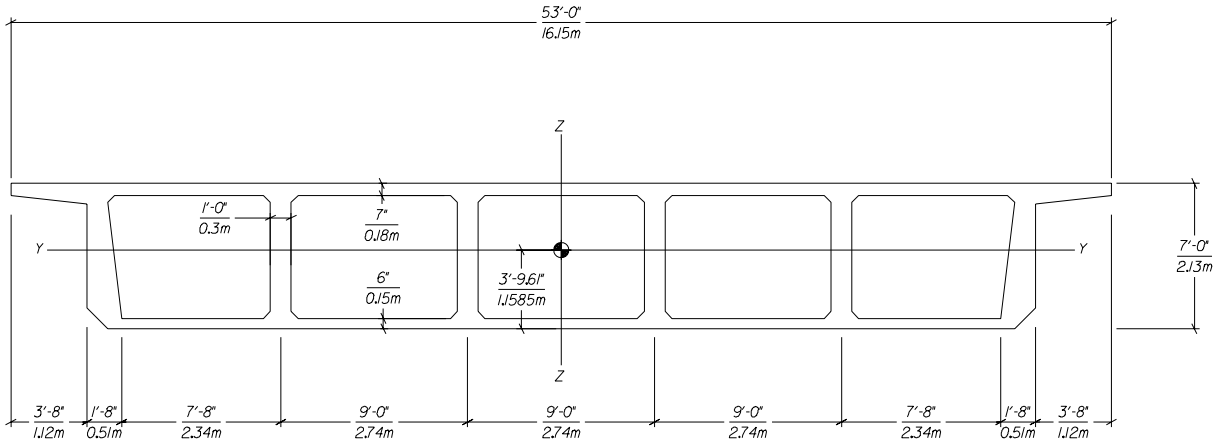

C.I.P. Prestressed Box Girder Section

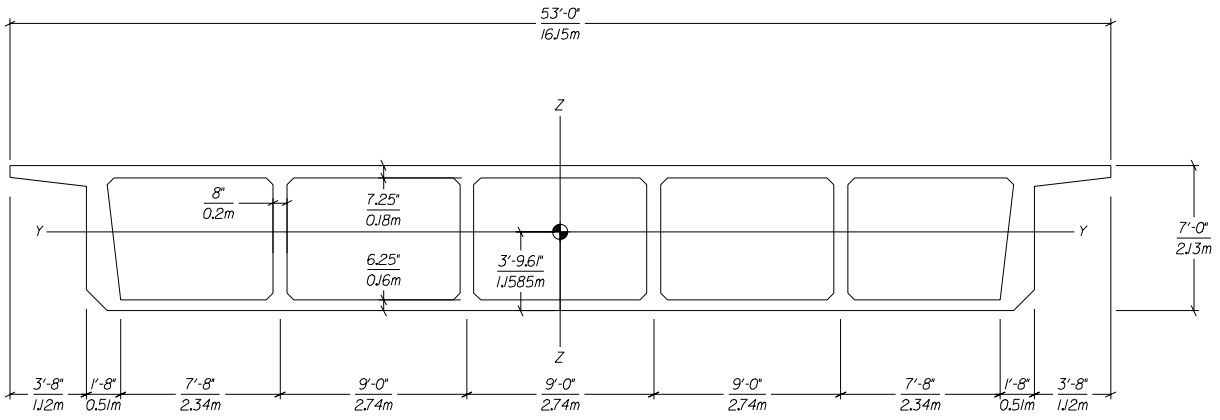

Reinforced Box Girder Section

Figure 2.5: Superstructure Box Girder Cross Sections

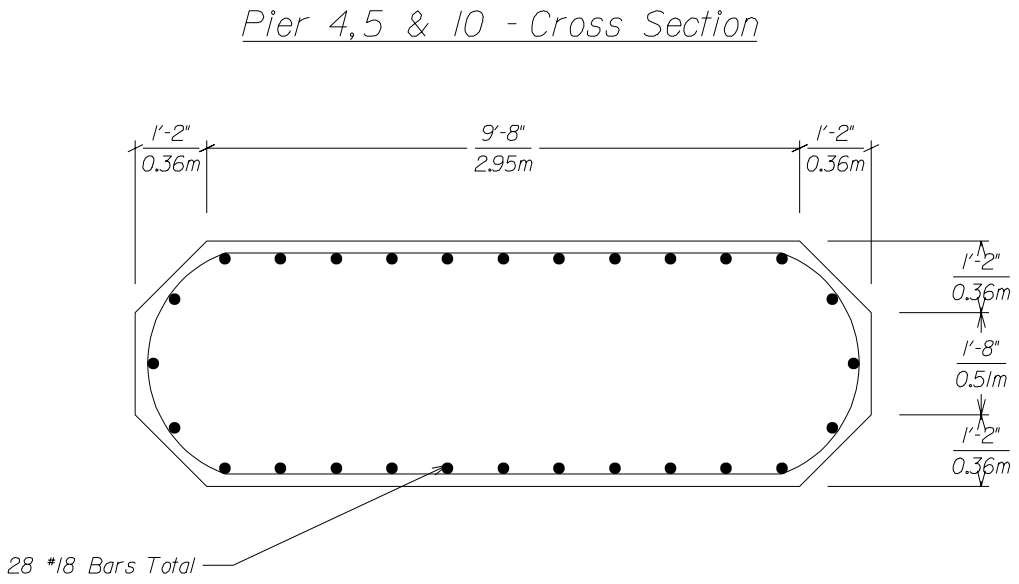

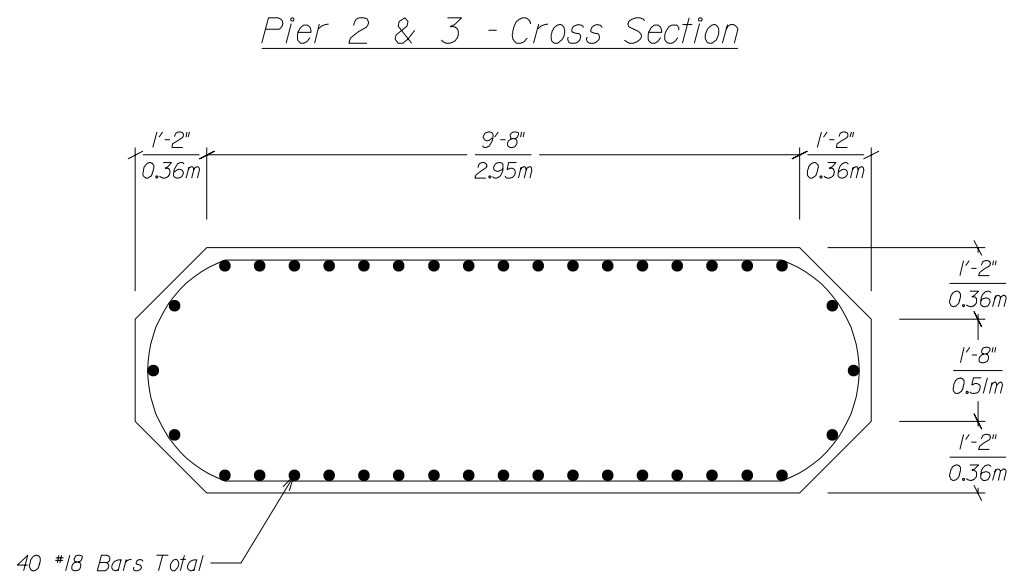

Figure 2.6: Column Cross Sections for Piers 2 to 5 and 10

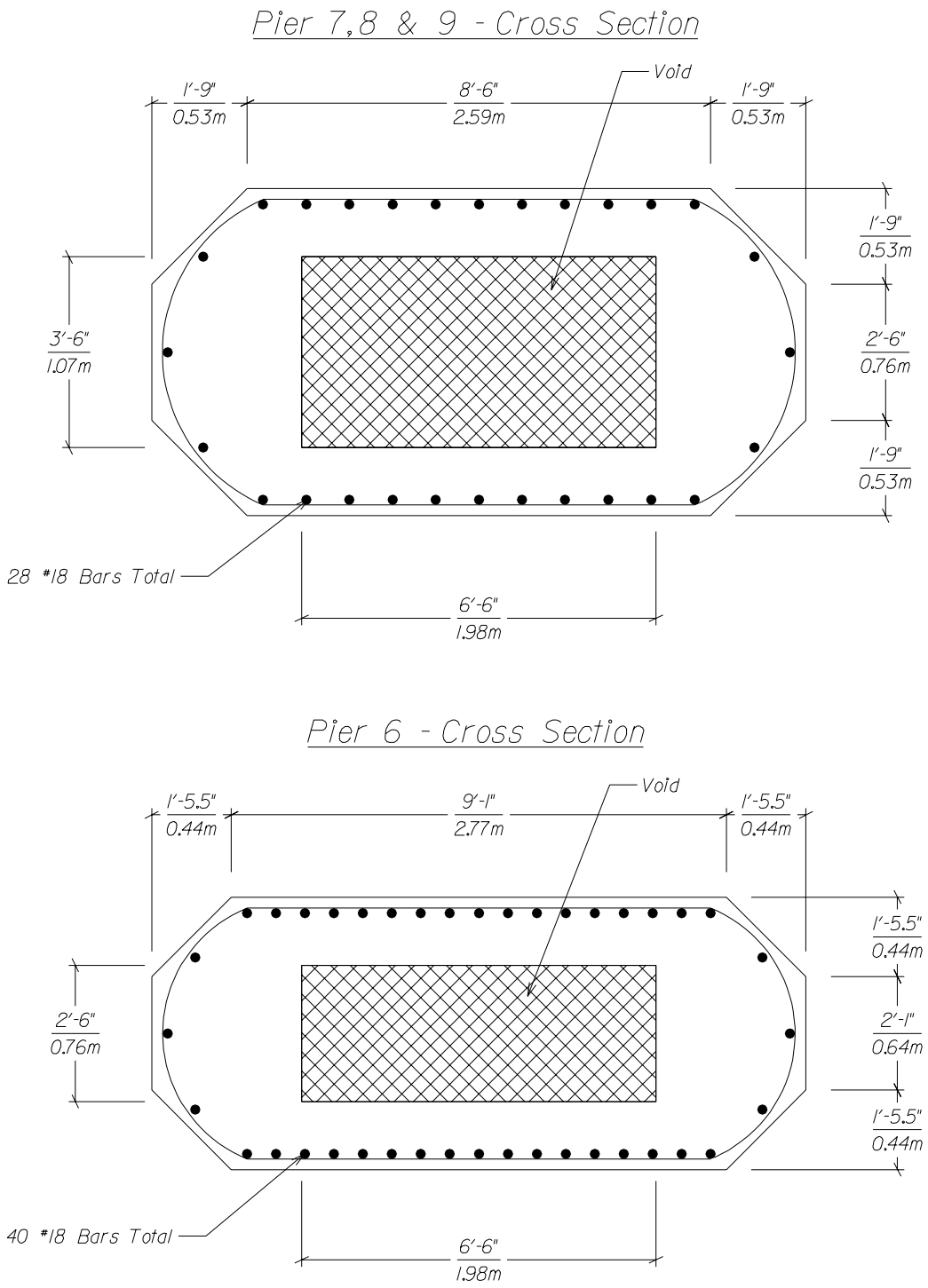

Figure 2.7: Column Cross Sections for Piers 6 to 9

2.2.3 Abutments and Hinges

The seat-type abutments are founded on spread footings with the layout shown in Figure 2.8. The abutment seat width is 600 mm (24 in.) and six elastomeric bearing pads support the box girder under the webs. Transverse displacement of the box girder at the abutment is restricted by external shear keys on either side of the abutment. The drawings show 25 mm (1 in.) of expansion joint material between the box girder and a 300 mm (12 in.) extension at the top of the backwall. There is a 250 mm (10 in.) gap between the box girder and the abutment backwall.

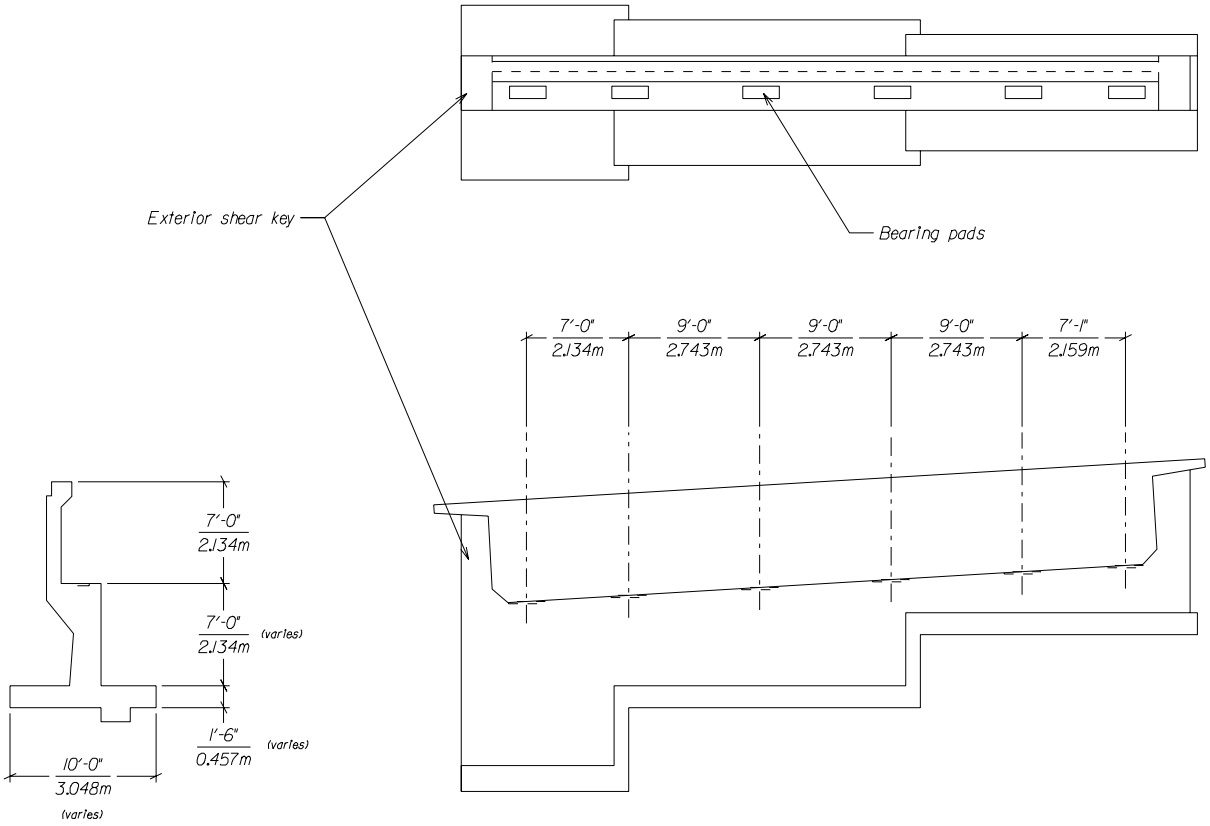

Figure 2.8: Plan and Elevation of Seat-Type Abutment

The superstructure frames are connected at intermediate, or in-span, hinges of the design shown in Figure 2.9. Each hinge is referred to herein by the number of its nearest pier. The hinges have seats with 350 mm (14 in.) seat length. The webs of the box girder are supported by six elastomeric bearing pads at the hinges. Relative transverse displacement of the hinges is restricted by a shear key 1700 mm (66 in.) long by 300 mm (12 in.) high.

During construction after the 1971 San Fernando earthquake longitudinal and vertical cable restrainers were installed in the intermediate hinges. The cables extend through diaphragms in the box girders. Hinge 4 has a Type 1 restrainer unit consisting of a circular array of seven cables with swagged fittings. The individual cables have nominal 20-mm (3/4-in.) diameter (area = 140 mm^2 or 0.22 in^2), and the yield force is 170 kN (39 kips) per cable.

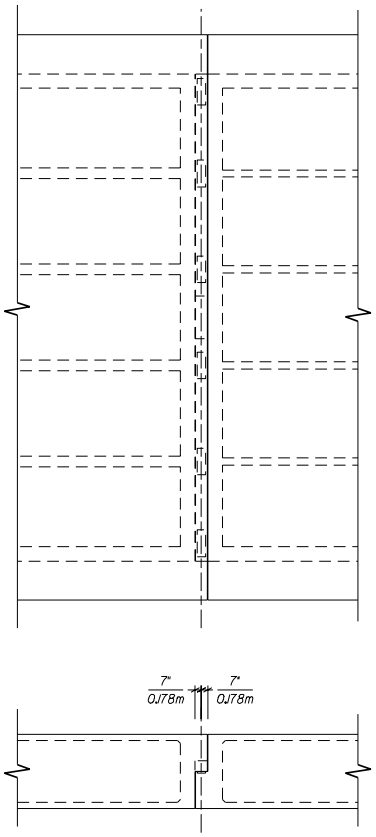

Figure 2.9: Typical Intermediate Hinge

For hinge 4 the restrainers are 1.83 m (6 ft) long and one unit is placed in each exterior cell. Hinges 5, 7 and 9 are fitted with type 2 hinge restrainer units with eight cables. Two units are located in the two outermost cells of the superstructure for a total of 32 cables per hinge. The restrainer cables at hinge 5 are 7.2 m (24 ft) long, and at hinges 7 and 9 the cables are 7.5 m (25 ft) long. The hinges also have four vertical restrainer cables, 20-mm (3/4-in.) in diameter, anchored above and below the hinge.

2.3 Ground Motion at the Site in the 1994 Northridge Earthquake

The M_w=6.7 Northridge earthquake occurred on a southwest dipping blind reverse thrust fault below the northern San Fernando Valley area of Los Angeles. The focal depth was a relatively deep 19 km (12 mi) and there was no evidence of fault slip above the 7 km (4.3 mi) depth nor of surface rupture (Wald and Heaton, 1994). The Route 14/Interstate 5 interchange is approximately 12 km (7.5 mi) north of the epicenter. With the fault strike at 119 deg, the updip rupture produced forward directivity effects at the interchange site. The interchange site is on the hanging wall, so it likely experienced increased motion due to that

effect (Somerville and Abrahamson, 1996).

No strong motion records were obtained at the interchange site in the main shock, although records are available from other locations in the epicentral region. Aftershock motion at the interchange were recorded and, as described below, used by other investigators to simulate the ground motion in the valley for the main event. This section summarizes the recorded and simulated strong motion records that are used in the demand analysis of the Separation and Overhead bridge.

2.3.1 Recorded Ground Motion Records

The recorded ground motions from the 1994 Northridge earthquake used in this study are from accelerograph stations at Arleta, Jensen Filter Plant Generator Station, Newhall, and Sylmar Hospital free-field. These strong motion records have the largest strong motion accelerations recorded near the interchange site and generally characterize the earthquake motion in the epicentral region. Tables 2.2, 2.3, and 2.4 give the peak ground motion values in the global X, Y, and Z-axes, respectively, as defined in Figure 2.4.

The Arleta Nordhoff Avenue Fire Station accelerograph was located 10 km (6.25 mi) from the epicenter (Darragh et al., 1994). Although the ground motion recorded at the Arleta station has smaller amplitude than the other records, it used to examine the effect of vertical ground motion on the bridge response because the peak vertical acceleration is greater than the peak horizontal acceleration. The acceleration histories are shown in Figure 2.10.

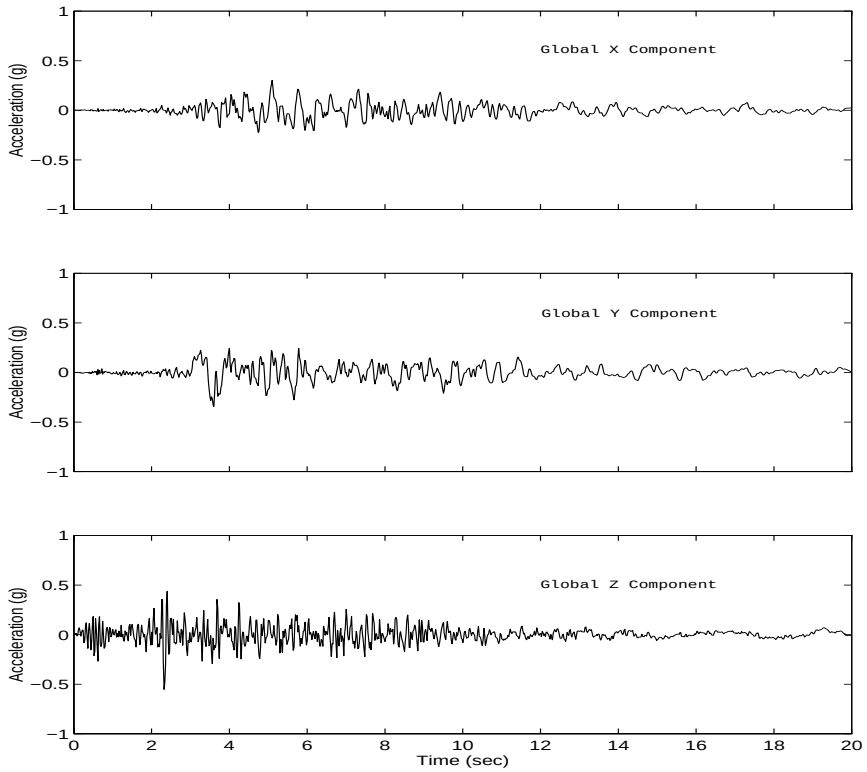

Figure 2.10: Free-Field Ground Motion Recorded at Arleta Station

The Jensen Filter Plant is located above the fault rupture zone (with an epicentral distance of 12 km or 7.5 mi), approximately 4 km (2.5 mi) south of the interchange. Of the three accelerographs at the plant, the one in the single-story generator building is closest to recording a free-field ground motion. However, comparisons between the Generator Station record with other rock free-field sites has led to speculation that adjacent structures or site response effects may have amplified the ground motion at the generator building (EERI, 1995). The acceleration histories are shown in Figure 2.11.

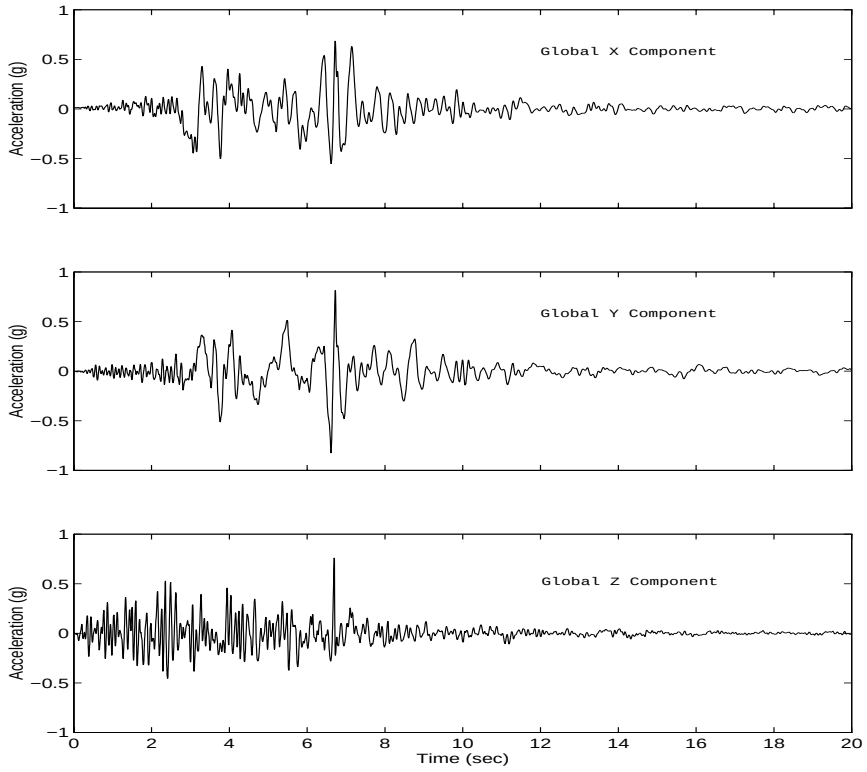

Figure 2.11: Free-Field Ground Motion Recorded at Jensen Filter Plant, Generator Building

The Newhall Los Angeles County Fire Station accelerograph located 7 km (4.3 mi) north of the interchange and 20 km (12 mi) north of the epicenter, showed a forward directivity pulse (Darragh et al., 1994). The velocity pulse was fairly large, leading to large peak ground displacement, which can be seen in Figure 2.12. The vertical component of the Newhall record has large pseudo- acceleration ordinates for periods from 0.25 sec to 0.40 sec. The bridge has significant vertical vibration modes in this period range.

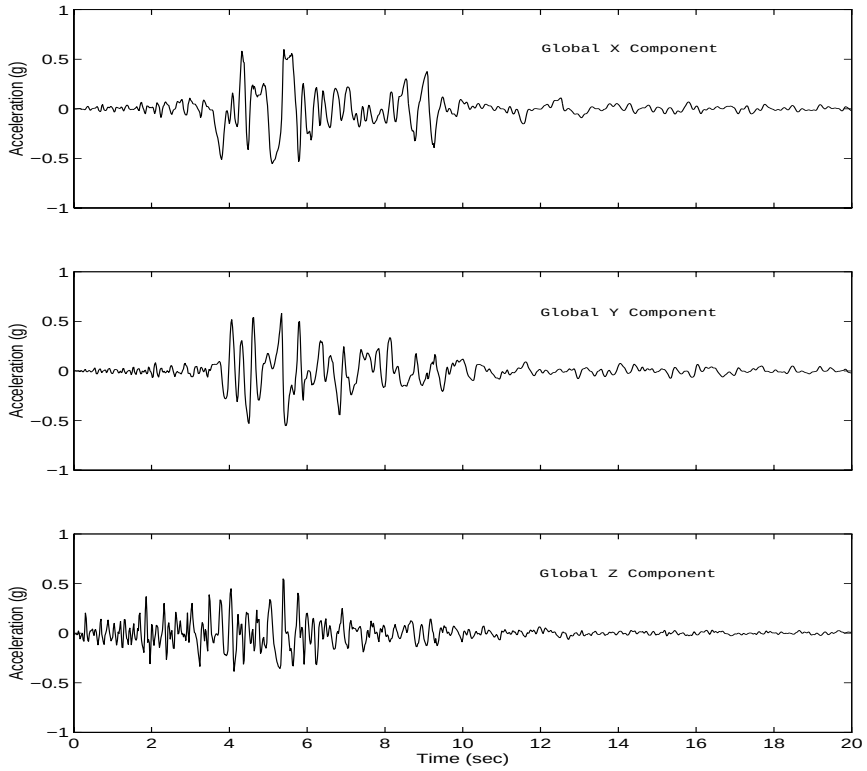

Figure 2.12: Free-Field Ground Motion Recorded at Newhall Station

The Sylmar County Hospital Parking lot (free-field) accelerograph was 16 km (10 mi) northeast of the epicenter and approximately 6 km (3.7 mi) east of the interchange (Darragh et al., 1994). The peak ground acceleration and velocity of 0.89 g and 1.29 m/sec (51 in./sec), respectively, were among the largest ever recorded in an earthquake. The acceleration histories are shown in Figure 2.13.

2.3.2 Simulated Ground Motions

Although strong motion records were obtained within 10 km (6.2 mi) of the the Separation and Overhead bridge, they may not completely represent the ground motion at the site. The narrow valley raises questions about the effect of topography and site response on the spatial variation of ground motion in the valley.

Horton and Barstow (1995) recorded data from 50 aftershocks with nine accelerographs deployed around the interchange. The low frequency motion (up to 3 Hz, which encompasses the important vibration modes of the bridge), was obtained from a deterministic finite fault model derived by inversion from main shock records (including Jensen, Newhall, and Sylmar Hospital). The high frequency simulation (up to 20 Hz) used aftershock data recorded at the site. The base motion has peak accelerations of 0.71 g, 0.77 g, and 0.34 g in the east, north, and vertical directions, respectively. The base motion was then modified by including a wave propagation, site response, and local site incoherence. The wave propagation is based on a shear wave velocity of 2.0 km/sec (1.2 mi/sec) in the base rock, a point source, and an angle

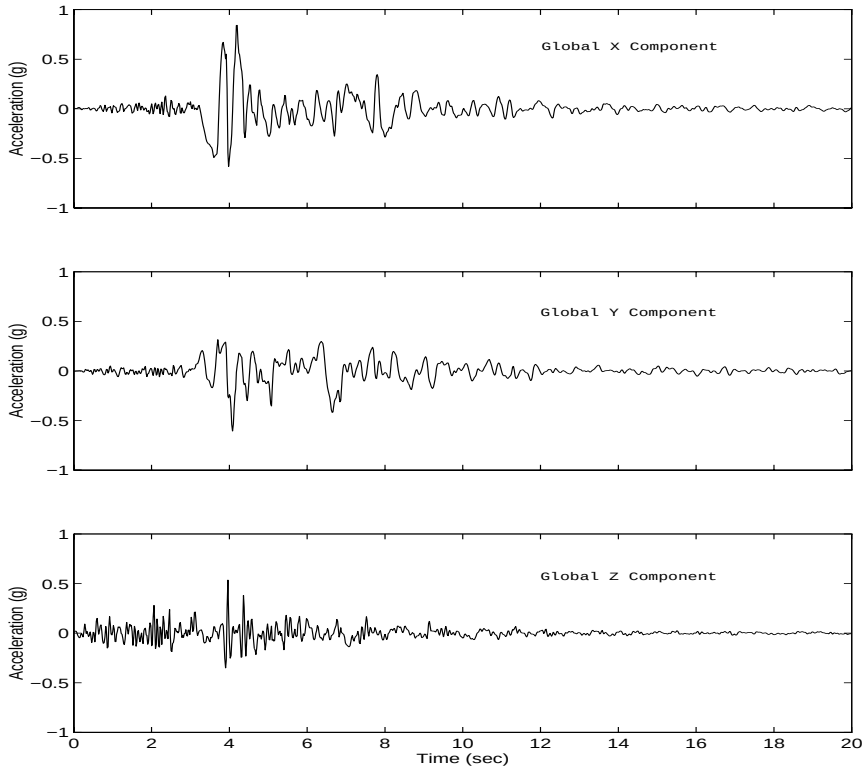

Figure 2.13: Free-Field Ground Motion Recorded at Sylmar Station

of incidence of 30 deg. The apparent propagation velocity is 3.9 km/sec (2.4 mi/sec), which produces a maximum time lag of 0.121 sec across the length of the bridge. The site response effect was incorporated by an analysis procedure that accounts for different waves in the soil layer. To simulate the incoherence observed in the aftershock data, the phase of the motion at each pier was randomized for components above 3 Hz. The results of the simulation were three components of acceleration, velocity, and displacement histories at the eleven supports of the bridge.

The simulated ground motion at the eleven supports of the bridge from the Horton and Barstow (1995) study are substantially similar. The maximum relative displacement along the chord axis of the bridge is 100 mm (3.9 in.). Although the abutment 1 motion is somewhat larger, the ground motion at pier 3 is considered representative of the motion for the bridge. Figure 2.14 plots the simulated simulated acceleration histories at pier 3.

In a separate study, Hutchings and Jarpe (1996) simulated motions at the interchange site using a different methodology. Aftershock data were recorded at three locations, each approximately 300 m (980 ft) apart, along the roughly north-south axis of the bridge. Spectral ratios of the aftershock records were analyzed to determine the topographic and site response characteristics in the valley. The data showed amplification factors that differ by a factor of 2 to 4 between the three sites. The differences are caused by focusing at the edge of the valley and differences in site response (Hutchings and Jarpe, 1996). Additional data indicated that the differences in ground motion were much less over separation distances of 50 to 100 m (160 to 320 ft). The ground motion in the main event was synthesized using empirical

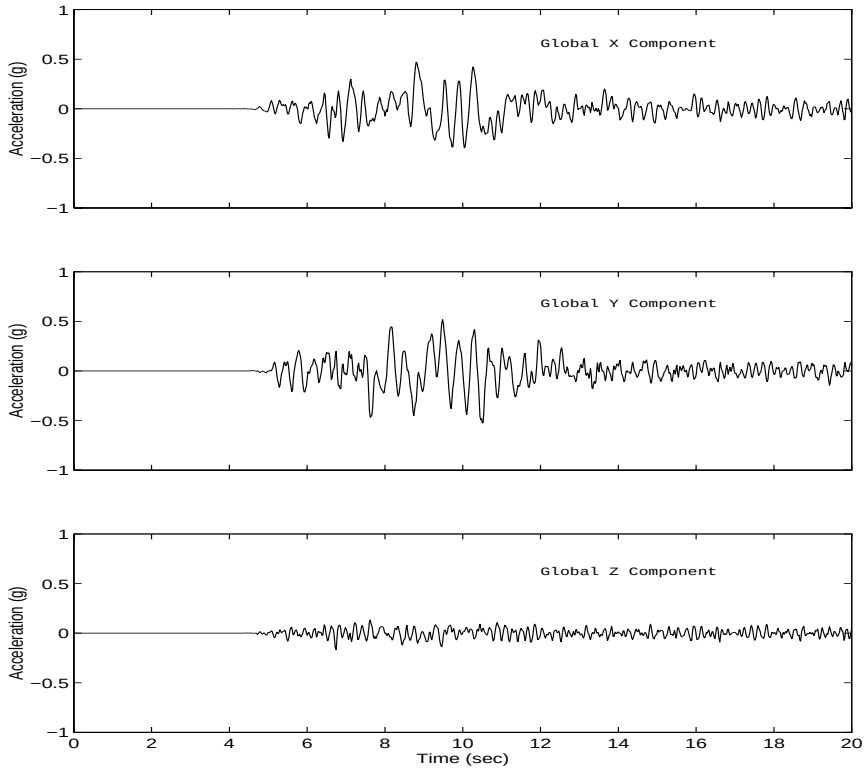

Figure 2.14: Horton et al. (1995) Simulated Ground Motion at Pier 3

Green's functions from 0.3 to 25 Hz (including all the vibration modes of the bridge), and synthetic Green's functions below 0.3 Hz (which effects slowly applied relative displacements of the bridge piers). A slip and rupture model for the source is used to represent the main event.

In the (Hutchings and Jarpe, 1996) simulation the peak acceleration differs by nearly a factor to two between the three sites, which is attributed to the topography and geology of the site. Tables 2.2, 2.3, and 2.4 give the peak ground motion parameters for the simulated motion at two locations (ICN and IRK) separated by 300 m (980 ft). Figures 2.15 and 2.16 plot the acceleration histories. The maximum differential displacement in the north-south direction is 400 mm (15 in.) over 300 m (980 ft) and 700 mm (28 in.) over 600 m (1960 ft). The latter value for differential ground displacement is seven times greater than from the Horton and Barstow (1995) simulation. The differential displacement represents an average strain greater than 0.001, which is quite large and would be expected to cause fracture of weak sandstones.

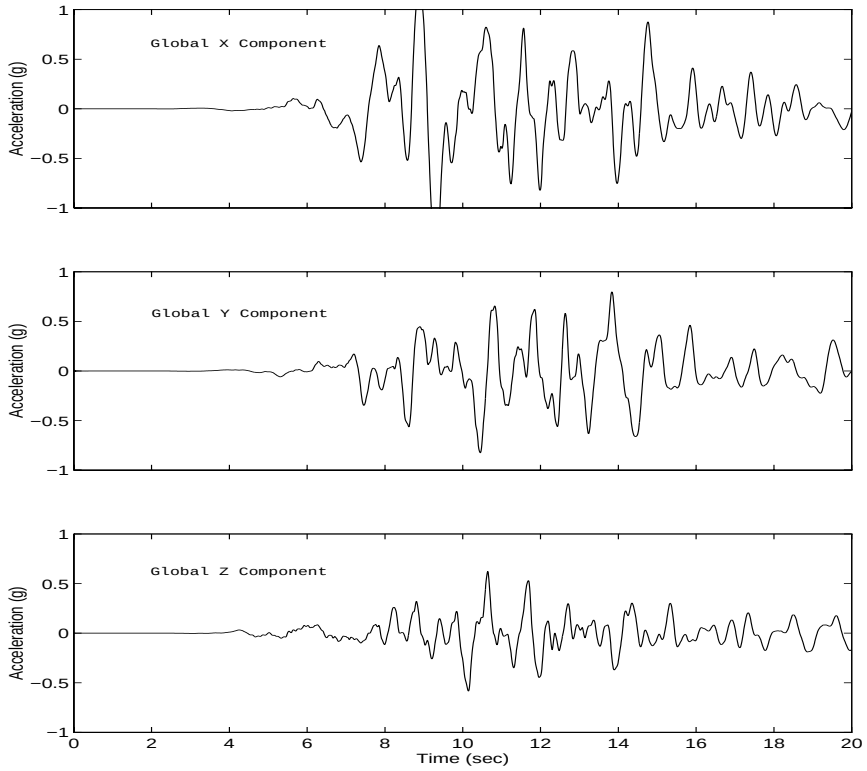

Figure 2.15: Hutchings et al. (1996) Simulated Ground Motion at IRK Station

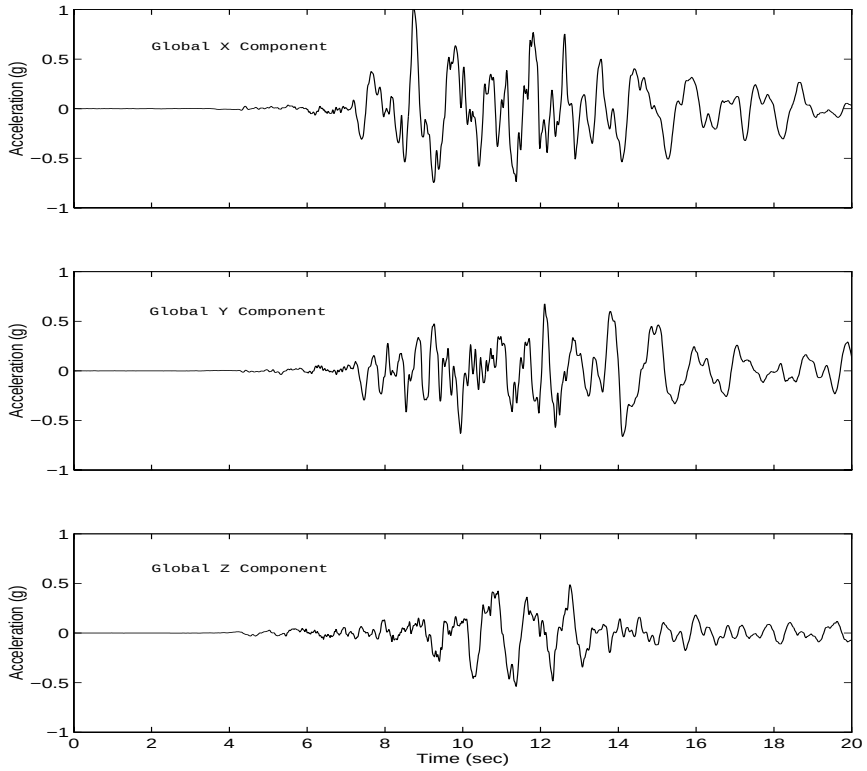

Figure 2.16: Hutchings et al. (1996) Simulated Ground Motion at ICN Station

2.3.3 Response Spectra

Figures 2.17 to 2.22 show the maximum (relative) displacement and pseudo-acceleration linear elastic response spectra (for 5% damping) for the six earthquake records. For reference, the lower vibration periods of frame 1 in the global X and global Y- axes are shown in the spectra plots. The frame 1 periods are associated with the vibration modes that have large mass participation for frame 1 in the corresponding direction of ground motion. These vibration periods are considerably shorter than the lower vibration modes for the entire bridge because frame 1 has short piers.

The spectra for the Hutchings, IRK simulated record are not shown in these figures. When compared with Hutchings, ICN record in Figures 2.23 and 2.24 for the global X components, the relative displacement and pseudo-acceleration for IRK are very large. For this reason, only the Hutchings, ICN record is considered in the demand analysis of the bridge.

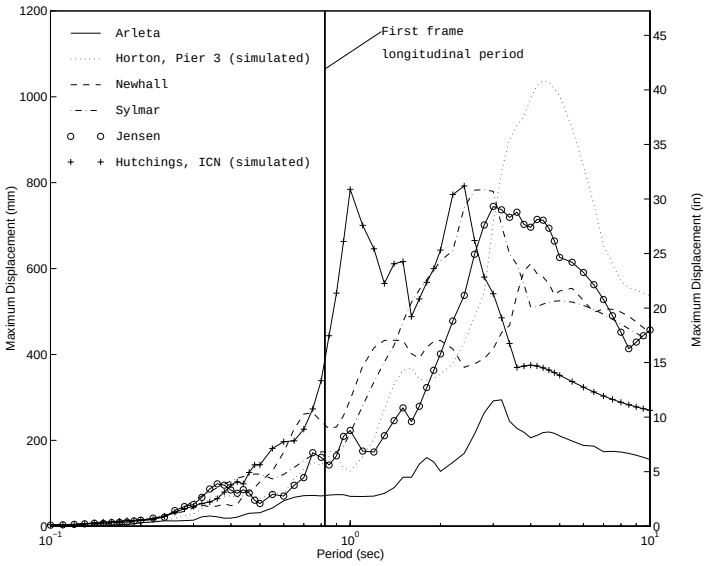

Figure 2.17: Relative Displacement for Global X Component ($\xi = 5\%$)

In the global X direction, the spectra in Figure 2.17 and 2.18 show that the six records vary in pseudo-acceleration from 0.42 g to 2.30 g at the first longitudinal period of 0.82 sec for frame 1. At 1 sec period, the Hutchings, ICN record is by far the strongest ground motion. The simulated Horton (1995) record has very large spectral displacements at 4 sec which, although not very significant for this bridge, may be an artifact of the simulation methodology. In the global Y direction, Figures 2.19 and 2.20, the motions are fairly consistent, with again the exception of the larger values for the Hutchings, ICN simulated record.

Although not shown in Figures 2.21 and 2.22, there are significant vertical vibration modes of the bridge at periods between 0.35 sec and 0.40 sec. At these periods the vertical component of the Newhall record has pseudo-acceleration ordinates considerably greater than the other records. The vertical component of the Hutchings, ICN record has very large relative displacements and pseudo- acceleration at period of 0.9 sec, which is correlated with the large spectral values for the horizontal components.

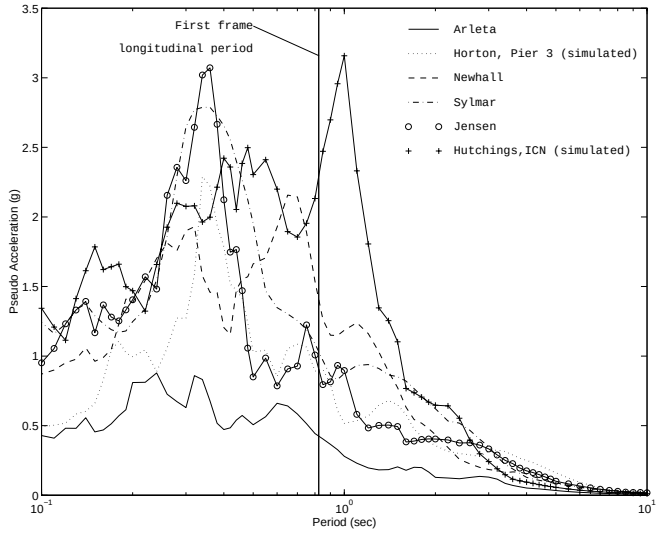

Figure 2.18: Pseudo-Acceleration for Global X Component ($\xi = 5\%$)

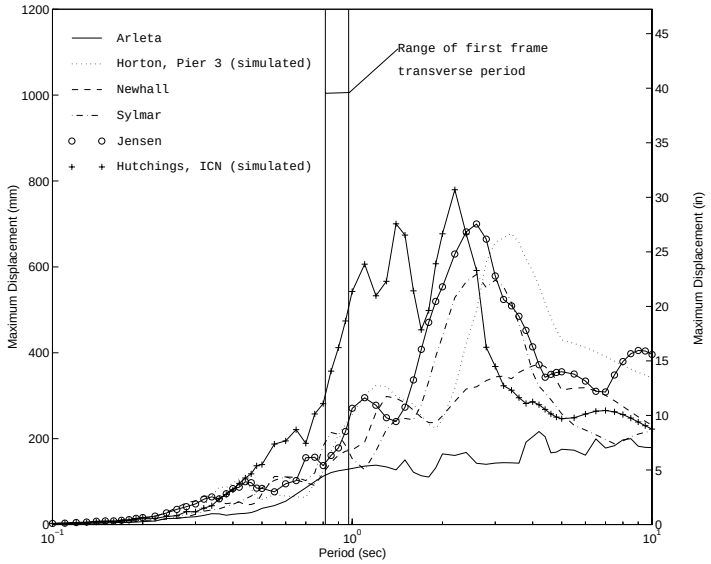

Figure 2.19: Relative Displacement for Global Y Component ($\xi = 5\%$)

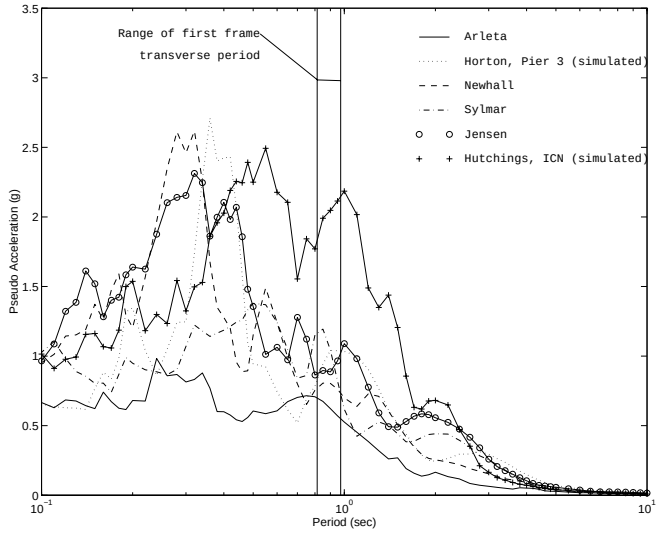

Figure 2.20: Pseudo-Acceleration for Global Y Component ($\xi = 5\%$)

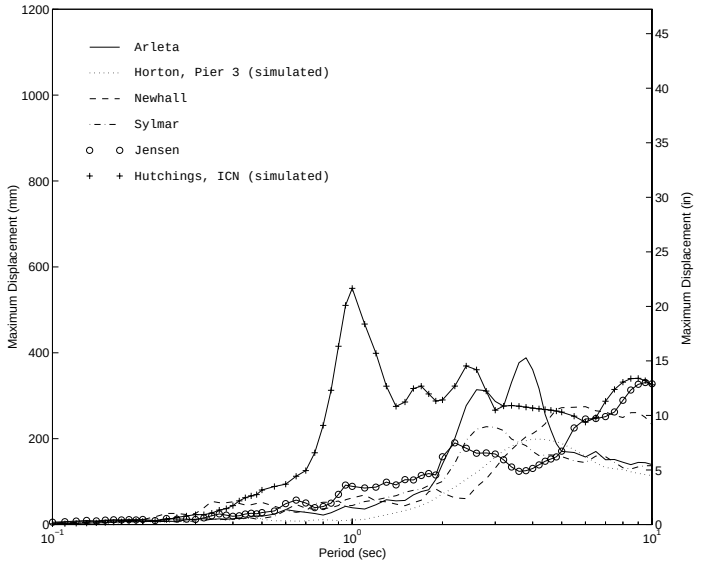

Figure 2.21: Relative Displacement for Global Z Component ($\xi = 5\%$)

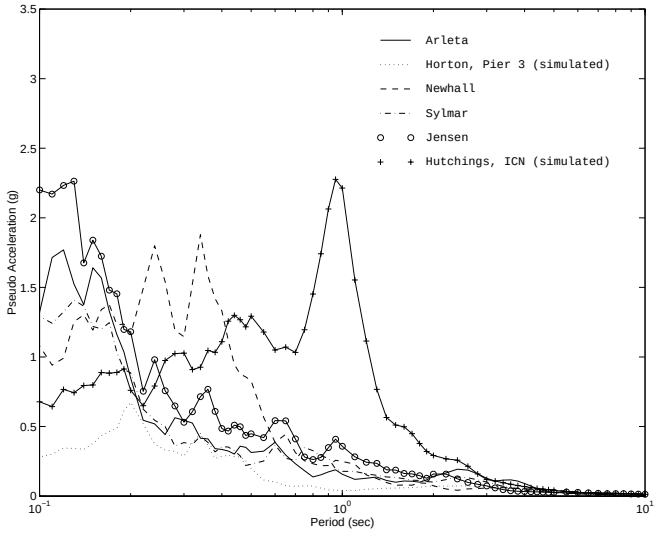

Figure 2.22: Pseudo-Acceleration for Global Z Component ($\xi = 5\%$)

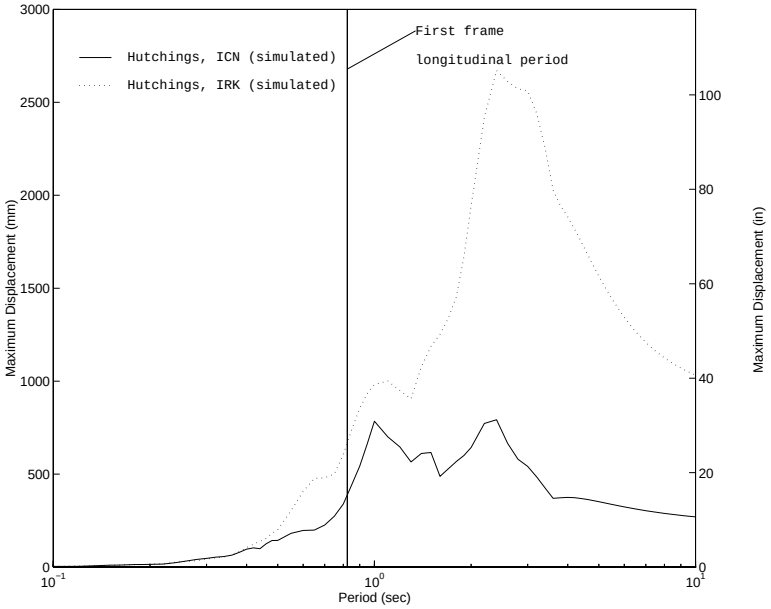

Figure 2.23: Relative Displacement for Global X Component ($\xi = 5\%$) with Hutchings et al. (1996), IRK Simulated Ground Motion

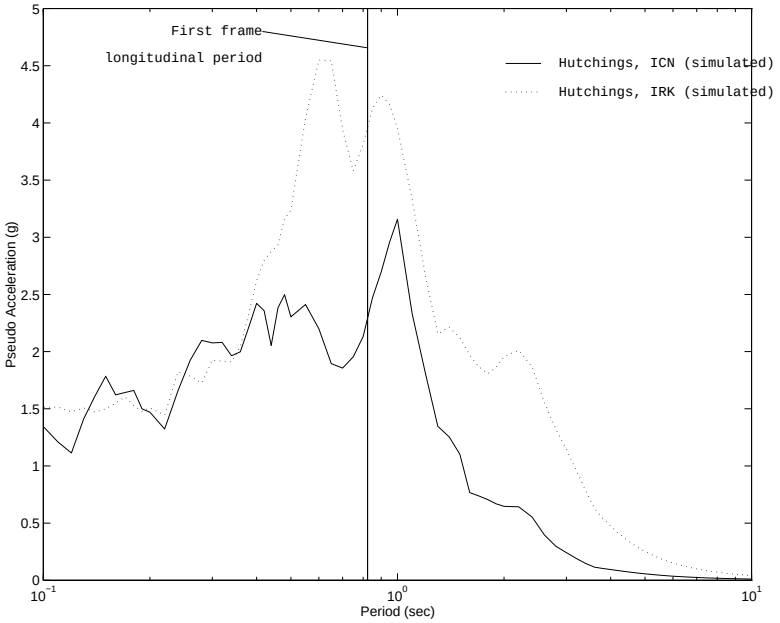

Figure 2.24: Pseudo-Acceleration for Global X Component ($\xi = 5\%$) with Hutchings et al. (1996), IRK Simulated Ground Motion

Table 2.2: Summary of Ground Motion for Global X Component

Record	Peak Ground Acceleration PGA g	Peak Ground Velocity PGV $\frac{\text{mm}}{\text{sec}}$ ($\frac{\text{in.}}{\text{sec}}$)	Peak Ground Displacement PGD mm (in.)	S_a at $T_1 = 0.82\ sec$ and $\xi = 5\%$ g
Arleta	0.30	230 (9.1)	82 (3.2)	0.42
Horton, Pier 3 (simulated)	0.47	840 (33)	430 (17)	0.90
Jensen Filter Plant (Generator Station)	0.68	870 (34)	320 (13)	0.84
Hutchings, ICN (simulated)	1.03	1300 (51)	230 (9.2)	2.30
Hutchings, IRK (simulated)	1.48	3300 (130)	890 (35)	3.98
Newhall	0.60	970 (38)	310 (12)	1.38
Sylmar	0.84	1300 (51)	320 (13)	1.03

Table 2.3: Summary of Ground Motion for Global Y Component

Record	Peak Ground Acceleration PGA g	Peak Ground Velocity PGV $\frac{mm}{sec}$ ($\frac{in.}{sec}$)	Peak Ground Displacement PGD mm (in.)	S_a at $T_1 = 0.89\ sec$ and $\xi = 5\%$ g
Arleta	0.34	400 (16)	90 (3.5)	0.63
Horton, Pier 3 (simulated)	0.52	830 (33)	290 (11)	1.03
Jensen Filter Plant (Generator Station)	0.82	680 (27)	260 (10)	0.89
Hutchings, ICN (simulated)	0.67	1100 (44)	260 (10)	2.04
Hutchings, IRK (simulated)	0.82	1300 (53)	390 (15)	2.61
Newhall	0.58	720 (28)	170 (6.8)	0.81
Sylmar	0.61	760 (30)	150 (5.9)	1.07

Table 2.4: Summary of Ground Motion for Global Z Component

Record	Peak Ground Acceleration PGA g	Peak Ground Velocity PGV $\frac{mm}{sec}$ ($\frac{in.}{sec}$)	Peak Ground Displacement PGD mm (in.)
Arleta	0.55	175 (6.9)	65 (2.5)
Horton, Pier 3 (simulated)	0.17	160 (6.3)	86 (3.4)
Jensen Filter Plant (Generator Station)	0.76	320 (12)	120 (4.7)
Hutchings, ICN (simulated)	0.54	840 (33)	540 (21)
Hutchings, IRK (simulated)	0.62	780 (31)	510 (20)
Newhall	0.55	310 (12)	130 (5.0)
Sylmar	0.54	190 (7.3)	76 (3.0)

Chapter 3

Structural, Footing, and Soil Modeling for the Bridge

3.1 Introduction

The earthquake demands on a bridge are estimated by analyzing a mathematical model of the superstructure, piers, footing, and soil system due to free-field ground motion. The model should represent the geometry, boundary conditions, gravity load, mass distribution, energy dissipation, and behavior of the components. The primary objective of an analysis is to determine the strains, deformation, and displacements of critical components. In some cases the forces are meaningful, particularly the forces in components that are intended to remain elastic.

Although bridge design is often based on a response spectrum analysis of a linearized model, this study uses a nonlinear dynamic analysis of the Separation and Overhead bridge. An inelastic model is developed model for nonlinear analysis of the bridge to determine the mode of failure in the 1994 Northridge earthquake and to simulate the earthquake response if the bridge had been seismically retrofit. In addition a model of the first frame (abutment 1 to hinge 4) is used for a nonlinear static analysis (or "pushover analysis") to examine the sequence of limit states and evaluate the displacement capacity of the frame. Generally the modeling follows the recommendations in recent guidelines for seismic design of bridges (ATC-32, 1996).

The modeling assumptions should be independent of the computer program used to perform the static and dynamic analysis. However, the models are often limited in some regard by the capabilities of the computer program. The DRAIN-3DX (Prakash et al., 1994) program is used for the analysis of the Separation and Overhead bridge. The description of the model in this chapter notes when the model is limited or specialized for the DRAIN-3DX program.

In situ data on the structural materials were not available. The concrete strength for the 20-plus year old bridge is assumed to be 34 MPa (5 ksi) for all columns and 30 MPa (4.4 ksi) for the superstructure. The Poisson's ratio for concrete is assumed to be 0.18 for concrete. Based on the standard ACI (1992) expression for normal weight concrete ($E_c = 57000\sqrt{f'_c}$ psi), the elastic modulus is 34 GPa (4000 ksi) for column concrete and 26 GPa (3800 ksi)

for the superstructure. The grade 60 flexural reinforcement is assumed to have an actual yield strength of 460 MPa (67 ksi). The prestressing steel present in the superstructure is assumed to be grade 270 with an ultimate tensile stress of 1860 MPa (270 ksi) and a yield stress that is 85% of the ultimate tensile stress.

3.2 Bridge Geometry and Superstructure

For the earthquake analysis of highway bridges it is common to use three-dimensional beam-column elements (line elements) to represent the behavior of the superstructure, as well as the components of the bents (columns and bent caps). The properties of the superstructure beam-column elements are selected to represent the properties of the box girder section. This approach is followed in the modeling of the Separation and Overhead bridge.

The geometry and connectivity of the elements and nodes of the model are shown in Figure 3.1. As recommended in (ATC-32, 1996), the box girder for each span is discretized using five elements of equal length (except for spans with intermediate hinges). The nodes lie on the geometric centroids of the superstructure. Each node is assigned a translational mass that is determined by the tributary mass associated with the node. Because many programs do not allow rotational masses and to visualize the displacements of the bridge, a massless but stiff outrigger is slaved at the top of each pier. Vertical translation masses are assigned to the ends of the outriggers to represent the rotational mass moment of inertia of the superstructure. The vertical mass is determined from the tributary mass of superstructure that flanks each pair of outrigger masses. Since the torsional modes of vibration are not expected to affect the earthquake response significantly, this coarse torsional mass discretization is sufficient for modeling the global response of the bridge.

The superstructure (with the cross sections shown in Figure 2.5) is modeled by linear elastic beam-column elements placed at the geometric centroid of the cross section. The flexural stiffnesses of the members are based on I_{gross} for prestressed box girders and $0.75I_{gross}$ for conventionally reinforced box girders. The torsional constant (J^{eff}) is taken to be $0.25J^{elastic}$, where $J^{elastic}$ is based on elementary mechanics for a multiply connected thin-walled section subjected to torsion (Ugural and Fenster, 1995). The total area of the cross section is used to model axial stiffness and transverse shear stiffness. The properties for box girder superstructure are summarized in Table 3.1.

ATC-32 (1996) recommends that the effective box girder stiffness be reduced because of shear lag effects near the piers. The stiffness in these regions is based on an effective width that is no greater than the width of the column plus twice the cap beam depth. For the Separation and Overhead, the column width at the soffit level is 7.9 m (26 ft) because of the taper and the cap beam depth is 2.1 m (7 ft). The effective width implied by these dimensions is 12.2 m (40 ft). Since this width is nearly the entire width of the superstructure, 13.9 m (45.7 ft), no reduction in stiffness due to shear lag is included in the model.

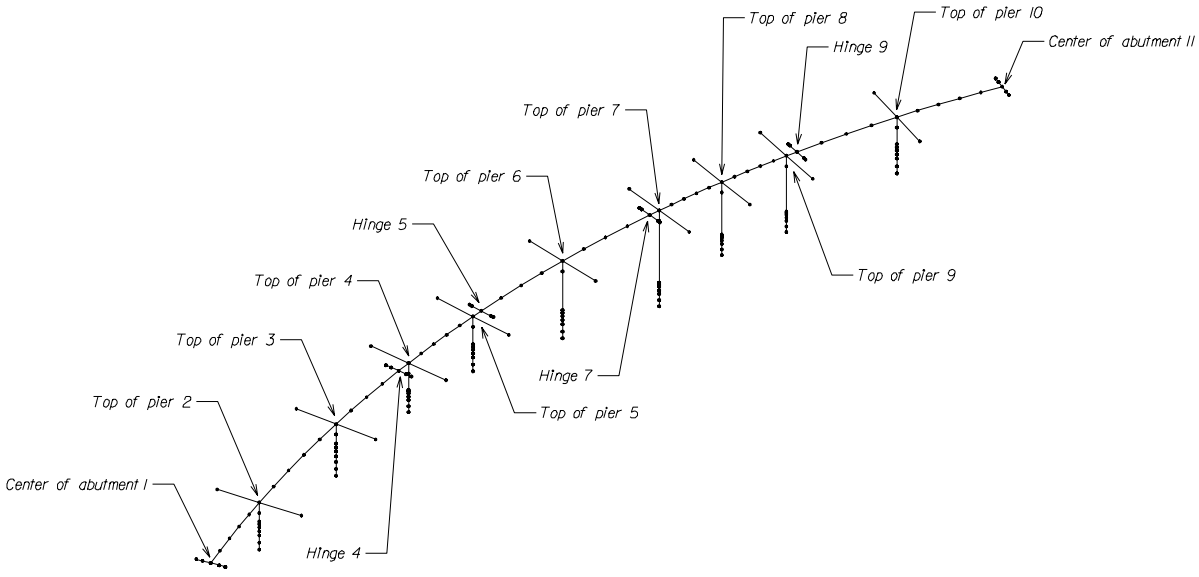

Figure 3.1: Model of Separation and Overhead Bridge

3.3 Pier Columns and Shafts

Inelastic three-dimensional beam-column elements are used to model the column and shaft for each of the piers in the bridge. Figure 3.2 shows the location of nodes in a column. A beam-column element connects each of the nodes at the geometric centroid of the column cross section. Six elements model the shaft from the base to the ground surface. One element models the prismatic portion of the column, and one element models the taper portion of the column. The taper element has a rigid offset at the top to represent the rigidity of the bent cap.

The beam-column element in DRAIN-3DX (Powell and Campbell, 1994) is Type 15 which

Table 3.1: Superstructure Section Properties

	Moment of Inertia I_{yy} m^4 (in.^{4})	Moment of Inertia I_{zz} m^4 (in.^{4})	Torsion Constant J^{eff} m^4 (in.^{4})	Area A_{gross} m^2 (in.^{2})
Prestressed Box Girder	5.75 (1.38×10^7)	184 (4.41×10^8)	16.2 (3.88×10^7)	8.62 (13400)
Reinforced Box Girder	4.26 (1.02×10^7)	134 (3.23×10^8)	17.0 (4.08×10^7)	8.04 (12500)

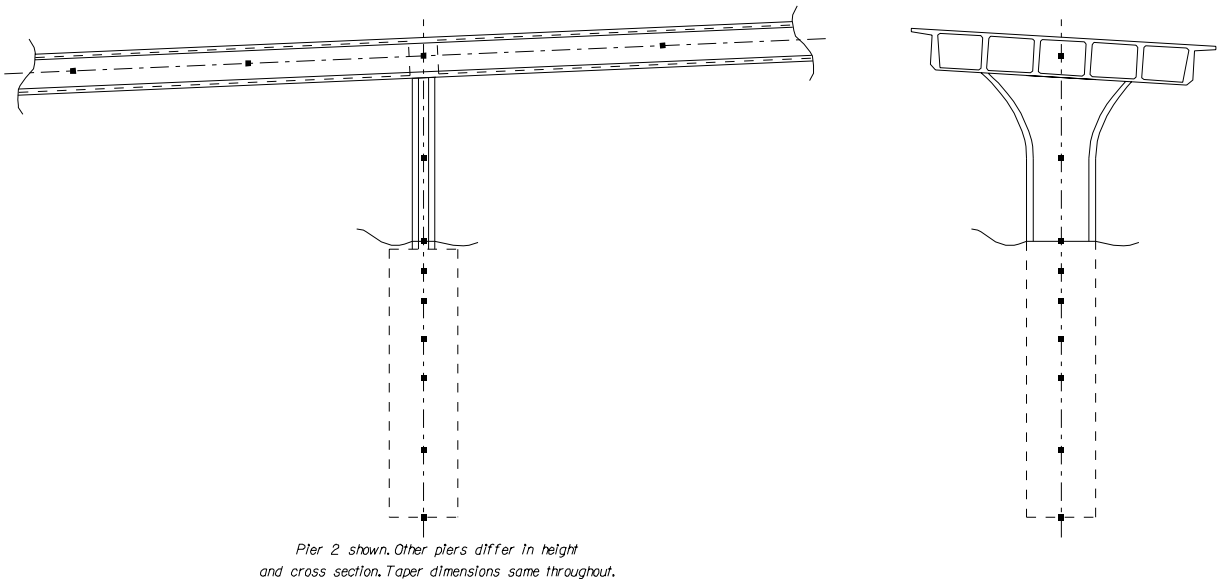

Figure 3.2: Typical Pier Model Showing Node Location in Column and Shaft

uses a fiber model of the cross section. Each fiber has a specified stress-strain relationship, which can be specified to represent unconfined concrete, confined concrete, and longitudinal steel reinforcement. The distribution of inelastic deformation and forces is sampled by specifying cross section slices along the length of the element. The fiber model approach provides versatile modeling of bi-axial moment-axial force interaction with distributed inelastic hinges. The fiber model can represent the loss of stiffness caused by concrete cracking, yielding of reinforcing steel due to flexural yielding, and strain hardening. The Type 15 element, however, is less successful representing degradation and softening after yielding. Pinching and bond slip are not included in the present model, although a limited capability to model these behaviors is provided in the Type 15 element. Shear and torsion behaviors are represented elastically.

3.3.1 Material Models

The reinforced concrete section analysis program BIAX (Wallace, 1992) was used to validate the DRAIN-3DX fiber model. BIAX performs moment-curvature analysis under monotonic loading. Several nonlinear material models are provided for concrete and steel. In the comparison, the BIAX model has approximately 1100 uniaxial fibers to model the cross section. BIAX does not include the effects of pinching or bond slip.

The model of Park et al. (1982) is used to represent the uniaxial stress strain behavior of concrete. This model defines a stress-strain relationship specified by:

$$f_c(\epsilon_c) = \left\{ \begin{array}{ll} Kf'_c \left[\frac{2\epsilon_c}{\epsilon_0 K} - \left(\frac{\epsilon_c}{\epsilon_0 K} \right)^2 \right] & \text{for} \quad \epsilon_c \leq \epsilon_0 K \\ \\ Kf'_c \left[1 - Z_m \left(\epsilon_c - \epsilon_0 K \right) \right] \geq 0.2 Kf'_c & \text{for} \quad \epsilon_c > \epsilon_0 K \end{array} \right\} \tag{3.1}$$

where:

$$
\begin{aligned}
\epsilon_c &= \text{Concrete strain.} \\
f_c &= \text{Concrete stress in MPa.} \\
K &= 1 + \frac{\rho_s f_{yh}}{f'_c} \\
Z_m &= \frac{0.5}{\frac{3+0.29\epsilon_0 f'c}{145 f'_c - 1000} + 0.75\rho_s \sqrt{\frac{h''}{s_h}} - \epsilon_0 K} \\
f_{yh} &= \text{Yield stress of transverse reinforcement in MPa.} \\
h'' &= \text{Width of the concrete core measured to the outside of hoops in mm.} \\
s_h &= \text{Center to center spacing of transverse reinforcement in mm.} \\
\rho_s &= \text{Reinforcement ratio for transverse reinforcement.} \\
\epsilon_0 &= \text{Strain at which peak concrete stress is attained for unconfined concrete.}
\end{aligned}
$$

The ϵ_0 peak strain is assumed to be 0.002 and the unconfined peak compressive stress f'_c is assumed to be 34 MPa (5 ksi).

BIAX uses the Park model explicitly, whereas the DRAIN-3DX model requires a piecewise linear approximation to the model. Due to the minimal volume of transverse reinforcement in the columns, the behavior of the core concrete is nearly that for unconfined concrete. The steeply descending stress-strain branch that is present in the BIAX concrete model is difficult to model with the DRAIN-3DX Type 15 element, and it causes problems with converging to an equilibrium solution. For this reason, the concrete material model shown in Figure 3.3 is used for the nonlinear analysis. The shallower descending slope in the analysis model is based on equation 3.1, but assuming that additional confinement is provided by a 13 mm (0.5 in.) thick elliptical steel[1] jacket placed around the entire column and pressure grouted. To more closely represent the unconfined material model, the increase in maximum concrete compressive stress that would be produced by steel jacket confinement is not modeled. The concrete tensile strength is neglected, and cyclic behavior is represented by elastic unloading and reloading following the backbone curve in Figure 3.3.

In summary, the concrete material model represents the in-situ concrete up to and shortly beyond the strain at maximum concrete stress. Since the failure mode in the 1994 Northridge earthquake is expected to be brittle, the error in not modeling the rapid softening of the unconfined concrete after the maximum stress will not appreciably affect the conclusions about the failure. On the other hand, the model with a post-peak behavior representative of a typical seismic retrofit can then be used to evaluate the expected response of the bridge in the Northridge earthquake if it had been retrofit.

[1] Jacket steel assumed to have $f_y = 340$ MPa (50 ksi)

The steel material model used for the analysis is based on the BIAX steel model which assumes an initial elastic behavior up to yield, a yield plateau, and then a strain hardening region. The strain hardening region is represented by a low order polynomial fit to three stress-strain points located at the end of the yield plateau, the peak stress in the hardening region, and the point of fracture. For the analysis model, the yield plateau is assumed to end at a strain of 0.006. The maximum hardening stress is assumed to be 660 MPa (95 ksi) at a strain of 0.08, and the fracture stress is assumed to be 600 MPa (87 ksi) at a strain of 0.13. The DRAIN-3DX steel fiber model is a piecewise linear approximation to the BIAX model, both of which are shown in Figure 3.4.

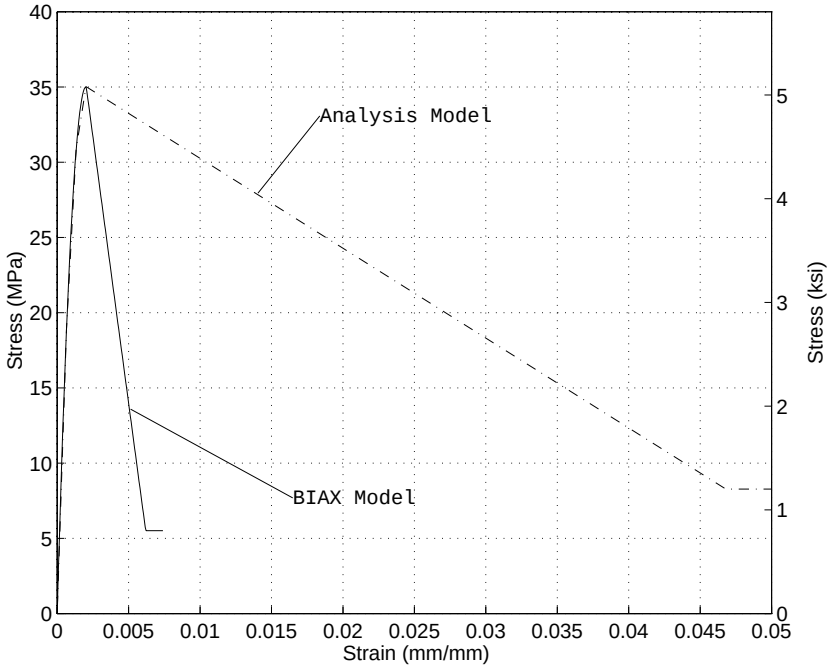

Figure 3.3: Uniaxial Stress-Strain Behavior for Concrete Models

3.3.2 Cross Section Behavior

The cross sectional discretizations of the pier columns and shafts for the DRAIN-3DX model are shown in Figures 3.5 and 3.6. Each cross section is represented by approximately 40 concrete and steel fibers. The concrete fibers are place at the geometric centroids of the concrete areas shown in the cross section discretization and the steel fibers are placed at the points shown in the figures. The number of #18 bars associated with the steel fibers is indicated in the figures. Where more than one longitudinal bar is lumped at a location, the fiber is placed at the geometric centroid of the lumped bar group.

The moment-curvature relationship for the column cross sections from DRAIN-3DX and the BIAX reference model are compared in Figures 3.7 through 3.10 for strong and weak axis bending under gravity axial load. The relationships under monotonic loading are similar, and the DRAIN-3DX model is sufficiently representative of the refined BIAX model for the

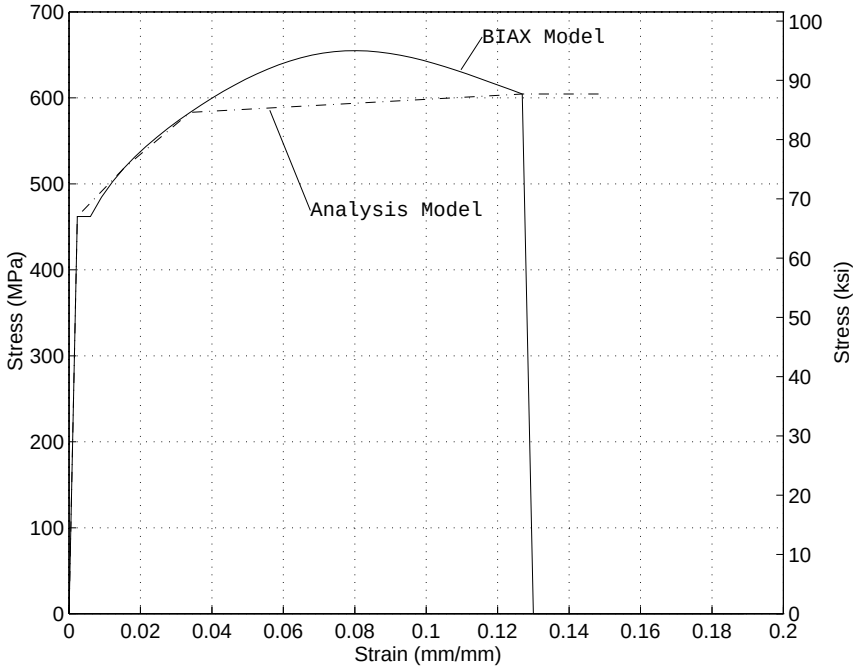

Figure 3.4: Uniaxial Stress-Strain Behavior for Steel Reinforcement Models

earthquake analysis of the bridge. The DRAIN-3DX model, however, is unable to represent significant softening of the section, as can be seen in Figures 3.7 through 3.10. However, since flexural degradation is not expected to affect the failure of the Separation and Overhead bridge.

3.3.3 Column Discretization

The fiber beam-column element discretization for the pier columns and shafts are shown in Figures 3.13, 3.14 and 3.15. The figures show the node location, beam-column elements between the nodes, and the elevations of the integration slices. Each integration point represents the behavior of the cross section, or slice, at one location in the element. The integration slices are selected to sample the inelastic curvature of the element near the expected location of plastic hinges. For elements above the ground and with sufficient length, eight integration slices are used with closer spacing between the slices at the end zones where plastic deformation is expected to occur. For the column taper elements, eight equally spaced integration slices are used along the length.

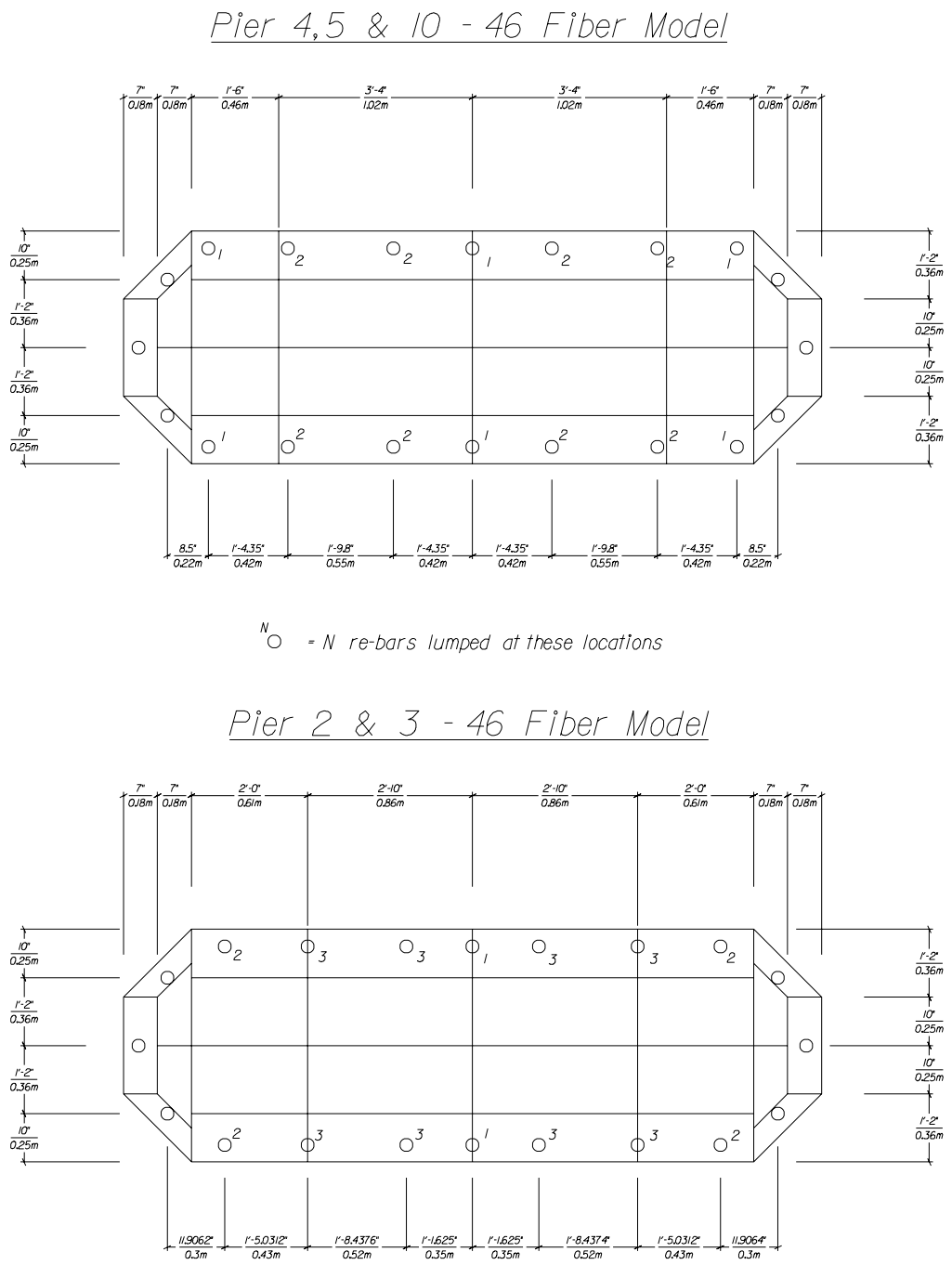

Figure 3.5: Cross Section Fiber Model for Piers 2-5 and 10

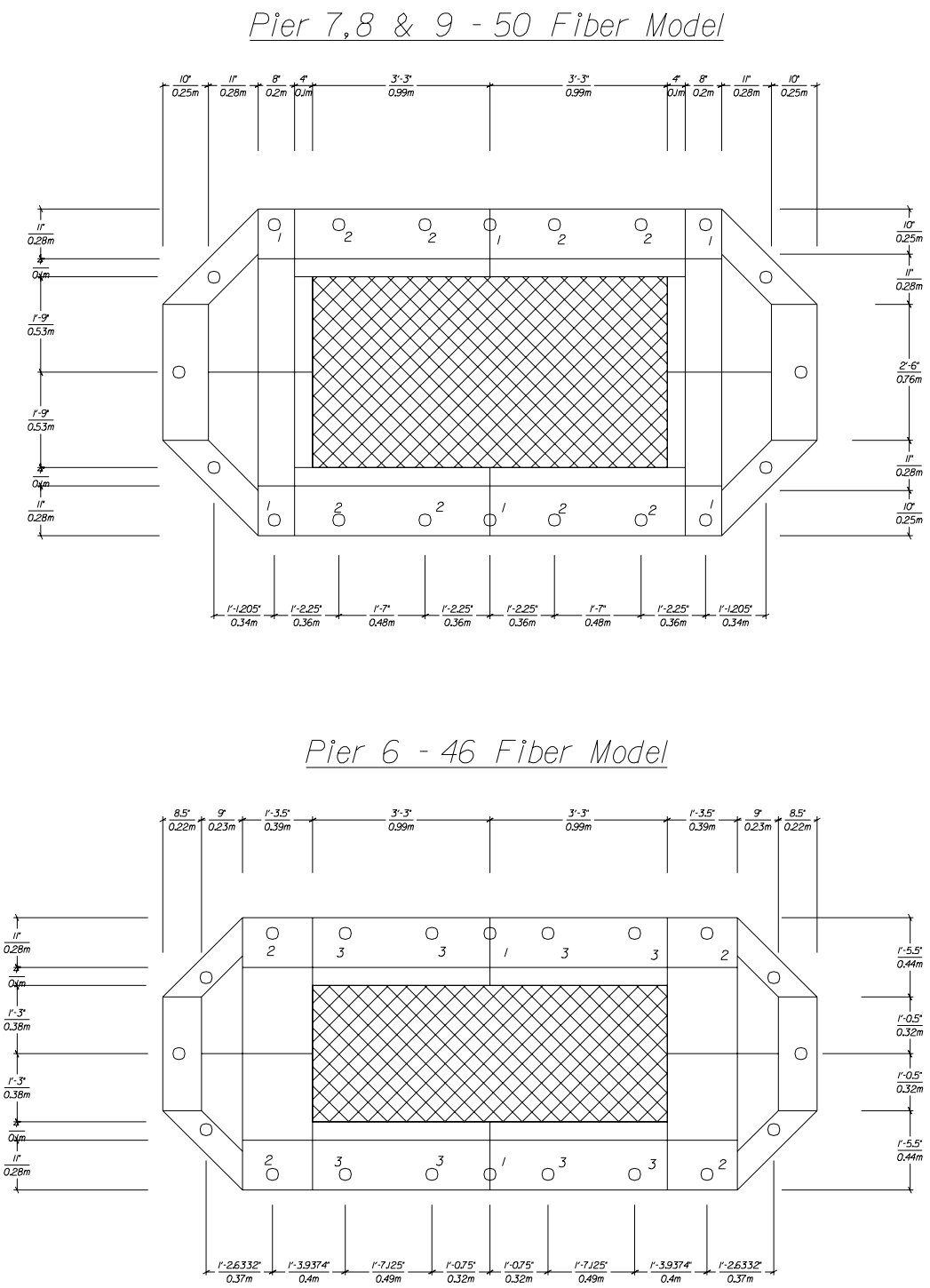

Figure 3.6: Cross Section Fiber Model for Piers 6-9

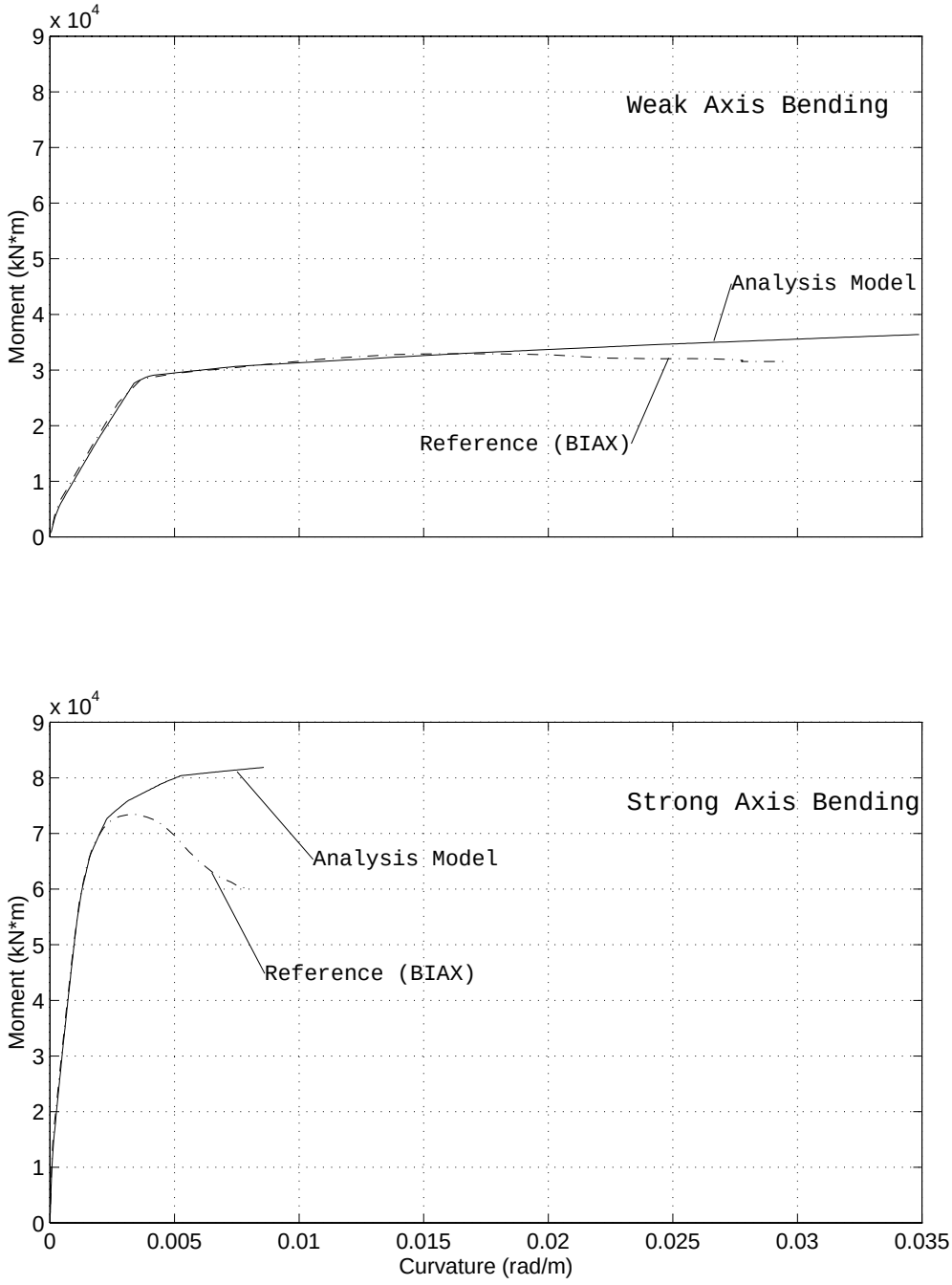

Figure 3.7: Moment-Curvature Relationship for Columns in Piers 2 and 3

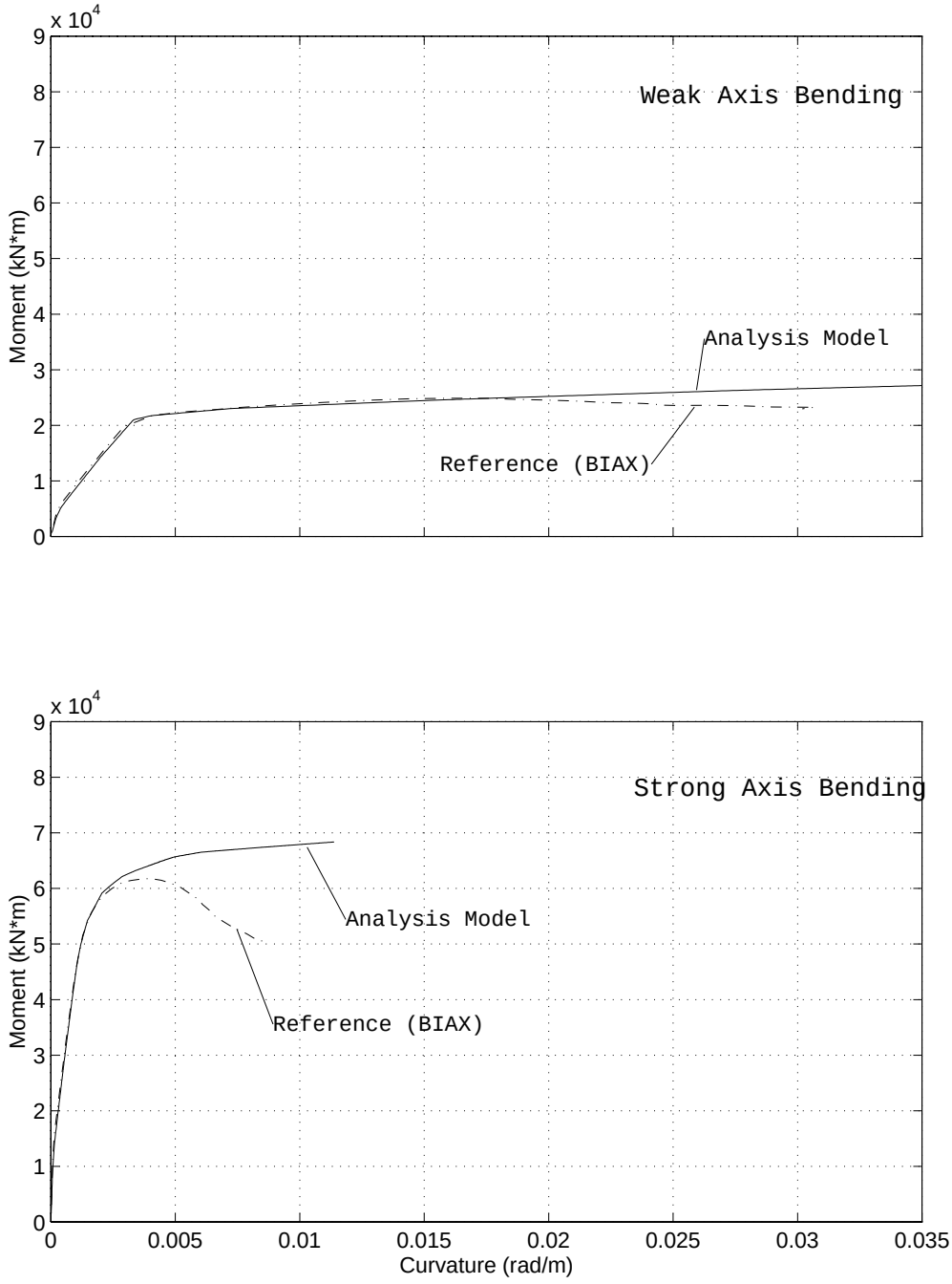

Figure 3.8: Moment-Curvature Relationship for Columns in Piers 4, 5 and 10

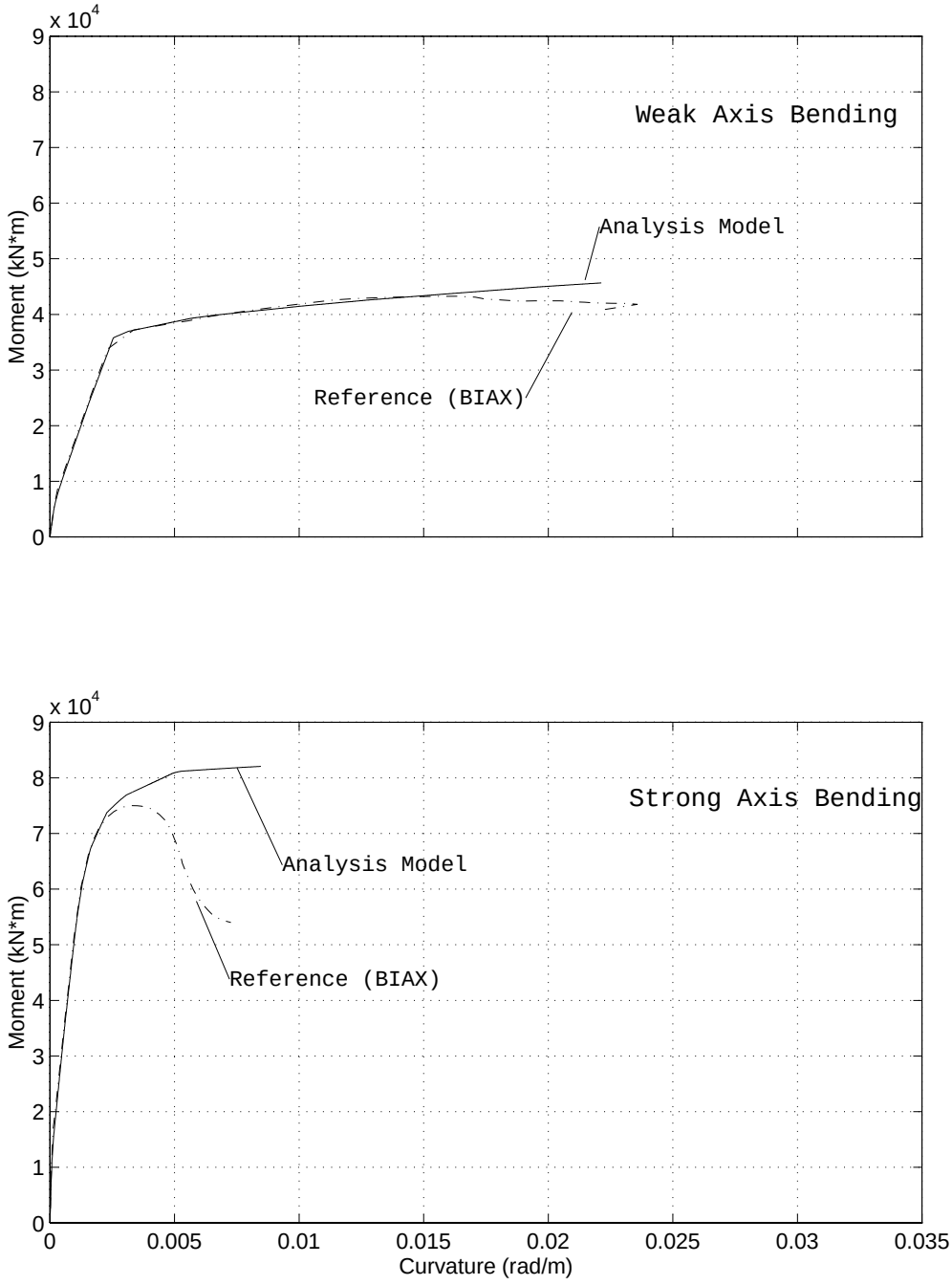

Figure 3.9: Moment-Curvature Relationship for Column in Pier 6

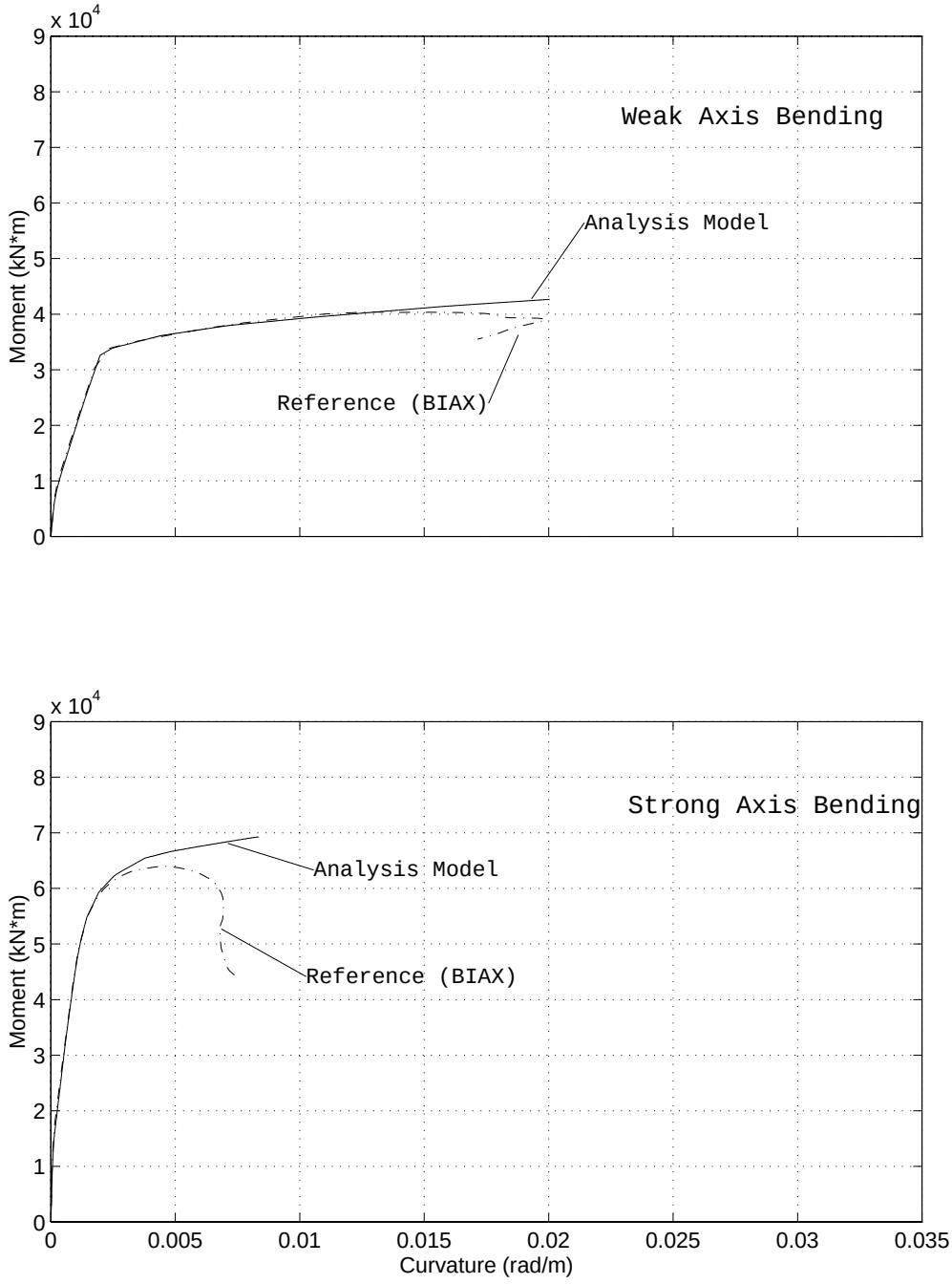

Figure 3.10: Moment-Curvature Relationship for Columns in Piers 7, 8 and 9

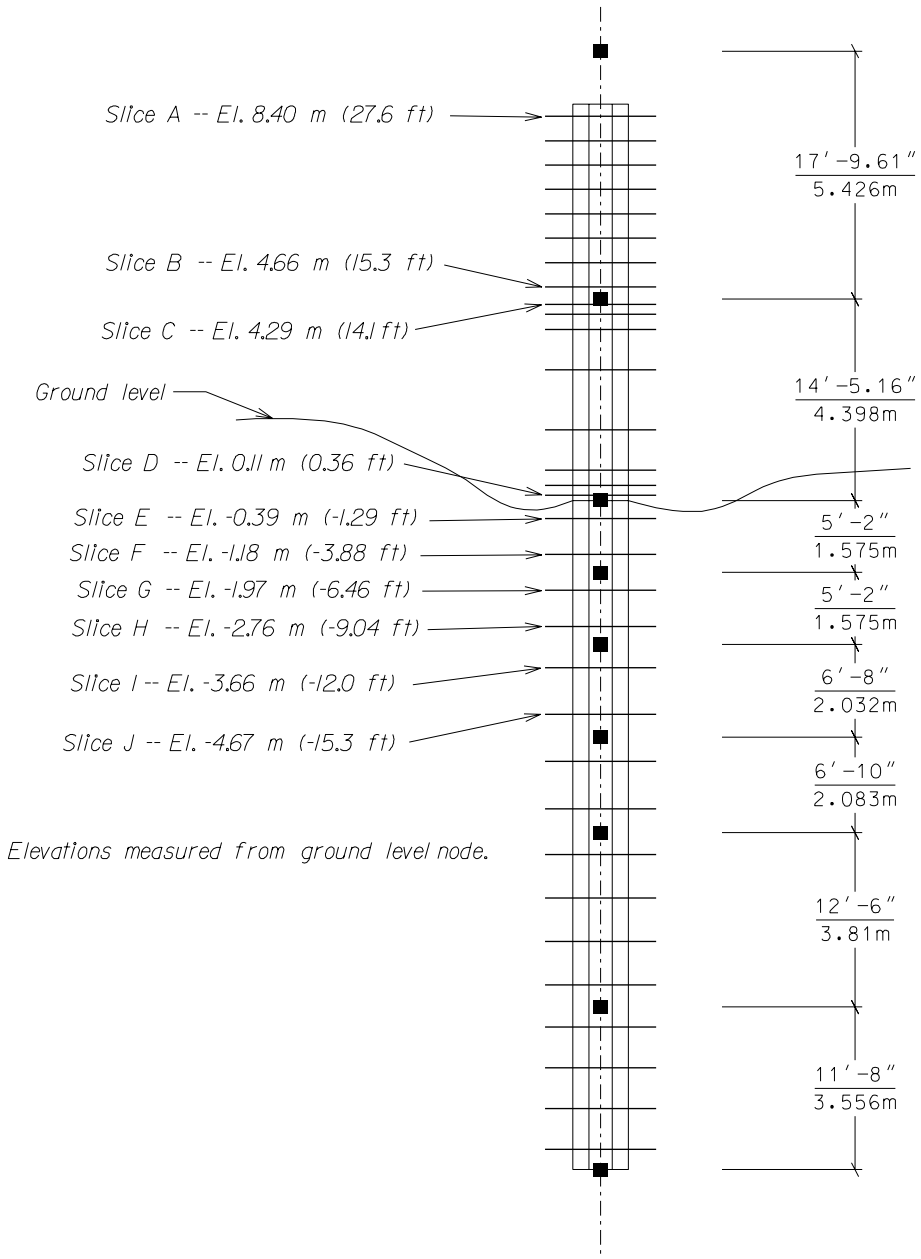

Figure 3.11: Location of Integration Slices Along Pier 2

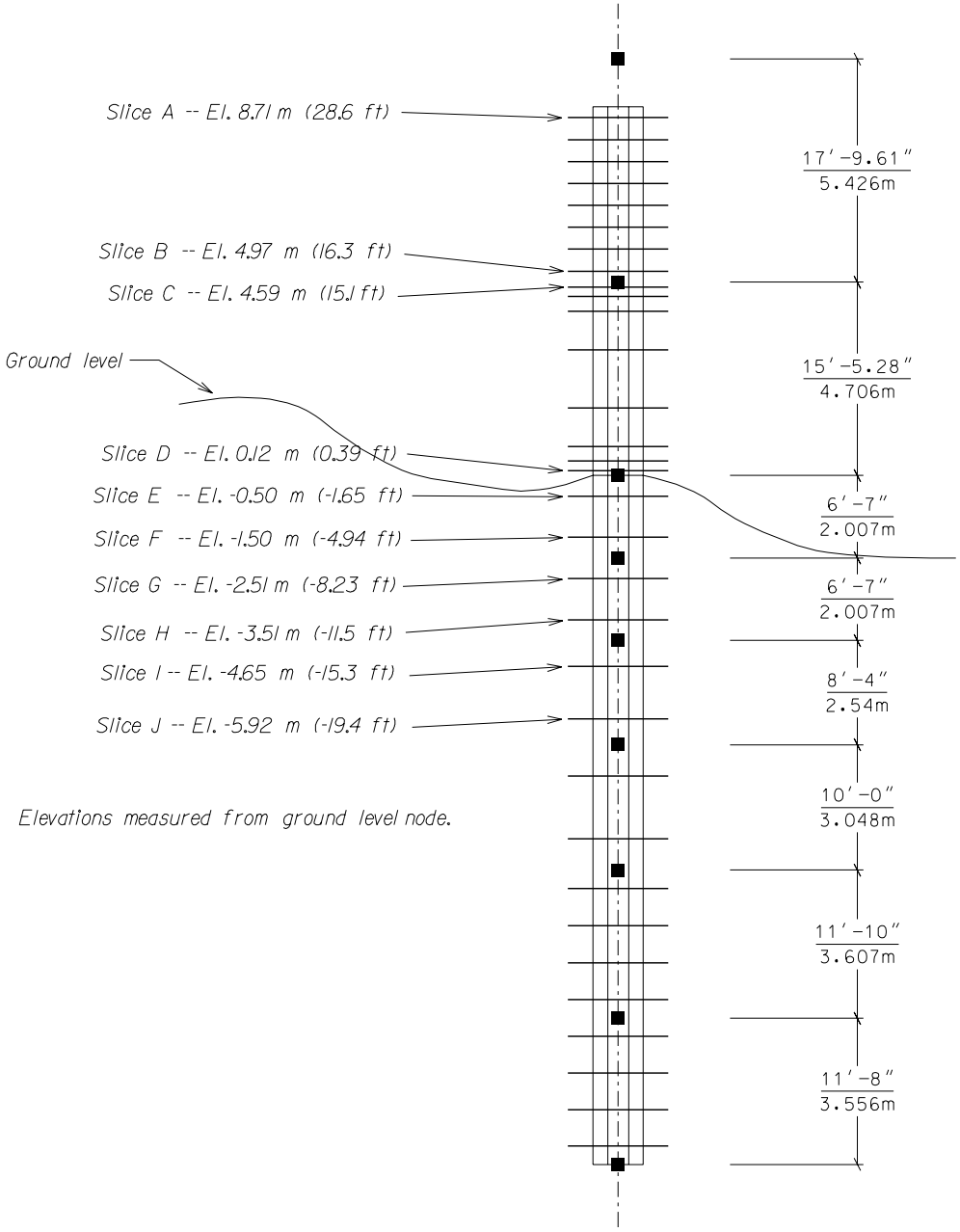

Figure 3.12: Location of Integration Slices Along Pier 3

The location of the slices for piers 2 and 3 are shown in Figures 3.11 and 3.12. These cross section slices will be referred to later when reporting moment-curvature results from the earthquake analyses. The longitudinal discretization along the length of pier 2 is summarized in Table 3.2. The other columns in the model have similar discretizations. The slices are placed more closely together at the ends of element 2 to represent the spread of plasticity in the plastic hinge zones. Since the elements below ground are short, fewer integration points along the length are specified. The use of too many or too closely spaced integration points can cause failure of convergence. Therefore, the discretization is such that each integration slice has a tributary length at least $0.25D_{column}$, where D_{column} is the diameter of the shaft.

Table 3.2: Distribution of Integration Slices in Elements for Pier 2 (see also Figure 3.11)

	Number of Slices	Slice	Tributary Length as a Percent of Element Length
Element 1 (Column Flare)	8	1	12.5
		2	12.5
		3	12.5
		4	12.5
		5	12.5
		6	12.5
		7	12.5
		8	12.5
Element 2 (Uniform)	8	1	5
		2	5
		3	10
		4	30
		5	30
		6	10
		7	5
		8	5
Element 3 (Sub-grade)	2	1	50
		2	50
Element 4 (Sub-grade)	2	1	50
		2	50
Element 5 (Sub-grade)	2	1	50
		2	50
Element 6 (Sub-grade)	2	1	50
		2	50
Element 7 (Sub-grade)	4	1	25
		2	25
		3	25
		4	25
Element 8 (Sub-grade)	4	1	25
		2	25
		3	25
		4	25

As noted in Section 2.2.2, all but eight of the column longitudinal reinforcement bars are terminated at a distance below ground that is 2/5 of the pile length but not exceeding 7.6 m (25 ft). Because of the complexity in modeling the reinforcement development in the bar cut-off region, no attempt was made to model the reduced capacity of the shaft below the cutoff location. In the model the longitudinal reinforcement continues for the entire length of the pile shaft. The bending moment demands in the shaft are checked against the actual moment capacity below the cutoff to determine whether this assumption is adequate for the earthquake analysis.

3.4 Soil-Structure Interaction

The dynamic interaction between the pile shaft and soil has a significant effect on the earthquake response of bridges. Soil-structure interaction can be classified into two effects. The first effect, kinematic interaction, is the modification of the free-field ground motion by the presence of the massless foundation. In this study, kinematic interaction for the large diameter pile shafts is neglected because the effects are primarily in the high frequencies which will have little effect on the bridge. The second form of interaction, inertial soil-structure interaction, is caused by the deformation of the soil by the time varying inertia induced forces developed in the footing.

The inertial soil-structure interaction for the pier shafts is modeled by bilinear (p-y) springs along the length of the shaft, as shown in Figure 3.16. The p-y springs are placed along two orthogonal axes aligned with the principal directions of the pier. The p-y springs represent the nonlinear force deformation relationship for the shaft and soil. Cyclic loading of the springs represents the hysteretic behavior and energy dissipation in the soil. Although it is a conservative assumption, radiation damping effects are neglected. Radiation damping is more important for the high frequency components. The relatively long vibration periods of the bridge do not dissipate significant energy.

The spring properties are selected according to the American Petroleum Institute (1993) for cohesionless soils, modified for the large diameter shaft. The lateral bearing capacity for a stiff sand is given by:

$$p_u = \min \left\{ \begin{array}{rcc} p_{us} & = & (C_1 H + C_2 D)\,\gamma H \\ p_{ud} & = & C_3 D \gamma H \end{array} \right\} \tag{3.2}$$

where:

p_u = ultimate resistance of soil at depth H in $\frac{\text{lbs}}{\text{in.}}$. p_{us} governs for small depths and p_{ud} governs for large depths.

γ = Effective soil weight in $\frac{\text{lbs}}{\text{in.}^3}$. A value of 0.076 $\frac{\text{lbs}}{\text{in.}^3}$ was assumed for this analysis.

H = Depth in in.

C_1, C_2, C_3 = Coefficients determined from charts given by API (1993) as a function of ϕ'. The values of of C_1, C_2 and C_3 for this analysis are assumed to be 4.7, 4.4 and 105, respectively.

ϕ' = Angle of internal friction of sand in degrees. A value of 40° was assumed for the stiff sands at the site.

D = Average pile diameter from surface to depth H in in. The diameter for all pile shafts in this model is 144 in.

The force-deformation relationship (p-y) for an individual spring is given by:

$$P(y) = A\, p_u \tanh\left[\frac{kH}{Ap_u}y\right] \tag{3.3}$$

where:

A = Factor to account for cyclic or static loading condition. Can be taken as 0.9 for cyclic loading and $\left(3.0 - 0.8\frac{H}{D}\right) \geq 0.9$ for static loading. Use 0.9 for this analysis.

p_u = Ultimate bearing capacity at depth H in $\frac{\text{lbs}}{\text{in.}}$.

k = Initial modulus of subgrade reaction in $\frac{lb}{in^3}$. Determined from charts provided by API (1993) as a function of ϕ'. As suggested by ATC-32 (1996), This value is multiplied by a factor $\sqrt{\frac{D}{24}}$ to account for a large diameter pile shaft[2](exceeding 24 in.).

y = Lateral deflection in in.

H = Depth to spring in in.

The role of depth of the spring below the ground surface is evident through the parameter H in p-y relationship because of the effect of overburden pressure on the strength of the soil. The uncertainty about the ground elevation at piers 2 and 3 leads to an uncertainty in the soil properties for these piers. Most of the demand analyses of the bridge are based on a pile shaft depth of 15 m (48 ft). To assess the effect of the ground elevation at pier 2, several cases are examined with the ground elevation 1.5 m (5 ft) higher than indicated on the design drawings. For these cases the overburden depth for the soil at pier 2 is increased by the same amount.

Another factor affecting the soil properties is that the design drawings show a significant excavation of the native soil near piers 2 and 3. The removal of the overburden from the excavation may not cause a reduction in shear strength of highly consolidated or overconsolidated soils. To account for the past overburden, an amount of overburden was assumed at piers 2 and 3 and added to the parameter H to establish reasonable strength for the soil. An overburden of 6.1 m (20 ft) and 1.5 m (5 ft) for piers 2 and 3, respectively, was selected for estimating the in situ strength of the soil.

Equation 3.2 gives a continuous nonlinear force-deformation relationship for the backbone p-y curve. The force-deformation relationship was simplified to an elastic-perfectly plastic model. Standard unloading and reloading rules are applied for cyclic loading. The bi-linear soil spring properties for the soil springs for each shaft are listed in Tables 3.3, 3.4, and 3.5. An example of the p-y curve given by the API (1993) and the linearized model used for the analysis is show in Figure 3.17 for spring 2 of pier 2.

[2]ATC-32 (1996) recommends increasing the initial subgrade modulus in *linear* proportion with the diameter in excess of 24 in., but this is a very large increase. For this study the modulus is increased by the square root of the ratio of diameter, 144 in., to 24 in.

Table 3.3: p-y Spring Parameters for Piers 2 - 5 Shafts

Spring Number	Pier 2			Pier 3		
	Tributary Length m (in.)	Stiffness $\frac{kN}{m}$ ($\frac{kips}{in.}$)	Yield Force kN (kips)	Tributary Length m (in.)	Stiffness $\frac{kN}{m}$ ($\frac{kips}{in.}$)	Yield Force kN (kips)
1 (ground level)	0.79 (31)	6.9×10^5 (3900)	4400 (990)	1.0 (40)	2.3×10^5 (1300)	960 (220)
2	1.6 (62)	1.6×10^6 (9200)	1.2×10^4 (2600)	2.0 (79)	8.3×10^5 (4700)	4300 (960)
3	1.8 (71)	2.4×10^6 (1.3×10^4)	1.8×10^4 (4100)	2.3 (90)	1.6×10^6 (9200)	9800 (2200)
4	2.1 (81)	3.1×10^6 (1.8×10^4)	3.0×10^4 (6700)	2.8 (110)	3.1×10^6 (1.8×10^4)	2.3×10^4 (5100)
5	2.9 (116)	5.6×10^6 (3.2×10^4)	5.6×10^4 (1.3×10^4)	3.3 (130)	4.9×10^6 (2.8×10^4)	4.7×10^4 (1.1×10^4)
6	3.7 (145)	8.7×10^6 (4.9×10^4)	1.1×10^5 (2.6×10^4)	3.6 (140)	6.8×10^6 (3.9×10^4)	8.3×10^4 (1.9×10^4)
7 (bottom of pier)	1.8 (70)	5.1×10^6 (2.9×10^4)	7.8×10^4 (1.7×10^4)	1.8 (70)	4.6×10^6 (2.6×10^4)	6.2×10^4 (1.4×10^4)

Spring Number	Pier 4			Pier 5		
	Tributary Length m (in.)	Stiffness $\frac{kN}{m}$ ($\frac{kips}{in.}$)	Yield Force kN (kips)	Tributary Length m (in.)	Stiffness $\frac{kN}{m}$ ($\frac{kips}{in.}$)	Yield Force kN (kips)
1 (ground level)	0.48 (19)	1.2×10^4 (69)	40 (9.0)	0.72 (29)	3.3×10^4 (190)	91 (20)
2	0.97 (38)	9.9×10^4 (560)	380 (86)	1.5 (58)	2.6×10^5 (1500)	940 (210)
3	1.3 (53)	2.9×10^5 (1.3)	1300 (290)	1.7 (68)	6.4×10^5 (3600)	2900 (650)
4	1.7 (68)	7.5×10^5 (4300)	4100 (930)	2.0 (78)	1.2×10^6 (7100)	7300 (1600)
5	2.5 (98)	1.7×10^6 (9700)	1.1×10^4 (2500)	2.8 (110)	2.7×10^6 (1.5×10^4)	1.8×10^4 (4100)
6	3.1 (120)	3.6×10^6 (2.1×10^4)	3.0×10^4 (6700)	3.6 (140)	5.5×10^6 (3.1×10^4)	4.8×10^4 (1.1×10^4)
7 (bottom of pier)	1.5 (59)	2.4×10^6 (1.4×10^4)	2.4×10^4 (5500)	1.7 (68)	3.3×10^6 (1.9×10^4)	3.9×10^4 (8700)

3.5 Abutments

The abutments are modeled by nonlinear spring elements to represent the support conditions and soil backfill. The initial gap between the box girder and the backwall is assumed to be 250 mm (10 in.), neglecting the weak lip at the top of the backwall (which has a smaller gap). Figure 3.18 is a schematic diagram of the abutment model. The abutments are modeled with slaved nodes that rigidly constrain a horizontal array of five nodes across the width of the superstructure. The two sets of nodes are connected with nonlinear springs to represent the support conditions. Two gap elements represent the 250 mm (10 in.) gap. Due to a paucity of information regarding the backfill soil conditions, the abutment is modeled as elastic-perfectly plastic component with a yield stress estimated to be 3.7 kPa (7.7 ksf) per 2.4 m (8 ft) of backwall height (ATC-32, 1996). This assumption results in a yield force

Table 3.4: p-y Spring Parameters for Piers 6 - 9 Shafts

Spring Number	Pier 6			Pier 7		
	Tributary Length m (in.)	Stiffness $\frac{kN}{m}$ ($\frac{kips}{in.}$)	Yield Force kN (kips)	Tributary Length m (in.)	Stiffness $\frac{kN}{m}$ ($\frac{kips}{in.}$)	Yield Force kN (kips)
1 (ground level)	0.79 (31)	3.8×10^4 (220)	100 (23)	0.55 (22)	1.8×10^4 (100)	48 (11)
2	1.6 (62)	3.4×10^5 (1900)	1100 (240)	1.1 (43)	1.5×10^5 (870)	470 (110)
3	1.8 (71)	7.7×10^5 (4400)	330 (730)	1.4 (57)	4.1×10^5 (2300)	1500 (340)
4	2.1 (81)	1.4×10^6 (8300)	8000 (1800)	1.8 (71)	8.9×10^5 (5100)	4600 (1000)
5	2.9 (120)	2.9×10^6 (1.6×10^4)	2.0×10^4 (4500)	2.6 (100)	2.0×10^6 (1.1×10^4)	1.2×10^4 (2700)
6	3.7 (150)	5.9×10^6 (3.4×10^4)	5.2×10^4 (1.2×10^4)	3.2 (130)	4.0×10^6 (2.3×10^4)	3.2×10^4 (7200)
7 (bottom of pier)	1.8 (70)	3.6×10^6 (2.0×10^4)	4.1×10^4 (9200)	1.5 (61)	2.7×10^6 (1.5×10^4)	2.6×10^4 (5800)

Spring Number	Pier 8			Pier 9		
	Tributary Length m (in.)	Stiffness $\frac{kN}{m}$ ($\frac{kips}{in.}$)	Yield Force kN (kips)	Tributary Length m (in.)	Stiffness $\frac{kN}{m}$ ($\frac{kips}{in.}$)	Yield Force kN (kips)
1 (ground level)	0.39 (16)	9.3×10^3 (53)	24 (5.5)	0.39 (16)	9.3×10^3 (53)	24 (5.5)
2	0.79 (31)	7.6×10^4 (440)	230 (51)	0.79 (31)	7.6×10^4 (440)	230 (51)
3	1.2 (47)	2.5×10^5 (1500)	820 (180)	1.2 (47)	2.5×10^5 (1500)	820 (180)
4	1.6 (64)	6.5×10^5 (3700)	2700 (670)	1.6 (64)	6.5×10^5 (3700)	2700 (670)
5	2.3 (92)	1.5×10^6 (8600)	8100 (1800)	2.3 (92)	1.5×10^6 (8600)	8100 (1800)
6	2.9 (120)	3.2×10^6 (1.8×10^4)	2.3×10^4 (5100)	2.9 (120)	3.2×10^6 (1.8×10^4)	2.3×10^4 (5100)
7 (bottom of pier)	1.4 (56)	2.0×10^6 (1.1×10^4)	1.8×10^4 (4200)	1.4 (56)	2.0×10^6 (1.1×10^4)	1.8×10^4 (4200)

of 5500 kN (1200 kips) for each of the two backwall springs in the abutment model. The stiffness of the abutment spring is estimated such that the yield strength is obtained at a displacement of 61 mm (2.4 in.), as suggested by Goel and Chopra (1997), giving a stiffness of 9.0×10^4 kN/m (510 kips/in.) for each of the two abutment backwall springs.

The bearing pads are modeled as elastic-perfectly plastic springs with a stiffness based on idealized shearing deformation given by $\frac{G_{elast}A}{h}$ where $G_{elast} = 1.0$ MPa (150 psi) is the assumed shear modulus for the elastomer, h is the 50 mm (2 in.) height of the bearing pads, and A is the cross section area in a horizontal plane of the pads. The stiffness of each of the two bearing pad springs in the abutment model is estimated as 1.0×10^4 kN/m (59 kips/in.) for abutment 1 and 1.1×10^4 (63 kips/in.) for abutment 11. The yield force of each spring is 520 kN (120 kips) for abutment 1 and 560 kN (130 kips) for abutment 11. The pads are assumed to yield at 50 mm (2 in.) of displacement, which corresponds to 100% shear strain.

Table 3.5: p-y Spring Parameters for Pier 10 Shaft

Spring Number	Pier 10		
	Tributary Length m (in.)	Stiffness $\frac{kN}{m}$ ($\frac{kips}{in.}$)	Yield Force kN (kips)
1 (ground level)	0.85 (34)	4.6×10^4 (260)	130 (29)
2	1.7 (67)	4.0×10^5 (2300)	1400 (300)
3	1.9 (75)	8.5×10^5 (4900)	4000 (900)
4	2.1 (83)	1.6×10^6 (9300)	9400 (2100)
5	3.0 (120)	3.4×10^6 (1.9×10^4)	2.3×10^4 (5200)
6	3.8 (150)	6.4×10^6 (3.6×10^4)	6.0×10^4 (1.4×10^4)
7 (bottom of pier)	1.8 (73)	4.1×10^6 (2.4×10^4)	4.8×10^4 (1.1×10^4)

Although it is likely that the bearing pads would cease to provide resistance at displacements much larger than 50 mm (2 in.). However, the degrading behavior of the bearing pad is not expected to have a significant effect on the global response so it was not included in the model.

3.6 Hinges and Restrainers

The intermediate hinges in the superstructure are modeled by nonlinear spring elements with kinematic constraints. A diagram of the hinge model is shown in Figure 3.19. The hinges are modeled with sets of slaved nodes that are rigidly constrained in a horizontal array of five nodes across the width of the superstructure. Each set of five nodes represents one side of the hinge and is connected to another set of five nodes via zero-length nonlinear spring elements. Hinges 4 and 5 have the same bearing pad properties as abutment 1, and hinges 7 and 9 have the same bearing pad properties as abutment 11. The hinge closing is modeled with compression only gap elements at the outer edges of the superstructure and with an initial gap of 12 mm (0.50 in.). The stiffness of the gap spring is approximately twice the axial stiffness of the adjacent superstructure beam element. The hinge restrainers are modeled as elastic-perfectly plastic tension-only springs with an initial slack of 12 mm (0.5 in.). The stiffness of the restrainers is given by $\frac{EA}{L}$ where E is the modulus of elasticity for the restrainer cables–assumed to be 69 kPa (1×10^4 ksi), A is the total cross sectional area of the cables, and L is the length of the restrainer cables. The total yield force is based on a yield force per cable of 174 kN (39.1 kips). With these assumptions, the stiffness for each of the two restrainer springs in the hinge model is 7.5×10^4 kN/m (430 kips/in.) for hinge 4, 3.2×10^4 kN/m (180 kips/in.) for hinge 5 and 2.2×10^4 kN/m (120 kips/in.) for hinges 7 and 9. The yield force of each spring is estimated as 2400 kN (550 kips) for hinge 4 and 2800 kN (630 kips) for hinges 5, 7 and 9.

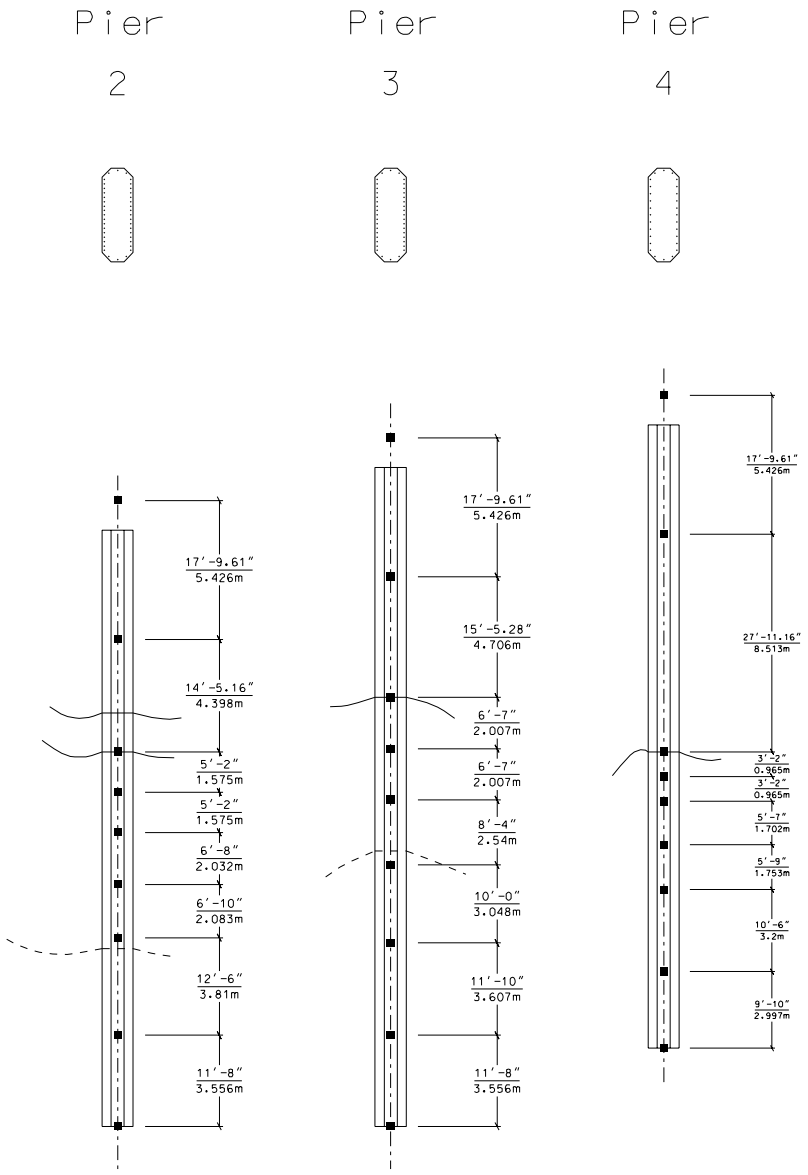

Figure 3.13: Node Locations in Column Elements for Piers 2, 3 and 4

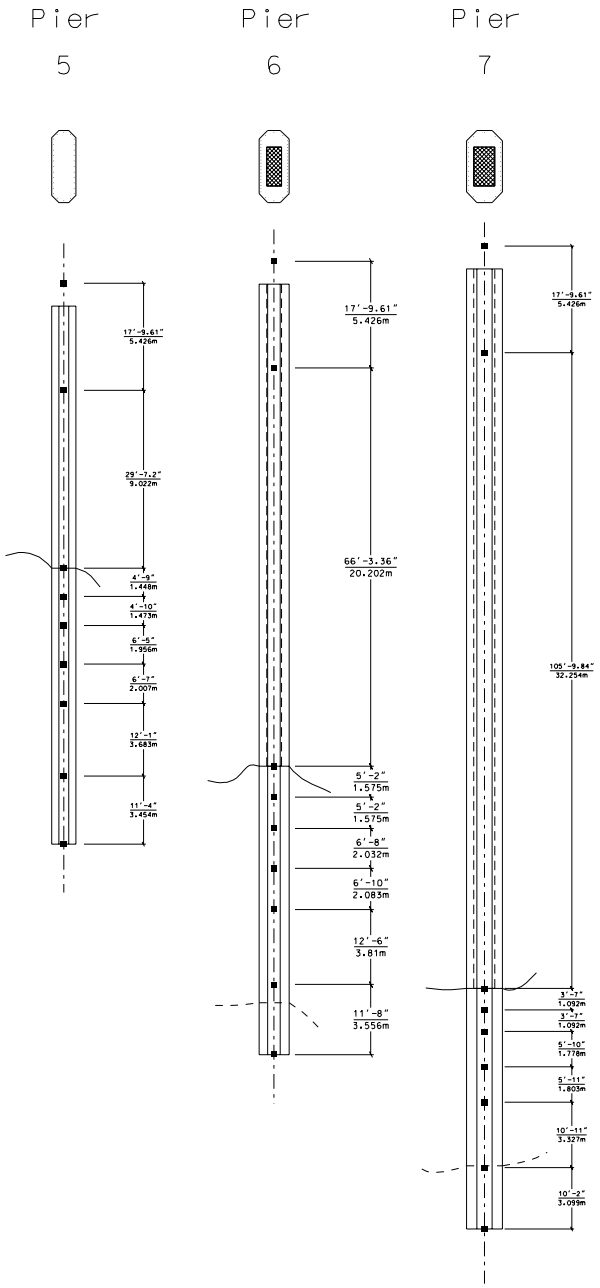

Figure 3.14: Node Locations in Column Elements for Piers 5, 6 and 7

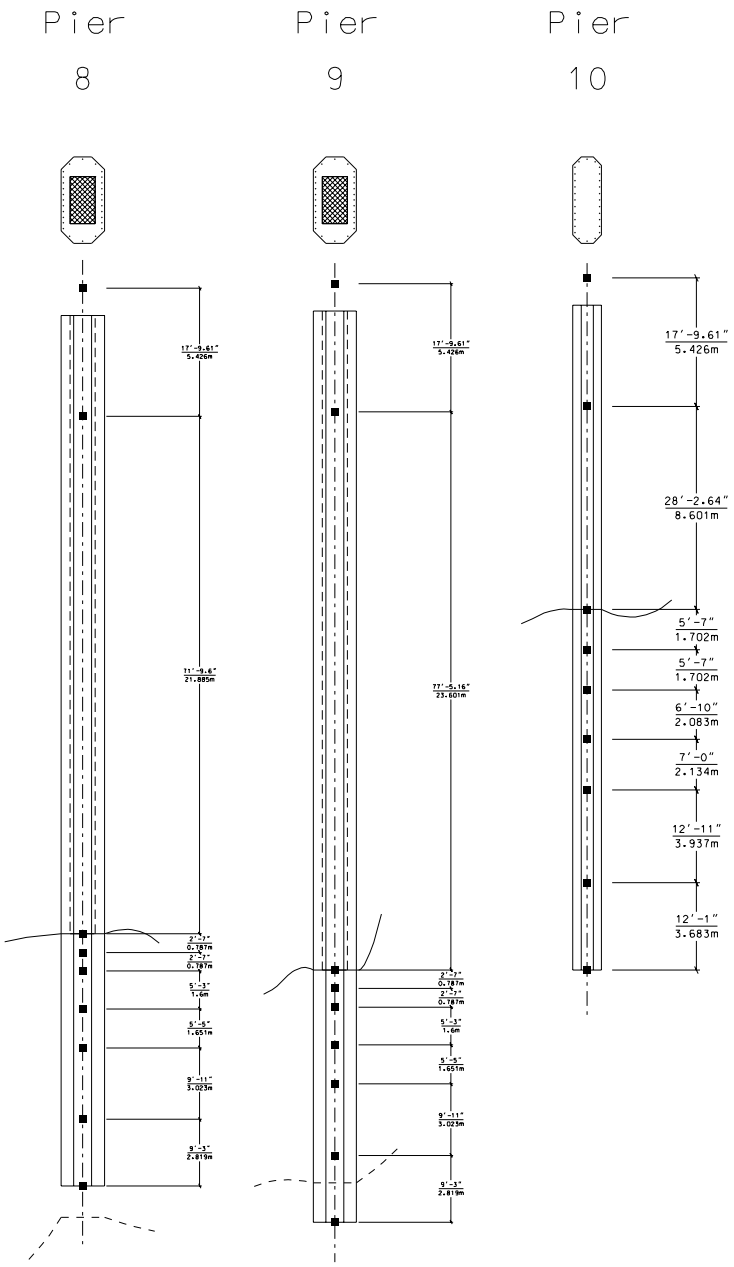

Figure 3.15: Node Locations in Column Elements for Piers 8, 9 and 10

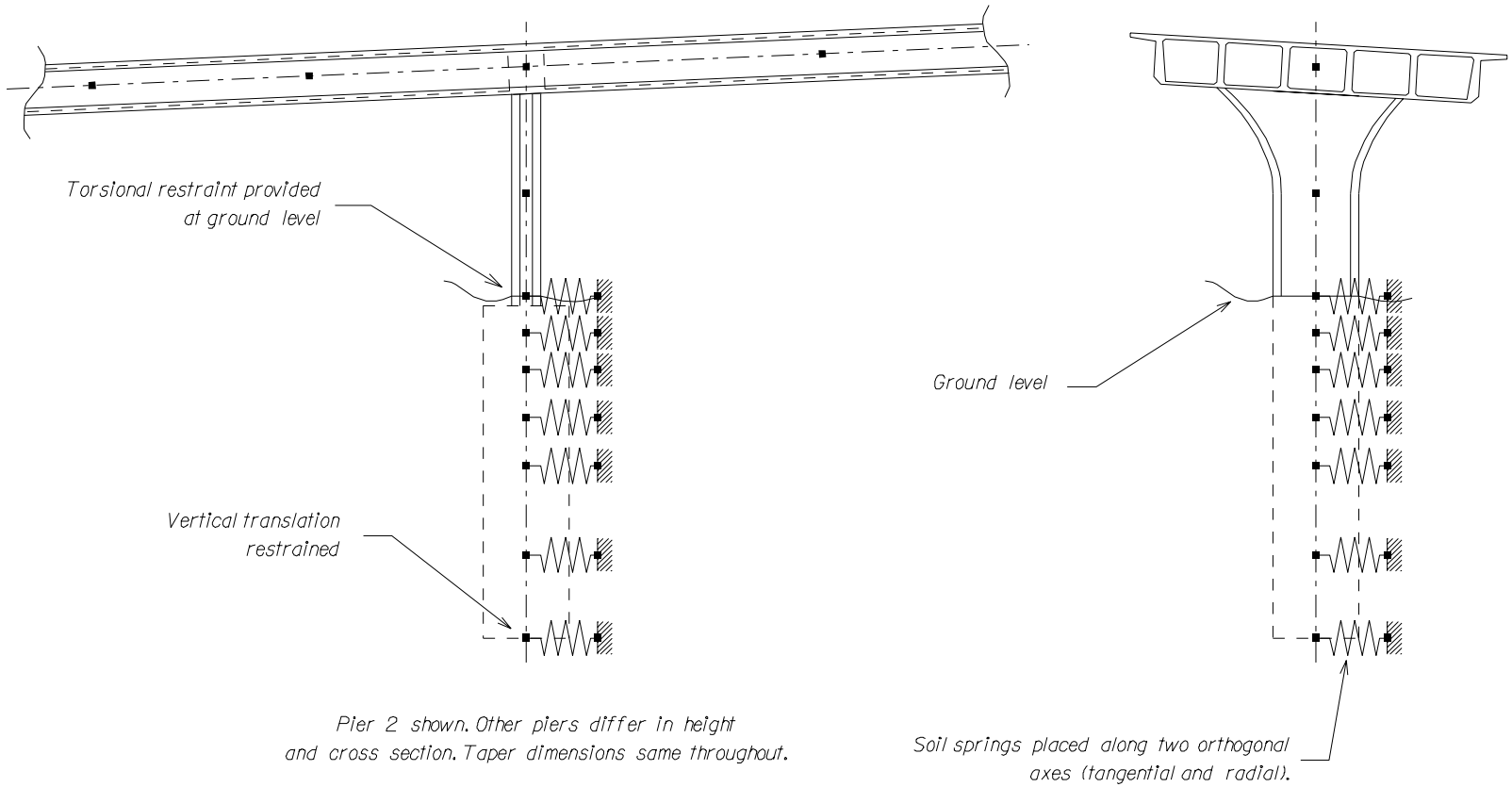

Figure 3.16: Model of Pier Shaft with P-Y Soil Springs

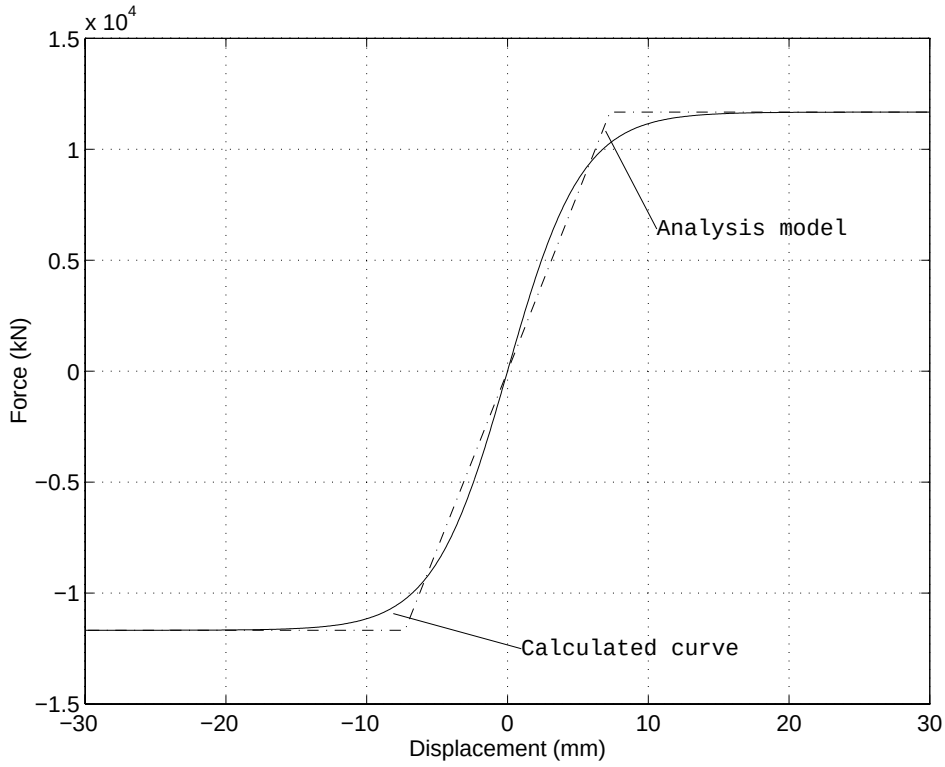

Figure 3.17: p-y Nonlinear Spring and Linearized Model for Pier 2, Spring 2

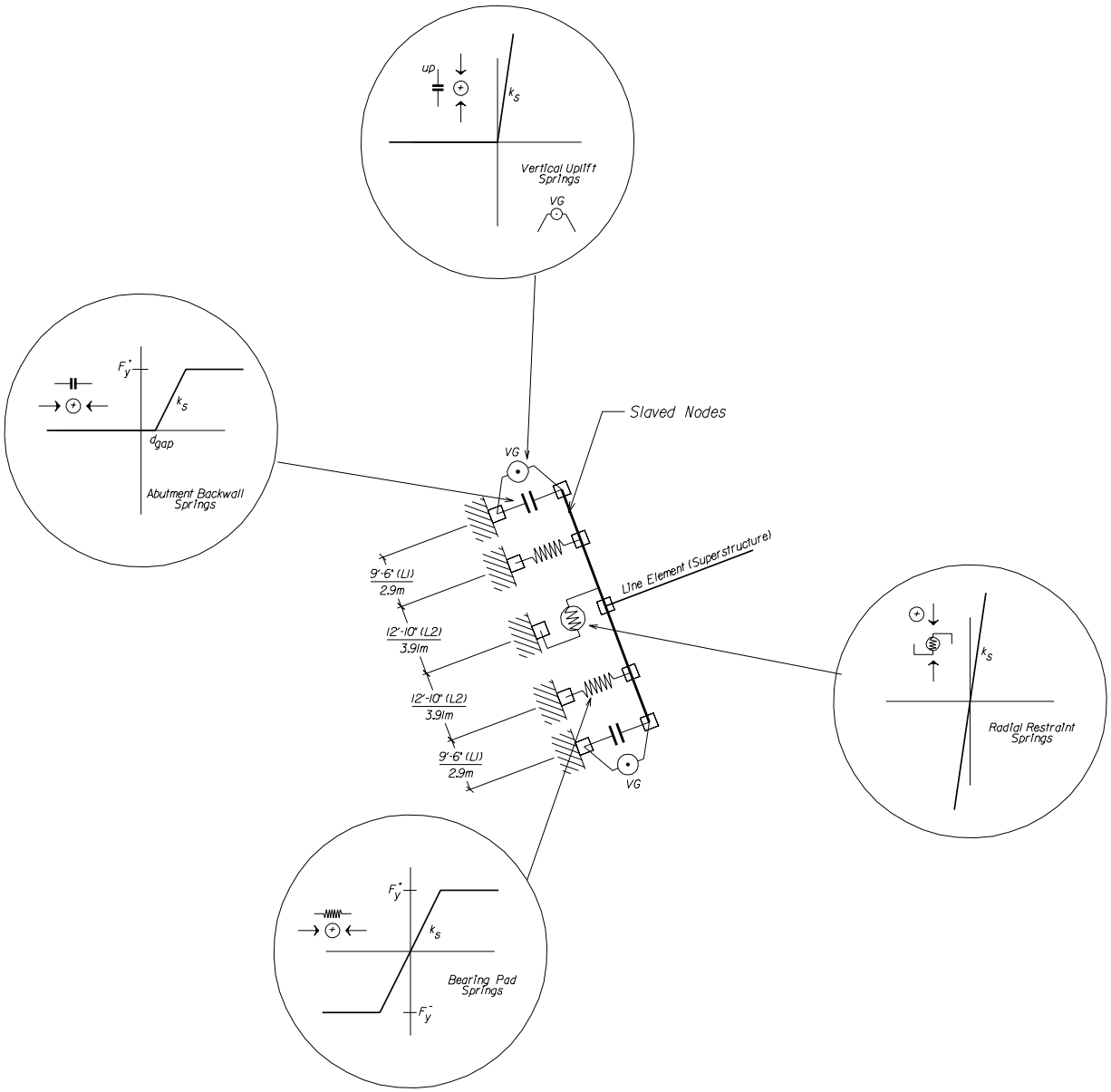

Figure 3.18: Schematic of Abutment Model

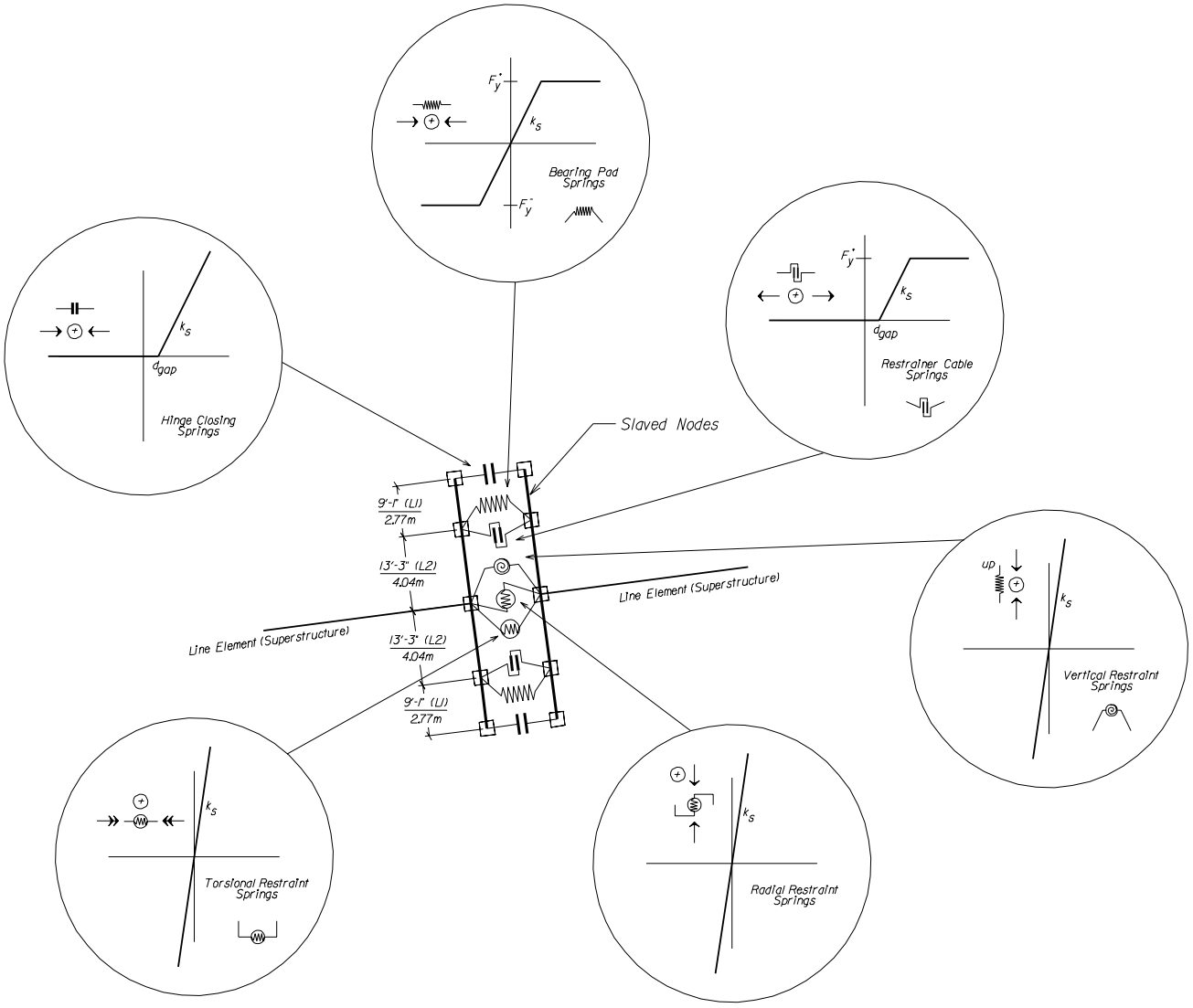

Figure 3.19: Schematic of Hinge Model

Chapter 4

Capacity Estimates

4.1 Introduction

The first step in the evaluation of the Separation and Overhead bridge in the 1994 Northridge earthquake is to estimate the capacities of components that may have contributed to the collapse of the first frame. The displacement capacity of a ductile bridge is limited by the deformation capacity of the plastic hinge zones in the piers, which is directly related to the maximum strain in the concrete and reinforcing steel. The maximum strain is selected based on the damage that can be tolerated, which in turns relates to the performance requirements for the bridge. However, ductile behavior can only be achieved if brittle failure modes do no occur prior to the structural components reaching their deformation capacity.

To examine the deformation capacity of the first frame, a model is constructed of the structural and foundation components between abutment 1 and hinge 4. The model of the frame is separated from the global bridge model by a vertical support at hinge 4, which eliminates all restraint and loading on the first frame from the rest of the bridge. Otherwise the model of the first frame follows the description in Chapter 3. Particular attention is directed to identifying brittle failure modes, such as shear failure of the pier columns and the box girder superstructure, and ductile modes not explicitly represented in the model, such as flexural yielding of the box girder.

4.2 Column Strength Capacities

The evaluation of shear capacity of bridge columns is an active area of research. The shear force capacity of a column depends on the contribution of the concrete, the transverse and longitudinal reinforcement, and on the axial force resisted by the column. The maximum shear force component resisted by the concrete depends on the amount of inelastic flexural deformation because of shear-flexure interaction and degradation of the concrete in the plastic hinge zone. Under small flexural deformation of a column, the concrete contribution to shear strength is up to five time greater than the shear strength under large inelastic deformation. The shear strength a column with elastic or a small amount of inelastic deformation is the brittle capacity, whereas the shear strength under large inelastic deformation is called

the ductile capacity. Based on experimental testing of reinforced concrete columns, various theories have been proposed for shear strength capacity (Aschheim and Moehle, 1996).

The formulation by Priestley and co-workers (Priestley et al., 1994b; Priestley et al., 1996) is used as to estimate the shear strength of the pier columns in the Separation and Overhead bridge. The shear model provides reasonable correlation with experimental data without excessive conservatism. The column shear strength is given as:

$$V_n = V_c + V_p + V_s \tag{4.1}$$

where V_c is the concrete component of shear strength, V_p is the contribution of the axial force in the column to the shear strength, and V_s is the steel component. The concrete component, V_c in MN, of the column shear strength is given as:

$$V_c = k\sqrt{f'_c}A_e \tag{4.2}$$

where:

k = Factor to account for member ductility. For this analysis, this factor is related to curvature ductility, as suggested by Priestley et al. (1996).

$$= \left\{ \begin{array}{ccc} 0.29 & for & \mu_\theta \leq 1 \\ 0.34 - 0.048\ \mu_\theta & for & 1 < \mu_\theta \leq 5 \\ 0.14 - 7.3 \times 10^{-3}\ \mu_\theta & for & 5 < \mu_\theta \leq 13 \\ 0.042 & for & \mu_\theta > 13 \end{array} \right\} \text{for biaxial ductility}$$

or:

$$= \left\{ \begin{array}{ccc} 0.29 & for & \mu_\theta \leq 3 \\ 0.43 - 0.048\ \mu_\theta & for & 3 < \mu_\theta \leq 7 \\ 0.15 - 7.3 \times 10^{-3}\ \mu_\theta & for & 7 < \mu_\theta \leq 15 \\ 0.042 & for & \mu_\theta > 13 \end{array} \right\} \text{for uniaxial ductility}$$

μ_θ = Curvature ductility.

f'_c = Compressive strength of concrete in MPa.

A_e = Effective shear area in m^2. Taken to be $0.8A_{gross}$ by Priestley et al. (1994b).

V_c = Concrete component of shear strength, in MN.

V_p is given as:

$$V_p = \frac{D - c}{2a}P \tag{4.3}$$

where:

D = Overall section depth or diameter in m.
c = Depth of the flexural compression zone in m.
a = L for single bending, $\frac{L}{2}$ for double bending.
L = Length of the member in m.
P = Axial load in member in MN (positive for compression).
V_p = Axial component of shear strength, in MN.

The contribution of the transverse reinforcement, V_s in MN, is given as:

$$V_s = \frac{A_v f_{yh} D'}{s} \cot(\phi) \tag{4.4}$$

where:

D' = Distance between centers of peripheral transverse reinforcement hoops in m.
f_{yh} = Yield stress of transverse reinforcement in MPa.
ϕ = Angle of inclined cracking. Priestley et al. (1994b) recommends 30°, but the more common design value of 45° is assumed for this analysis.
A_v = Area of transverse reinforcement per layer in m^2
s = Spacing of transverse reinforcement layers along member axis, in m.
V_s = Steel component of shear strength, in MN.

The brittle shear capacity of the columns is determined using $k = 0.29$. For purposes of evaluating shear failure modes of the columns, the ductile capacity is tabulated using $k = 0.10$, which corresponds to a curvature ductility of $\mu_\theta = 5.5$. The concrete strength can decrease further with larger inelastic deformation. For example, the components of the shear strength for pier 2 in the longitudinal direction are:

$$\begin{aligned} V_c &= 0.29\sqrt{34.5}\,3.37 \text{ (upper bound)} \\ &= 5.7 \text{ MN} \end{aligned}$$

$$
\begin{aligned}
V_c &= 0.10\sqrt{34.5}\,3.37 \text{ (lower bound)} \\
&= 2.0 \text{ MN}
\end{aligned}
$$

$$
\begin{aligned}
V_s &= \frac{(7.7\times10^{-4})(310)(1.07)}{0.305}\cot(45^\circ) \\
&= 0.840 \text{ MN}
\end{aligned}
$$

$$
\begin{aligned}
V_p &= \frac{1.22-0.25}{2\left(\frac{8.64}{2}\right)}\,14.2 \\
&= 1.6 \text{ MN}
\end{aligned}
$$

Then:

$$
\begin{aligned}
V_n &= V_c + V_s + V_p \\
&= 8.2 \text{ MN (upper bound)} \\
&= 4.4 \text{ MN (lower bound)}
\end{aligned}
$$

Similar calculations are performed to the local transverse direction and for other piers. The capacities of the columns given by the shear strength model are summarized in Table 4.1.

Table 4.1: Strength Capacities of Columns

Pier	Weak Axis			Strong Axis		
	Shear		Moment	Shear		Moment
	V_{nb} (brittle) kN $(kips)$	V_{nd} (ductile) kN $(kips)$	M_n $kN \times m$ $(kip \times in)$	V_{nb} (brittle) kN $(kips)$	V_{nd} (ductile) kN $(kips)$	M_n $kN \times m$ $(kip \times in)$
2	8200 (1800)	4400 (990)	3.2×10^4 (2.8×10^5)	9400 (2100)	5600 (1300)	7.2×10^4 (6.4×10^5)
3	8200 (1800)	4300 (970)	3.2×10^4 (2.8×10^5)	9400 (2100)	5500 (1200)	7.2×10^4 (6.4×10^5)
4	7400 (1700)	3600 (820)	2.4×10^4 (2.1×10^5)	8300 (1900)	4600 (1000)	6.1×10^4 (5.4×10^5)
5	7400 (1700)	3600 (810)	2.4×10^4 (2.1×10^5)	8300 (1900)	4500 (1000)	6.1×10^4 (5.4×10^5)
6	6800 (1500)	3600 (800)	4.0×10^4 (3.5×10^5)	7300 (1600)	4000 (890)	7.5×10^4 (6.6×10^5)
7	7300 (1600)	3700 (830)	3.8×10^4 (3.4×10^5)	7300 (1600)	3700 (840)	6.3×10^4 (5.6×10^5)
8	7300 (1600)	3700 (840)	3.8×10^4 (3.4×10^5)	7400 (1700)	3800 (850)	6.3×10^4 (5.6×10^5)
9	7400 (1700)	3800 (860)	3.8×10^4 (3.4×10^5)	7500 (1700)	3900 (870)	6.3×10^4 (5.6×10^5)
10	7700 (1700)	3900 (870)	2.4×10^4 (2.1×10^5)	8700 (2000)	5000 (1100)	6.1×10^4 (5.4×10^5)

Another approach for shear capacity has been developed in ATC-32 (1996). The ATC-32 expression for column shear strength is:

$$V_n = V_c + V_s \tag{4.5}$$

where V_c is the concrete component of the strength and V_s is the steel component. V_c is given by:

$$V_c = \left\{ \begin{array}{l} 0.17 \left[1 + \frac{P_e}{13.8\ A_g}\right] \sqrt{f'_c}\, A_e \text{ outside of plastic hinge region} \\ \\ 0.17 \left[0.5 + \frac{P_e}{13.8\ A_g}\right] \sqrt{f'_c}\, A_e \text{ within plastic hinge region} \end{array} \right\} \tag{4.6}$$

where:

P_e	=	Compressive axial load in member in MN (other expressions are given for tensile axial loads).
A_g	=	Gross cross section area of member in m^2
A_e	=	Effective cross section area of member in m^2. Taken to be $0.8A_g$ for columns.
f'_c	=	Concrete compressive strength in MPa.
V_c	=	Concrete component of shear strength in MN.

V_s is given by:

$$V_s = \frac{A_v f_{yh} d}{s} \tag{4.7}$$

where:

d	=	Distance from the outside to outside of transverse hoops, in m. ATC-32 (1996) suggests that this be taken as 0.8 times the depth of the member in the direction of the shear force being considered.
s	=	Spacing of transverse reinforcement along length of member in m.
A_v	=	Area of transverse steel reinforcement parallel to applied shear force, in m^2
f'_{yh}	=	Yield stress of transverse reinforcement in MPa.

The ATC-32 (1996) shear strength estimates are listed in Table 5.2 in the next chapter. The ATC-32 shear capacity esimates are compared with the values from Table 4.1 according to Priestley et al. (1994b) and the shear force demands from earthquake analysis of the bridge. The ATC-32 approach gives brittle shear capacities that are 60-70% of the capacities according to Priestley et al. (1994b). For the ductile shear strength, the ATC-32 capacity is 70-75% of the Priestley et al. (1994b) capacity for the short columns and about 90% for the tall columns. It has been argued that the conservatism in the ATC-32 approach is appropriate for design. The Priestley et al. (1994b) shear capacity estimates are used in this study because they provide a predictive model without design conservatism.

The flexural strength of the columns in the piers is calculated using the flexural theory of reinforced concrete members (Park and Paulay, 1975). The calculations are performed using the BIAX analysis program, as described in Section 3.3. The estimates from BIAX compare favorably with simple estimates of strength based on an equivalent compressive stress block and elastic-perfectly-plastic steel material. The flexural strength of the columns is listed in Table 4.1. The flexural deformation capacity is limited by the maximum strain acceptable for the confined concrete and longitudinal reinforcement.

4.3 Nonlinear Static Analysis of Frame 1

The purpose of a nonlinear static analysis ("pushover analysis") of a bridge is to determine amount and distribution of deformation in the components as the lateral displacement increases. Events of interest including yielding of components, reaching deformation or strain capacity of components, and brittle failure modes. Of particular interest in the first frame of the Separation and Overhead bridge is whether the shear capacity of the columns is reached at longitudinal displacement less than the displacement corresponding to the flexural deformation capacity of the plastic hinge zones. To examine the question, this section presents a pushover analysis of the frame under longitudinal lateral load.

The longitudinal load is applied, as shown in Figure 4.1, in proportion to the tributary mass of each pier. The frame was pushed to a displacement of 450 mm (18 in.) away from abutment 1. The analysis for longitudinal load towards the abutment would be the same as away from the abutment for the first 254 mm (10 in.) because of the gap between the box girder and the backwall (neglecting the lip at the top of the backwall). Beyond that point, the passive pressure of the abutment soil is activated.

The relationship between the longitudinal shear force and top displacement of piers 2 and 3 are shown in Figures 4.2 and 4.3, respectively, as determined from the pushover analysis. The force-displacement relationship for the entire frame is shown in Figure 4.4. The displacement in the three figures is in the direction of the frame 1 chord axis so that the forces may be compared between figures. The shear force in Figures 4.2 and 4.3 is in the longitudinal direction (weak bending direction) for each pier, whereas the force in Figure 4.4 is the total force along the frame 1 chord axis. The pushover curves show the typical reduction of stiffness due to yielding of the columns in the plastic hinge zones and yielding of the soil because of displacement of the pile shaft. Selected events in the behavior of the

frame are identified in the plots, including yielding of soil springs and yielding of longitudinal steel.

Also plotted in Figures 4.2 to 4.3 for piers 2 and 3 are the estimates of shear capacity, as discussed in the previous section. Comparing the pushover curve with the shear strength curve, it is clear that the shear capacity of the columns will be reached at a displacement substantially less than the maximum flexural deformation capacity. Pier 2 reaches its shear capacity at a longitudinal chord displacement of the frame of 135 mm (5.3 in.) and pier 3 reaches its shear capacity at a displacement of 170 mm (6.7 in.). The shear capacity for both columns occurs in the brittle/ductile transition zone corresponding to low curvature ductility. Although pier 2 reaches its shear capacity at a longitudinal displacement less than that for pier 3, the two values are fairly close given the uncertainty in the assumptions about material properties, particularly the soil properties and ground elevation. This analysis indicates that piers 2 and 3 can be expected to fail in shear at a small longitudinal displacement, less than 200 mm (7.8 in.), in a brittle/ductile mode with little inelastic flexural deformation.

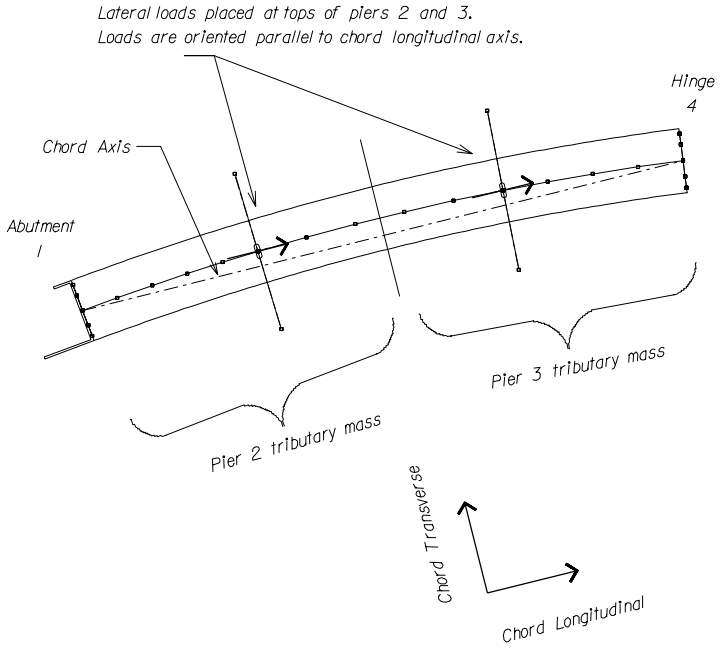

Figure 4.1: Coordinate System for Frame 1

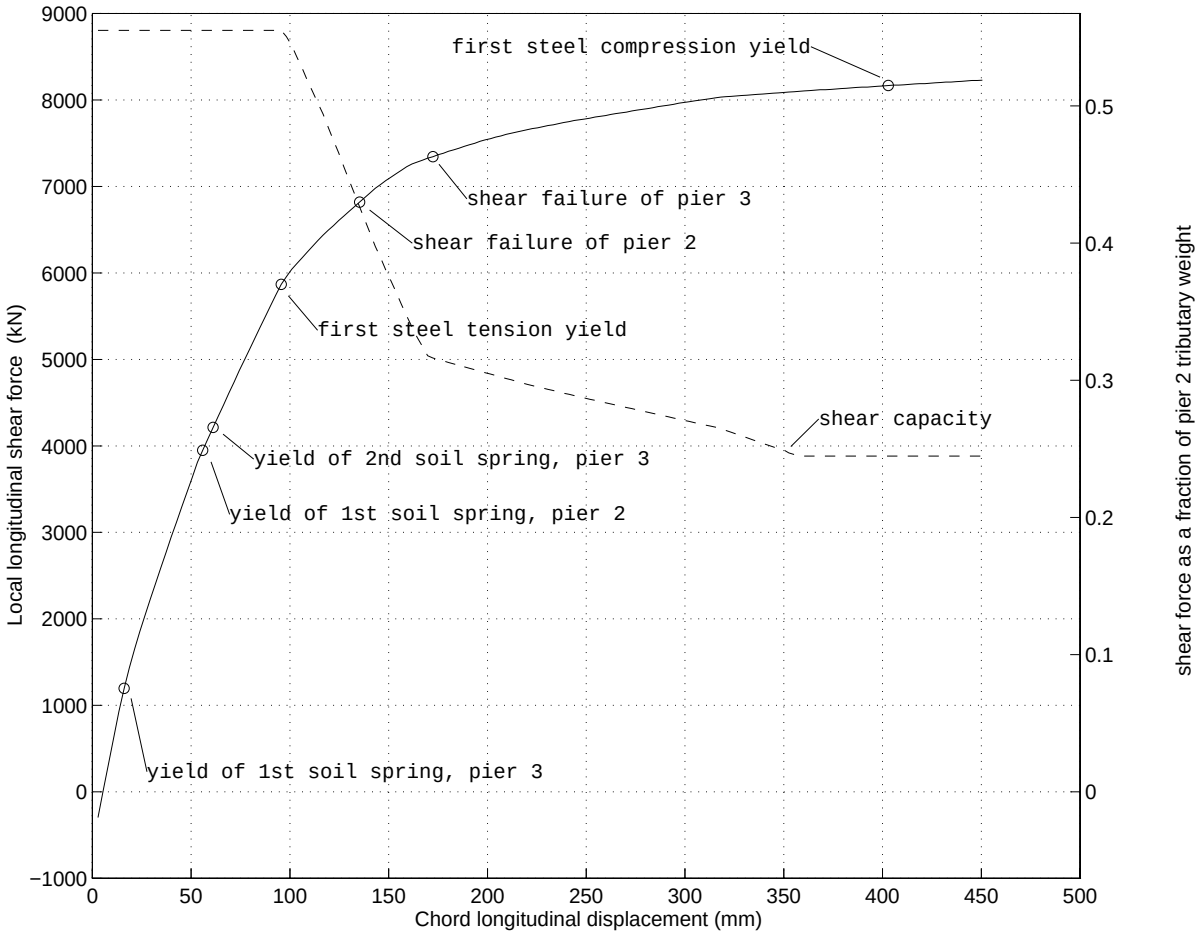

Figure 4.2: Pier 2 Force-Displacement for Longitudinal Static Pushover of Frame 1

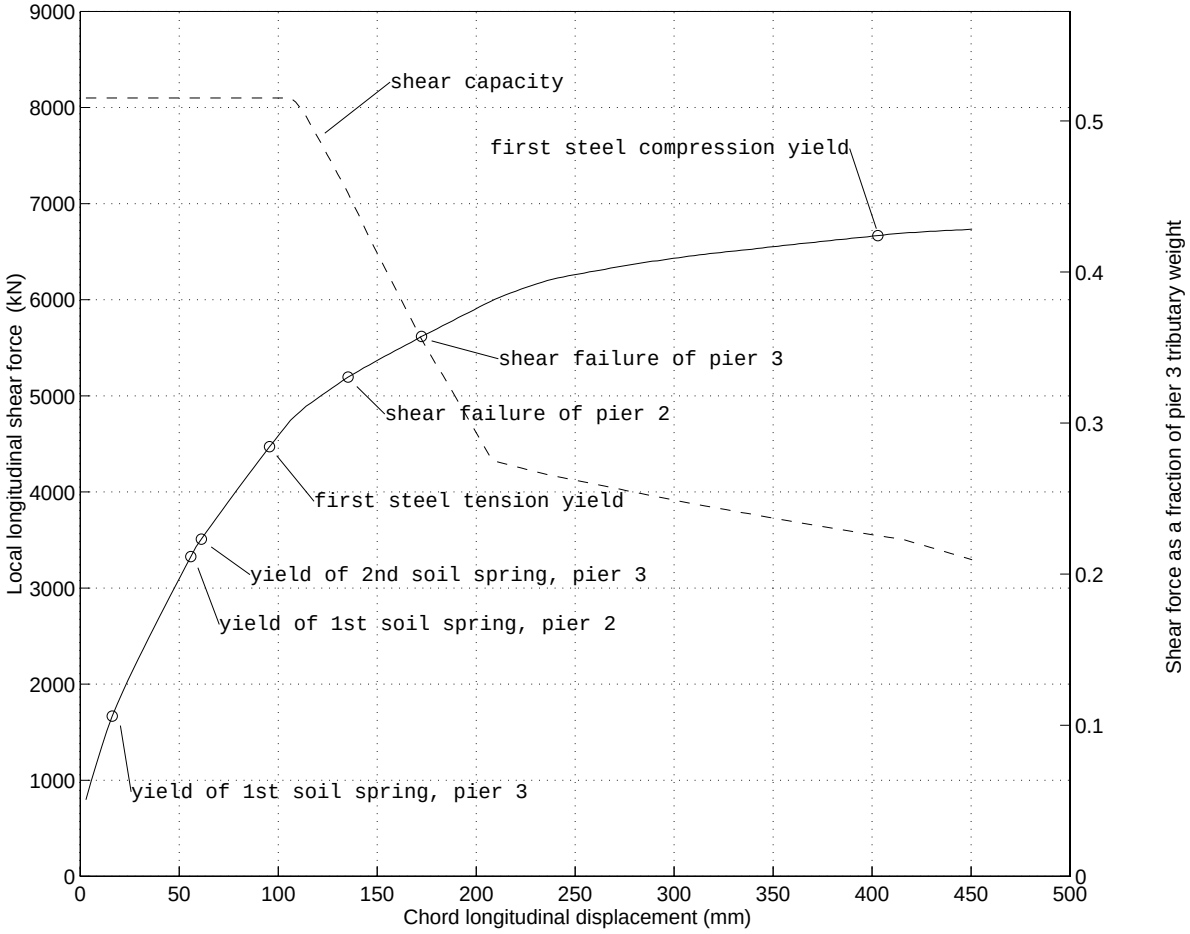

Figure 4.3: Pier 3 Force-Displacement for Longitudinal Static Pushover of Frame 1

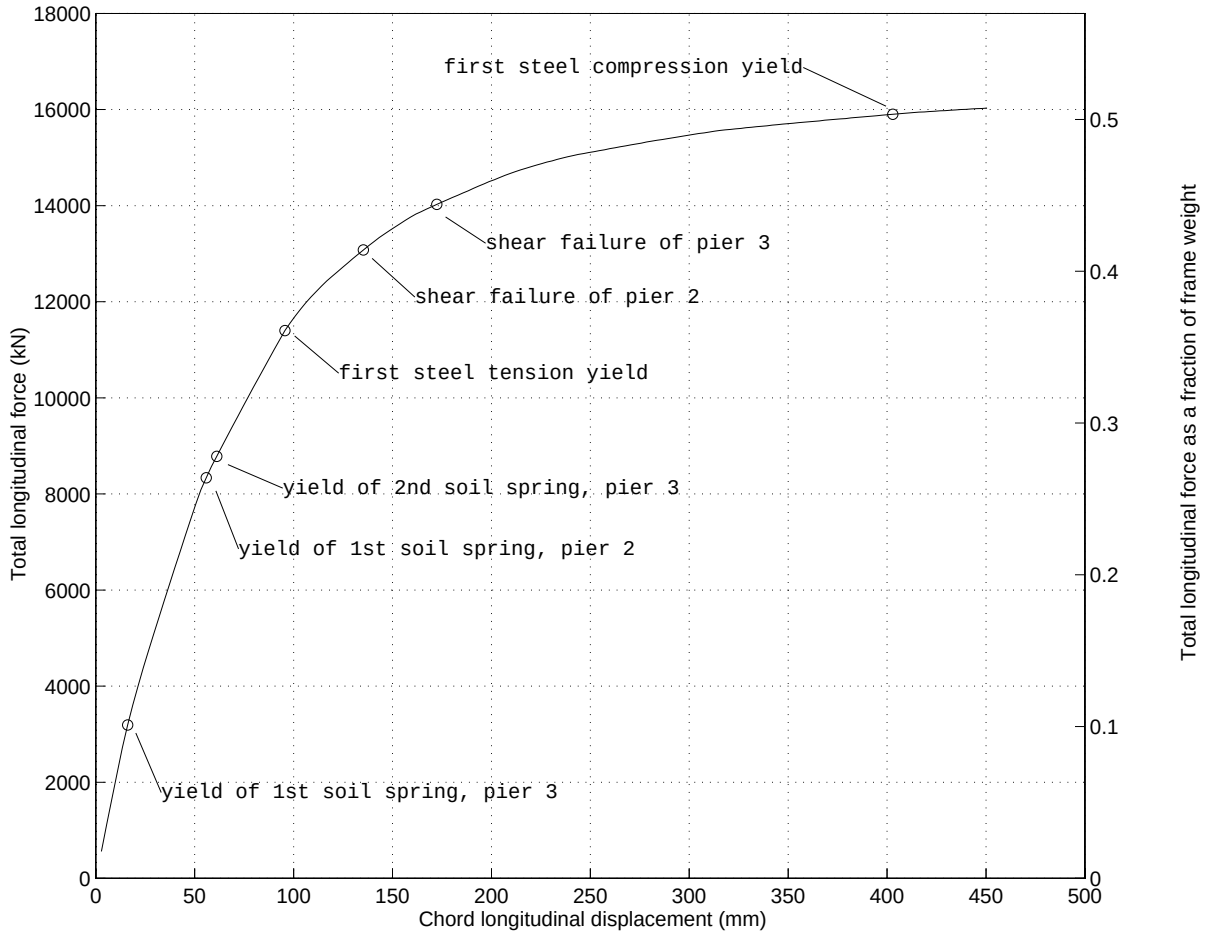

Figure 4.4: Frame 1 Force-Displacement for Longitudinal Static Pushover of Frame 1

4.4 Superstructure Strength Capacities

Since the superstructure box girder is modeled with linear elastic beam-column elements, the capacity of the box girder must be compared with maximum forces from the earthquake analyses. The flexural strength of the box girder is evaluated using the equivalent stress block approach (ACI, 1992; Naaman, 1982).

For example, the weak axis ultimate flexural strength of the superstructure in negative bending at pier 2 is estimated as follows, assuming:

f_{pu} = Ultimate stress in prestressing steel, assumed to be 1860 MPa.

f_{pi} = Initial stress in prestressing steel, assumed to be 75% of f_{pu}, 1400 MPa.

f_{pei} = Initial effective stress in prestressing steel, assumed to be 85% of f_{pi} or 1190 MPa (to account for losses due to creep, shrinkage, relaxation, etc.)

= 1190 MPa

Frictional losses are accounted for with the expression (Naaman, 1982):

$$f_{pe,\,pier\ 2} = f_{pei}\, e^{-(\mu\,\alpha + K\,s)} \tag{4.8}$$

where:

μ = Coefficient of angular friction. Assumed to be 0.25.

K = Wobble coefficient, per unit length (m). Assumed to be 0.001 $\frac{\text{rad}}{\text{m}}$.

α = Change in angle between force at the anchorage and the force at pier 2, in radians. Estimated to be 0.25 radians.

s = Length of tendon from anchorage point to pier 2. Estimated to be 46.6 m.

$f_{pe,\,pier\ 2}$ = Effective stress in prestressing steel at pier 2. Calculated to be 1060 MPa

To calculate the prestress in the tendons under ultimate conditions for an unbonded tendon, ACI (1992) recommends:

$$f_{ps,\,pier\ 2} = f_{pe,\,pier\ 2} + 69 + \frac{f'_c}{100\ \rho_p}\ \text{(in MPa)} \tag{4.9}$$

where:

f'_c = Concrete compressive stress, in MPa. Assumed to be 34.5 MPa for this strength estimate.

ρ_p = Prestressing reinforcement ratio, $\frac{A_{ps}}{b\ d_{ps}}$. Estimated as 1.36×10^{-3}.

$f_{ps,\,pier\ 2}$ = Effective prestress in tendons at pier 2 under ultimate conditions, in MPa. Calculated to be 1390 MPa.

A_{ps} = Area of prestressing steel, 3.55×10^{-2} m^2.

b = Width of compression block (soffit width, in this case), 13.9 m.

d_{ps} = Depth from the compression face of the member to the geometric center of the prestressing steel at pier 2, 1.88 m.

To estimate the flexural strength, the depth of the compression block is determined by iteration until the internal forces are in equilibrium. The results are summarized by:

a = Depth of equivalent compression stress block. Note that compressive strain at the extreme compression fiber is assumed to be 0.003, as suggested by ACI (1992)
= 0.132 m (determined by iteration)

c = Depth from the compression face of the member to the plastic neutral axis. Taken to be $\frac{a}{0.8}$, as suggested by ACI (1992).
= 0.166 m

A_{cc} = Approximate area of concrete compression block.
= 1.84 m^2

Three rows of conventional steel reinforcement in the superstructure are considered in the capacity analysis–#4 bars in the top of the deck slab, #5 bars in the bottom of the deck slab, and #6 bars in the soffit slab. The geometric properties are:

$$
\begin{aligned}
d_{steel,bot.} &= \text{Depth from the compression face of the member to the geometric center of the bottom bars (25–\#6 bars).} \\
&= 8.89 \times 10^{-2} \text{ m}
\end{aligned}
$$

$$
\begin{aligned}
A_{steel,bot.} &= \text{Area of bottom bar steel.} \\
&= 7.13 \times 10^{-3} \text{ m}^2
\end{aligned}
$$

$$
\begin{aligned}
d_{steel,top\ 1} &= \text{Depth from the compression face of the member to the geometric center of bars in the top of the deck slab (37–\#4 bars).} \\
&= 2.07 \text{ m}
\end{aligned}
$$

$$
\begin{aligned}
A_{steel,top\ 1} &= \text{Area of steel in top of deck slab.} \\
&= 4.69 \times 10^{-3} \text{ m}^2
\end{aligned}
$$

$$
\begin{aligned}
d_{steel,top\ 2} &= \text{Depth from the compression face of the member to the geometric center of bars in the bottom of the deck slab (50–\#5 bars).} \\
&= 2.01 \text{ m}
\end{aligned}
$$

$$
\begin{aligned}
A_{steel,top\ 2} &= \text{Area of steel in bottom of deck slab.} \\
&= 9.90 \times 10^{-3} \text{ m}^2
\end{aligned}
$$

Based on the location of the bars and the location of the plastic neutral axis, the strain and stress in the reinforcement can be estimated:

$$
\begin{aligned}
\varepsilon_{steel,bot.} &= \text{Compression strain in soffit steel.} \\
&= \frac{(c - d_{steel,bot.})}{c} 3.0 \times 10^{-3} \\
&= 1.39 \times 10^{-3}
\end{aligned}
$$

$$
f^{steel,bot.} = \text{Compressive stress in soffit steel.}
$$

$$= 279 \text{ MPa}$$

$\varepsilon_{steel,top\ 1}$ = Tensile strain in top deck steel.

$$= \frac{(d_{steel,top\ 1} - c)}{c} 3.0 \times 10^{-3}$$
$$= 3.44 \times 10^{-2}$$

$f_{steel,top\ 1}$ = Tensile stress in top deck steel.

$$= 462 \text{ MPa}$$

$\varepsilon_{steel,top\ 2}$ = Tensile strain in bottom deck steel.

$$= \frac{(d^{steel,top\ 2} - c)}{c} 3.0 \times 10^{-3}$$
$$= 3.33 \times 10^{-2}$$

$f_{steel,top\ 2}$ = Tensile stress in bottom deck steel.

$$= 462 \text{ MPa}$$

The stress in each steel group is calculated based on an elastic-perfectly-plastic model with an elastic modulus (E_s) of 2.0×10^5 MPa and a yield strain (ε_{yield}) of 2.31×10^{-3}.

The estimate of flexural strength is then given by summing the moments due to all internal forces about the compression face, which gives:

M_{ult} = Ultimate flexural strength estimate.

$$= (d_{steel,top\ 1}\ f_{steel,top\ 1}\ A_{steel,top\ 1} + d_{steel,top\ 2}\ f_{steel,top\ 2}\ A_{steel,top\ 2} + d_{ps}\ f_{ps}\ A_{ps})$$
$$- \left(\frac{a}{2} 0.85\ f'_c\ A_{cc} + d_{steel,bot.}\ f_{steel,bot.}\ A_{steel,bot.}\right)$$
$$= 1.0 \times 10^5 \text{ kN} \times \text{m}$$

The flexural strength at other locations in the superstructure are summarized in Table 4.2.

The shear strength of the box girder is bounded by the limiting values suggested by Naaman (1982). The total shear strength (V_n) consists of a concrete component and a steel component:

$$V_n = V_c + V_s$$

The lower and upper bounds on the concrete component (V_c) of shear strength are given by:

$$V_c = \left\{ \begin{array}{ll} 0.166\ \sqrt{f'_c}\ A_{web} & \text{(lower bound)} \\ 0.415\ \sqrt{f'_c}\ A_{web} & \text{(upper bound)} \end{array} \right\}$$

where:

$$\begin{array}{rcl} f'_c & = & \text{Concrete compressive strength in MPa.} \\ A_{web} & = & \text{Effective web area of superstructure in m}^2\text{.} \\ V_c & = & \text{Concrete component of shear strength in MN.} \end{array}$$

The steel component of shear strength is given by:

$$V_s = \frac{d_p\ A_v\ f_y}{s}$$

where:

$$\begin{array}{rcl} d_p & = & \text{Depth to prestressing steel from compression face of member in m.} \\ s & = & \text{Spacing of transverse reinforcement along length of member in m.} \\ A_v & = & \text{Area of transverse steel reinforcement parallel to applied shear force, in m}^2\text{.} \\ f_y & = & \text{Yield stress of transverse reinforcement in MPa.} \\ V_s & = & \text{Steel component of shear strength in MN.} \end{array}$$

As an example of the shear strength calculation, the lower bound on the concrete contribution to shear strength at the middle of the first span is 2.8 MN based on $f'_c = 34.5$ MPa and $A_{web} \approx 2.83$ m^2. The steel contribution to shear strength at the same location is 3.3 MN based on $d_p = 1.55$ m, $s = 0.51$ m, $A_v = 2.38 \times 10^{-3}$ m^2, and $f_y = 462$ MPa. The sum of contributions gives the total shear strength of 6.1 MN, or 6100 kN. The bounds on shear strength of the box girder for the first two spans are summarized in Table 4.2.

Table 4.2: Superstructure Capacities for Frame 1

Location	Moment		Shear	
	Positive M_n^+ $kN \times m$ $(kip \times in)$	Negative M_n^- $kN \times m$ $(kip \times in)$	Positive V_n^+ kN $(kips)$	Negative V_n^- kN $(kips)$
Middle of First Span	8.2×10^4 (7.2×10^5)	-3.9×10^4 (-3.5×10^5)	6100 (1400) to 1.0×10^4 (2300)	-6100 (-1400) to -1.0×10^4 (-2300)
At Pier 2	1.3×10^4 (1.2×10^5)	-1.0×10^5 (-9.1×10^5)	1.1×10^4 (2600) to 1.6×10^4 (3700)	-1.1×10^4 (-2600) to -1.6×10^4 (-3700)
Middle of Second Span	9.2×10^4 (8.2×10^5)	-1.8×10^4 (-1.6×10^5)	7500 (1700) to 1.3×10^4 (2800)	-7500 (-1700) to -1.3×10^4 (-2800)
At Pier 3	1.3×10^4 (1.2×10^5)	-9.2×10^4 (-8.2×10^5)	1.1×10^4 (2600) to 1.6×10^4 (3700)	-1.1×10^4 (-2600) to -1.6×10^4 (-3700)
Middle of Third Span	6.4×10^4 (5.7×10^5)	-3.4×10^4 (-3.0×10^5)	6100 (1400) to 1.0×10^4 (2300)	-6100 (-1400) to -1.0×10^4 (-2300)

Chapter 5

Earthquake Analysis and Evaluation of Damage

5.1 Introduction

This chapter presents the earthquake response analysis of the global model of the Separation and Overhead bridge described in Chapter 3. The objective of the analysis is to estimate the demands on the bridge during the 1994 Northridge earthquake using the six earthquake ground motion records discussed in Section 2.3. The free-field ground motion is assumed to be uniform for the supports of the bridge, so spatial variation of the ground motion is not included. The model includes soil-structure interaction effects The role of the vertical ground motion component on bridge behavior is examined. Several analyses are repeated to investigate the impact of the assumed ground elevation at pier 2.

5.2 Dynamic Analysis

Before commencing with the dynamic analysis, the natural vibration modes of the bridge were evaluated with the stiffness under dead load only. For this linearization, the gap elements at the hinges are open, so the global vibration modes represent those of a linearized model with no longitudinal connectivity at the intermediate hinges (similar to a linear "tension" model). Table 5.1 lists the vibration periods and percentage of participating mass in the three global directions. The lowest vibration mode, with a 2.15 sec period, involves transverse vibration of the entire bridge, but with predominant participation of the tall frames. The second mode (1.64 sec period) is the longitudinal vibration of the tall frames. Mode 7 with a 0.82 sec period is the longitudinal vibration mode for frame 1. The vertical vibration modes have periods of 0.35 sec to 0.45 sec, including modes 14 and 15 in Table 5.1.

The inelastic model of the columns and soil provide hysteretic energy dissipation. The energy dissipation in the other components, including radiation damping for the footings, is represented as viscous damping using the Rayleigh approach (Clough and Penzien, 1993). Five percent damping is assumed at vibration periods of 2.5 sec and 0.60 sec to represent a broad range of high-participation modes and the softening that takes place as the columns

and soil yield. Using standard expressions (Clough and Penzien, 1993), the mass proportional coefficient is $\alpha = 0.203$ sec^{-1} and the stiffness proportional coefficient is $\beta = 0.00770$ sec. With this Rayleigh damping model, the damping coefficients for the vibration modes are listed in Table 5.1.

Table 5.1: Summary of Principal Vibration Modes for Global Model

Mode No.	Period sec	Modal Mass Participation as a Fraction of Total Mass			Viscous Damping percent
		Global X	Global Y	Global Z	
1	2.15	0.005	0.316	0.000	4.6
2	1.64	0.514	0.003	0.000	4.1
3	1.47	0.000	0.086	0.000	4.0
4	1.19	0.029	0.004	0.000	4.0
5	1.03	0.000	0.192	0.000	4.0
6	0.96	0.016	0.000	0.000	4.1
7	0.82	0.257	0.000	0.000	4.3
8	0.81	0.014	0.091	0.000	4.3
9	0.72	0.000	0.000	0.000	4.5
10	0.63	0.004	0.000	0.008	4.9
11	0.56	0.000	0.000	0.000	5.2
12	0.56	0.003	0.000	0.000	5.2
13	0.53	0.005	0.051	0.000	5.4
14	0.45	0.002	0.000	0.018	6.1
15	0.40	0.002	0.000	0.046	6.7
Sum	-	0.851	0.743	0.072	

The dynamic analysis uses the implicit Newmark integration scheme with the event-to-event state determination strategy in DRAIN-3DX. To reduce the number of events and hence computation time, the force overshoot factors for event determination are not greater than 1% of the yield force for the nonlinear elements, and less than 0.1% for many of the elements. Based on a trade-off between accuracy and amount of computation, an integration time step of 0.01 sec was used for all dynamic analyses. The accuracy of the solution was monitored by the unbalanced forces and error in energy terms.

The model has approximately 750 degrees-of-freedom. The computation time for 2000 time steps is approximately 30-45 minutes (depending on the ground motion) on a Digital AlphaStation 500 workstation computer.

5.3 Evaluation of Earthquake Response

5.3.1 Shear Force Demands

The maximum shear forces in the nine piers are listed in Table 5.2 for each of the six ground motion records. The shear forces are the maximum value, over the response history, in the local longitudinal and transverse direction, for each pier. The maximum shear force can be compared with the estimates of shear strength, as discussed in Section 4.2. When comparing the column shear demands with capacities, it should be emphasized that the columns had a small amount of transverse reinforcement with #5 hoops at 300 mm (12 in.) and cross-

bars. The bridge satisfied the pre-1971 design specification, but the coluumns clearly have inadequate shear capacity according to capacity-design principles.

Considering the estimates of column shear strength using the Priestley et al. (1994b) theory, the longitudinal shear force demand in pier 2 exceeds the brittle capacity for the Sylmar, Jensen, Newhall, and Hutchings, ICN ground motion records. All the records produce longitudinal shear forces greater than the ductile shear capacity. The longitudinal shear force demand in pier 3 does not exceed the brittle capacity for any record, although the Sylmar and Hutchings, ICN simulated records reach 90% of the brittle capacity; the longitudinal shear force in pier 3 exceeds the ductile capacity for all the ground motion records, with the exception of the lower-amplitude Arleta record. The transverse shear forces in piers 2 and 3 are greater than the ductile shear capacity for most records, but less than the brittle shear capacity.

The second frame of the bridge is supported by piers 4 and 5, for which the maximum longitudinal shear forces for all records are less than the ductile shear capacity of the piers. Several of the records produce transverse shear forces greater than the ductile shear capacity of piers 4 or 5, but less than the brittle capacity. For piers 6 to 9 the maximum shear forces from the demand analysis are less than the ductile shear capacity of the piers. At the other end of the bridge, pier 10 is relatively short and the longitudinal shear force exceeds the ductile capacity for the Sylmar and Hutchings, ICN records.

Examining the pier response in more detail, Figures 5.1 to 5.6 show the shear force demand history in piers 2, 3, and 4 for the six ground motion records, each including the vertical ground motion component. The computed transverse, longitudinal, and resultant shear forces for the pier are plotted as a function of time. The longitudinal response dominates the shear force demand for these three piers. Also plotted on the shear force history figures for piers 2 and 3 are the shear capacity estimates from Priestley et al. (1994b). The transition from brittle to ductile shear capacity is based on the curvature ductility of the columns as obtained from the demand analysis.

When interpreting the shear demands and capacity estimates it must be recognized that there are many assumptions in the demand and capacity models and the selection of earthquake ground motion representative of the site. Nevertheless, the shear force histories provide insight into the behavior of the bridge in the 1994 Northridge earthquake. Considering the computed response to the Symlar record in Figure 5.1, the first large shear excursion for piers 2 and 3 reaches the theoretical shear capacity between the brittle and ductile zones as the bridge displaces longitudinally away from abutment 1. The second large response pulse exceeds the ductile shear capacity by nearly a factor of two as the bridge moves longitudinally towards abutment 1. The shear force demand in pier 4 is less than the ductile shear capacity for that pier. The shear response computed for the Newhall and Jenson records in Figures 5.2 and 5.3, respectively, is similar to the behavior noted for the Sylmar record. The low amplitude of the Arleta record gives shear demands less than the ductile capacity for the piers, as shown in Figure 5.4. The computed shear demands for the two simulated records in Figures 5.5 and 5.6 give more cycles of peak response than the recorded ground motions. According to the analysis for these ground motions, piers 2 and 3 have shear force demands greater than the degraded shear capacity after several cycles in the case of the Hutchings, ICN simulated record. For the Horton simulated record, both piers and 2 and 3 just reach

the shear capacity after several cycles.

Another view of the computed column shear demands is shown in Figures 5.7 to 5.24, in which the shear force locus for each pier is plotted as longitudinal shear force against transverse shear force. The loci plots also show the brittle and ductile envelopes of shear capacity, which are elliptical in shape based on the longitudinal and transverse shear capacities using Priestley et al. (1994b). Considering the computed response to the Sylmar record in Figure 5.7, the demands in piers 2 and 3 pierce the ductile shear capacity envelope, primarily in the longitudinal direction, whereas the pier 4 shear demand only touches the ductile shear capacity envelope. In Figures 5.8 and 5.9 the shear demand locus just touches the ductile capacity envelope for piers 5 and 10; piers 6 to 9 have adequate shear capacity according to the analysis. The computed responses for the Newhall and Jensen records, Figures 5.10 to 5.15, are similar to that for Sylmar. It is interesting to note the predominant transverse response for the tall piers 5 to 7 in Figure 5.14. The Arleta record produces relatively small shear demands, as shown in Figures 5.16 to 5.18.

The computed shear response for the Hutchings, ICN simulated record is plotted in Figures 5.19 to 5.21. The response follows the general trends observed for the recorded ground motion records, but the shear force loci have more bi-directional response and a greater number of peak excursions. The shear force response to the Horton simulated record, Figures 5.22 to 5.24, does not have as many excursions beyond the ductile capacity as the Hutchings, ICN simulated record. The response for the short piers near the ends of the bridge is predominantly longitudinal and the response of the tall piers in the middle of the bridge is predominantly transverse.

Table 5.2: Maximum Column Shear Force Demands and Capacity Estimate

Record			Pier 2 kN	Pier 3 kN	Pier 4 kN	Pier 5 kN	Pier 6 kN	Pier 7 kN	Pier 8 kN	Pier 9 kN	Pier 10 kN
Arleta	With Vertical Motion	Longitudinal	-4710	-2900	-1320	1260	997	582	981	831	1890
		Transverse	3530	4280	3440	3150	1680	1220	1230	856	-1920
	Without Vertical Motion	Longitudinal	-4670	-2860	-1280	1120	985	583	991	841	1880
		Transverse	3570	4270	3380	3170	1650	1210	1220	910	-1920
Sylmar	With Vertical Motion	Longitudinal	-10100	-7260	-3500	-3170	-2600	-1370	-2720	-2320	-4380
		Transverse	5060	5760	4570	-3500	2700	1920	-2630	-1520	-3680
	Without Vertical Motion	Longitudinal	-9950	-7170	-3450	-3150	-2630	-1390	-2740	-2380	-4320
		Transverse	4920	5790	4590	-3500	2720	1920	-2610	-1550	-3790
Jensen	With Vertical Motion	Longitudinal	-8220	-6450	-2960	2830	2140	1170	1990	1740	3460
		Transverse	4510	-5990	-3870	-6330	-3440	2200	2630	1940	4430
	Without Vertical Motion	Longitudinal	-8370	-6200	-2830	2660	2060	1100	2013	1770	3330
		Transverse	4560	-6150	-3890	-6350	3380	-2170	2640	1930	4400
Horton, Pier 3	With Vertical Motion	Longitudinal	-7240	4870	-2290	-1960	1930	1130	2230	1970	3720
		Transverse	5350	-6620	-4540	-5960	3390	2330	2530	-1540	-3910
	Without Vertical Motion	Longitudinal	-7310	4870	2230	-2010	1970	1160	2220	1970	3730
		Transverse	5590	6670	-4540	-6050	3400	2340	2500	-1520	-3880
Newhall	With Vertical Motion	Longitudinal	-9050	-6730	3260	-2950	-2220	1270	-2350	1980	-3680
		Transverse	4730	4750	5140	-5300	-2230	-1810	2000	-1440	3020
	Without Vertical Motion	Longitudinal	-9110	-6690	-3180	-2850	-2130	1190	2170	1880	-3590
		Transverse	5210	-5200	5350	-5380	2230	-1760	1970	-1360	2760
Hutchings, ICN	With Vertical Motion	Longitudinal	9590	7580	3520	3530	2970	1660	2850	2650	4460
		Transverse	-6240	8970	6700	4430	3150	2050	2330	2080	-3750
	Without Vertical Motion	Longitudinal	9560	7410	3330	3330	2800	1510	2800	2580	-4290
		Transverse	6190	8930	6600	-4800	2940	1900	2190	2100	3700
Capacity, (Priestley et al., 1994b)	Brittle	Longitudinal	8170	8100	7400	7360	6840	7270	7320	7400	7670
		Transverse	9360	9260	8350	8300	7270	7330	7370	7450	8740
	Ductile	Longitudinal	4400	4330	3630	3590	3550	3680	3720	3810	3890
		Transverse	5590	5490	4580	4530	3980	3740	3780	3860	4970
Capacity, (ATC-32, 1996)	Brittle	Longitudinal	4850	4840	4660	4660	4670	4930	4780	4910	4860
		Transverse	5250	5240	5060	5060	4880	4960	4810	4930	5260
	Ductile	Longitudinal	3210	3200	3020	3020	3240	3370	3220	3340	3220
		Transverse	3610	3600	3420	3520	3450	3390	3250	3370	3620

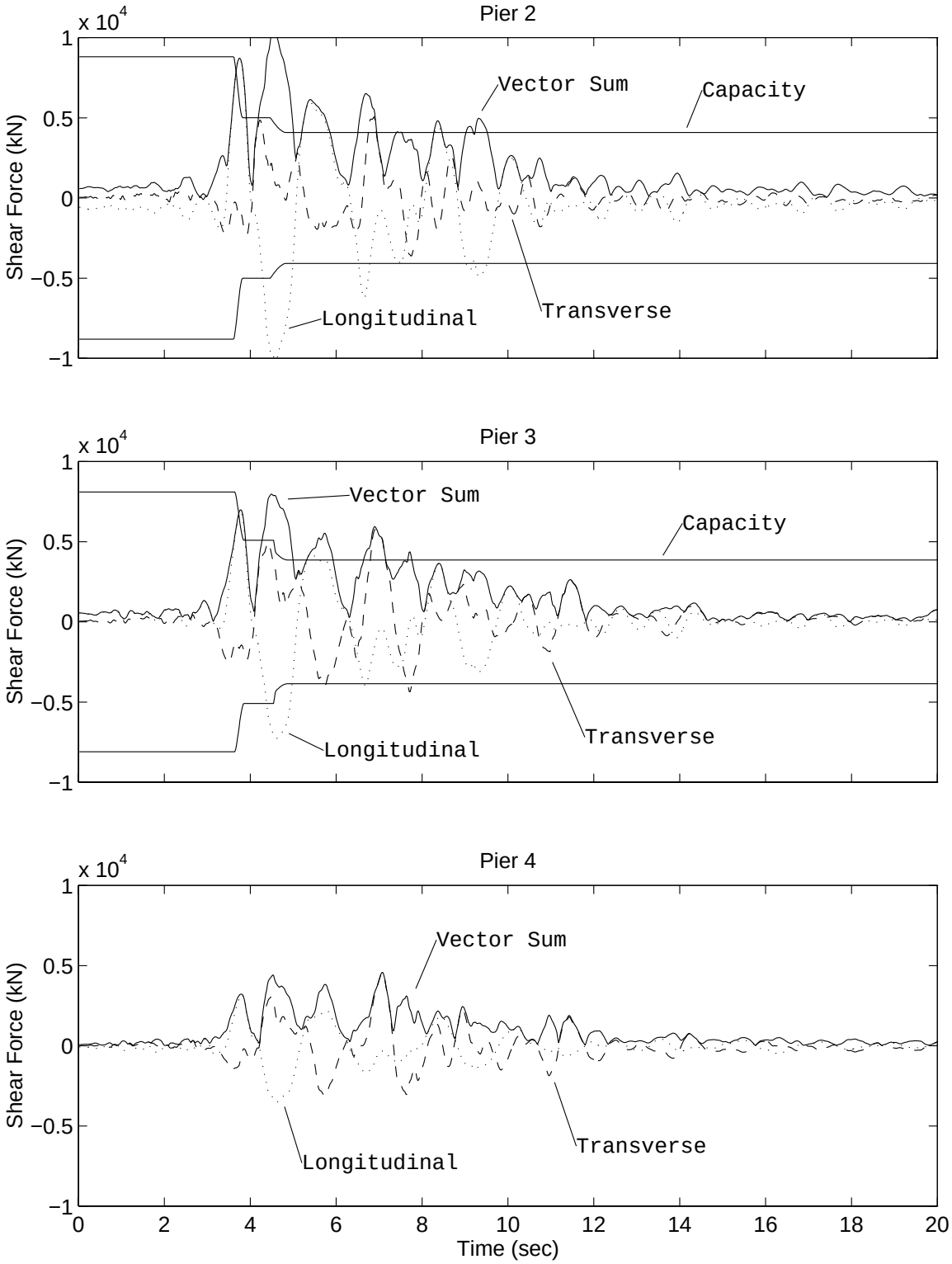

Figure 5.1: Column Shear Force Demand vs. Capacity, Sylmar Ground Motion

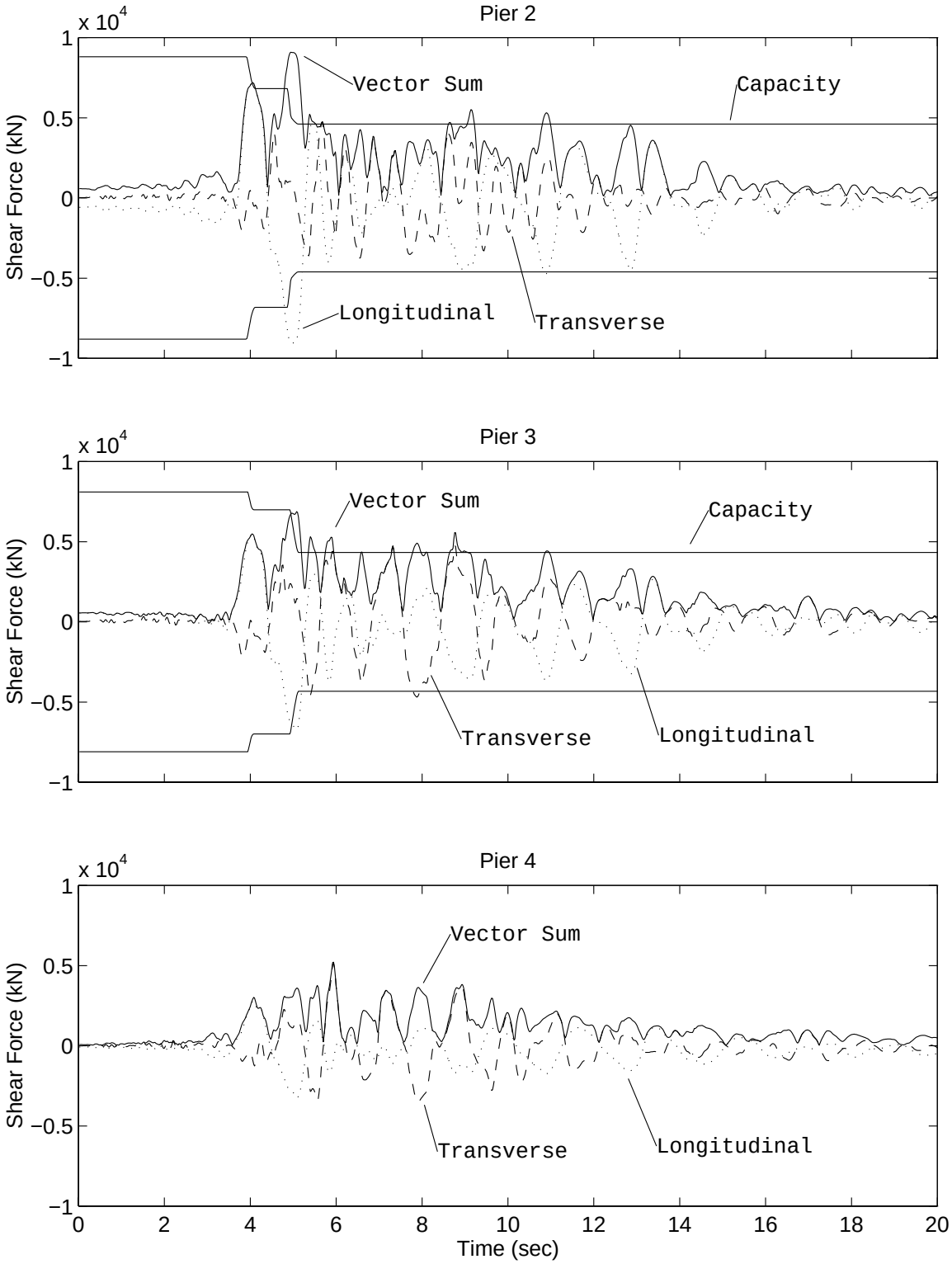

Figure 5.2: Column Shear Force Demand vs. Capacity, Newhall Ground Motion

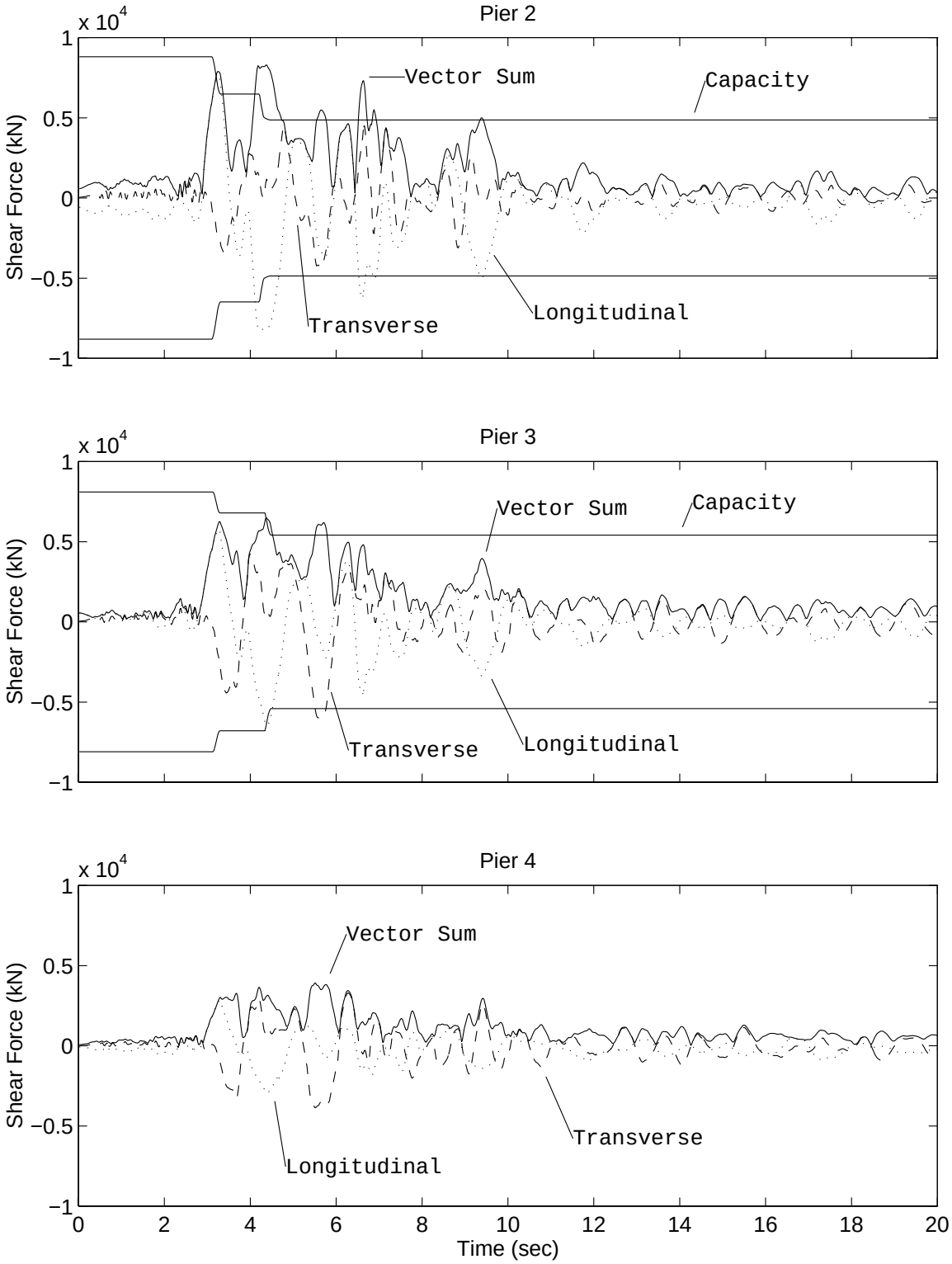

Figure 5.3: Column Shear Force Demand vs. Capacity, Jensen Ground Motion

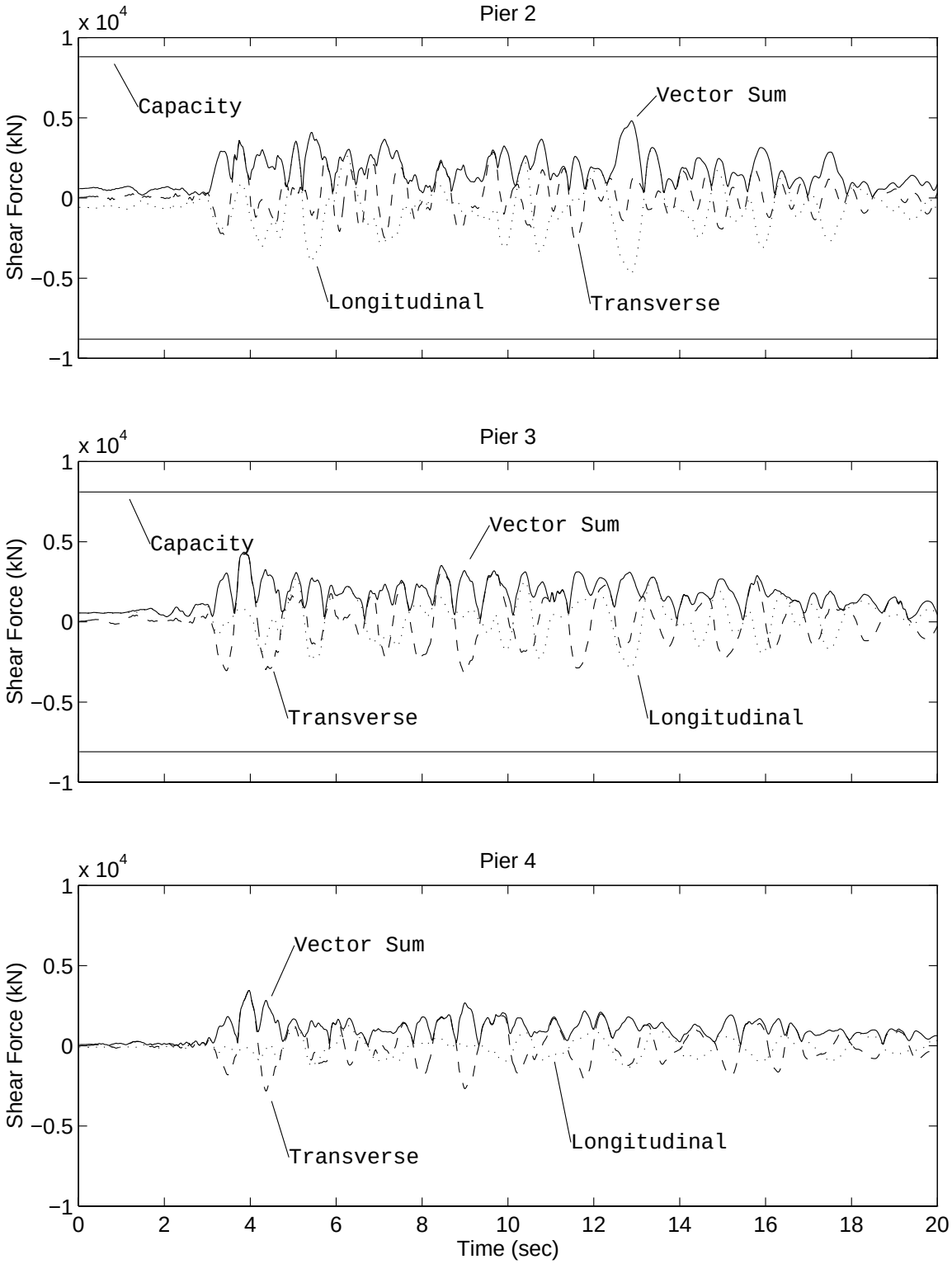

Figure 5.4: Column Shear Force Demand vs. Capacity, Arleta Ground Motion

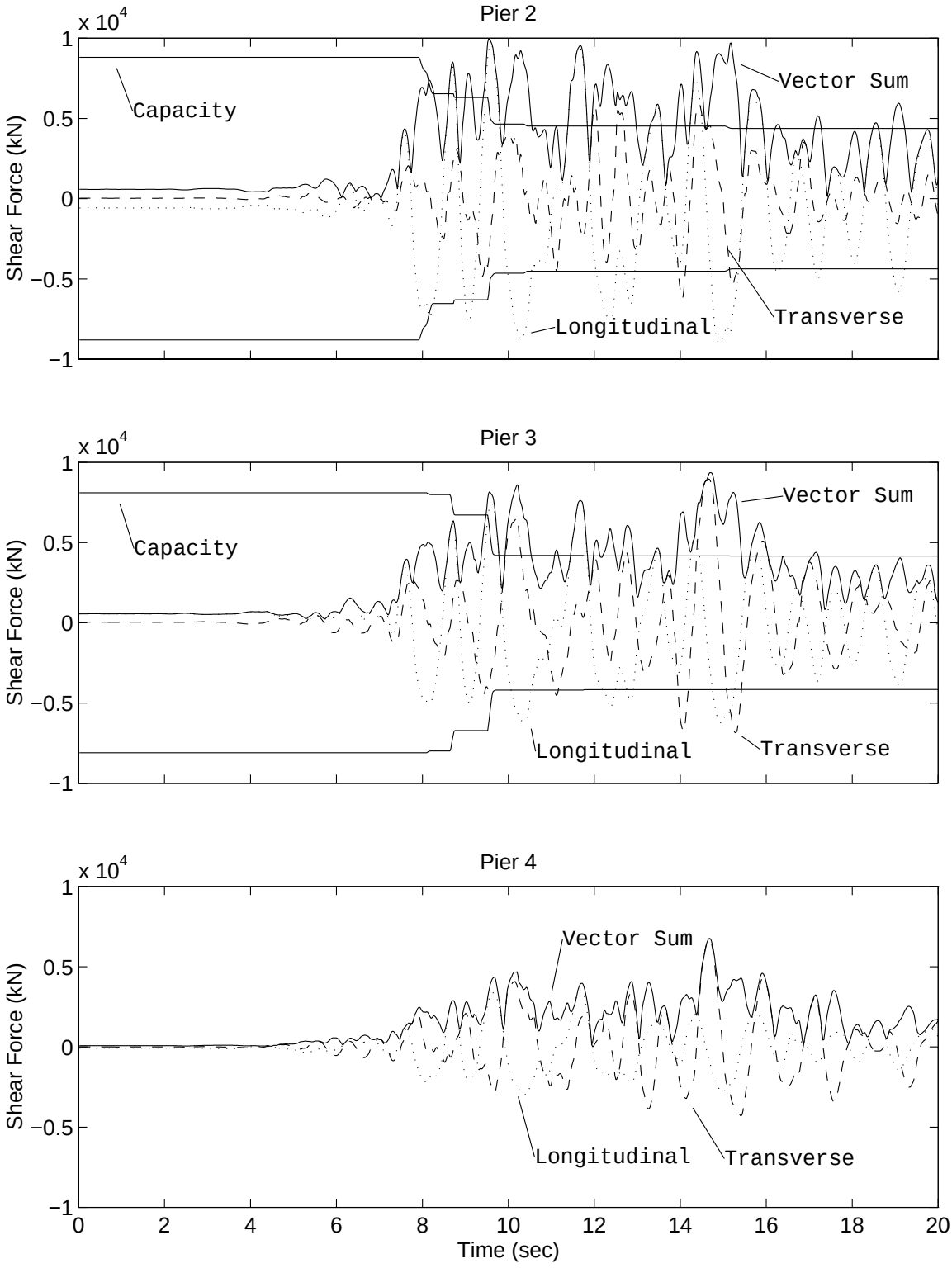

Figure 5.5: Column Shear Force Demand vs. Capacity, Hutchings et al. (1996) ICN Simulated Ground Motion

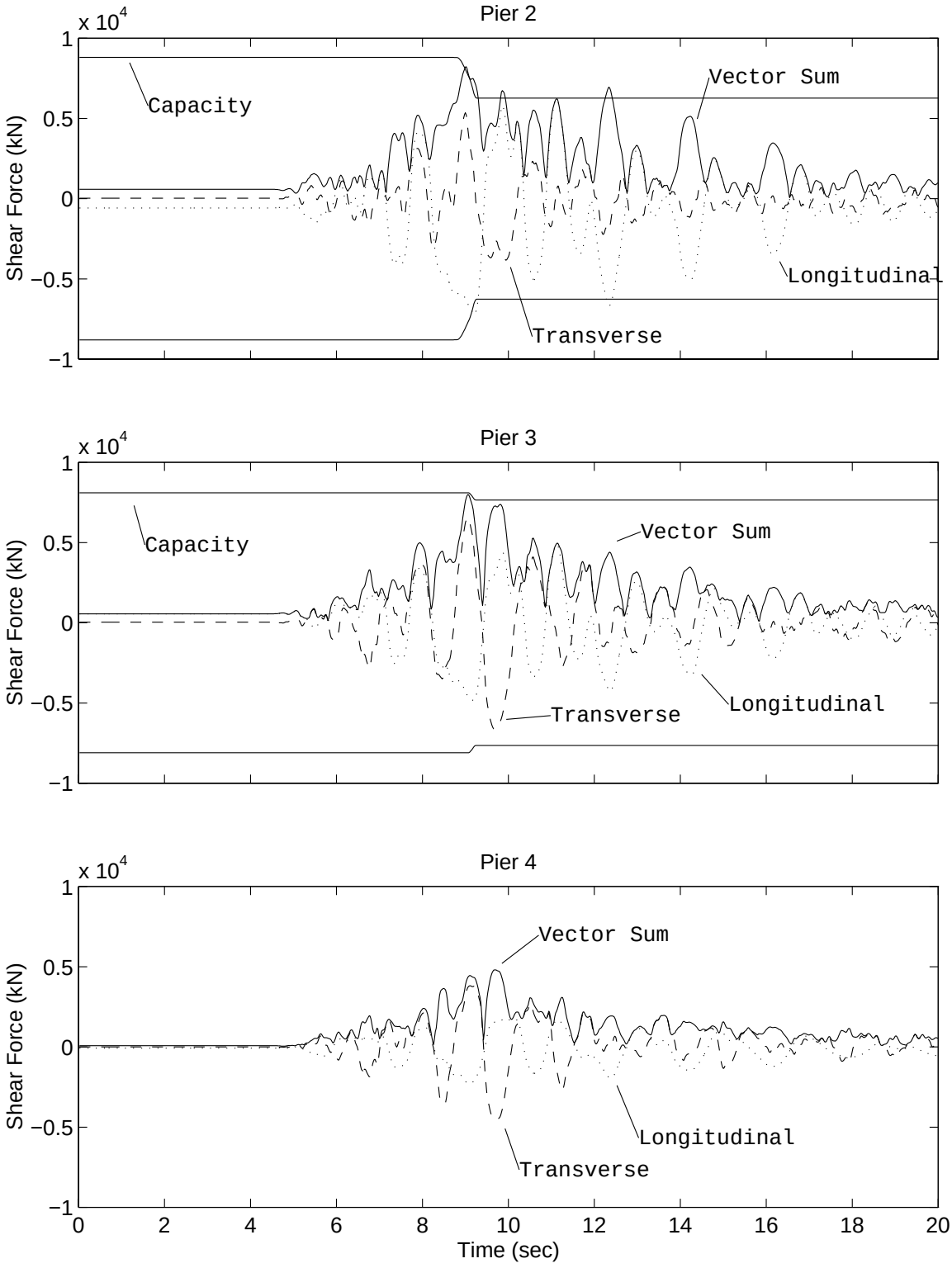

Figure 5.6: Column Shear Force Demand vs. Capacity, Horton et al. (1995) Pier 3 Simulated Ground Motion

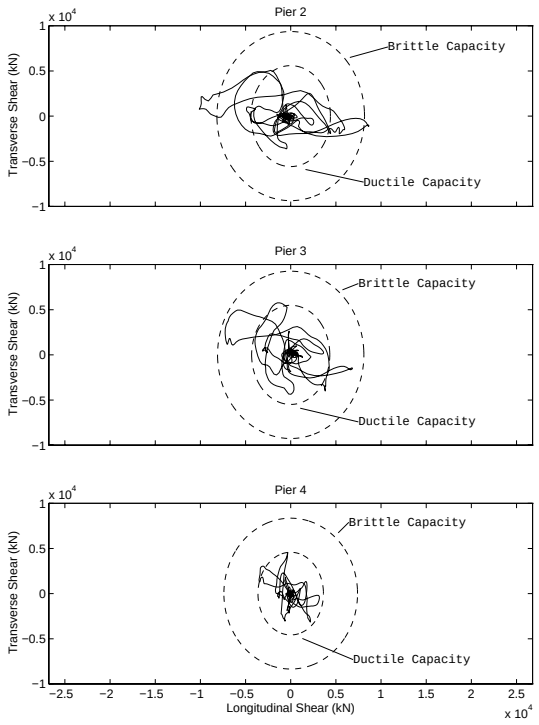

Figure 5.7: Column Shear Force (Piers 2 to 4), Longitudinal vs. Transverse, Sylmar Ground Motion

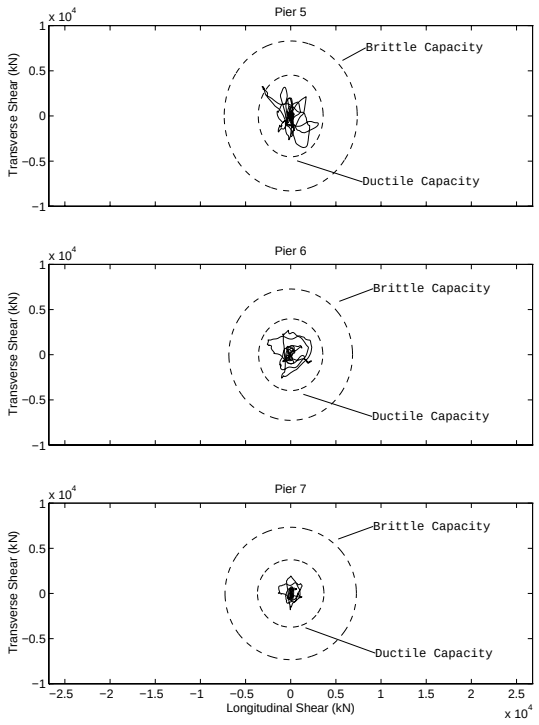

Figure 5.8: Column Shear Force (Piers 5 to 7), Longitudinal vs. Transverse, Sylmar Ground Motion

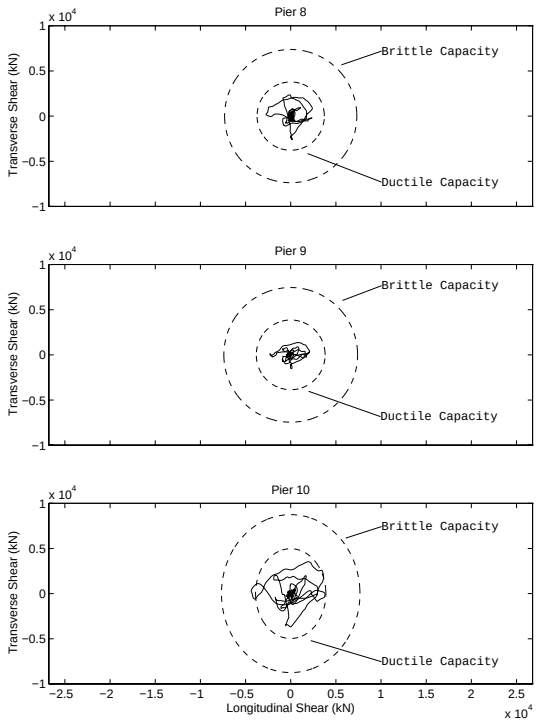

Figure 5.9: Column Shear Force (Piers 8 to 10), Longitudinal vs. Transverse, Sylmar Ground Motion

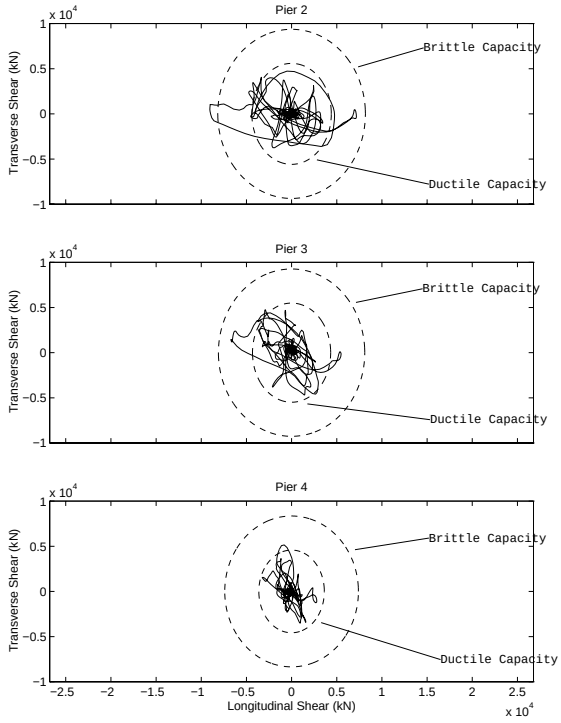

Figure 5.10: Column Shear Force (Piers 2 to 4), Longitudinal vs. Transverse, Newhall Ground Motion

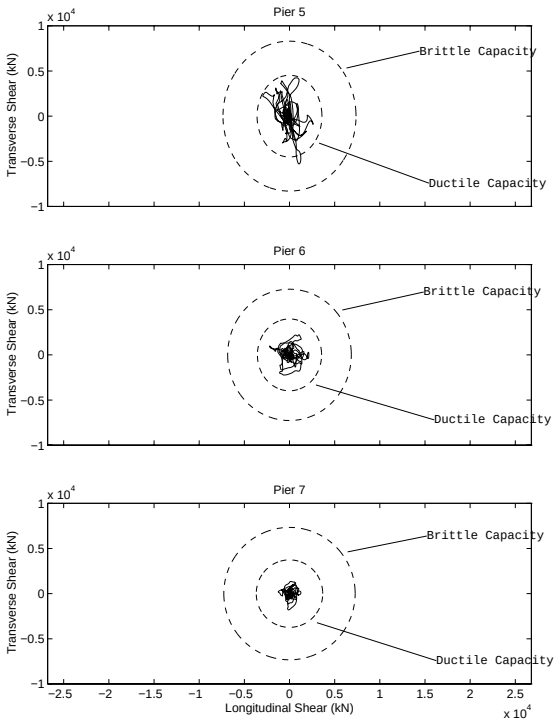

Figure 5.11: Column Shear Force (Piers 5 to 7), Longitudinal vs. Transverse, Newhall Ground Motion

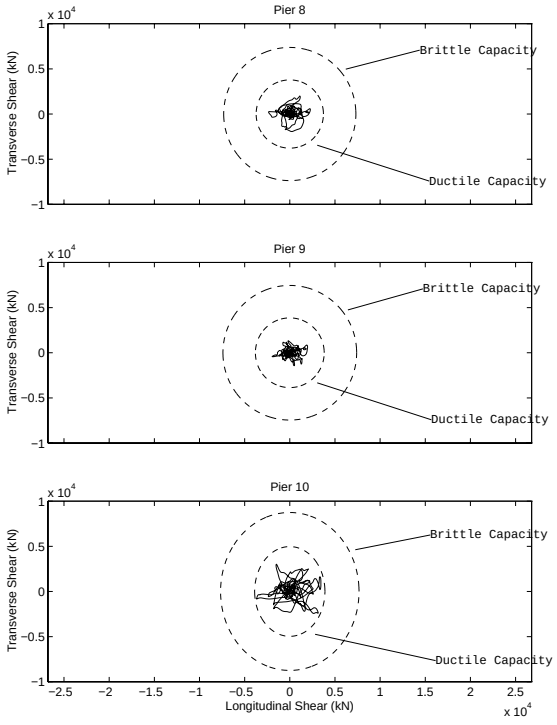

Figure 5.12: Column Shear Force (Piers 8 to 10), Longitudinal vs. Transverse, Newhall Ground Motion

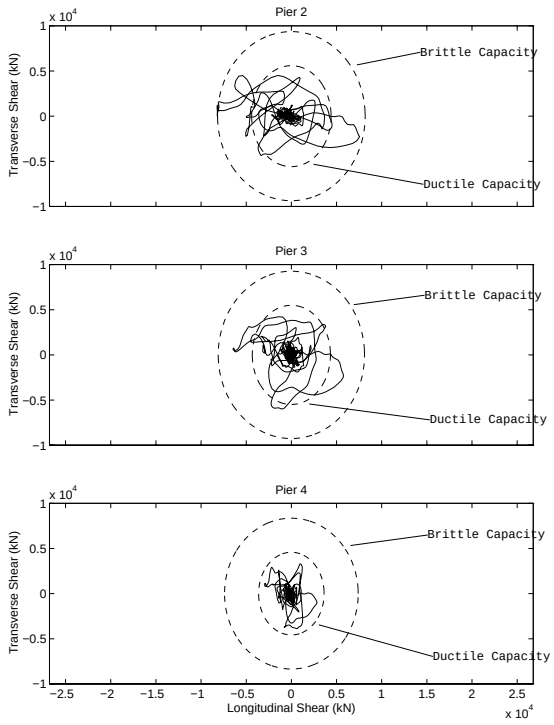

Figure 5.13: Column Shear Force (Piers 2 to 4), Longitudinal vs. Transverse, Jensen Ground Motion

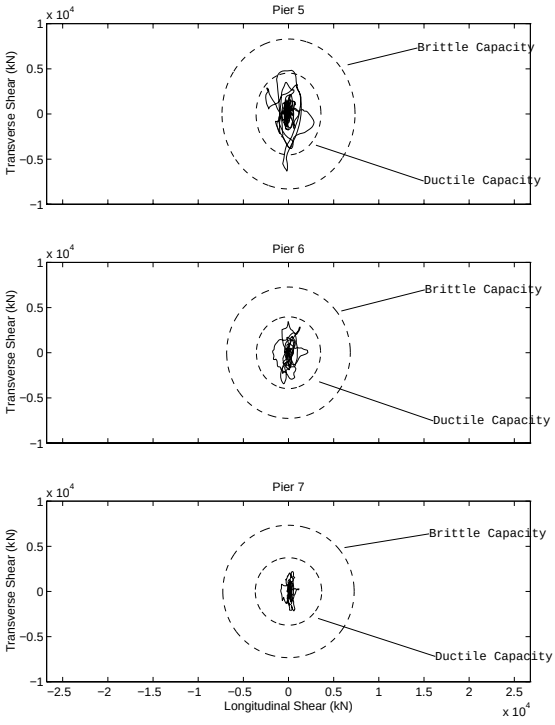

Figure 5.14: Column Shear Force (Piers 5 to 7), Longitudinal vs. Transverse, Jensen Ground Motion

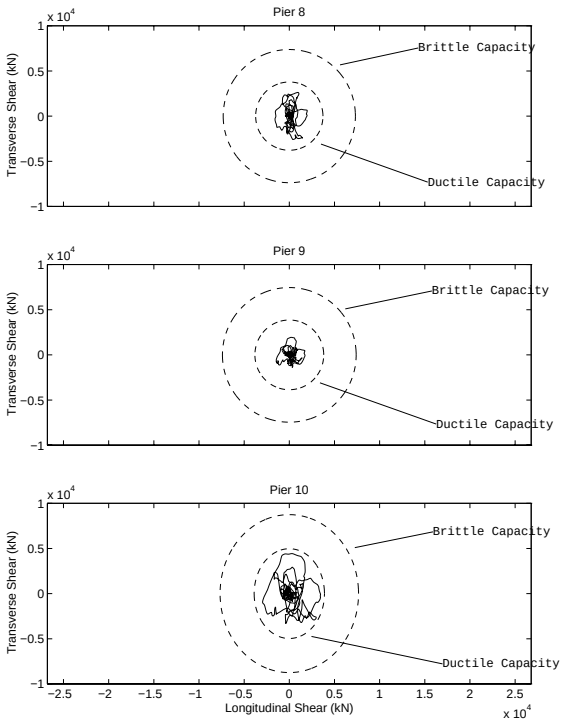

Figure 5.15: Column Shear Force (Piers 8 to 10), Longitudinal vs. Transverse, Jensen Ground Motion

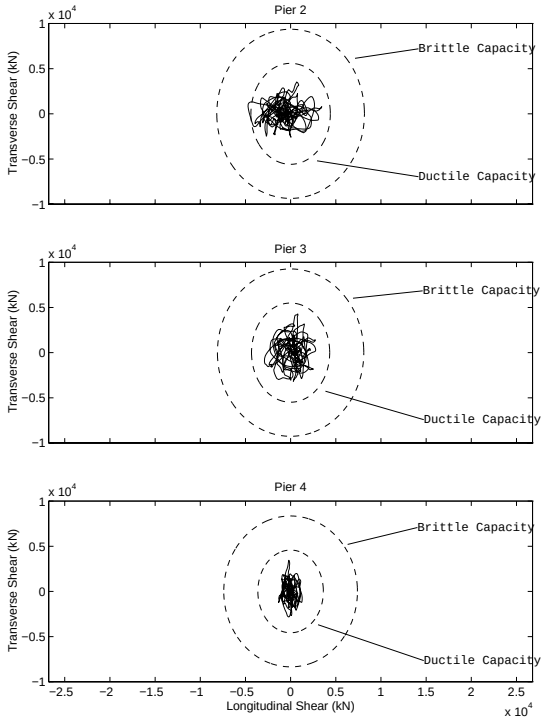

Figure 5.16: Column Shear Force (Piers 2 to 4), Longitudinal vs. Transverse, Arleta Ground Motion

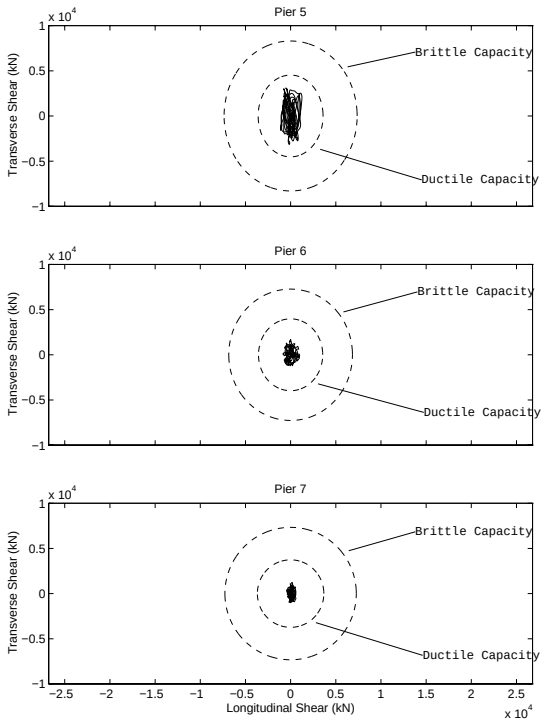

Figure 5.17: Column Shear Force (Piers 5 to 7), Longitudinal vs. Transverse, Arleta Ground Motion

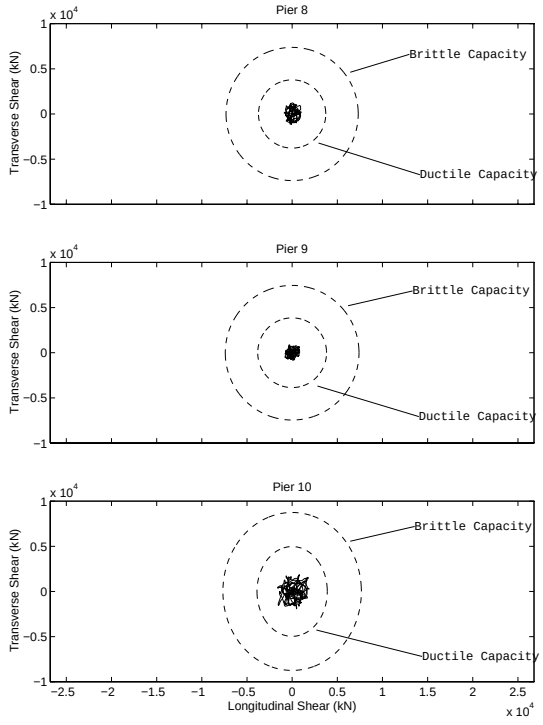

Figure 5.18: Column Shear Force (Piers 8 to 10), Longitudinal vs. Transverse, Arleta Ground Motion

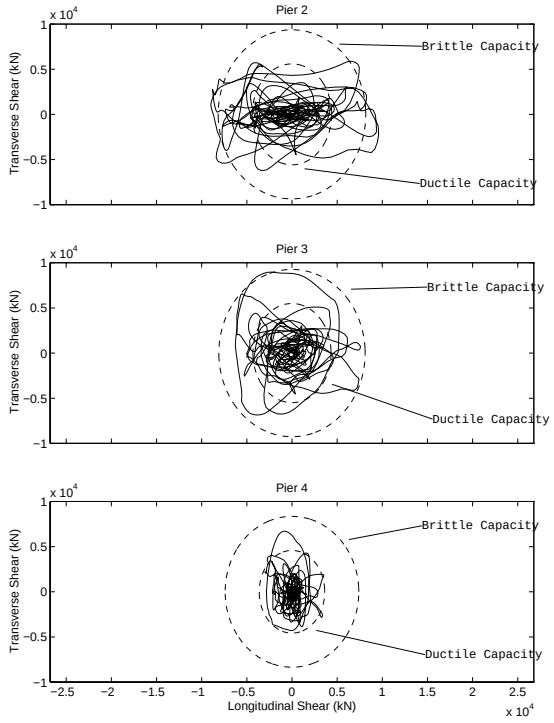

Figure 5.19: Column Shear Force (Piers 2 to 4), Longitudinal vs. Transverse, Hutchings et al. (1996) ICN Simulated Ground Motion

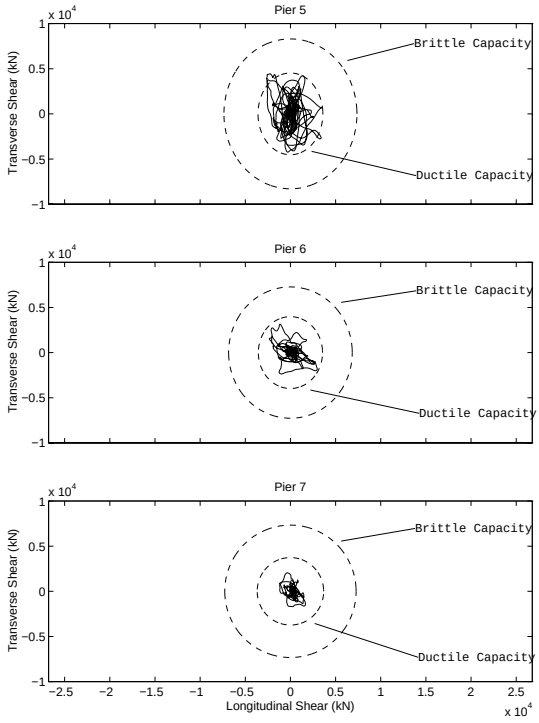

Figure 5.20: Column Shear Force (Piers 5 to 7), Longitudinal vs. Transverse, Hutchings et al. (1996) ICN Simulated Ground Motion

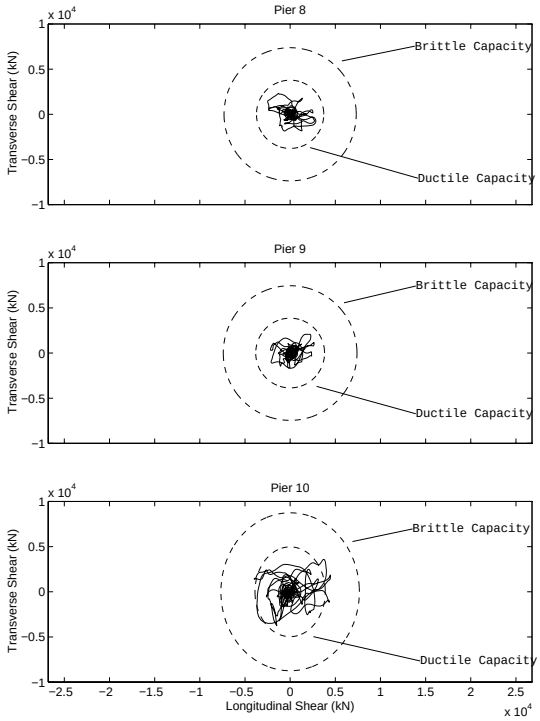

Figure 5.21: Column Shear Force (Piers 8 to 10), Longitudinal vs. Transverse, Hutchings et al. (1996) ICN Simulated Ground Motion

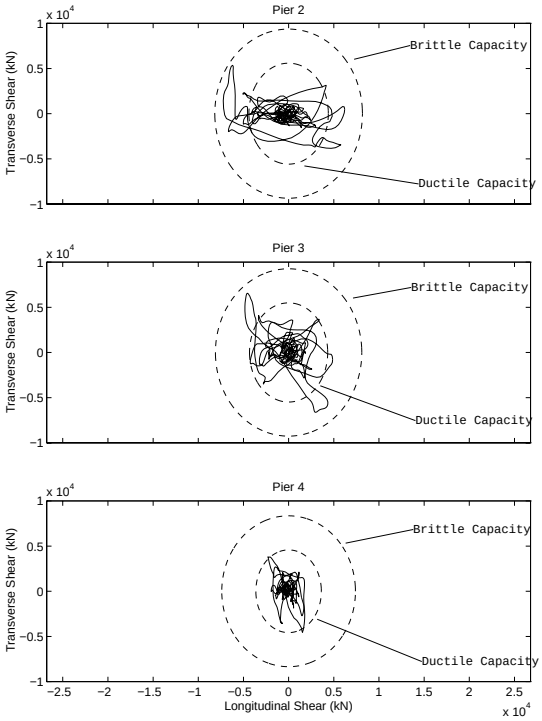

Figure 5.22: Column Shear Force (Piers 2 to 4), Longitudinal vs. Transverse, Horton et al. (1995) Pier 3 Simulated Ground Motion

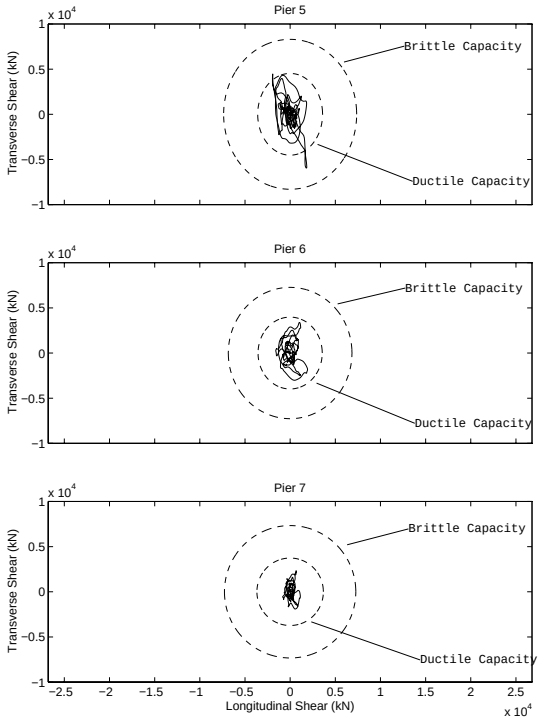

Figure 5.23: Column Shear Force (Piers 5 to 7), Longitudinal vs. Transverse, Horton et al. (1995) Pier 3 Simulated Ground Motion

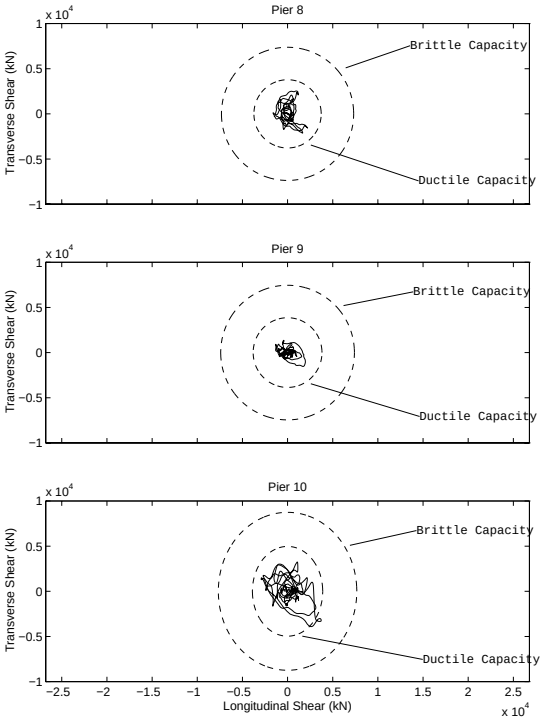

Figure 5.24: Column Shear Force (Piers 8 to 10), Longitudinal vs. Transverse, Horton et al. (1995) Pier 3 Simulated Ground Motion

5.3.2 Examination of Other Structural Demands

The analyses presented in the previous section show that piers 2 and 3 had deficient shear capacity for the estimated demands in the 1994 Northridge earthquake. The other piers in the bridge, with the exception of pier 10, had adequate shear capacity for the Northridge earthquake ground motions. (The columns are shear-critical and would be expected to fail in larger ground motions.) The computed history of shear force demands in piers 2 and 3 show that the capacity is reached early in the earthquake during the first large cycle of longitudinal displacement of the bridge.

To examine whether inadequate shear capacity of piers 2 and 3 initiated the collapse of the first frame, other demands in the bridge at the time that the column shear capacity is reached must be compared with the corresponding capacity estimates. The following computed response quantities are examined: shear force and bending moment of the box girder superstructure; the bending moment in the pier shafts at the longitudinal bar cutoff points; and opening displacement of the intermediate hinges. Table 5.3 lists for each quantity the maximum ratio of demand to capacity, where the capacity is given in Chapter 4 and the demand is the maximum response to the time the shear capacity in pier 2 is exhausted. The demand-capacity comparison is for the largest ground motion records, Sylmar, Newhall, and tbe Hutchings, ICN simulated record.

The first section of Table 5.3 gives the demand-capacity ratio for bending moment in the superstructure for the first three spans. For the Sylmar record and Hutchings, ICN simulated record the maximum ratio is 0.74 and 0.85, respectively, for negative bending at the middle the span between piers 2 and 3. Otherwise the bending moment demand-capacity ratio does not exceed 0.60.

The computed response for the Newhall record to the time at which pier 2 reaches the theoretical shear capacity shows an important effect of the vertical ground motion on box girder forces. These effects do not occur for the other ground motion records. The maximum bending moment in the box girder for Newhall without the vertical ground motion (only including longitudinal and transverse ground motion components) is limited to 0.63 of the capacity for negative bending of span 2 at pier 3. When all three ground components of the Newhall record are included in the earthquake analysis, the demand-capacity ratio for the box girder bending moment is 2.62 and 1.92 for positive bending at piers 2 and 3. As discussed in conjunction with Figure 2.21 in Section 2.3.3, the vertical component of the Newhall record has significant energy in the period range of the vertical vibration modes of the superstructure which leads to the reversal of bending moments over piers 2 and 3. Although the box girder has some flexural ductility, the response analysis indicates that the positive moment reinforcement could have yielded very early in the earthquake response before piers 2 and 3 reached their shear capacity. It should be noted that current bridge design practice is to avoid inelastic deformation in the superstructure.

As discussed in Section 1.3, one postulated cause for the failure of frame 1 was a punching shear failure of the box girder at pier 3. The second section of Table 5.3 gives the demand/ capacity ratio for shear force in the box girder to the time piers 2 and 3 reach their shear capacity. The largest demand-capacity ratio is 0.74 for the Newhall record including the vertical ground motion component. The largest ratio for the other records is 0.61. The

response analyses indicate that the box girder had sufficient shear capacity for the postulated ground motions.

The reduced capacity in the shaft below cutoff of the longitudinal reinforcement was not included in the model, as discussed in Section 3.3.3. To examine this issue, the third section of Table 5.3 gives the ratio of maximum bending moment in the shafts below the cutoff relative to the flexural capacity below the cutoff. The flexural demand on the piers 2 and 3 shafts do not exceed the flexural capacity. The demand-capacity ratio exceeds unity primarily for piers 6 and 8 to 10. The largest ratio is 1.4, indicating that a small amount of flexural yielding may have occurred in the pier shafts below the longitudinal bar cutoff. The demand ratio is small enough that the actual strength of the shaft may have accommodated the demand with minor yielding, recognizing that the surrounding soil provides some confinement.

The last section of Table 5.3 gives the maximum opening displacements at the four intermediate hinges in the bridge. The opening displacement at hinge 4 is less than the 20% of the hinge seat width for all of the ground motion records. With the small hinge displacements predicted from the model and postulated ground motion, it is unlikely that the failure of frame 1 initiated with unseating at hinge 4. The largest demand-capacity ratio for the other hinges is 0.43 for hinge 5. The post-earthquake inspection of the bridge revealed local damage at hinge 5 caused by impact of the box girders. Hinges that undergo large opening displacements may experience pounding when they close.

5.4 Effect of Pier 2 Ground Elevation

As observed by Priestley et al. (1994a) the ground elevation at pier 2 may have been approximately 1.5 m (5 ft) higher than the design drawings indicate. To investigate the effect of the ground elevation of pier 2, an alternate model is considered in which the pier 2 ground level is 1.5 m (5 ft) higher than the original model. The effective overburden elevation for the purpose of estimating the properties of the p-y soil springs remains unchanged. The alternate model is compared with the original model for the three largest ground motions (Newhall, Sylmar, and Hutchings, ICN), including the vertical components. The summary results are given for the entire response history, not just to the time of shear failure of piers 2 and 3.

The trends in column shear demand relative to capacity observed in Section 5.3.1 for the original model are evident in the model with a higher pier 2 ground elevation. Table 5.4 summarizes the maximum shear force demand for the two models. The longitudinal shear force in pier 2 increases between 13-16% for the shorter pier 2 compared with the original model. Shortening pier 2 decreases the maximum longitudinal shear force on pier 3 by 1-3on the shear forces in the other piers.

The histories of shear force demands for the alternate model with higher ground elevation of pier 2 are shown in Figures 5.25 to 5.27. The computed responses for the Newhall record and Hutchings, ICN simulated record clearly that pier 2 reaches its shear capacity in the brittle-ductile transition zone prior to pier 3 reaching its capacity. As with the reference model, the response analysis for the Sylmar record shows that piers 2 and 3 reach their respective capacities at approximately the same time. However, the demand-to-capacity ratio is larger for pier 2 than pier 3 at the time the capacity is reached.

Table 5.3: Demands and Capacities at Time of Shear Failure of Pier 2

Superstructure Moments											
Location			Capacity kN×m	Newhall with Vertical		Newhall without Vertical		Sylmar		Hutchings, ICN	
				Net Demand kN×m	Demand/Capacity	Net Demand kN×m	Demand/Capacity	Net Demand kN×m	Demand/Capacity	Net Demand kN×m	Demand/Capacity
Span 1	Mid-span	Max	8.2×10^4	2.4×10^4	0.30	7.0×10^3	0.09	2.1×10^4	0.25	2.5×10^4	0.31
		Min	-3.9×10^4	-3.4×10^4	0.87	-2.6×10^4	0.67	-2.5×10^4	0.63	-2.2×10^4	0.57
	Right	Max	1.3×10^4	8.8×10^3	0.67	-1.0×10^4	0.10	-7.4×10^3	0.07	3.2×10^3	0.25
		Min	-1.0×10^5	-6.9×10^4	0.67	-4.7×10^4	0.46	-5.3×10^4	0.52	-4.5×10^4	0.44
Span 2	Left	Max	1.3×10^4	3.4×10^4	2.62	3.6×10^3	0.27	5.9×10^3	0.45	-5.9×10^3	0.06
		Min	-1.0×10^4	-4.9×10^4	0.48	3.2×10^4	0.31	-4.7×10^4	0.46	-5.8×10^4	0.57
	Mid-span	Max	9.2×10^4	1.7×10^4	0.18	4.7×10^3	0.05	1.1×10^4	0.12	3.4×10^3	0.04
		Min	-1.8×10^4	-2.6×10^4	1.41	-1.2×10^4	0.63	-1.4×10^4	0.74	-1.6×10^4	0.85
	Right	Max	1.3×10^4	0	0	-2.0×10^4	0.22	-1.5×10^4	0.16	0	0
		Min	-9.2×10^4	-8.1×10^4	0.88	-5.8×10^4	0.63	-6.6×10^4	0.72	-5.6×10^4	0.60
Span 3	Left	Max	1.3×10^4	2.5×10^4	1.92	-1.1×10^4	0.12	-8.0×10^3	0.09	-2.0×10^4	0.22
		Min	-9.2×10^4	-4.6×10^4	0.50	-3.3×10^4	0.36	-4.3×10^4	0.47	-4.6×10^4	0.50
	Mid-span	Max	6.4×10^4	4.6×10^4	0.72	1.4×10^4	0.21	1.8×10^4	0.28	1.9×10^4	0.30
		Min	-3.4×10^4	-1.8×10^4	0.54	4.1×10^3	0.06	-6.8×10^3	0.20	-9.6×10^3	0.29

Superstructure Shear Forces									
Location		Capacity kN	Newhall with Vertical		Newhall without Vertical		Sylmar		Hutchings, ICN	
			Net Demand kN	Demand/Capacity	Net Demand kN	Demand/Capacity	Net Demand kN	Demand/Capacity	Net Demand kN	Demand/Capacity
Span 1	Mid-span	6.1×10^3	2.6×10^3	0.42	1.8×10^3	0.30	2.0×10^3	0.32	1.8×10^3	0.29
	Right	1.1×10^4	8.1×10^3	0.73	5.7×10^3	0.52	6.6×10^3	0.60	6.3×10^3	0.58
Span 2	Left	1.1×10^4	6.6×10^3	0.60	5.3×10^3	0.48	6.5×10^3	0.59	6.2×10^3	0.56
	Mid-span	7.5×10^3	1.2×10^3	0.15	9.5×10^2	0.13	1.3×10^3	0.18	1.2×10^3	0.16
	Right	1.1×10^4	7.4×10^3	0.67	6.2×10^3	0.56	6.7×10^3	0.61	6.2×10^3	0.56
Span 3	Left	1.1×10^4	8.2×10^3	0.74	5.1×10^3	0.47	6.4×10^3	0.58	6.1×10^3	0.55
	Mid-span	6.1×10^3	9.1×10^2	0.15	2.8×10^2	0.05	6.1×10^2	0.10	6.9×10^2	0.11

Subgrade Pier Moments at Bar Cut–off Location (Weak Axis Only)									
Location	Capacity kN×m	Newhall with Vertical		Newhall without Vertical		Sylmar		Hutchings, ICN	
		Net Demand kN×m	Demand/Capacity	Net Demand kN×m	Demand/Capacity	Net Demand kN×m	Demand/Capacity	Net Demand kN×m	Demand/Capacity
Pier 2	1.2×10^4	3.7×10^3	0.31	3.8×10^3	0.31	5.0×10^3	0.42	3.9×10^3	0.32
Pier 3	1.2×10^4	7.6×10^3	0.63	8.0×10^3	0.66	4.9×10^3	0.40	6.5×10^3	0.54
Pier 4	1.2×10^4	1.4×10^4	1.17	1.3×10^4	1.11	1.7×10^4	0.39	1.1×10^4	0.89
Pier 5	1.2×10^4	8.5×10^3	0.70	7.9×10^3	0.66	1.0×10^4	0.83	5.3×10^3	0.44
Pier 6	1.6×10^4	1.9×10^4	1.20	1.8×10^4	1.16	1.7×10^4	1.09	9.6×10^3	0.61
Pier 7	1.9×10^4	1.9×10^4	0.96	1.7×10^4	0.86	1.8×10^4	0.91	9.5×10^3	0.49
Pier 8	1.9×10^4	2.5×10^4	1.31	2.5×10^4	1.31	2.5×10^4	1.30	1.5×10^4	0.79
Pier 9	1.9×10^4	2.5×10^4	1.27	2.3×10^4	1.22	2.4×10^4	1.26	1.5×10^4	0.80
Pier 10	1.2×10^4	1.5×10^4	1.28	1.6×10^4	1.29	1.7×10^4	1.39	8.5×10^3	0.70

Hinge Displacement									
Location	Capacity mm	Newhall with Vertical		Newhall without Vertical		Sylmar		Hutchings, ICN	
		Net Demand mm	Demand/Capacity	Net Demand mm	Demand/Capacity	Net Demand mm	Demand/Capacity	Net Demand mm	Demand/Capacity
Hinge 4	330	55	0.17	56	0.17	43	0.13	28	0.08
Hinge 5	330	140	0.42	140	0.43	140	0.43	38	0.11
Hinge 7	330	37	0.11	37	0.11	18	0.05	29	0.09
Hinge 9	330	16	0.05	15	0.05	9	0.03	26	0.08

The effect of the pier 2 ground elevation on the displacements of the bridge is summarized in Tables 5.5 to 5.7. The shorter pier 2 reduces the displacement at the top of the piers for frame 1 6-10% because of the increased stiffness of the pier. However, the larger forces in the frame 1 piers produce larger displacement of the piers at the ground surface because of the of the increased forces on the soil. In Table 5.6, the shorter pier 2 increases the displacement at the ground surface for pier 2 from 38-56 mm (1.5-2.2 in.) to 66-81 mm (2.6-3.2 in.). The effect of the pier 2 ground elevation is further confirmed in Table 5.7, which shows that the maximum curvature in pier 2 increases by 10-30% with the increased ground elevation. The maximum curvature for the other piers generally decreases with the increase in the assumed pier 2 ground elevation. Table 5.8 shows that the pier elevation has a negligible effect on the superstructure force demands.

Table 5.4: Effect of Pier 2 Ground Elevation on Column Shear Force Demands

Record			Pier 2 kN	Pier 3 kN	Pier 4 kN	Pier 5 kN	Pier 6 kN	Pier 7 kN	Pier 8 kN	Pier 9 kN	Pier 10 kN
Sylmar	Pier 2 Ground at Nominal	Longitudinal	-10100	-7260	-3500	-3170	-2600	-1370	-2720	-2320	-4380
		Transverse	5060	5760	4570	-3500	2700	1920	-2630	-1520	-3680
	Pier 2 Ground at Nominal+5 ft	Longitudinal	-11700	-7180	-3430	-3050	-2490	-1350	-2650	-2240	-4260
		Transverse	5800	5640	4600	-3620	2680	1870	-2610	-1570	-3800
Newhall	Pier 2 Ground at Nominal	Longitudinal	-9050	-6730	3260	-2950	-2220	1270	-2350	1980	-3680
		Transverse	4730	4750	5140	-5300	-2230	-1810	2000	-1440	3020
	Pier 2 Ground at Nominal + 5 ft	Longitudinal	-10200	-6500	-3080	-2820	-2130	1260	2270	1970	-3480
		Transverse	5180	4670	5130	-5510	2300	-1820	2040	-1480	2990
Hutchings, ICN	Pier 2 Ground at Nominal	Longitudinal	9590	7580	3520	3530	2970	1660	2850	2650	4460
		Transverse	-6240	8970	6700	4430	3150	2050	2330	2080	-3750
	Pier 2 Ground at Nominal + 5 ft	Longitudinal	11100	7310	3340	3340	3000	1680	2880	2680	4500
		Transverse	-7400	8920	6690	4600	3220	2140	2410	2110	3730
Capacity, (Priestley et al., 1994b)	Brittle	Longitudinal	8170	8100	7400	7360	6840	7270	7320	7400	7670
		Transverse	9360	9260	8350	8300	7270	7330	7370	7450	8740
	Ductile	Longitudinal	4400	4330	3630	3590	3550	3680	3720	3810	3890
		Transverse	5590	5490	4580	4530	3980	3740	3780	3860	4970
Capacity, (ATC-32, 1996)	Brittle	Longitudinal	4850	4840	4660	4660	4670	4930	4780	4910	4860
		Transverse	5250	5240	5060	5060	4880	4960	4810	4930	5260
	Ductile	Longitudinal	3210	3200	3020	3020	3240	3370	3220	3340	3220
		Transverse	3610	3600	3420	3520	3450	3390	3250	3370	3620

Table 5.5: Effect of Pier 2 Ground Elevation on Displacement Demands at Top of Piers

Record			Abutment 1 mm	Pier 2 mm	Pier 3 mm	Pier 4 mm	Pier 5 mm	Pier 6 mm	Pier 7 mm	Pier 8 mm	Pier 9 mm	Pier 10 mm	Abutment 11 mm
Sylmar	Pier 2 Ground at Nominal	Longitudinal	-341	-344	-350	-373	-385	-419	-453	-463	-470	-479	-479
		Transverse	0	62.8	144	223	200	-404	-690	-579	-451	-189	0
	Pier 2 Ground at Nominal + 5 ft	Longitudinal	-319	-321	-327	-351	-365	-399	-433	-443	-450	-456	-455
		Transverse	0	59.6	138	221	204	-399	-681	-581	-461	-198	0
Newhall	Pier 2 Ground at Nominal	Longitudinal	-240	-240	-243	-263	-272	308	338	336	332	-317	-316
		Transverse	0	57.6	-110	-196	-217	298	469	361	242	97.6	0
	Pier 2 Ground at Nominal + 5 ft	Longitudinal	-217	-218	-220	-240	-249	306	336	334	330	312	309
		Transverse	0	47.9	-104	-195	-222	302	482	370	248	100	0
Hutchings, ICN	Pier 2 Ground at Nominal	Longitudinal	-299	-298	-290	324	321	461	519	528	529	545	540
		Transverse	0	124	352	528	374	443	668	473	318	175	0
	Pier 2 Ground at Nominal + 5 ft	Longitudinal	-278	-277	-217	-292	-309	477	531	540	540	557	553
		Transverse	0	116	339	509	377	451	686	482	318	187	0

Table 5.6: Effect of Pier 2 Ground Elevation on Column Displacement Demands at Ground Surface

Record			Pier 2 mm	Pier 3 mm	Pier 4 mm	Pier 5 mm	Pier 6 mm	Pier 7 mm	Pier 8 mm	Pier 9 mm	Pier 10 mm
Sylmar	Pier 2 Ground at Nominal	Longitudinal	-56.1	-98.5	-82.7	-81.7	-46.8	-25.5	-48.0	-43.1	-113
		Transverse	8.40	31.5	43.9	33.4	-31.0	27.5	-47.9	-25.5	-33.1
	Pier 2 Ground at Nominal + 5 ft	Longitudinal	-80.8	-92.6	-78.8	-77.4	-44.1	-24.6	-45.9	-41.5	-107
		Transverse	11.7	30.0	43.6	34.2	-30.4	26.8	-47.3	-26.5	-34.9
Newhall	Pier 2 Ground at Nominal	Longitudinal	-38.0	-64.9	-56.1	-57.2	34.2	21.8	32.2	28.4	71.0
		Transverse	7.05	-21.9	38.0	-43.6	23.7	-21.4	26.5	11.6	15.9
	Pier 2 Ground at Nominal + 5 ft	Longitudinal	-53.6	-59.1	-51.0	-53.0	34.0	21.6	31.9	28.2	70.7
		Transverse	8.86	21.5	37.3	-45.5	24.0	-21.2	27.4	12.0	16.4
Hutchings, ICN	Pier 2 Ground at Nominal	Longitudinal	-43.7	80.7	-71.3	71.7	51.2	29.2	51.6	46.1	128
		Transverse	14.0	89.5	120	59.5	36.9	29.1	35.7	23.9	32.4
	Pier 2 Ground at Nominal + 5 ft	Longitudinal	-65.7	-73.0	-69.7	-66.9	52.5	29.9	52.9	47.2	131
		Transverse	20.0	85.5	116	61.7	37.7	30.6	36.6	23.6	35.1

Table 5.7: Effect of Pier 2 Ground Elevation on Column Curvature Demands

Record			Pier 2 1/m	Pier 3 1/m	Pier 4 1/m	Pier 5 1/m	Pier 6 1/m	Pier 7 1/m	Pier 8 1/m	Pier 9 1/m	Pier 10 1/m
Sylmar	Pier 2 Ground at Nominal	Weak Axis	3.65×10^{-2}	2.59×10^{-2}	1.47×10^{-2}	1.29×10^{-2}	2.39×10^{-3}	1.39×10^{-3}	3.26×10^{-3}	2.54×10^{-3}	1.81×10^{-2}
		Strong Axis	1.29×10^{-3}	1.59×10^{-3}	1.67×10^{-3}	1.48×10^{-3}	1.11×10^{-3}	1.09×10^{-3}	1.60×10^{-3}	9.61×10^{-4}	1.66×10^{-3}
	Pier 2 Ground at Nominal + 5 ft	Weak Axis	4.10×10^{-2}	2.43×10^{-2}	1.32×10^{-2}	1.15×10^{-2}	2.13×10^{-3}	1.30×10^{-3}	2.94×10^{-3}	2.28×10^{-3}	1.73×10^{-2}
		Strong Axis	1.11×10^{-3}	1.55×10^{-3}	1.65×10^{-3}	1.48×10^{-3}	1.09×10^{-3}	1.06×10^{-3}	1.60×10^{-3}	9.83×10^{-4}	1.62×10^{-3}
Newhall	Pier 2 Ground at Nominal	Weak Axis	2.50×10^{-2}	1.58×10^{-2}	7.40×10^{-3}	5.50×10^{-3}	1.64×10^{-3}	1.20×10^{-3}	1.71×10^{-3}	1.44×10^{-3}	1.11×10^{-2}
		Strong Axis	1.08×10^{-3}	1.09×10^{-3}	1.10×10^{-3}	1.37×10^{-3}	8.60×10^{-4}	8.34×10^{-4}	9.71×10^{-4}	5.26×10^{-4}	7.28×10^{-4}
	Pier 2 Ground at Nominal + 5 ft	Weak Axis	2.62×10^{-2}	1.33×10^{-2}	5.95×10^{-3}	4.43×10^{-3}	1.61×10^{-3}	1.19×10^{-3}	1.69×10^{-3}	1.41×10^{-3}	9.80×10^{-3}
		Strong Axis	9.21×10^{-4}	1.03×10^{-3}	1.13×10^{-3}	1.49×10^{-3}	8.69×10^{-4}	8.28×10^{-4}	9.99×10^{-4}	5.42×10^{-4}	7.11×10^{-4}
Hutchings, ICN	Pier 2 Ground at Nominal	Weak Axis	3.01×10^{-2}	1.95×10^{-2}	1.07×10^{-2}	1.03×10^{-2}	2.70×10^{-3}	1.68×10^{-3}	4.76×10^{-3}	2.65×10^{-3}	2.08×10^{-2}
		Strong Axis	2.51×10^{-3}	4.69×10^{-3}	4.13×10^{-3}	2.84×10^{-3}	1.35×10^{-3}	1.16×10^{-3}	1.46×10^{-3}	1.07×10^{-3}	1.82×10^{-3}
	Pier 2 Ground at Nominal + 5 ft	Weak Axis	3.31×10^{-2}	1.76×10^{-2}	1.00×10^{-2}	8.35×10^{-3}	2.90×10^{-3}	1.71×10^{-3}	4.86×10^{-3}	2.77×10^{-3}	2.14×10^{-2}
		Strong Axis	2.75×10^{-3}	4.35×10^{-3}	3.98×10^{-3}	2.93×10^{-3}	1.36×10^{-3}	1.19×10^{-3}	1.48×10^{-3}	1.08×10^{-3}	1.94×10^{-3}

Table 5.8: Effect of Pier 2 Ground Elevation on Maximum Superstructure Force Demands

Record		Span 1							
		Middle				Right			
		Bending Moment kN×m		Shear Force kN		Bending Moment kN×m		Shear Force kN	
		pos.	neg.	pos.	neg.	pos.	neg.	pos.	neg.
Sylmar	Pier 2 Ground at Nominal	2.97×10^4	-3.30×10^4	2030	0	N/A	-5.39×10^4	6720	0
	Pier 2 Ground at Nominal+5 ft	2.99×10^4	-3.65×10^4	2110	0	N/A	-5.80×10^4	6840	0
Newhall	Pier 2 Ground at Nominal	4.99×10^4	-3.47×10^4	4490	0	N/A	-8.30×10^5	10200	0
	Pier 2 Ground at Nominal+5 ft	5.60×10^4	-3.96×10^4	4320	-100	N/A	-8.50×10^5	10400	0
Hutchings, ICN	Pier 2 Ground at Nominal	4.62×10^4	-3.49×10^4	3480	-310	N/A	-9.30×10^5	9310	0
	Pier 2 Ground at Nominal+5 ft	2.40×10^4	-3.67×10^4	3450	-260	N/A	-9.30×10^5	9310	0

Record		Span 2											
		Left				Middle				Right			
		Bending Moment kN×m		Shear Force kN		Bending Moment kN×m		Shear Force kN		Bending Moment kN×m		Shear Force kN	
		pos.	neg.	pos.	neg.	pos.	neg.	pos.	neg.	pos.	neg.	pos.	neg.
Sylmar	Pier 2 Ground at Nominal	N/A	-8.40×10^4	0	-7340	1.09×10^4	N/A	1330	-1640	N/A	-6.63×10^4	6970	0
	Pier 2 Ground at Nominal+5 ft	N/A	-8.70×10^4	0	-7560	1.46×10^4	N/A	1290	-1670	N/A	-6.60×10^4	7200	0
Newhall	Pier 2 Ground at Nominal	N/A	-8.40×10^4	0	-9220	2.38×10^4	N/A	1160	-1400	N/A	-9.10×10^4	8750	0
	Pier 2 Ground at Nominal+5 ft	3.94×10^4	-8.90×10^4	0	-9070	2.71×10^4	N/A	1150	-1420	N/A	-9.40×10^4	9100	0
Hutchings, ICN	Pier 2 Ground at Nominal	N/A	-8.40×10^4	0	-8750	3.77×10^4	N/A	1700	-1310	3.84×10^3	-1.17×10^5	10100	0
	Pier 2 Ground at Nominal+5 ft	N/A	-8.60×10^4	0	-8830	3.83×10^4	N/A	1700	-1430	3.61×10^3	-1.17×10^5	10000	0

Record		Span 3							
		Left				Middle			
		Bending Moment kN×m		Shear Force kN		Bending Moment kN×m		Shear Force kN	
		pos.	neg.	pos.	neg.	pos.	neg.	pos.	neg.
Sylmar	Pier 2 Ground at Nominal	N/A	-5.66×10^4	0	-6450	2.96×10^4	-2.09×10^4	500	-1250
	Pier 2 Ground at Nominal+5 ft	N/A	-5.60×10^4	0	-6510	3.05×10^4	-2.19×10^4	520	-1270
Newhall	Pier 2 Ground at Nominal	N/A	-9.10×10^4	870	-11200	5.96×10^4	-4.95×10^4	910	-1050
	Pier 2 Ground at Nominal+5 ft	N/A	-9.00×10^4	920	-11200	5.95×10^4	-5.08×10^4	990	-860
Hutchings, ICN	Pier 2 Ground at Nominal	N/A	-7.90×10^4	0	-9050	4.86×10^4	-3.34×10^4	660	-1130
	Pier 2 Ground at Nominal+5 ft	N/A	-7.70×10^4	0	-9060	4.76×10^4	-3.31×10^4	600	-1140

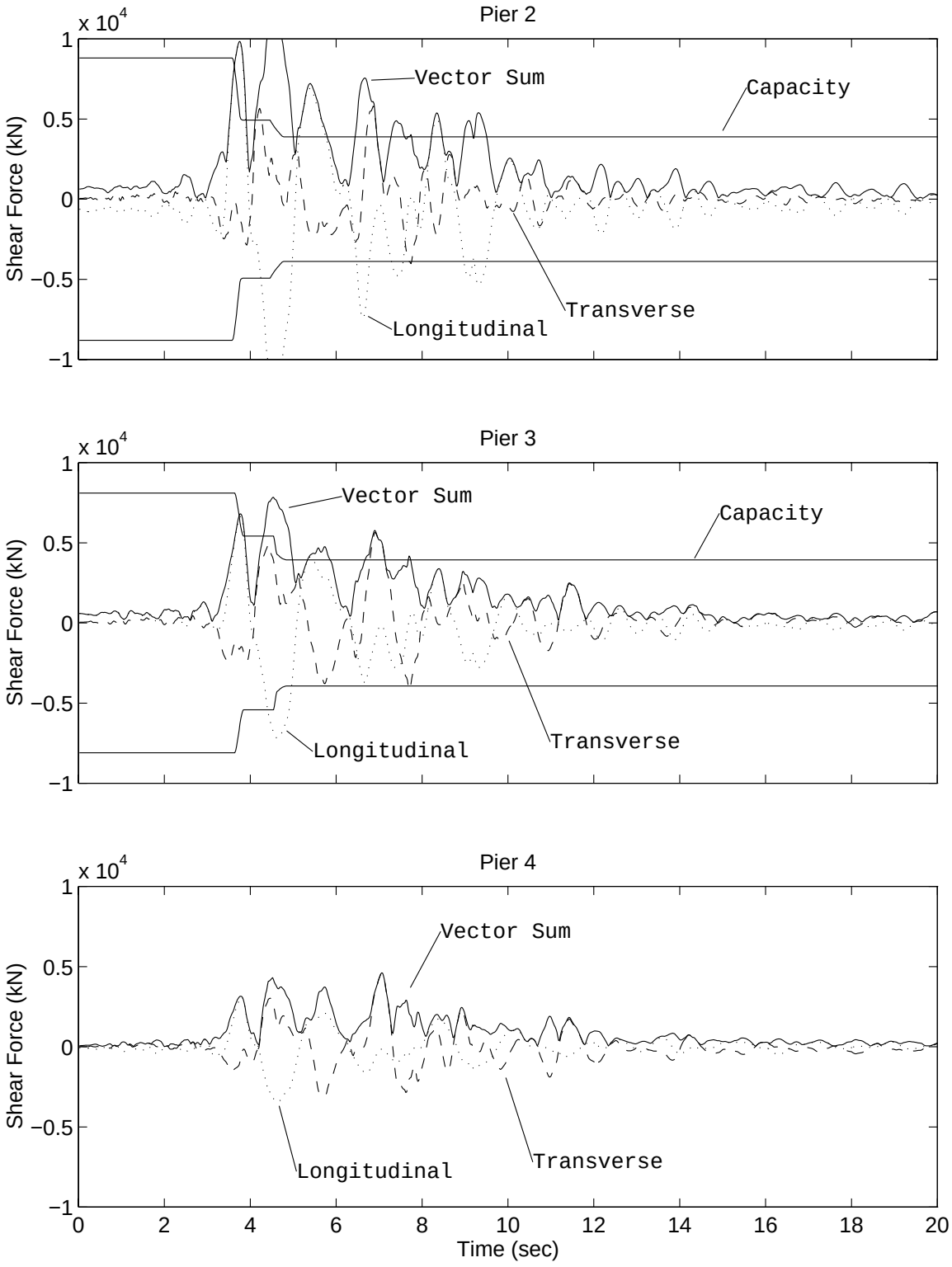

Figure 5.25: Column Shear Force Demand vs. Capacity for Increased Pier 2 Ground Elevation, Sylmar Ground Motion

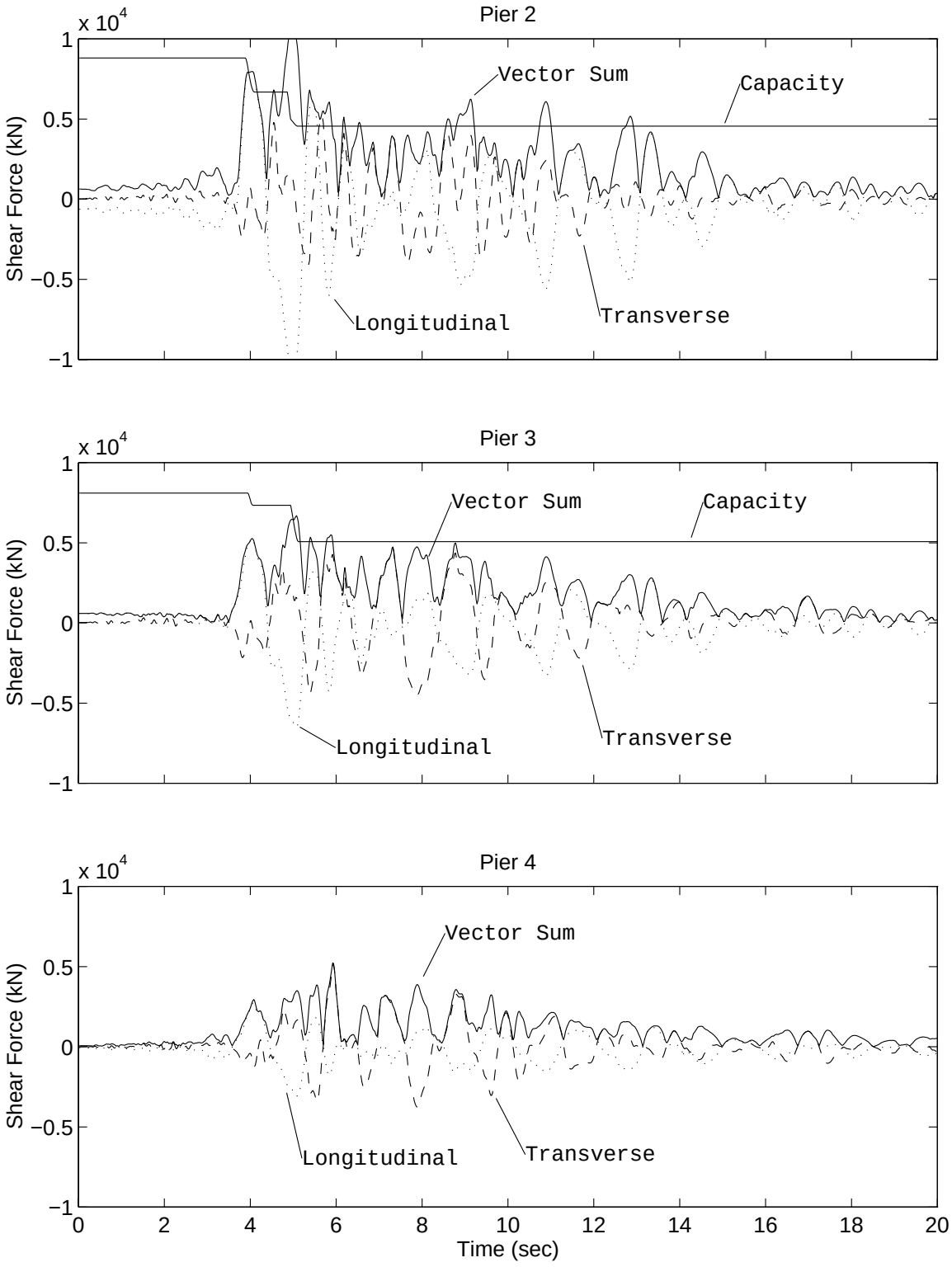

Figure 5.26: Column Shear Force Demand vs. Capacity for Increased Pier 2 Ground Elevation, Newhall Ground Motion

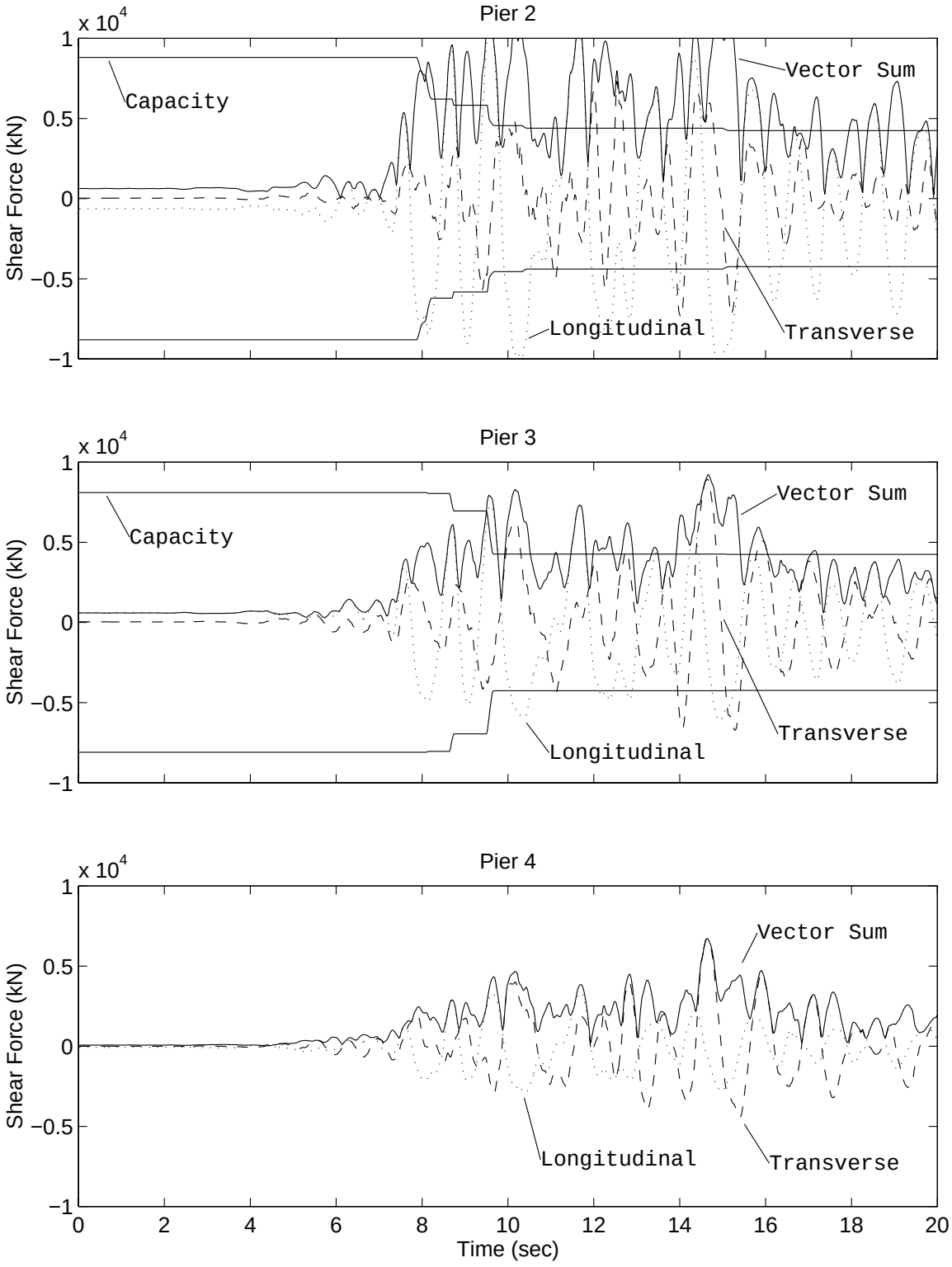

Figure 5.27: Column Shear Force Demand vs. Capacity for Increased Pier 2 Ground Elevation, Hutchings et al. (1996) ICN Simulated Ground Motion

Chapter 6

Hypothetical Earthquake Response with Column Shear Failure Prevented

6.1 Introduction

This chapter examines the earthquake response of the Separation and Overhead bridge assuming that shear failure in the piers did not occur. The analyses provide insight into the bridge performance that may have been expected if the columns had been retrofitted prior to the 1994 Northridge earthquake. The earthquake response of the bridge discussed in this chapter is hypothetical because of the sequence of failures discussed in the previous chapter.

As described in Chapter 3, the model of the columns does not represent the shear capacity of the columns. The results of the dynamic analyses can be interpreted as the bridge response if the piers had been retrofitted to prevent shear failure. Of particular interest in the analyses of hypothetical performance are the displacement and inelastic deformation demands on the columns.

This chapter also examines two linearized models of the bridge to assess the ability of typical models used in bridge design to estimate displacement demands. Displacement demands from dynamic analyses of a tension model and compression model are compared with displacements from the inelastic model.

6.2 Displacement and Inelastic Deformation Demands

Table 6.1 summarizes the maximum displacements at the top of the piers for the six ground motions. The displacements are reported at the centroid of the superstructure above each pier and abutment in the local longitudinal and transverse directions, as shown in Figure 2.4. Comparing the longitudinal push-over analysis of frame 1 (Figures 4.2 to 4.4) it is clear that the displacements are associated with flexural yielding in the columns. The columns in frame 1 predominately displace longitudinally. However, the taller piers (6 to 9) primarily displace in the transverse direction. The maximum drift angle (pier displacement divided by column height above ground) for piers 2 and 3 is approximately 4%. The drift angles for the other piers are generally less than 2%. The displacement of the pier in the drift angle calculation,

however, includes a rigid body component (due to rotation at ground level) in addition to the elastic and inelastic deformation of the pier. For example, the maximum rotation at the ground level of pier 6 is approximately 0.0058 rad for the Newhall ground motion. The rigid body displacement at the top of pier due to the rotation is 143 mm (5.6 in.) or nearly one-half of the maximum displacement of 308 mm (12.1 in.) in the longitudinal direction. The contribution of rigid body rotation in the transverse direction for the same pier is more dramatic. The maximum rotation is 0.0099 rad, which contributes 244 mm (9.6 in.) to the transverse displacement of 298 mm (11.7 in.) at the top of the pier. In general the rigid body displacement accounts for approximately one-half of the longitudinal displacement and generally more than one-half of the transverse displacement. The degree to which the rigid body component of displacement figures into the total displacement of the superstructure is sensitive to the soil spring modeling assumptions. The maximum displacement at the ground for each pier is given in Table 6.2. The vertical component of ground motion has a very small effect on the displacement demands.

Representative displacement histories are shown for the Sylmar and Hutchings, ICN ground motions, including the vertical ground motion component, in Figures 6.1 to 6.10 and 6.11 to 6.20, respectively. The displacement histories show the nature of the response to near-source ground motion. The large pulse in the ground motion produces two or three cycles of large displacements, with the amplitude of displacement decaying rapidly after the peak excursions. As postulated in Chapter 5, the shear failure at pier 2 occurred in the first longitudinal excursion away from abutment 1. The analysis of shear demand and capacity indicated that the response in the reverse direction never occurred in frame 1. With shear failure prevented by an appropriate column retrofit, the frame 1 would have displaced primarily in the longitudinal direction. The taller piers have comparable transverse and longitudinal response, which are out-of-phase for the Sylmar record, but in-phase for the Hutchings, ICN simulated record. The longitudinal displacement at abutment 11 is generally greater than for abutment 1, and the superstructure uplifts at the abutments depending on the ground motion. The vertical displacement history at the center of spans in frame 1 show the vertical mode participation. The effect of the vertical ground motion on the vertical response of the superstructure is discussed subsequently.

Table 6.1: Maximum Displacement at Top of Piers

Record			Abutment 1 mm	Pier 2 mm	Pier 3 mm	Pier 4 mm	Pier 5 mm	Pier 6 mm	Pier 7 mm	Pier 8 mm	Pier 9 mm	Pier 10 mm	Abutment 11 mm
Arleta	With Vertical Motion	Longitudinal	-58.3	-58.4	-58.5	-68.0	-65.7	103	115	110	106	107	106
		Transverse	0	34.1	89.5	157	131	148	246	151	-124	-53.3	0
	Without Vertical Motion	Longitudinal	-57.7	-57.9	-57.9	-67.6	-65.3	102	115	110	106	107	106
		Transverse	0	34.4	90.4	158	133	148	246	150	-125	-53.3	0
Sylmar	With Vertical Motion	Longitudinal	-341	-344	-350	-373	-385	-419	-453	-463	-470	-479	-479
		Transverse	0	62.8	144	223	200	-404	-690	-579	-451	-189	0
	Without Vertical Motion	Longitudinal	-335	-339	-345	-367	-382	-417	-450	-460	-466	-481	-481
		Transverse	0	62.6	144	222	203	-399	-677	-574	-458	-194	0
Jensen	With Vertical Motion	Longitudinal	-192	-193	-194	-210	-216	289	303	302	301	290	289
		Transverse	0	-70.1	-167	-251	-316	484	-743	645	577	286	0
	Without Vertical Motion	Longitudinal	-192	-193	195	-211	-217	288	302	301	301	290	289
		Transverse	0	-70.7	-168	-252	-315	487	-738	646	580	288	0
Horton, Pier 3	With Vertical Motion	Longitudinal	-141	-142	-151	-170	-191	300	349	364	377	381	384
		Transverse	0	78.3	-204	-344	-400	-454	757	487	-317	-154	0
	Without Vertical Motion	Longitudinal	-141	-142	-151	-170	-190	299	350	365	378	382	385
		Transverse	0	78.0	-203	-342	-401	-455	756	487	-317	-154	0
Newhall	With Vertical Motion	Longitudinal	-240	-240	-243	-263	-272	308	338	336	332	-317	-316
		Transverse	0	57.6	-110	-196	-217	298	469	361	242	97.6	0
	Without Vertical Motion	Longitudinal	-240	-240	-243	-263	-271	308	337	334	331	-314	-313
		Transverse	0	54.0	-112	-203	-221	299	467	358	238	96.8	0
Hutchings, ICN	With Vertical Motion	Longitudinal	-299	-298	-290	324	321	461	519	528	529	545	540
		Transverse	0	124	352	528	374	443	668	473	318	175	0
	Without Vertical Motion	Longitudinal	-294	-293	-284	325	321	452	509	519	519	536	532
		Transverse	0	132	357	525	370	439	658	459	322	175	0

Table 6.2: Maximum Displacement of Piers at Ground Surface

Record			Pier 2 mm	Pier 3 mm	Pier 4 mm	Pier 5 mm	Pier 6 mm	Pier 7 mm	Pier 8 mm	Pier 9 mm	Pier 10 mm
Arleta	With Vertical Motion	Longitudinal	-8.6	-12.7	-12.7	-10.6	8.9	5.8	9.1	7.4	20.4
		Transverse	4.5	18.1	28.4	21.5	10.9	11.4	10.2	-7.1	8.5
	Without Vertical Motion	Longitudinal	-8.5	-12.5	-12.3	-10.5	8.7	5.8	9.2	7.5	20.3
		Transverse	4.4	18.1	28.2	22.0	10.9	11.3	10.2	-6.9	-8.3
Sylmar	With Vertical Motion	Longitudinal	-56.1	-98.5	-82.7	-81.7	-46.8	-25.5	-48.0	-43.1	-113
		Transverse	8.4	31.5	43.9	33.4	-31.0	27.5	-47.9	-25.5	-33.1
	Without Vertical Motion	Longitudinal	-55.0	-96.7	-82.3	-80.1	-46.2	-25.1	-48.3	-42.6	-113
		Transverse	8.2	31.4	43.7	33.6	-30.5	27.5	-47.1	-26.1	-33.9
Jensen	With Vertical Motion	Longitudinal	-28.5	-54.3	-46.6	-44.3	30.9	17.4	29.0	24.3	65.8
		Transverse	-8.4	-35.5	-44.0	-66.9	43.2	-37.5	54.7	36.1	50.3
	Without Vertical Motion	Longitudinal	-29.1	-53.1	-45.3	-43.7	30.0	17.0	29.0	24.6	65.0
		Transverse	-8.6	-36.0	-43.8	-66.5	-33.4	-35.9	-53.7	36.3	51.1
Horton, Pier 3	With Vertical Motion	Longitudinal	-21.0	-41.7	-38.0	-36.9	32.2	20.5	36.6	32.6	89.2
		Transverse	9.8	-45.0	-62.5	-80.2	36.6	40.0	38.3	-20.2	-28.7
	Without Vertical Motion	Longitudinal	-21.1	-41.8	37.3	-37.4	32.0	20.7	36.7	32.1	89.4
		Transverse	10	-44.6	-61.6	-80.8	36.7	39.8	38.4	-19.9	-28.7
Newhall	With Vertical Motion	Longitudinal	-38.0	-64.9	-56.1	-57.2	34.2	21.8	32.2	28.4	71.0
		Transverse	7.1	-21.9	38.0	-43.6	23.7	-21.4	26.5	11.6	15.9
	Without Vertical Motion	Longitudinal	-38.0	-64.9	-56.8	-55.9	33.2	19.2	33.1	27.8	71.2
		Transverse	7.5	-23.4	38.4	-44.6	23.8	-21.1	26.0	11.4	15.7
Hutchings, ICN	With Vertical Motion	Longitudinal	-43.7	80.7	-71.3	71.7	51.2	29.2	51.6	46.1	128
		Transverse	14.0	89.5	120	59.5	36.9	29.1	35.7	23.9	32.4
	Without Vertical Motion	Longitudinal	43.6	81.5	71.6	69.4	49.1	26.7	49.9	44.8	124
		Transverse	14.5	90.7	119	60.4	36.2	27.9	33.8	24.4	33.2

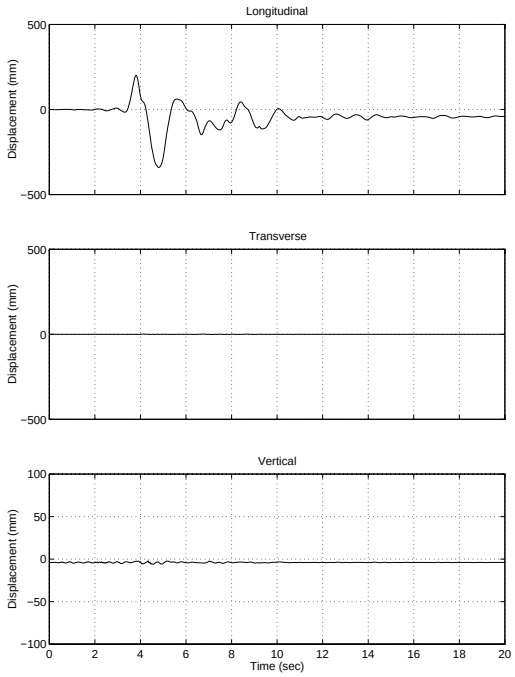

Figure 6.1: Displacement History at Center of Abutment 1, Sylmar Ground Motion

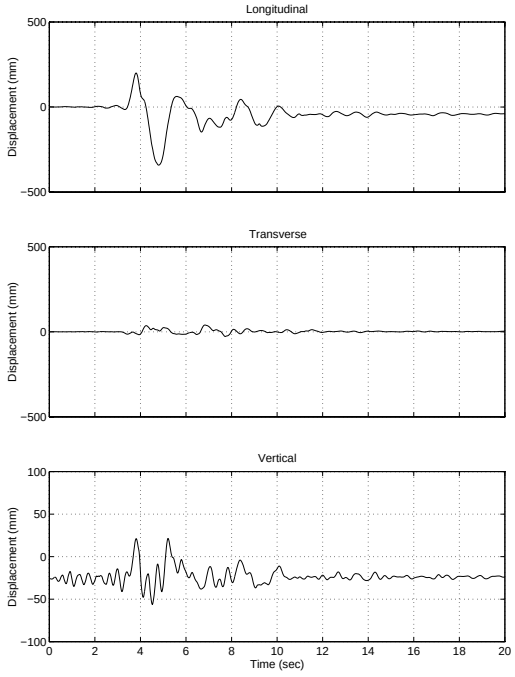

Figure 6.2: Displacement History at Center of Span 1, Sylmar Ground Motion

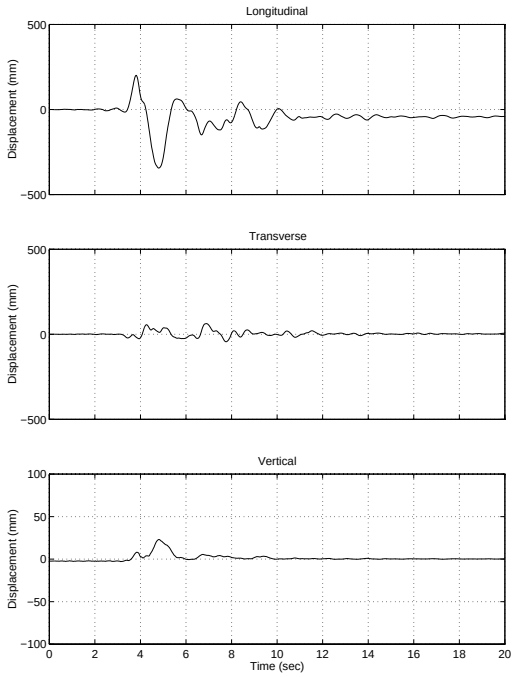

Figure 6.3: Displacement History at Top of Pier 2, Sylmar Ground Motion

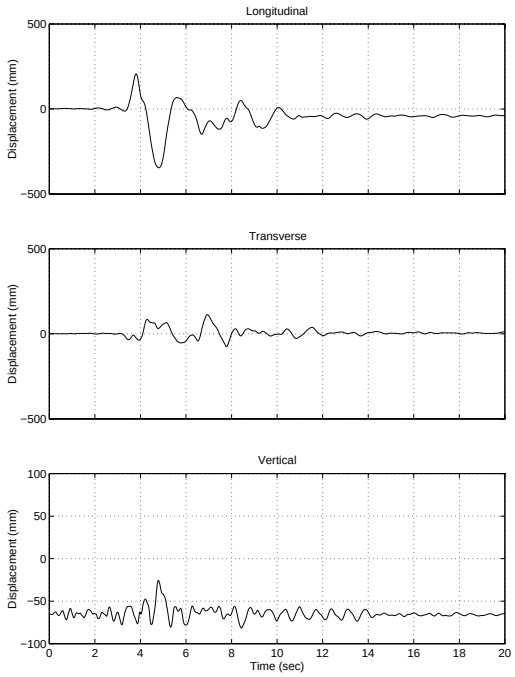

Figure 6.4: Displacement History at Center of Span 2, Sylmar Ground Motion

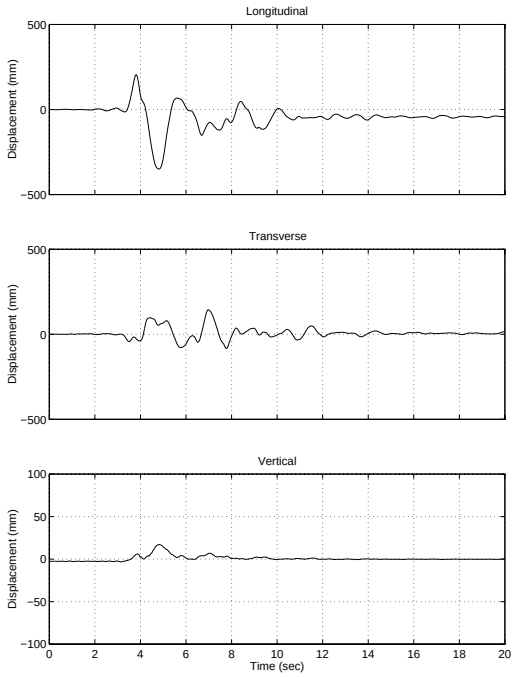

Figure 6.5: Displacement History at Top of Pier 3, Sylmar Ground Motion

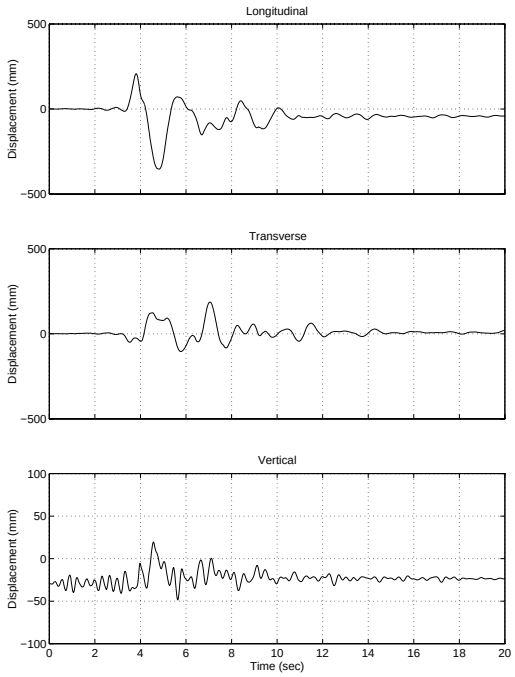

Figure 6.6: Displacement History at Center of Span 3, Sylmar Ground Motion

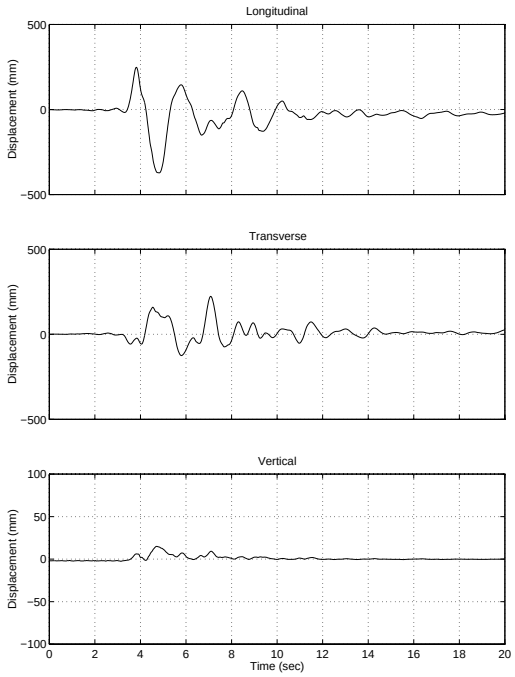

Figure 6.7: Displacement History at Top of Pier 4, Sylmar Ground Motion

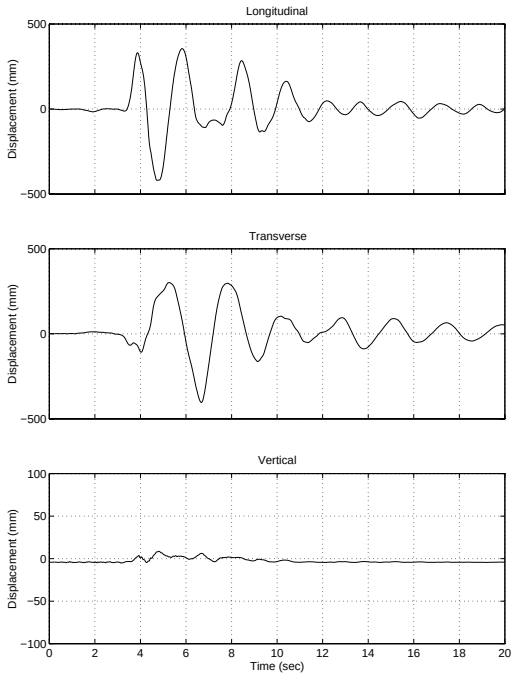

Figure 6.8: Displacement History at Top of Pier 6, Sylmar Ground Motion

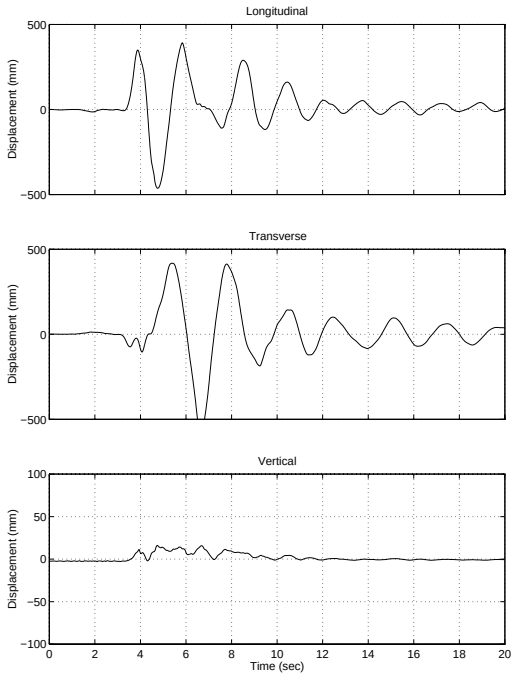

Figure 6.9: Displacement History at Top of Pier 8, Sylmar Ground Motion

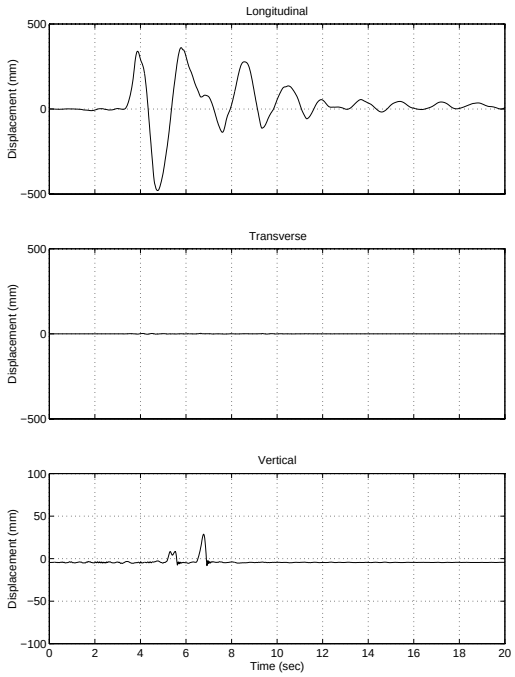

Figure 6.10: Displacement History at Center of Abutment 11, Sylmar Ground Motion

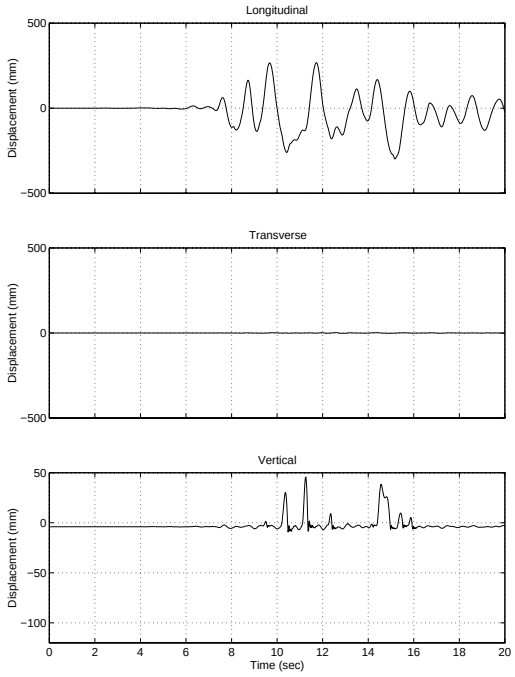

Figure 6.11: Displacement History at Center of Abutment 1, Hutchings et al. (1996) ICN Simulated Ground Motion

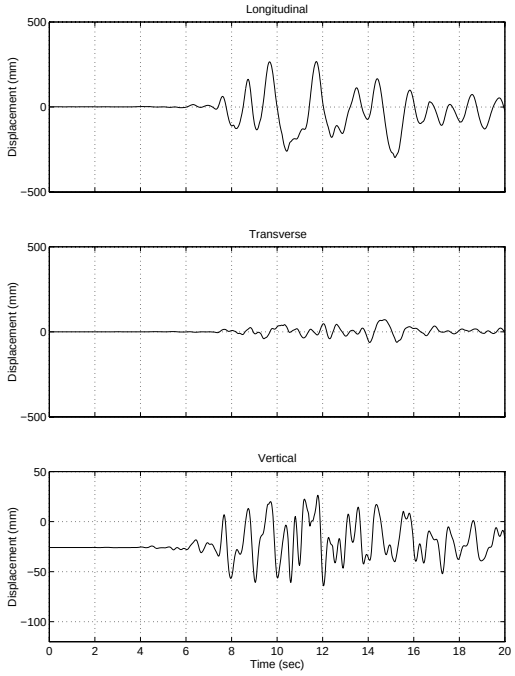

Figure 6.12: Displacement History at Center of Span 1, Hutchings et al. (1996) ICN Simulated Ground Motion

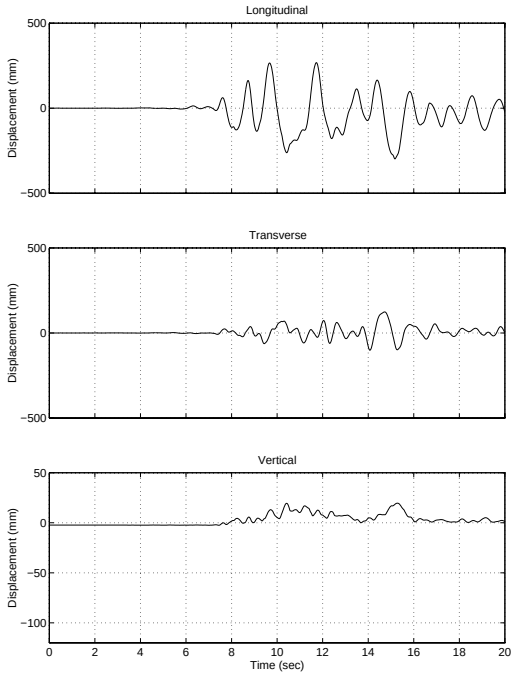

Figure 6.13: Displacement History at Top of Pier 2, Hutchings et al. (1996) ICN Simulated Ground Motion

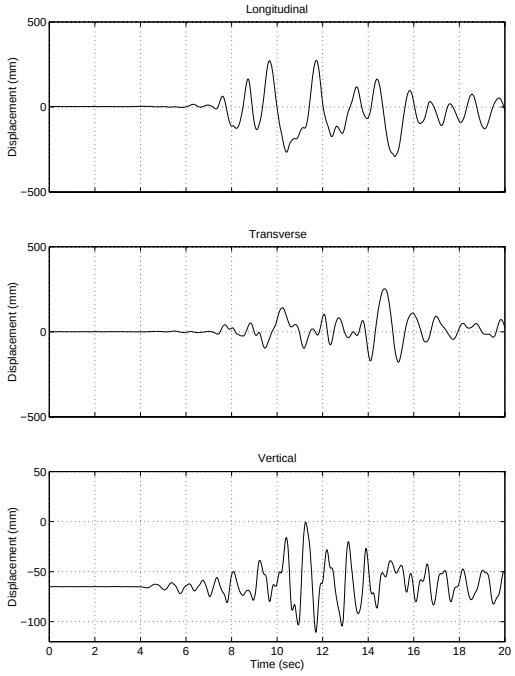

Figure 6.14: Displacement History at Center of Span 2, Hutchings et al. (1996) ICN Simulated Ground Motion

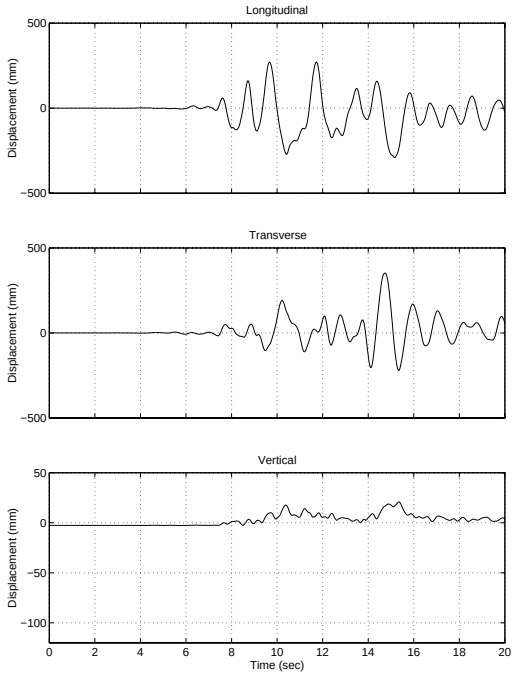

Figure 6.15: Displacement History at Top of Pier 3, Hutchings et al. (1996) ICN Simulated Ground Motion

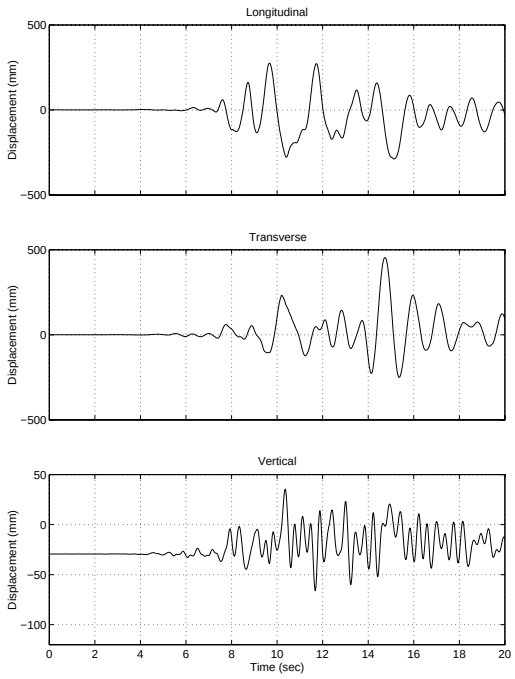

Figure 6.16: Displacement History at Center of Span 3, Hutchings et al. (1996) ICN Simulated Ground Motion

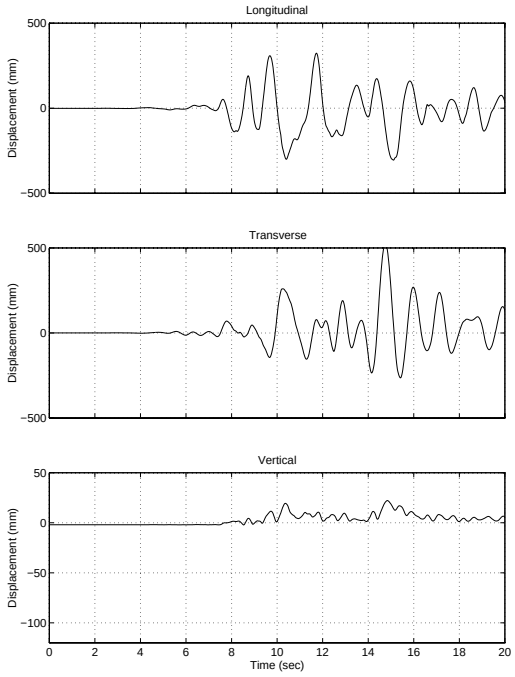

Figure 6.17: Displacement History at Top of Pier 4, Hutchings et al. (1996) ICN Simulated Ground Motion

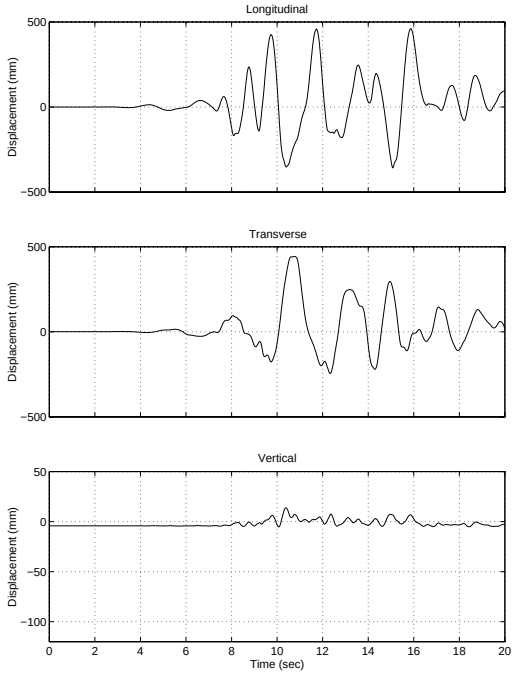

Figure 6.18: Displacement History at Top of Pier 6, Hutchings et al. (1996) ICN Simulated Ground Motion

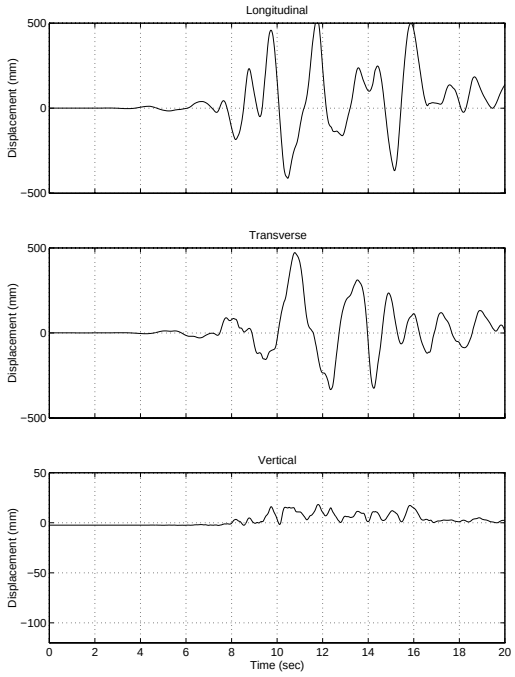

Figure 6.19: Displacement History at Top of Pier 8, Hutchings et al. (1996) ICN Simulated Ground Motion

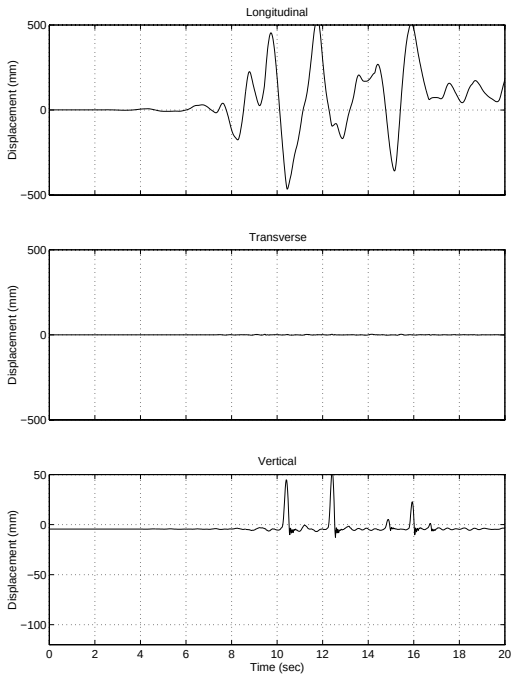

Figure 6.20: Displacement History at Center of Abutment 11, Hutchings et al. (1996) ICN Simulated Ground Motion

The maximum curvatures for each pier are summarized in Table 6.3. These curvature demands can be compared with the yield curvature of 3.5×10^{-3} 1/m for piers 2-6 and 10 in weak axis bending, 1.6×10^{-3} 1/m for piers 2-6 and 10 in strong axis bending, 2.1×10^{-3} 1/m for piers 7-9 in weak axis bending, and 1.2×10^{-3} 1/m for piers 7-9 in strong axis bending. For example, the analysis for the Hutchings, ICN simulated ground motion gives a maximum curvature ductility demand of 8.6 at pier 2. The curvature demands would be within the capacities of the columns had they been retrofitted to provide adequate shear capacity. The effect of the vertical ground motion on the inelastic deformation demand is minor, even for the Newhall record.

The maximum strains in the concrete (compressive) and longitudinal steel reinforcement (tensile) for the columns are listed in Table 6.4 for the Newhall, Sylmar, and Hutchings, ICN ground motions, including the vertical component. The maximum compressive strain in the concrete is slightly greater than 0.002, except for pier 4 with the Hutchings, ICN simulated ground motion which has a strain of 0.0045. The maximum longitudinal steel strain is 0.037 in pier 2 for Sylmar, but significantly less for the other piers and ground motions. When interpreting strains from an inelastic analysis, the uncertainty in the modeling assumptions, particularly related to strain hardening and degradation, must be recognized. These values give an overall indication of inelastic demands but the localized quantities may be significantly influences by variation of the assumed parameters.

The moment–curvature response for sections of piers 2 and 3 is plotted in Figures 6.21 to 6.30 and 6.32 to 6.41 for the Sylmar and Hutchings, ICN ground motions, respectively. The section identification is indicated by a letter code defined Figure 3.11 or 3.12. For the Sylmar ground motion, the largest plastic rotations occur in weak axis bending (due to longitudinal displacement) at the top of the piers and, to a lesser extent, several meters below ground. Compared with the plastic hinge at the top of the pier, the plastic rotation below ground is spread along a greater length, with the curvature demands at each location less severe, because of soil resistance interacts with the pier shaft resistance to distribute the inelastic deformation. The plastic rotations in the strong axis direction are not significant for the piers in frame 1. The pulse in Sylmar ground motion produces the peak curvature demand in a single, large excursion. The subsequent cycles produce much less inelastic deformation. The general trend in moment-curvature response of the piers is similar for the Hutchings, ICN ground motion. The simulated ground motion induces more cycles of inelastic response than does the Sylmar ground motion, as for example at the top of pier 2 (Figure 6.32). The pinched hysteretic response of Figure 6.32 highlights the ability of the model to represent the effects of opening and closing of cracks in the concrete and the influence of axial load on the flexural response. As noted earlier, however, the model does not include degradation of concrete or bond-slip of the longitudinal reinforcement.

The axial force demand in the piers is summarized in Table 6.5. In all but one case, the piers remain in compression (negative values in the table) for the duration of the ground motion. The influence of vertical motion on the axial force in the column is significant, generally broadening the dynamic variation of compression in the piers. The vertical component of the Newhall motion, for which the structure is particularly sensitive to the influence of vertical motion, effects the structure so much that one column (pier 4) is driven briefly into tension. History plots of the axial force in the piers are shown for piers 2 through 4 in Figure

6.31 for the Sylmar ground motion and in Figure 6.42 for the Hutchings, ICN simulated ground motion. The dynamic variation in axial load is more dramatic for the Hutchings, ICN ground motion. The axial load variation was not accounted for in the shear capacity estimates. A more refined evaluation is warranted, particularly for ground motions that produce large participation of vertical vibration of the superstructure.

The computed response can be interpreted in terms of damage to bridge after the earthquake if the columns had been retrofitted. Concrete at several of the piers would have spalled. Piers 2 and 3 would have the most severe damage and possibly isolated bar buckling, depending on the retrofit details. The analyses indicate that the bridge would have remained serviceable after the earthquake.

Table 6.3: Maximum Column Curvatures

Record			Pier 2 1/m	Pier 3 1/m	Pier 4 1/m	Pier 5 1/m	Pier 6 1/m	Pier 7 1/m	Pier 8 1/m	Pier 9 1/m	Pier 10 1/m
Arleta	With Vertical Motion	Weak Axis Strong Axis	2.27×10^{-3} 4.17×10^{-4}	1.45×10^{-3} 7.97×10^{-4}	1.13×10^{-3} 9.38×10^{-4}	1.09×10^{-3} 7.63×10^{-4}	5.27×10^{-4} 4.40×10^{-4}	4.04×10^{-4} 4.69×10^{-4}	6.41×10^{-4} 4.08×10^{-4}	4.43×10^{-4} 2.95×10^{-4}	1.67×10^{-3} 3.33×10^{-4}
	Without Vertical Motion	Weak Axis Strong Axis	2.27×10^{-3} 4.21×10^{-4}	1.49×10^{-3} 8.04×10^{-4}	1.09×10^{-3} 9.40×10^{-4}	9.95×10^{-4} 7.74×10^{-4}	5.19×10^{-4} 4.40×10^{-4}	4.04×10^{-4} 4.70×10^{-4}	6.36×10^{-4} 4.07×10^{-4}	4.41×10^{-4} 2.97×10^{-4}	1.67×10^{-3} 2.31×10^{-4}
Sylmar	With Vertical Motion	Weak Axis Strong Axis	3.65×10^{-2} 1.29×10^{-3}	2.59×10^{-2} 1.59×10^{-3}	1.47×10^{-2} 1.67×10^{-3}	1.29×10^{-2} 1.48×10^{-3}	2.39×10^{-3} 1.11×10^{-3}	1.39×10^{-3} 1.09×10^{-3}	3.26×10^{-3} 1.60×10^{-3}	2.54×10^{-3} 9.61×10^{-4}	1.81×10^{-2} 1.66×10^{-3}
	Without Vertical Motion	Weak Axis Strong Axis	3.58×10^{-2} 1.29×10^{-3}	2.55×10^{-2} 1.57×10^{-3}	1.46×10^{-2} 1.64×10^{-3}	1.28×10^{-2} 1.51×10^{-3}	2.25×10^{-3} 1.09×10^{-3}	1.38×10^{-3} 1.09×10^{-3}	3.25×10^{-3} 1.58×10^{-3}	2.54×10^{-3} 9.65×10^{-4}	1.80×10^{-2} 1.65×10^{-3}
Jensen	With Vertical Motion	Weak Axis Strong Axis	1.94×10^{-2} 1.20×10^{-3}	1.21×10^{-2} 1.54×10^{-3}	4.37×10^{-3} 1.46×10^{-3}	3.51×10^{-3} 2.00×10^{-3}	1.55×10^{-3} 1.46×10^{-3}	1.04×10^{-3} 1.32×10^{-3}	1.59×10^{-3} 1.79×10^{-3}	1.23×10^{-3} 1.31×10^{-3}	8.96×10^{-3} 1.86×10^{-3}
	Without Vertical Motion	Weak Axis Strong Axis	1.98×10^{-2} 1.22×10^{-3}	1.20×10^{-2} 1.54×10^{-3}	4.01×10^{-3} 1.52×10^{-3}	3.14×10^{-3} 2.17×10^{-3}	1.53×10^{-3} 1.46×10^{-3}	9.94×10^{-4} 1.31×10^{-3}	1.59×10^{-3} 1.76×10^{-3}	1.27×10^{-3} 1.32×10^{-3}	8.73×10^{-3} 1.89×10^{-3}
Horton, Pier 3	With Vertical Motion	Weak Axis Strong Axis	1.16×10^{-2} 1.13×10^{-3}	4.66×10^{-3} 1.98×10^{-3}	2.66×10^{-3} 2.18×10^{-3}	2.92×10^{-3} 3.17×10^{-3}	1.61×10^{-3} 1.29×10^{-3}	1.09×10^{-3} 1.48×10^{-3}	2.02×10^{-3} 1.48×10^{-3}	1.61×10^{-3} 7.94×10^{-4}	1.23×10^{-2} 1.36×10^{-3}
	Without Vertical Motion	Weak Axis Strong Axis	1.16×10^{-2} 1.13×10^{-3}	4.55×10^{-3} 1.97×10^{-3}	2.62×10^{-3} 2.17×10^{-3}	2.32×10^{-3} 3.19×10^{-3}	1.60×10^{-3} 1.29×10^{-3}	1.12×10^{-3} 1.47×10^{-3}	2.04×10^{-3} 1.47×10^{-3}	1.60×10^{-3} 7.41×10^{-4}	1.24×10^{-2} 1.38×10^{-3}
Newhall	With Vertical Motion	Weak Axis Strong Axis	2.50×10^{-2} 1.08×10^{-3}	1.58×10^{-2} 1.09×10^{-3}	7.40×10^{-3} 1.10×10^{-3}	5.50×10^{-3} 1.37×10^{-3}	1.64×10^{-3} 8.60×10^{-4}	1.20×10^{-3} 8.34×10^{-4}	1.71×10^{-3} 9.71×10^{-4}	1.44×10^{-3} 5.26×10^{-4}	1.11×10^{-2} 7.28×10^{-4}
	Without Vertical Motion	Weak Axis Strong Axis	2.49×10^{-2} 1.06×10^{-3}	1.59×10^{-2} 1.08×10^{-3}	7.42×10^{-3} 1.14×10^{-3}	5.72×10^{-3} 1.39×10^{-3}	1.61×10^{-3} 8.61×10^{-4}	1.11×10^{-3} 8.32×10^{-4}	1.70×10^{-3} 9.64×10^{-4}	1.46×10^{-3} 4.98×10^{-4}	1.10×10^{-2} 7.42×10^{-4}
Hutchings, ICN	With Vertical Motion	Weak Axis Strong Axis	3.01×10^{-2} 2.51×10^{-3}	1.95×10^{-2} 4.69×10^{-3}	1.07×10^{-2} 4.13×10^{-3}	1.03×10^{-2} 2.84×10^{-3}	2.70×10^{-3} 1.35×10^{-3}	1.68×10^{-3} 1.16×10^{-3}	4.76×10^{-3} 1.46×10^{-3}	2.65×10^{-3} 1.07×10^{-3}	2.08×10^{-2} 1.82×10^{-3}
	Without Vertical Motion	Weak Axis Strong Axis	2.98×10^{-2} 2.69×10^{-3}	2.03×10^{-2} 4.81×10^{-3}	1.09×10^{-2} 4.23×10^{-3}	1.01×10^{-2} 2.91×10^{-3}	2.58×10^{-3} 1.33×10^{-3}	1.58×10^{-3} 1.13×10^{-3}	4.58×10^{-3} 1.40×10^{-3}	2.49×10^{-3} 1.06×10^{-3}	2.00×10^{-2} 1.84×10^{-3}

Table 6.4: Maximum Longitudinal Strains in Columns

Record		Pier 2 mm/mm	Pier 3 mm/mm	Pier 4 mm/mm	Pier 5 mm/mm	Pier 6 mm/mm	Pier 7 mm/mm	Pier 8 mm/mm	Pier 9 mm/mm	Pier 10 mm/mm
Sylmar	Compressive	2.05×10^{-3}	1.49×10^{-3}	1.42×10^{-3}	1.13×10^{-3}	1.66×10^{-3}	1.13×10^{-3}	1.07×10^{-3}	9.40×10^{-4}	1.44×10^{-3}
	Tensile	3.71×10^{-2}	2.63×10^{-2}	1.49×10^{-2}	1.32×10^{-2}	2.92×10^{-3}	2.67×10^{-3}	4.88×10^{-3}	3.73×10^{-3}	1.82×10^{-2}
Newhall	Compressive	1.59×10^{-3}	1.37×10^{-3}	1.11×10^{-3}	9.54×10^{-4}	1.27×10^{-3}	9.66×10^{-4}	1.15×10^{-3}	8.65×10^{-4}	1.26×10^{-3}
	Tensile	2.52×10^{-2}	1.58×10^{-2}	6.99×10^{-3}	5.12×10^{-3}	2.20×10^{-3}	2.06×10^{-3}	2.71×10^{-3}	1.97×10^{-3}	1.10×10^{-2}
Hutchings, ICN	Compressive	1.99×10^{-3}	1.61×10^{-3}	4.53×10^{-3}	1.22×10^{-3}	2.16×10^{-3}	1.38×10^{-3}	1.18×10^{-3}	1.87×10^{-3}	1.63×10^{-3}
	Tensile	3.06×10^{-2}	1.96×10^{-2}	1.15×10^{-2}	1.01×10^{-2}	3.58×10^{-3}	2.76×10^{-3}	7.68×10^{-3}	4.11×10^{-3}	2.08×10^{-2}

Table 6.5: Maximum Axial Force in Columns

Record			Pier 2 kN	Pier 3 kN	Pier 4 kN	Pier 5 kN	Pier 6 kN	Pier 7 kN	Pier 8 kN	Pier 9 kN	Pier 10 kN
Arleta	With Vertical Motion	Maximum	−10000	−9830	−6270	−6090	−10300	−4360	−3830	−4610	−10300
		Minimum	−17300	−17600	−14100	−14400	−19800	−17300	−12800	−16200	−17400
	Without Vertical Motion	Maximum	−12700	−12000	−9150	−9440	−14600	−11300	−8750	−10600	−14200
		Minimum	−15600	−16200	−13100	−13000	−15800	−12700	−9820	−12300	−15100
Sylmar	With Vertical Motion	Maximum	−10000	−10200	−7230	−7390	−12200	−8090	−5620	−8380	−11200
		Minimum	−18700	−18000	−14200	−13800	−18800	−17300	−13300	−15300	−17800
	Without Vertical Motion	Maximum	−11800	−11400	−8960	−8790	−14100	−10200	−7190	−9190	−12100
		Minimum	−17800	−16500	−13900	−12500	−16600	−14700	−12200	−13300	−17500
Jensen	With Vertical Motion	Maximum	−9020	−7600	−5040	−6260	−10100	−5450	−4240	−5400	−9950
		Minimum	−21700	−22700	−18000	−15500	−21600	−18500	−14500	−16800	−20500
	Without Vertical Motion	Maximum	−11300	−11100	−8130	−8050	−12800	−10100	−6880	−9010	−11200
		Minimum	−17100	−16800	−13700	−13200	−16600	−13900	−11100	−13500	−17900
Horton, Pier 3	With Vertical Motion	Maximum	−10500	−8770	−6450	−7930	−13200	−9660	−7210	−9300	−12300
		Minimum	−18600	−17900	−14300	−15600	−18000	−14900	−11800	−14000	−17300
	Without Vertical Motion	Maximum	−11100	−9560	−7060	−7840	−13200	−10300	−7290	−9810	−13400
		Minimum	−17600	−19100	−14900	−16100	−17200	−13600	−10700	−13200	−15900
Newhall	With Vertical Motion	Maximum	−6810	−6730	890	−1890	−4510	−5360	−3000	−5040	−4620
		Minimum	−23100	−22000	−20600	−18500	−25900	−18600	−18600	−17200	−24900
	Without Vertical Motion	Maximum	−11800	−9750	−6270	−8140	−13400	−10500	−7590	−9460	−13200
		Minimum	−17000	−17900	−15000	−14800	−17600	−14400	−12000	−13100	−15900
Hutchings, ICN	With Vertical Motion	Maximum	−4190	−3890	−3870	−3100	−5280	−4480	−4480	−4200	−3730
		Minimum	−22900	−24700	−18500	−17400	−24400	−17600	−15900	−18200	−25300
	Without Vertical Motion	Maximum	−10000	−8890	−6830	−7280	−13600	−10000	−7270	−9190	−12500
		Minimum	−18100	−19600	−14800	−14400	−17500	−14100	−12300	−14200	−16800

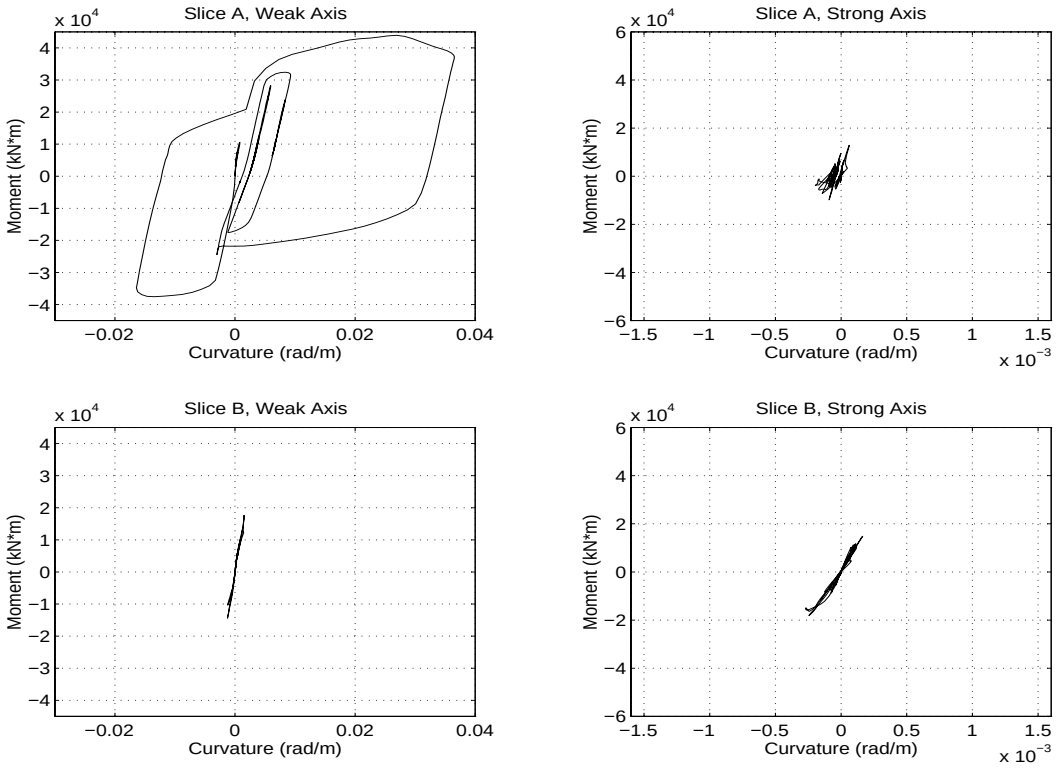

Figure 6.21: Pier 2 Moment-Curvature at Slices A and B, Sylmar Ground Motion

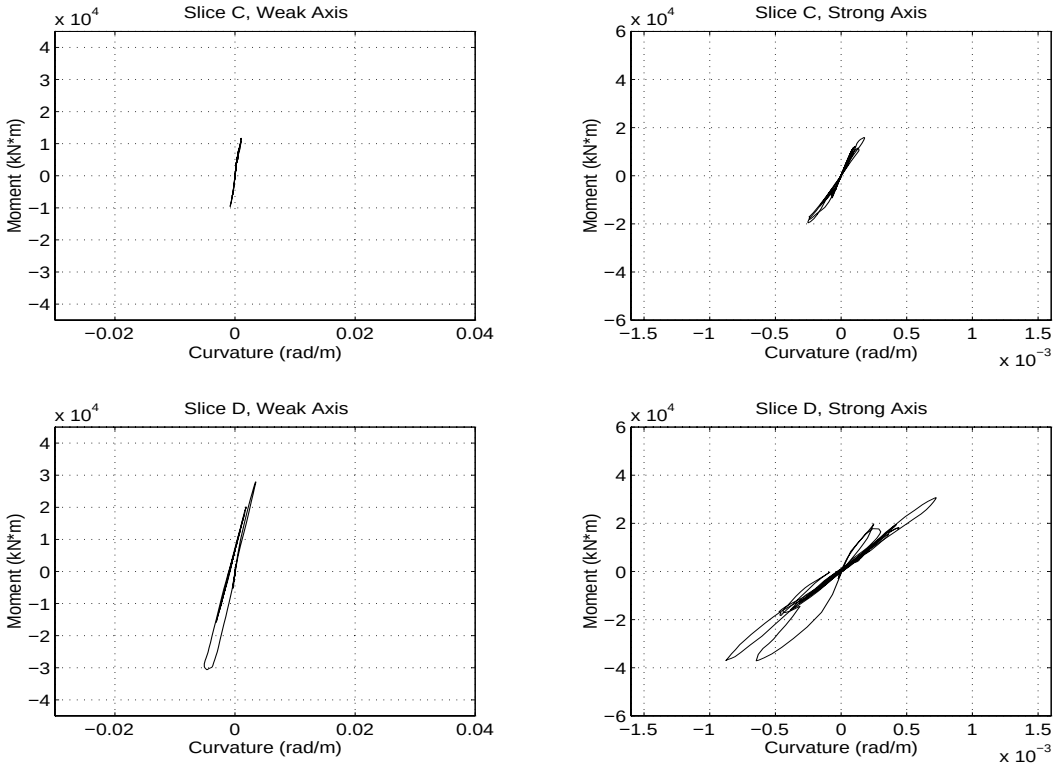

Figure 6.22: Pier 2 Moment-Curvature at Slices C and D, Sylmar Ground Motion

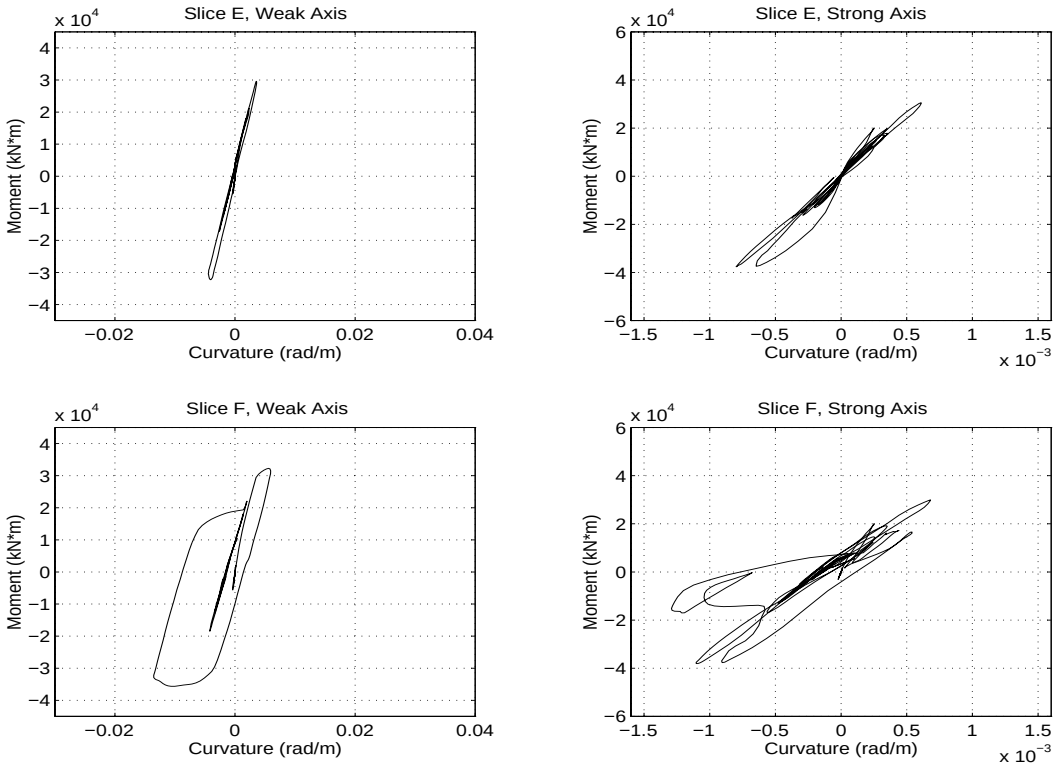

Figure 6.23: Pier 2 Moment-Curvature at Slices E and F, Sylmar Ground Motion

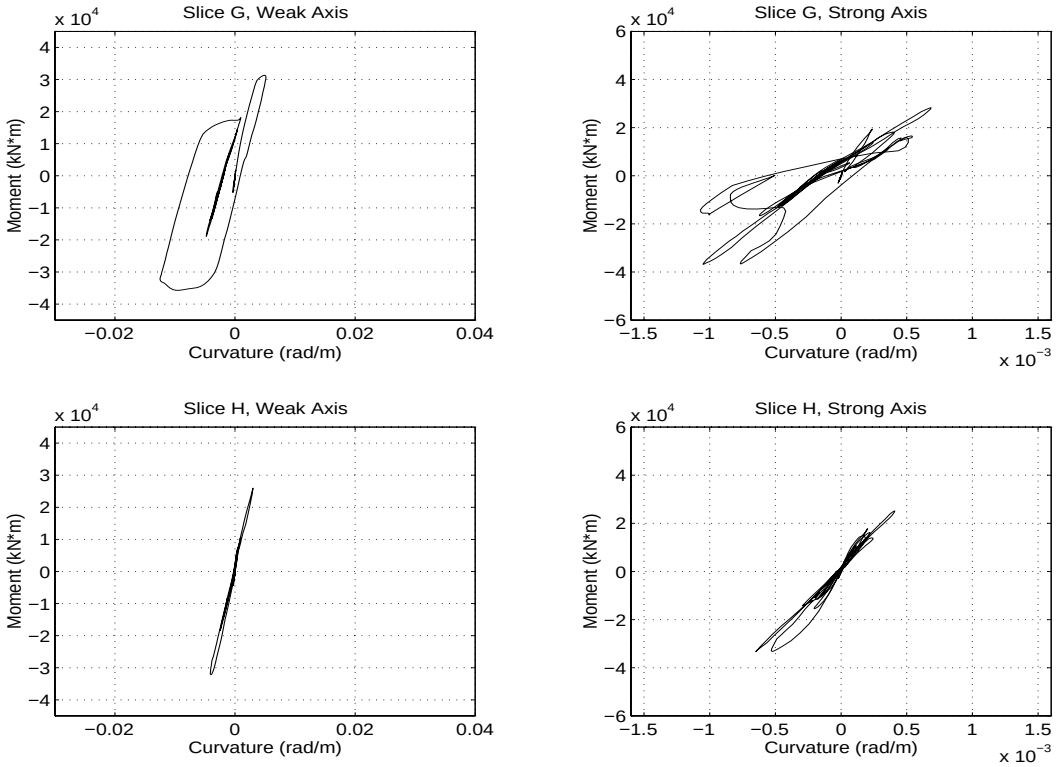

Figure 6.24: Pier 2 Moment-Curvature at Slices G and H, Sylmar Ground Motion

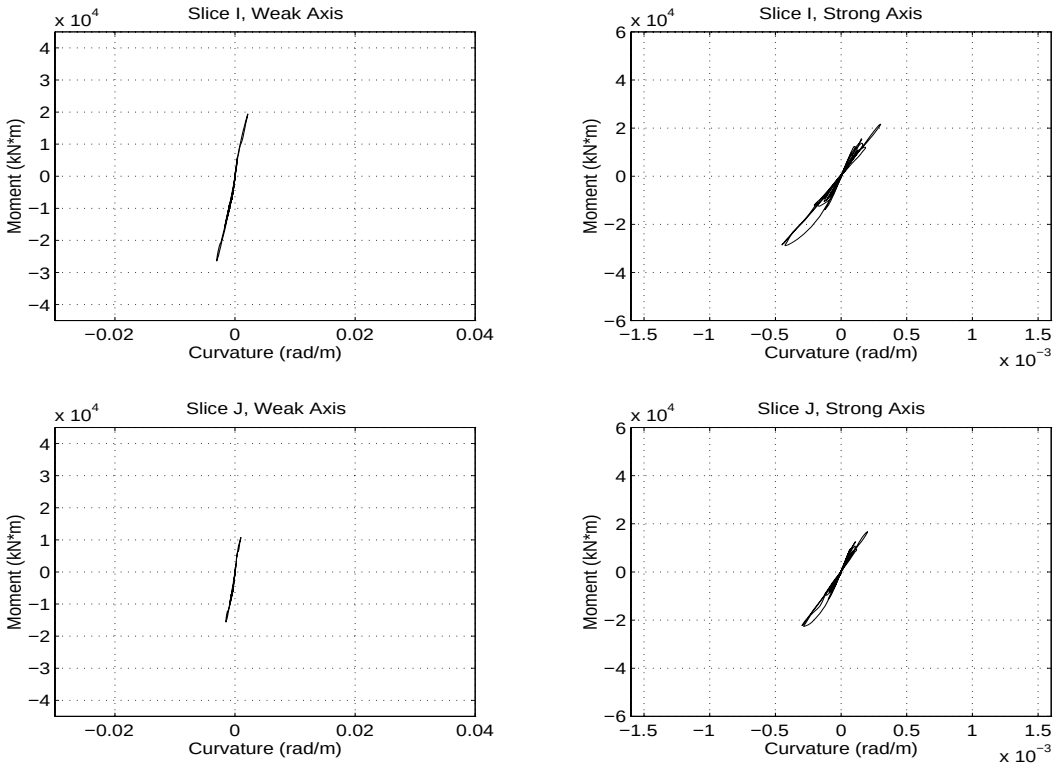

Figure 6.25: Pier 2 Moment-Curvature at Slices I and J, Sylmar Ground Motion

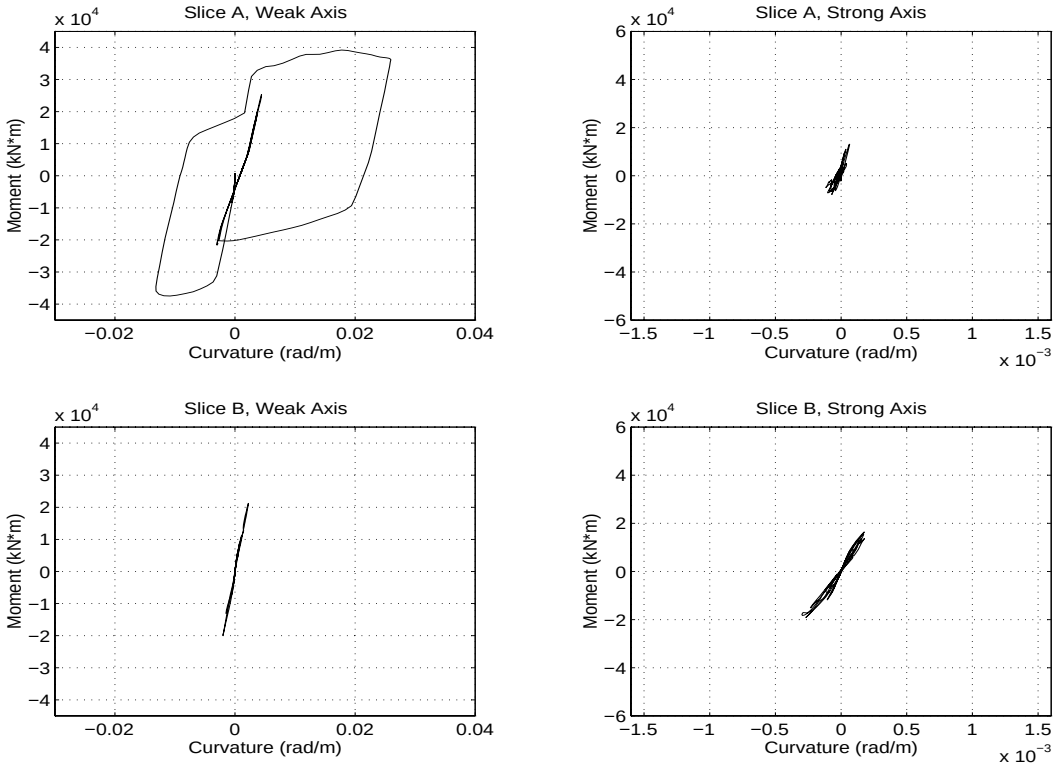

Figure 6.26: Pier 3 Moment-Curvature at Slices A and B, Sylmar Ground Motion

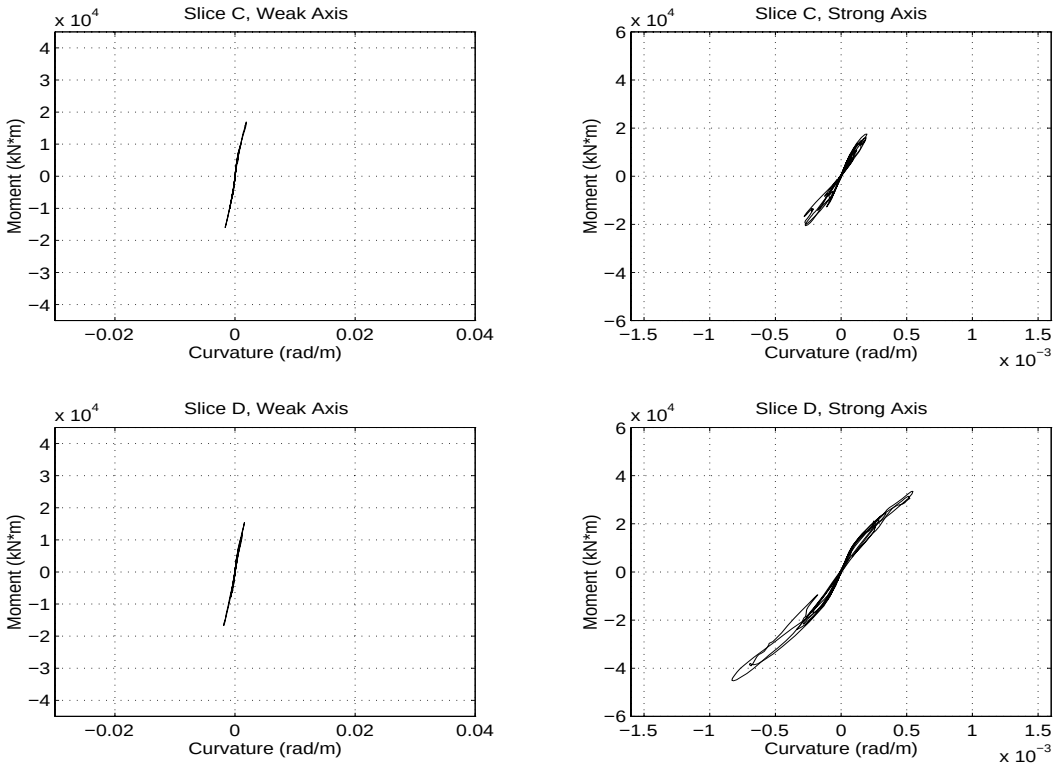

Figure 6.27: Pier 3 Moment-Curvature at Slices C and D, Sylmar Ground Motion

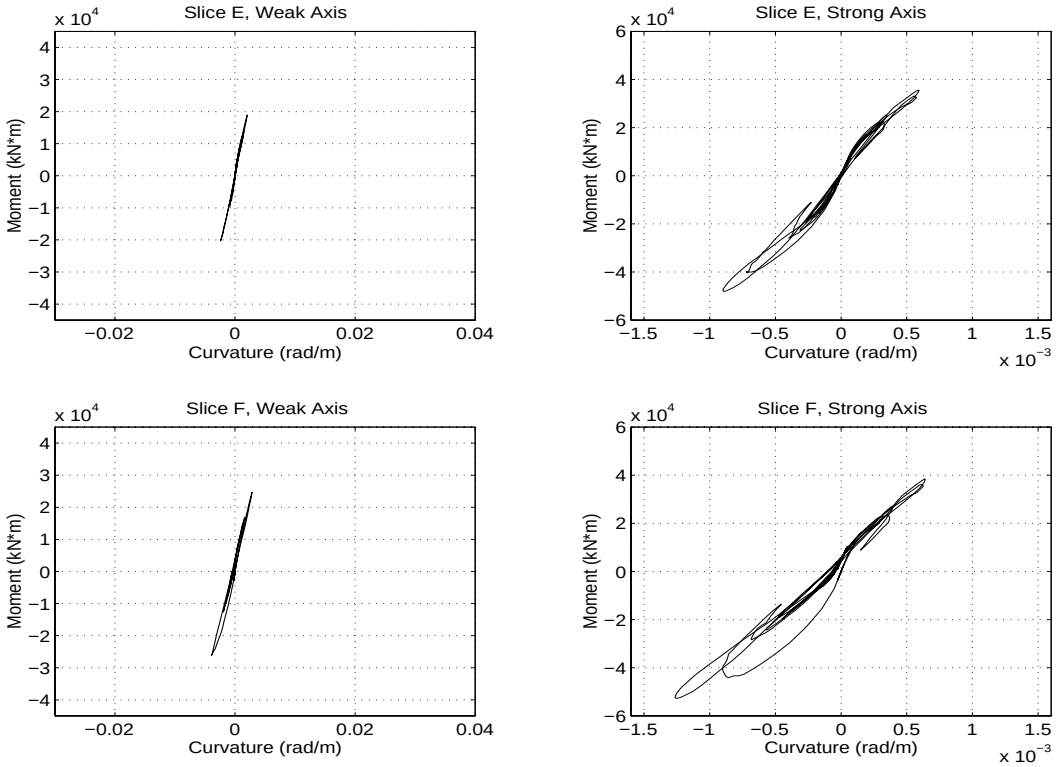

Figure 6.28: Pier 3 Moment-Curvature at Slices E and F, Sylmar Ground Motion

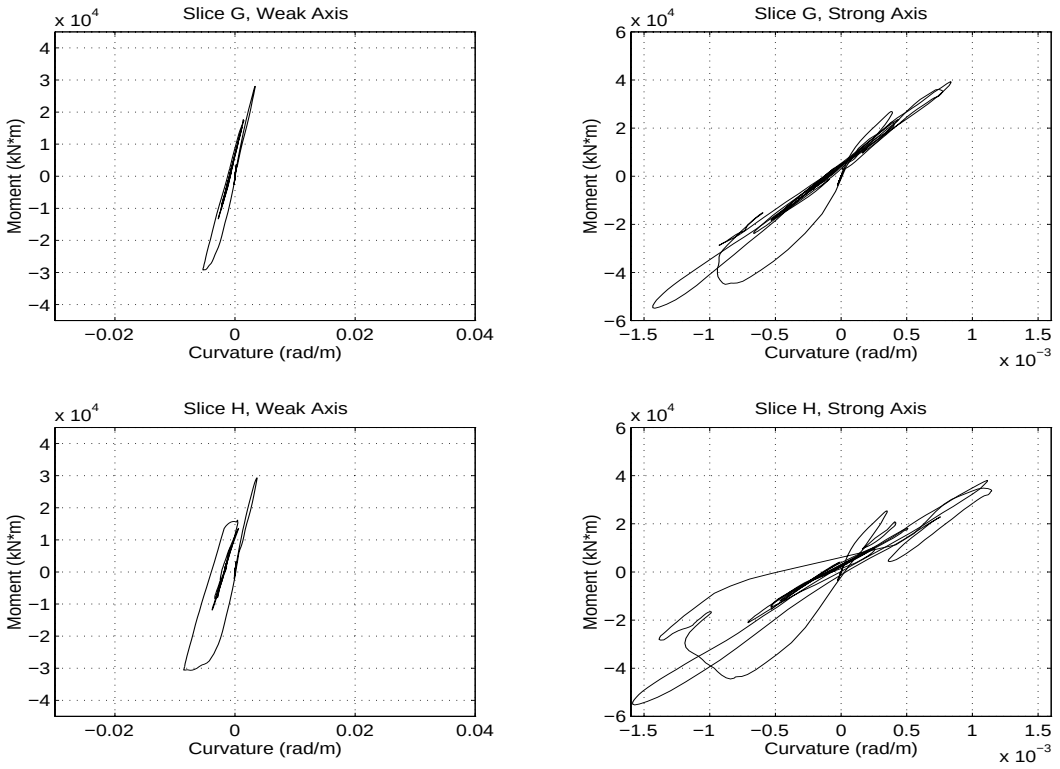

Figure 6.29: Pier 3 Moment-Curvature at Slices G and H, Sylmar Ground Motion

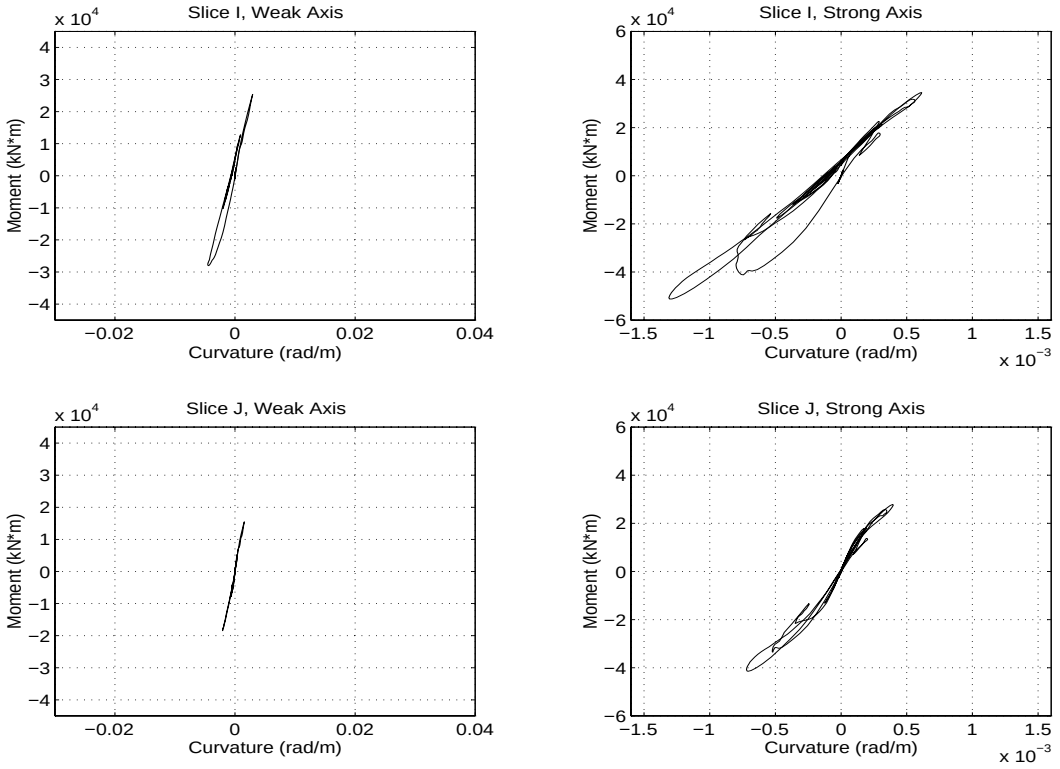

Figure 6.30: Pier 3 Moment-Curvature at Slices I and J, Sylmar Ground Motion

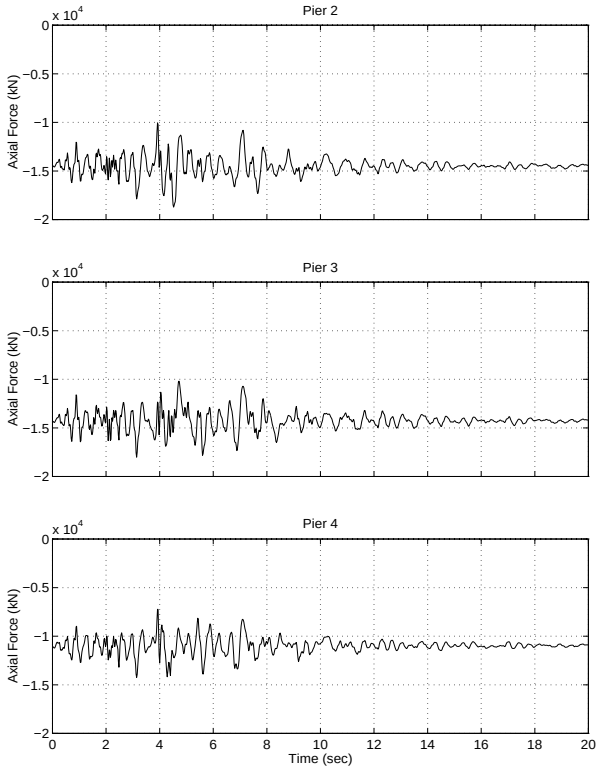

Figure 6.31: Axial Force History for Piers 2 to 4, Sylmar Ground Motion

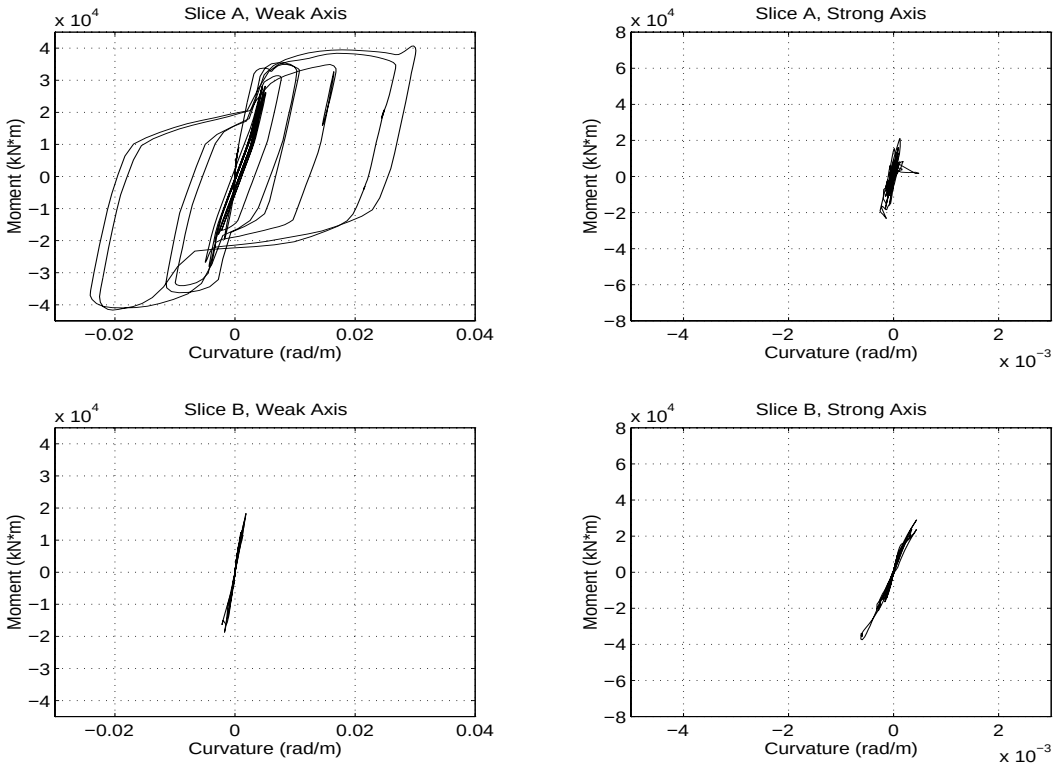

Figure 6.32: Pier 2 Moment-Curvature at Slices A and B, Hutchings et al. (1996) ICN

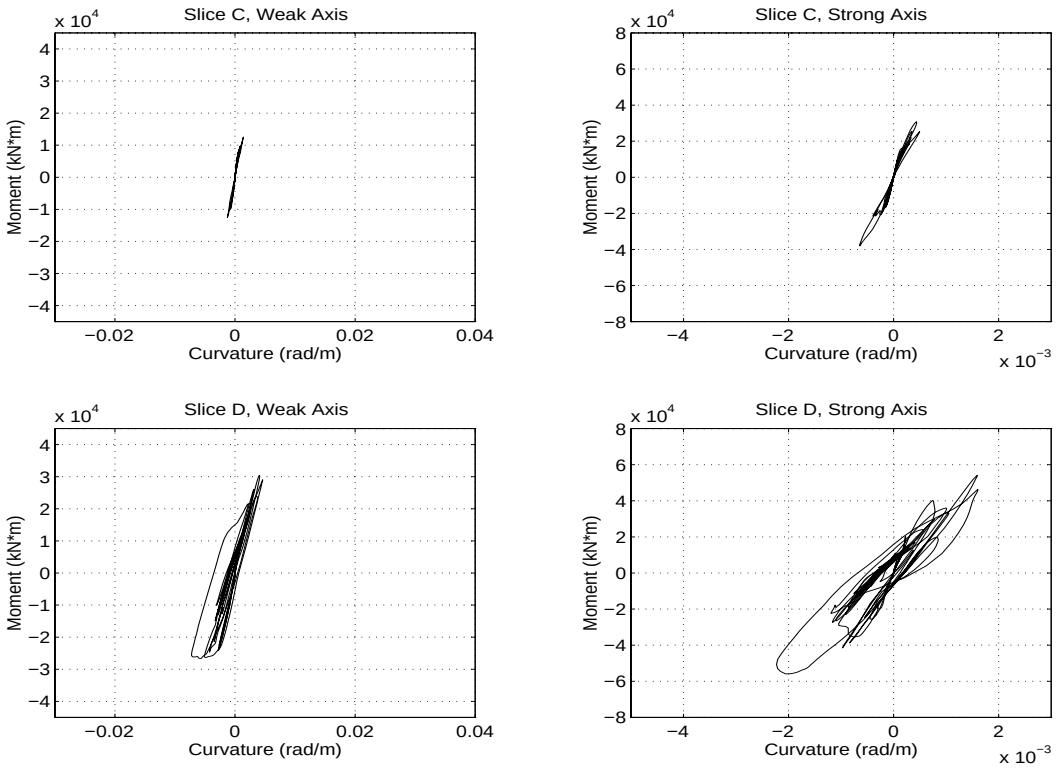

Figure 6.33: Pier 2 Moment-Curvature at Slices C and D, Hutchings et al. (1996) ICN

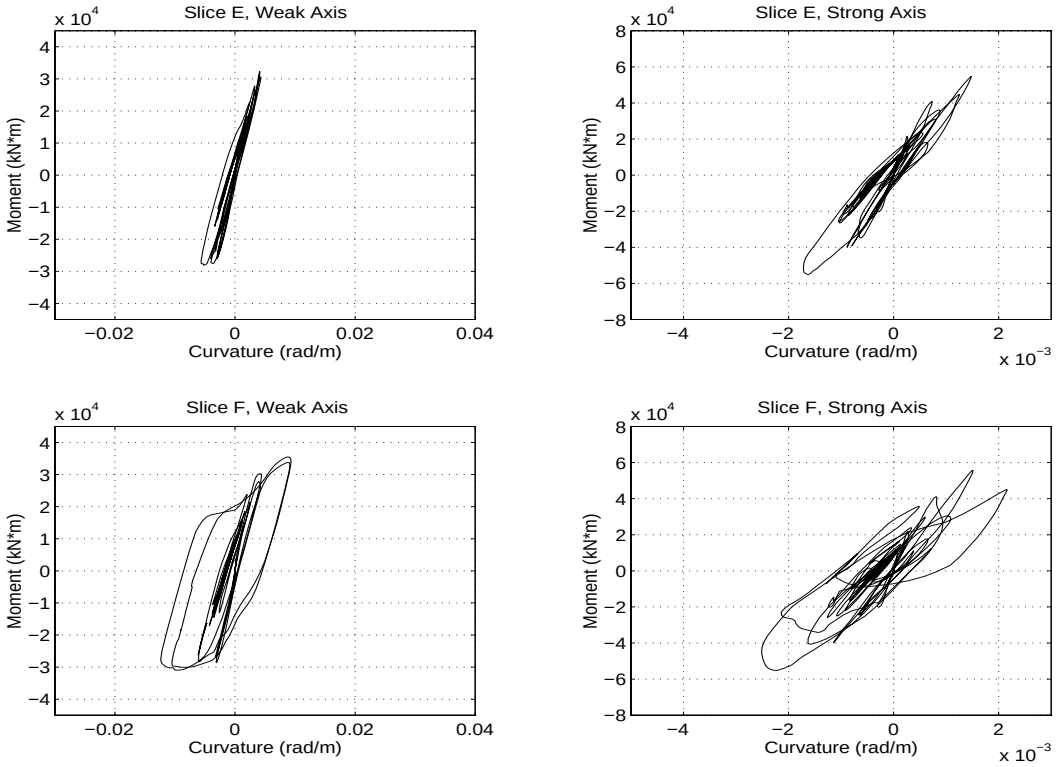

Figure 6.34: Pier 2 Moment-Curvature at Slices E and F, Hutchings et al. (1996) ICN

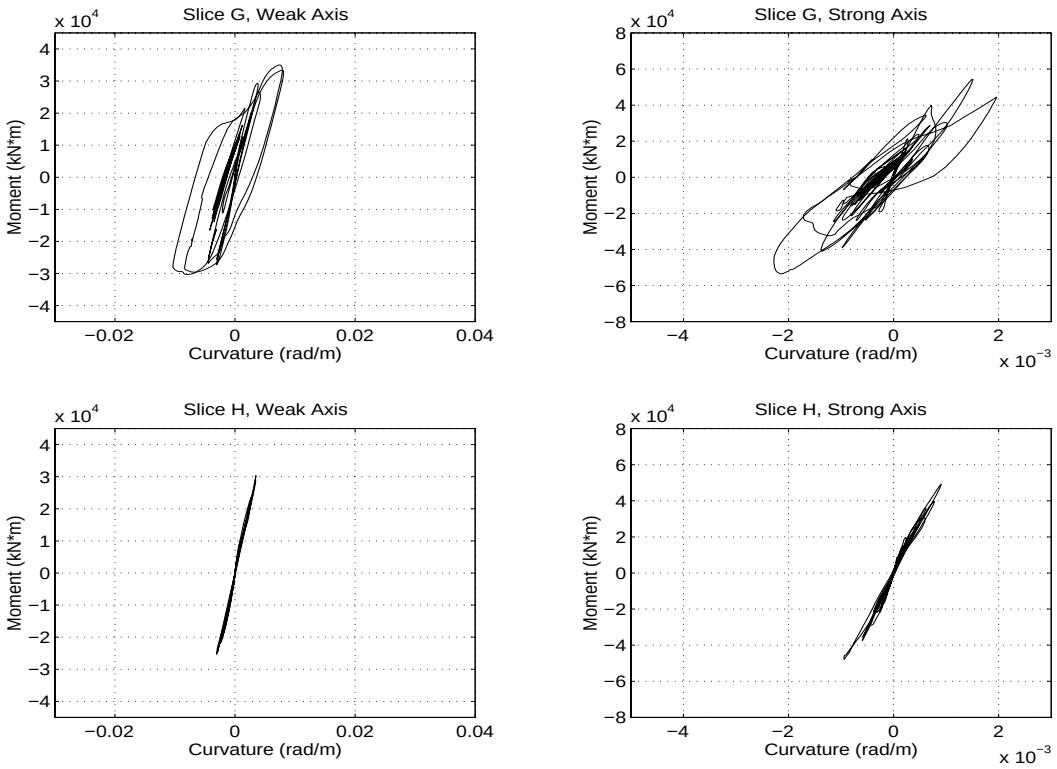

Figure 6.35: Pier 2 Moment-Curvature at Slices G and H, Hutchings et al. (1996) ICN

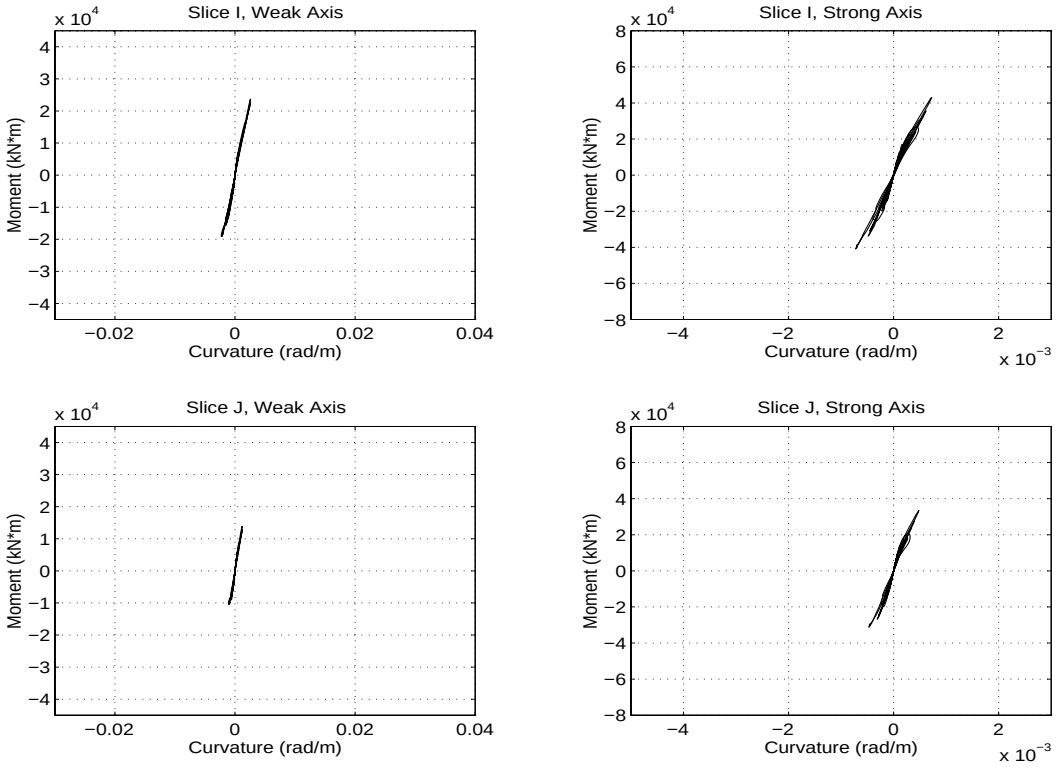

Figure 6.36: Pier 2 Moment-Curvature at Slices I and J, Hutchings et al. (1996) ICN

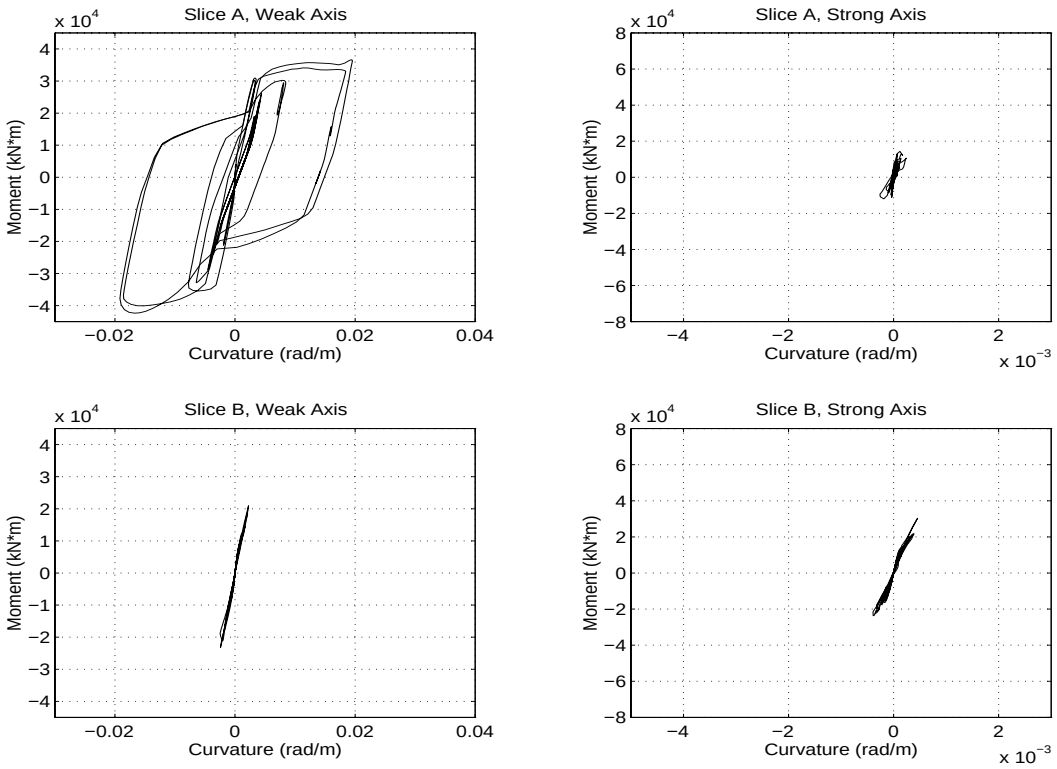

Figure 6.37: Pier 3 Moment-Curvature at Slices A and B, Hutchings et al. (1996) ICN

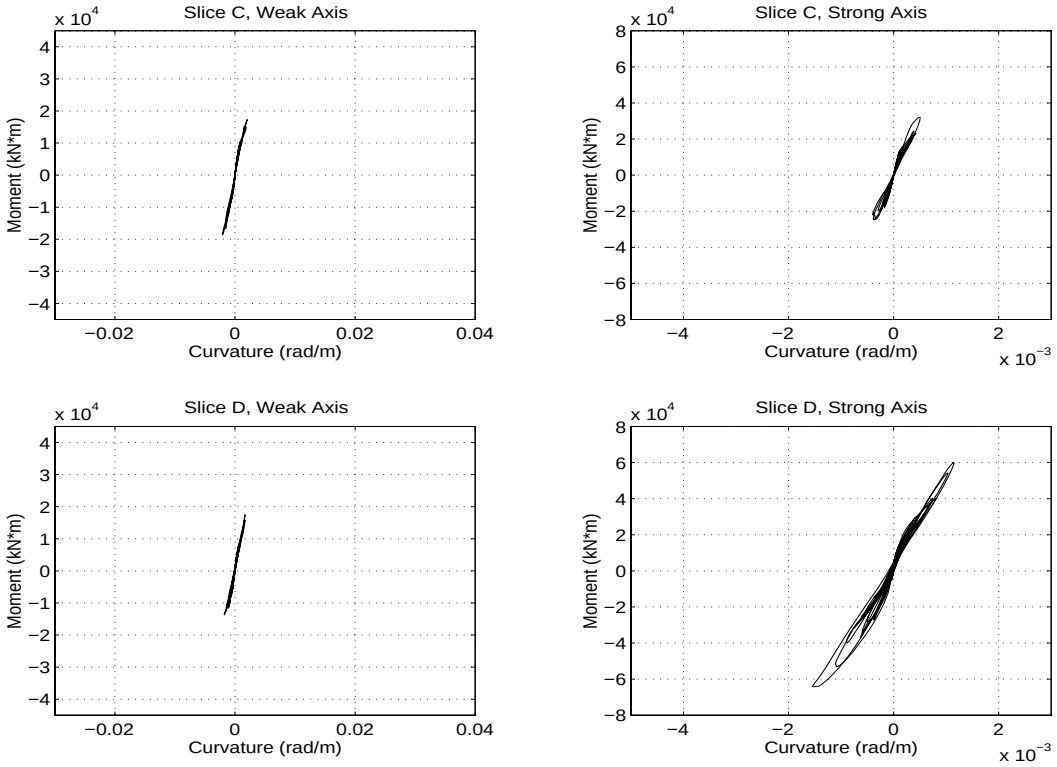

Figure 6.38: Pier 3 Moment-Curvature at Slices C and D, Hutchings et al. (1996) ICN

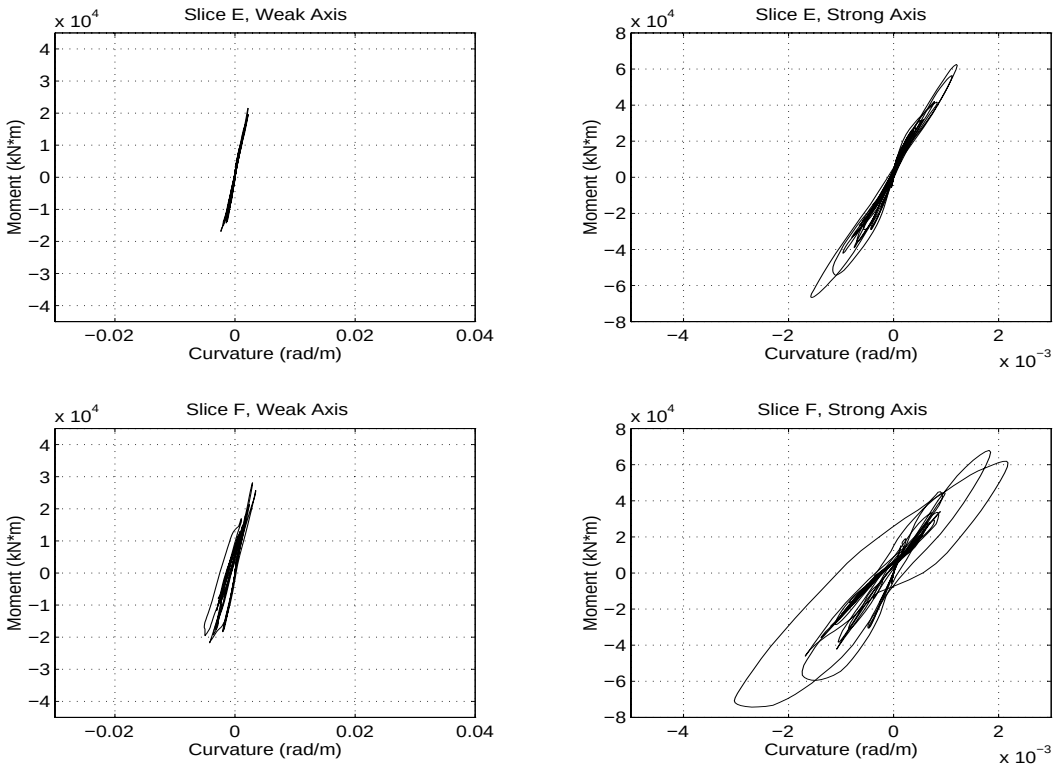

Figure 6.39: Pier 3 Moment-Curvature at Slices E and F, Hutchings et al. (1996) ICN

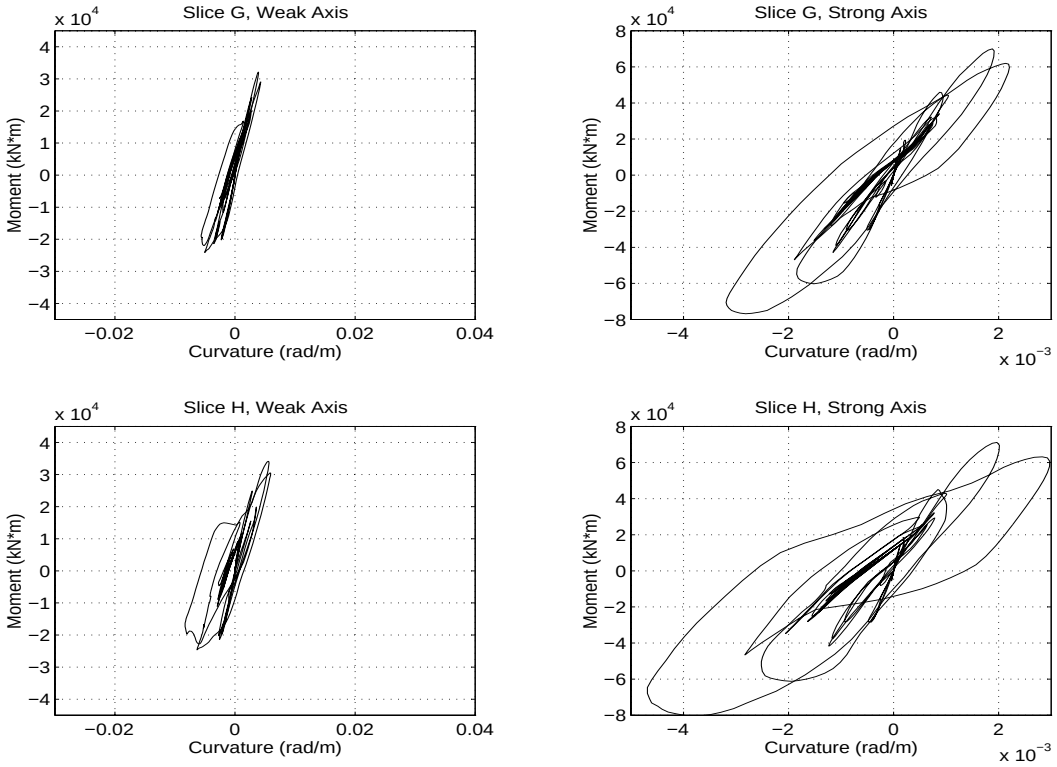

Figure 6.40: Pier 3 Moment-Curvature at Slices G and H, Hutchings et al. (1996) ICN

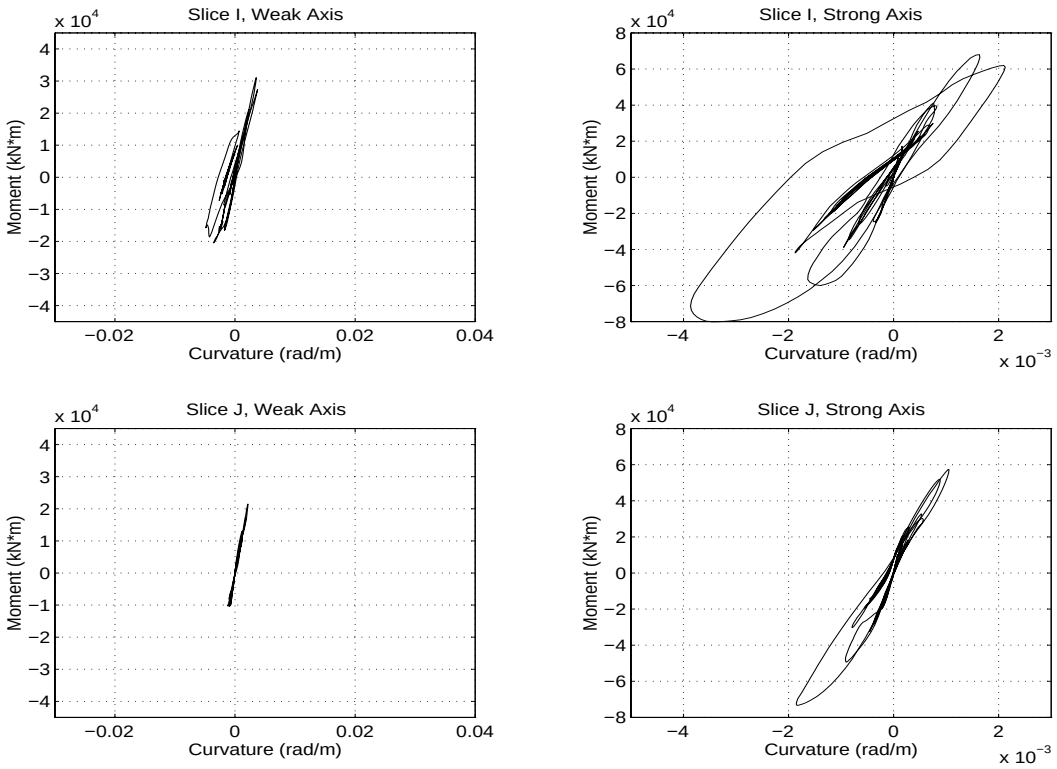

Figure 6.41: Pier 3 Moment-Curvature at Slices I and J, Hutchings et al. (1996) ICN

6.3 Acceleration Response

Acceleration histories of the bridge at the piers and abutments are plotted in Figures 6.43 and 6.44 for the Sylmar ground motion and in Figures 6.46 and 6.47 for the Hutchings, ICN simulated ground motion. These acceleration levels are fairly moderate, being limited by the flexural capacity of the piers, but there are distinct peaks when pounding of the superstructure at intermediate hinges occurs. The peaks in the vertical acceleration are associated with small uplift and subsequent impact at the abutment seat.

The acceleration histories at superstructure centerline on both sides of hinge 4 are shown in Figures 6.45 and 6.48 for the Sylmar and Hutchings, ICN ground motions, respectively. Upon impact, the acceleration spikes on the two sides of the hinge are nearly equal and opposite, as expected to satisfy conservation of momentum for frames of nearly equal mass. The magnitude of the acceleration peaks at the hinges is very large (on the order of 10 g) because of the sudden transfer of momentum. The amplitude of the acceleration spikes is sensitive to the assumptions of post–closing hinge spring stiffness.

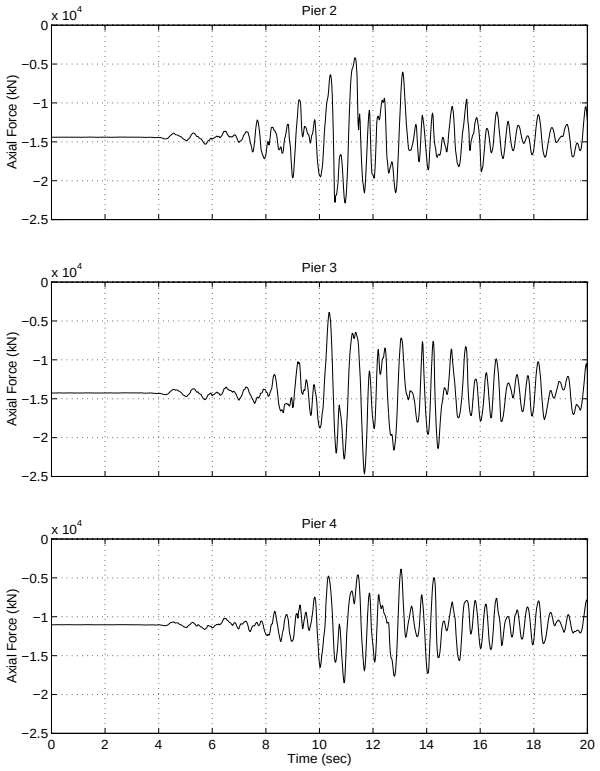

Figure 6.42: Axial Force History for Piers 2 to 4, Hutchings et al. (1996) ICN

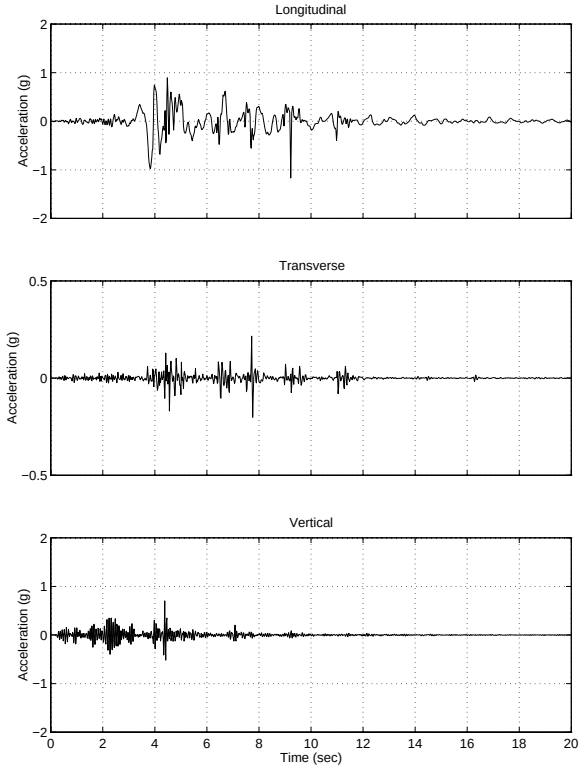

Figure 6.43: Acceleration History at Center of Abutment 1, Sylmar Ground Motion

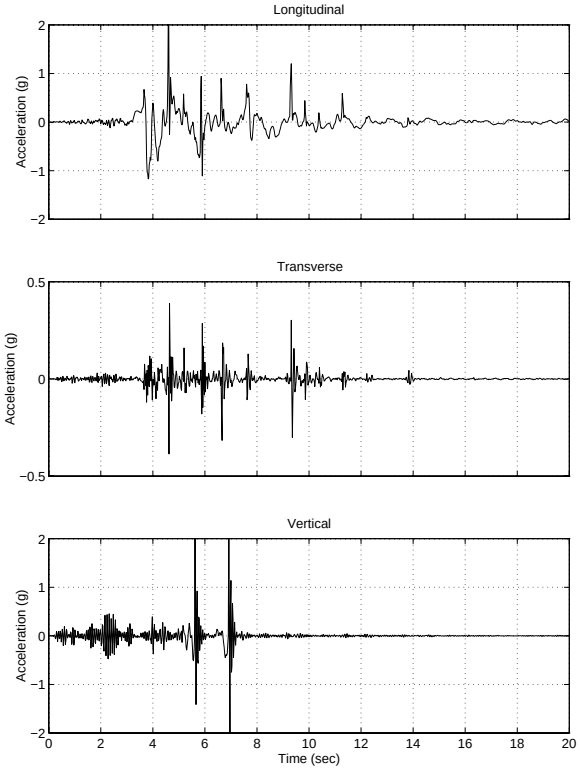

Figure 6.44: Acceleration History at Center of Abutment 11, Sylmar Ground Motion

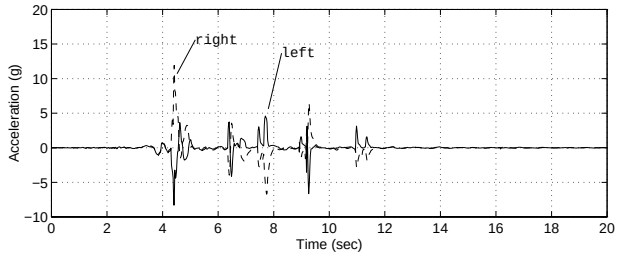

Figure 6.45: Acceleration History at Center of Hinge 4, Sylmar Ground Motion

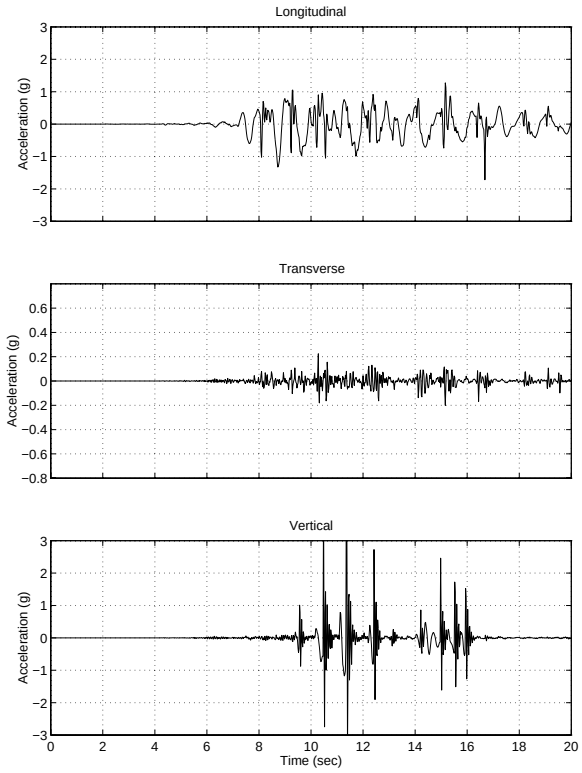

Figure 6.46: Acceleration History at Center of Abutment 1, Hutchings et al. (1996) ICN

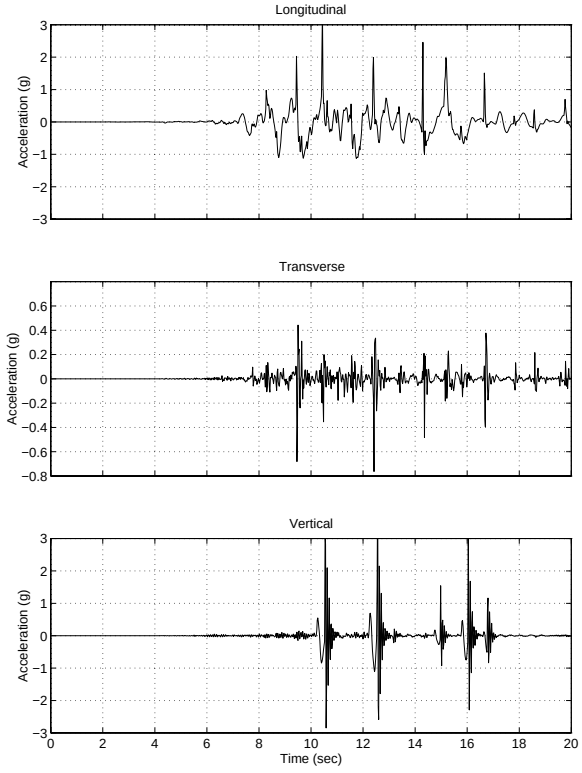

Figure 6.47: Acceleration History at Center of Abutment 11, Hutchings et al. (1996) ICN

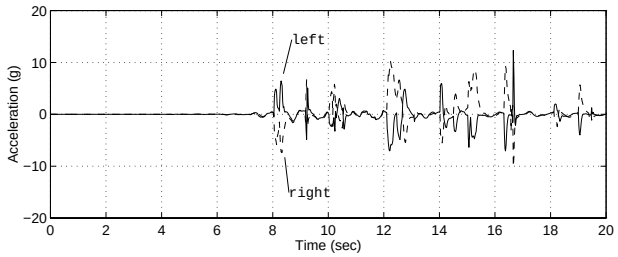

Figure 6.48: Acceleration History at Center of Hinge 4, Hutchings et al. (1996) ICN

6.4 Hinge and Abutment Response

The maximum hinge displacements are listed in Table 6.6. The hinge opening displacements are the average maximum displacement for the two gap springs described in Section 3.6. The nominal hinge seat length is 360 mm (14 in.). Assuming 300 mm of usable hinge seat, unseating only becomes critical at hinge 5 when the model is subjected to the Hutchings, ICN simulated ground motion record. All other ground motion analyses indicate that hinge unseating would not have been a critical failure mode for this structure, with the demand in most cases not more than one-half of the usable seat capacity.

The relative displacement histories for hinge 4 are plotted in Figures 6.49 and 6.51 for the Sylmar and Hutchings, ICN ground motions, respectively. The plots show the hinge opening (positive displacement) and hinge closing at -12.5 mm (0.5 in.) for the nodes at the outside and inside edges of the superstructure. Figures 6.50 and 6.52 show the force–displacement response of the restrainer and bearing pads for the Sylmar and Hutchings, ICN ground motions, respectively. The restrainers at hinge 4 yield substationally. The Sylmar response is characterized, as with the other response quantities, by a single excursion with significant inelastic displacements. The response to the Hutchings, ICN simulated ground motion has five substantial excursions and with increasing inelastic deformation.

Table 6.6: Maximum Hinge Opening Displacements

Record		Hinge 4 mm	Hinge 5 mm	Hinge 7 mm	Hinge 9 mm
Arleta	With Vertical Motion	36.2	64.4	63.8	38.6
	Without Vertical Motion	36.2	64.1	64.1	38.2
Sylmar	With Vertical Motion	82.8	208	140	78.7
	Without Vertical Motion	78.0	216	137	74.9
Jensen	With Vertical Motion	58.4	147	180	66.2
	Without Vertical Motion	58.0	147	180	65.2
Horton, Pier 3	With Vertical Motion	77.4	142	197	120
	Without Vertical Motion	77.7	141	196	120
Newhall	With Vertical Motion	61.6	153	120	82.0
	Without Vertical Motion	63.2	154	121	83.6
Hutchings, ICN	With Vertical Motion	118	321	153	105
	Without Vertical Motion	118	314	153	104

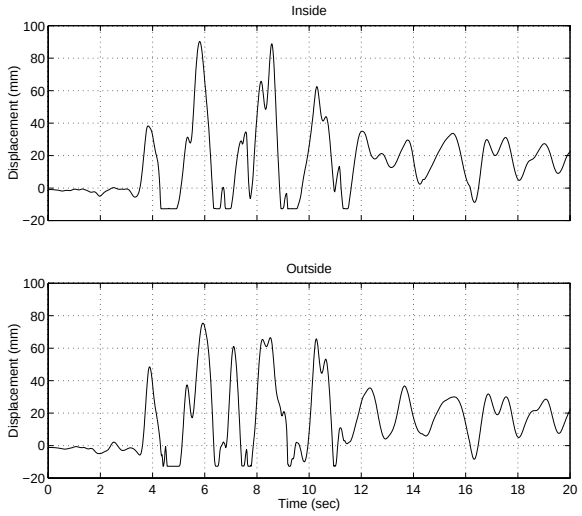

Figure 6.49: Time History for Hinge 4 Gap Closing Elements, Sylmar Ground Motion

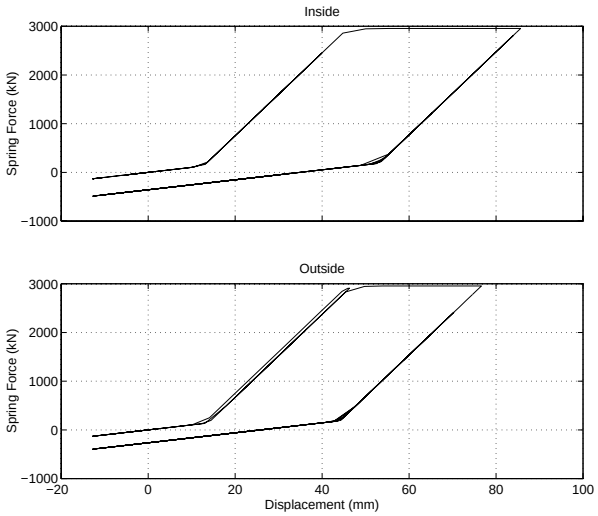

Figure 6.50: Force Displacement for Hinge 4 Restrainer and Bearing Pad Elements, Sylmar Ground Motion

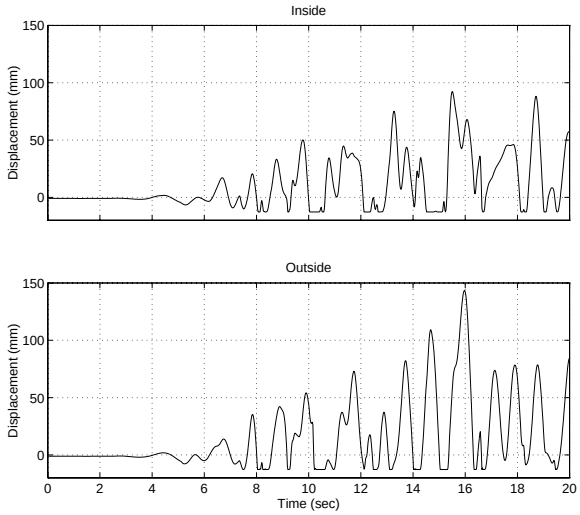

Figure 6.51: Time History for Hinge 4 Gap Closing Elements, Hutchings et al. (1996) ICN Simulated Ground Motion

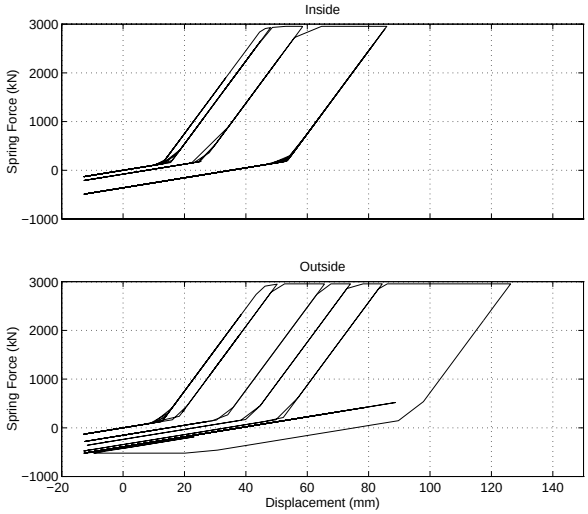

Figure 6.52: Force Displacement for Hinge 4 Restrainer and Bearing Pad Elements, Hutchings et al. (1996) ICN Simulated Ground Motion

6.5 Superstructure Forces

The superstructure force demands for frame 1 are summarized in Table 6.7. The bending moments include the effects of dead loads, primary prestressing moments, and earthquake induced forces. Secondary prestressing moments are not accounted for in the force demands.

These analyses indicate that the superstructure would experience some flexural yielding if the shear failure at pier 2 had been prevented by the column retrofit. In particular, the box girder would be expected to yield at the right of span 2 for the Hutchings, ICN ground motion and at the middle of span 3 for the Newhall ground motion. Some of the values in Table 6.7 are listed as "N/A"because of inadequacies in post-processing of the computer analysis results. It is likely, however, that the superstructure would exhibit some flexural yielding, particularly due to reversal of moments when subject to the three most critical ground motions (Sylmar, Newhall, and Hutchings, ICN).

As observed in Section 5.3.2, the axial force in the piers is influenced by the vertical ground motion component for the Newhall record. The axial forces in the pier are primarily caused by vertical vibration of the superstructure. The vertical ground motion component, as expected, has a significant effect on the superstructure. The maximum bending moment with the vertical component can be as large as twice the demands without the vertical component.

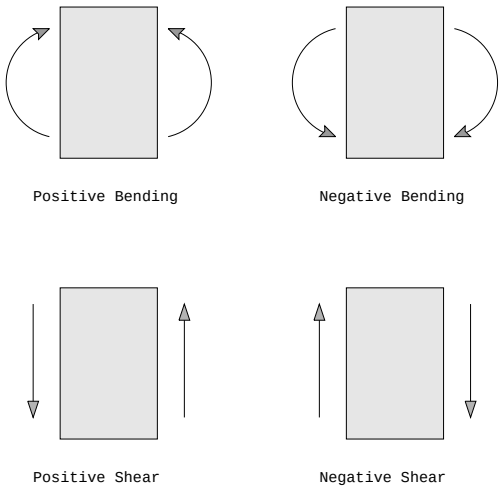

Figure 6.53: Sign Convention for Superstructure Forces

6.6 Linear Models for Earthquake Displacement Demand Analysis

This section examines the ability of a linear model to estimate the displacement demand for Separation and Overhead bridge. Linear models are commonly used in design because of they are simpler to use than nonlinear models for global dynamic analysis. Two linear models are investigated: a compression model and a tension model. The two models attempt

Table 6.7: Maximum Superstructure Force Demands

Record		Span 1							
		Middle				Right			
		Bending Moment kN×m		Shear Force kN		Bending Moment kN×m		Shear Force kN	
		pos.	neg.	pos.	neg.	pos.	neg.	pos.	neg.
Arleta	With Vertical Motion	2.22×10^4	N/A	1920	0	N/A	-4.56×10^4	6490	0
	Without Vertical Motion	1.42×10^4	N/A	1550	0	N/A	-3.36×10^4	5630	0
Sylmar	With Vertical Motion	2.97×10^4	-3.30×10^4	2030	0	N/A	-5.39×10^4	6720	0
	Without Vertical Motion	2.76×10^4	-3.03×10^4	1940	0	N/A	-5.27×10^4	6290	0
Jensen	With Vertical Motion	2.67×10^4	-2.98×10^4	2160	0	N/A	-5.74×10^4	7280	0
	Without Vertical Motion	2.43×10^4	N/A	1880	0	N/A	-4.96×10^4	5920	0
Horton, Pier 3	With Vertical Motion	3.30×10^4	-3.28×10^4	2600	0	N/A	-5.78×10^4	7860	0
	Without Vertical Motion	2.76×10^4	-3.22×10^4	2350	0	N/A	-5.40×10^4	1510	0
Newhall	With Vertical Motion	4.99×10^4	-3.77×10^4	4490	0	N/A	-8.30×10^4	10200	0
	Without Vertical Motion	2.08×10^4	-2.70×10^4	1840	0	N/A	-4.75×10^4	6090	0
Hutchings, ICN	With Vertical Motion	4.62×10^4	-3.49×10^4	3480	-310	N/A	-9.30×10^4	9310	0
	Without Vertical Motion	2.84×10^4	-3.60×10^4	2590	0	N/A	-5.94×10^4	6470	0
Primary Moment		-	-2.4×10^4	-	-	3.6×10^4	-	-	-

Record		Span 2											
		Left				Middle				Right			
		Bending Moment kN×m		Shear Force kN		Bending Moment kN×m		Shear Force kN		Bending Moment kN×m		Shear Force kN	
		pos.	neg.	pos.	neg.	pos.	neg.	pos.	neg.	pos.	neg.	pos.	neg.
Arleta	With Vertical Motion	N/A	-4.70×10^4	0	-6480	0.34×10^4	N/A	539	-663	N/A	-5.16×10^4	6250	0
	Without Vertical Motion	N/A	-4.16×10^4	0	-5650	0	N/A	569	-556	N/A	-4.27×10^4	5690	0
Sylmar	With Vertical Motion	N/A	-8.40×10^4	0	-7340	1.09×10^4	N/A	1330	-1640	N/A	-6.63×10^4	6970	0
	Without Vertical Motion	N/A	-7.90×10^4	0	-6890	0.90×10^4	N/A	1300	-1630	N/A	-6.47×10^4	6420	0
Jensen	With Vertical Motion	N/A	-7.50×10^4	0	-8550	1.42×10^4	N/A	1040	-1560	N/A	-6.90×10^4	7540	0
	Without Vertical Motion	N/A	-6.05×10^4	0	-6200	0.55×10^4	N/A	950	-1430	N/A	-5.75×10^4	6240	0
Horton, Pier 3	With Vertical Motion	N/A	-6.38×10^4	0	-6570	0.75×10^4	N/A	940	-1040	N/A	-5.66×10^4	6760	0
	Without Vertical Motion	N/A	-5.64×10^4	0	-6040	0.74×10^4	N/A	900	-1000	N/A	-5.67×10^4	6550	0
Newhall	With Vertical Motion	N/A	-8.40×10^4	0	-9220	2.38×10^4	N/A	1160	-1400	N/A	-9.10×10^4	8750	0
	Without Vertical Motion	N/A	-6.70×10^4	0	-6480	0.70×10^4	N/A	950	-1290	N/A	-5.77×10^4	6210	0
Hutchings, ICN	With Vertical Motion	N/A	-8.40×10^4	0	-8750	3.77×10^4	N/A	1700	-1310	3.84×10^4	-1.17×10^5	10100	0
	Without Vertical Motion	N/A	-6.70×10^4	0	-6820	1.30×10^4	N/A	1510	-1280	N/A	-7.30×10^4	7140	0
Primary Moment		3.6×10^4	-	-	-	-	-4.3×10^4	-	-	3.2×10^4	-	-	-

Record		Span 3							
		Left				Middle			
		Bending Moment kN×m		Shear Force kN		Bending Moment kN×m		Shear Force kN	
		pos.	neg.	pos.	neg.	pos.	neg.	pos.	neg.
Arleta	With Vertical Motion	N/A	-4.24×10^4	0	-6360	2.52×10^4	N/A	410	-470
	Without Vertical Motion	N/A	-3.66×10^4	0	-5410	1.38×10^4	N/A	170	-340
Sylmar	With Vertical Motion	N/A	-5.66×10^4	0	-6450	2.96×10^4	-2.09×10^3	500	-1250
	Without Vertical Motion	N/A	-5.69×10^4	0	-5970	1.78×10^4	N/A	430	-1150
Jensen	With Vertical Motion	N/A	-8.0×10^4	0	-9190	3.44×10^4	-3.90×10^4	590	-1420
	Without Vertical Motion	N/A	-4.81×10^4	0	-6110	1.52×10^4	N/A	290	-860
Horton, Pier 3	With Vertical Motion	N/A	-4.99×10^4	0	-6210	2.06×10^4	N/A	310	-650
	Without Vertical Motion	N/A	-4.39×10^4	0	-6070	2.34×10^4	N/A	410	-770
Newhall	With Vertical Motion	N/A	-9.10×10^4	870	-11200	5.96×10^4	-4.95×10^4	910	-1050
	Without Vertical Motion	N/A	-5.11×10^4	0	-5580	1.72×10^4	N/A	290	-870
Hutchings, ICN	With Vertical Motion	N/A	-7.90×10^4	0	-9050	4.86×10^4	-3.34×10^4	660	1130
	Without Vertical Motion	N/A	-5.75×10^4	0	-6770	2.18×10^4	N/A	510	-1080
Primary Moment		3.2×10^4	-	-	-	-	-1.9×10^4	-	-

to bound the nonlinear behavior of the intermediate hinges. The compression model assumes the hinges are closed and the tension model assumes the hinges are open. The nonlinear behavior of the piers is represented by the cracked section properties, and the behavior of the abutment and pier shafts are linearized with stiffness coefficients consistent with their maximum deformations.

The geometry and layout of the linear models is identical to the nonlinear model described in Section 3.2. The piers, in contrast, are modeled as linear elastic beam elements with an effective flexural stiffness based on $0.45I_g$, as suggested by ATC-32 (1996). The tapered segments of the piers are modeled as linear elastic beam elements with rotational stiffness factors calculated for a tapered beam (assuming a parabolically varying depth). As an example, the stiffness matrix for end rotations (as shown in Figure 6.54) for the tapered element in piers 2–5 and 10 for weak axis bending is:

$$\begin{bmatrix} 7.019 & 2.915 \\ 2.915 & 4.540 \end{bmatrix} \frac{E\,I_{weak}}{L}$$

where the moment of inertia, I, is at the narrow end and equal tothe moment of inertia for the prismatic column section below the taper. The rotational stiffness coefficients for strong axis bending are:

$$\begin{bmatrix} 17.829 & 5.597 \\ 5.597 & 5.630 \end{bmatrix} \frac{E\,I_{strong}}{L}$$

The stiffness coefficients are included directly in the DRAIN-3DX model. The values are not reduced for the effects of cracking, perhaps overemphasizing their stiffness relative to the column. The axial and shear stiffness are based on the gross area of the taper section at the mid-height of the taper. The torsional stiffness is based on $0.25J$ where J is the torsional moment of inertia at the mid-height of the taper.

The soil springs along the length of the pier shafts are linearized by a secant stiffness equal to the maximum force divided by the maximum displacement from one of the nonlinear time-history analyses. The nonlinear response computed for the Sylmar ground motion was selected for linearizing the model for all ground motions. For each soil spring the largest displacement from the nonlinear dynamic analysis in the longitudinal or transverse is taken as the displacement for computing the secant linearization of that soil spring. the secant stiffness for that soil spring.

The abutment connectivity is also simplified for the purpose of the linear model. At each abutment, the superstructure is restrained against vertical and radial translation and against torsion about the longitudinal superstructure axis. The abutment backwall springs that represent the closing of the backwall gap. The yielding of the abutment backwall in the nonlinear model are also linearized by assigning the springs a stiffness value equal to one half of the maximum force divided by the maximum displacement towards the backwall. As with the soil springs, the maximum force and displacement values are taken from the nonlinear time-history analysis for the Sylmar ground motion. The factor of 1/2 applied to the stiffness is recommended by ATC-32 (1996) to account for the fact that a linearized abutment spring will not accurately reflect the abutment's ability to resist only compressive

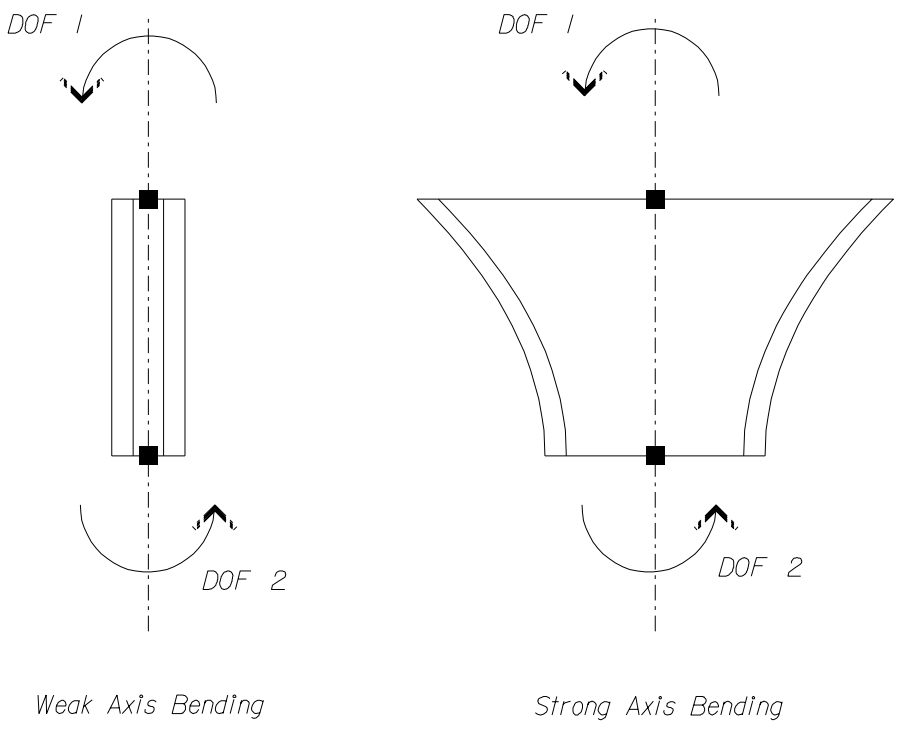

Figure 6.54: Degrees of Freedom for Tapered Column Stiffness

forces. Bending moments about the strong and weak axis of the superstructure are assumed to be unrestrained at the abutment.

The two linear models are distinguished by the model of the intermediate hinges. The linear "compression" model attempts to model the conditions in the structure when the hinges are closed in compression. As such, the hinge is modeled with complete translational fixity in the radial, longitudinal and vertical directions. Torsional fixity is also provided at the hinges. Superstructure bending moments, about the strong and weak axes, are released at the hinges. The linear "tension" model attempts to simulate conditions in the structure when the hinges are open. The tension model hinge is fixed in vertical and radial translation and fixed in torsion about the longitudinal axis. Strong and weak superstructure bending moments are released at the hinges. The longitudinal translation is linked by linearized springs that have stiffness equal to the initial stiffness of restrainer cables. These springs are in the same location along the width of the hinge model as in Section 3.6.

Time-history analyses were performed on these linear models for the six ground motions described in Chapter 2. The maximum displacement at the top of each pier and abutment is summarized in Table 6.8, and the maximum displacement at the ground level is in Table 6.9. The displacements of the bridge are compared for the two linear models and the nonlinear model in Figures 6.55 through 6.66. The general trend is that the linear tension model overestimates the global structural displacements. The linear compression model provides a better estimate of the maximum displacement from the nonlinear analysis. However, the compression model overestimates the displacement in many cases and underestimates it in

a few others. Based on this case, the larger of the displacements from the two linear models is excessively conservative.

Table 6.8: Maximum Displacements at Top of Piers from Linear Models

Record			Abutment 1 mm	Pier 2 mm	Pier 3 mm	Pier 4 mm	Pier 5 mm	Pier 6 mm	Pier 7 mm	Pier 8 mm	Pier 9 mm	Pier 10 mm	Abutment 11 mm
Arleta	Tension Model	Longitudinal	-86.2	-85.3	-83.0	-106	-111	-176	207	208	209	205	204
		Transverse	0	-46.4	-105	165	-192	-135	-174	-155	-159	-87.8	0
	Compression Model	Longitudinal	-76.8	-77.2	-80.5	-90.7	100	114	121	122	120	116	115
		Transverse	0	-46.0	102	176	198	-134	-208	-155	-183	-98.1	0
Sylmar	Tension Model	Longitudinal	-285	-285	-291	-377	-380	638	797	777	762	726	722
		Transverse	0	-94.2	-185	255	295	-446	-841	-704	-564	-252	0
	Compression Model	Longitudinal	492	494	508	534	549	565	-532	-530	-529	-532	-531
		Transverse	0	91.0	211	-352	472	508	-935	-711	-489	-205	0
Jensen	Tension Model	Longitudinal	170	171	176	231	236	403	-399	-381	-370	-429	-426
		Transverse	0	-103	-244	-316	378	618	-945	-662	477	223	0
	Compression Model	Longitudinal	222	221	216	-229	-243	-253	259	294	316	331	335
		Transverse	0	-96.9	250	365	512	730	995	664	469	219	0
Horton, Pier 3	Tension Model	Longitudinal	176	176	178	212	231	401	454	477	497	460	463
		Transverse	0	88.0	-216	-338	-524	-608	1070	-696	-542	-248	0
	Compression Model	Longitudinal	251	253	264	285	-313	360	418	448	470	489	494
		Transverse	0	95.6	-256	-431	-612	-679	1180	670	-381	-183	0
Newhall	Tension Model	Longitudinal	186	188	194	-234	-245	-420	-548	-547	-545	-560	-557
		Transverse	0	90.0	179	337	-409	-336	584	455	435	225	0
	Compression Model	Longitudinal	351	352	362	388	402	420	423	422	427	437	438
		Transverse	0	88.0	135	218	265	310	534	388	289	149	0
Hutchings, ICN	Tension Model	Longitudinal	-524	-523	-528	-656	-659	-877	-721	-703	-682	859	853
		Transverse	0	-260	-588	-767	863	401	707	427	-551	-308	0
	Compression Model	Longitudinal	588	584	568	549	531	-542	553	556	557	554	552
		Transverse	0	171	389	547	-815	419	716	377	-313	149	0

Table 6.9: Maximum Displacement of Piers at Ground Surface from Linear Models

Record			Pier 2 mm	Pier 3 mm	Pier 4 mm	Pier 5 mm	Pier 6 mm	Pier 7 mm	Pier 8 mm	Pier 9 mm	Pier 10 mm
Arleta	Tension Model	Longitudinal	-20.6	-31.1	-29.6	-27.7	-20.4	12.5	25.2	-19.7	58.6
		Transverse	-7.7	-25.1	32.5	-35.6	10.2	-10.3	-13.6	-14.2	-18.6
	Compression Model	Longitudinal	-19.1	31.9	-26.1	26.3	13.0	7.6	14.9	10.9	33.4
		Transverse	-7.9	25.0	35.2	38.7	-9.3	-12.8	-13.5	-15.8	-20.7
Sylmar	Tension Model	Longitudinal	-66.6	-108	-104	-98.8	73.7	47.1	94.5	72.7	210
		Transverse	-16.0	-45.2	49.8	56.6	-37.1	36.1	-62.4	-35.6	-49.3
	Compression Model	Longitudinal	114	195	147	142	64.1	-32.5	-64.3	-50.5	-153
		Transverse	15.2	-51.2	-65.2	90.2	40.2	-43.1	-64.5	-28.7	-38.5
Jensen	Tension Model	Longitudinal	38.6	67.5	-61.0	65.4	46.0	-25.6	-48.0	-37.4	-125
		Transverse	-17.0	-59.4	-61.4	69.6	49.6	-44.9	-61.0	32.0	44.2
	Compression Model	Longitudinal	-49.9	84.0	-65.5	-64.4	-31.4	-17.0	33.7	28.0	94.2
		Transverse	-15.9	60.6	71.0	95.0	60.0	-52.5	61.9	31.8	43.6
Horton, Pier 3	Tension Model	Longitudinal	40.3	71.0	59.0	60.5	47.0	29.5	60.4	48.2	132
		Transverse	14.4	-51.6	-62.3	-98.6	49.3	53.4	-62.8	-35.0	-49.0
	Compression Model	Longitudinal	58.0	103	-80.4	-79.6	41.6	26.3	55.4	44.3	141
		Transverse	15.4	-61.9	-76.9	-115	-51.5	61.0	64.2	-26.4	-36.9
Newhall	Tension Model	Longitudinal	41.8	76.8	-63.4	-63.4	-47.0	-31.0	-64.8	-49.7	-161
		Transverse	15.9	43.6	66.9	-80.6	-26.3	-29.8	41.5	34.5	46.4
	Compression Model	Longitudinal	79.9	141	108	105	44.7	24.8	48.6	37.6	122
		Transverse	15.3	32.5	-40.4	53.9	25.8	22.8	35.1	22.9	30.6
Hutchings, ICN	Tension Model	Longitudinal	-121	-200	-177	-176	-102	43.4	-85.9	-64.9	247
		Transverse	-43.0	-143	-143	170	32.1	37.7	40.3	-48.6	-64.4
	Compression Model	Longitudinal	134	219	149	138	61.3	31.7	67.0	51.7	159
		Transverse	28.4	95.6	109	167	34.3	-39.9	34.9	-24.4	29.5

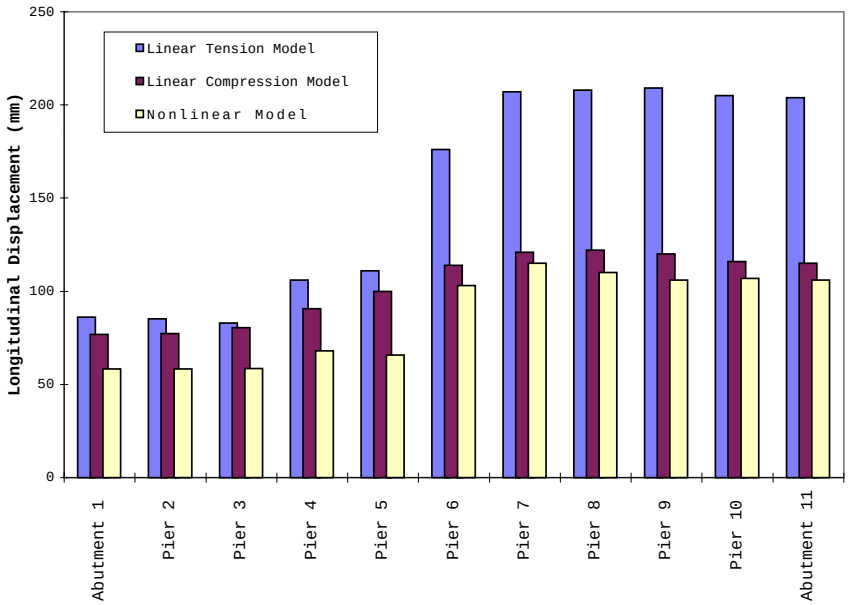

Figure 6.55: Longitudinal Displacement at Top of Piers for Arleta Ground Motion

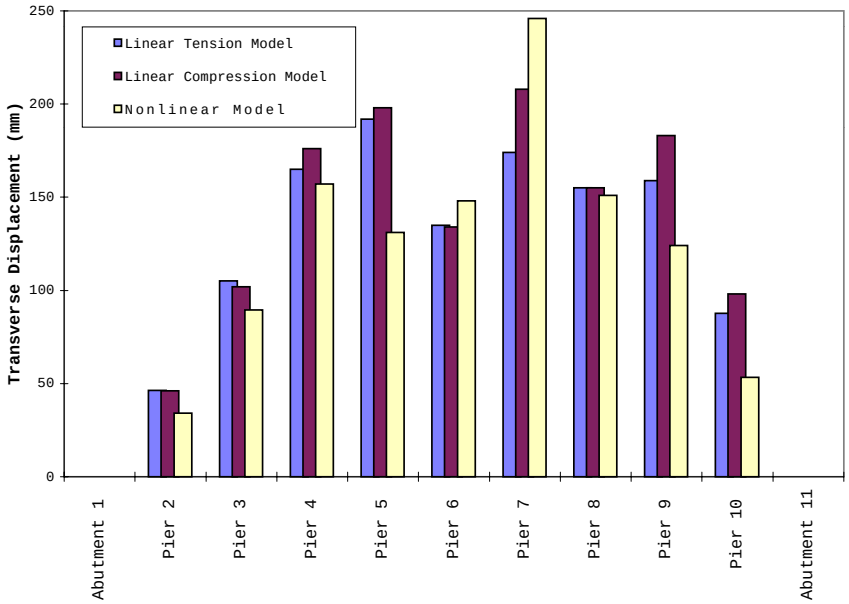

Figure 6.56: Transverse Displacement at Top of Piers for Arleta Ground Motion

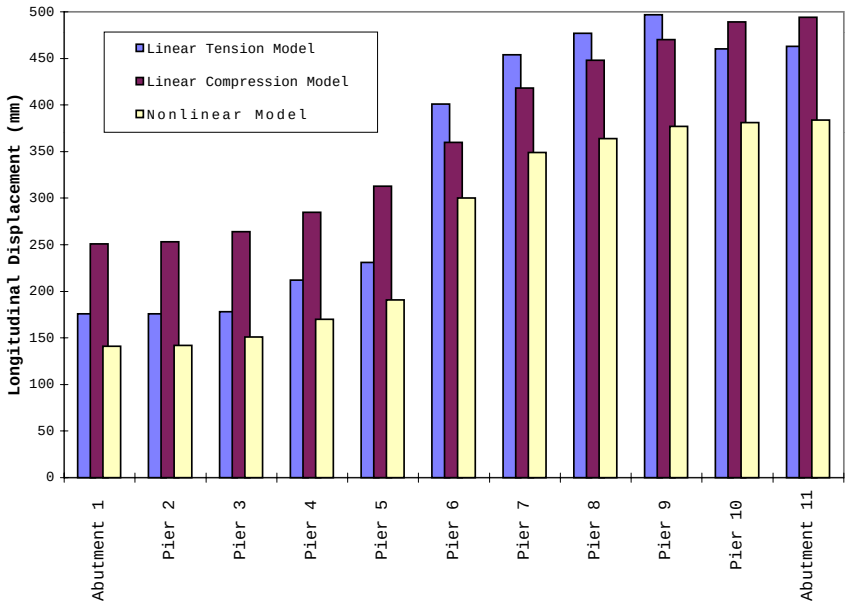

Figure 6.57: Longitudinal Displacement at Top of Piers for Horton et al. (1995) Pier 3 Simulated Ground Motion

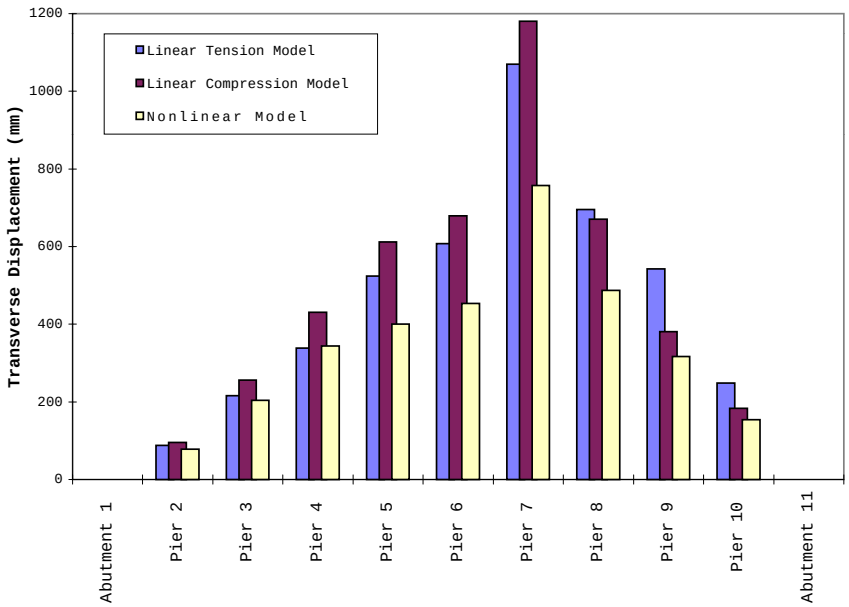

Figure 6.58: Transverse Displacement at Top of Piers for Horton et al. (1995) Pier 3 Simulated Ground Motion

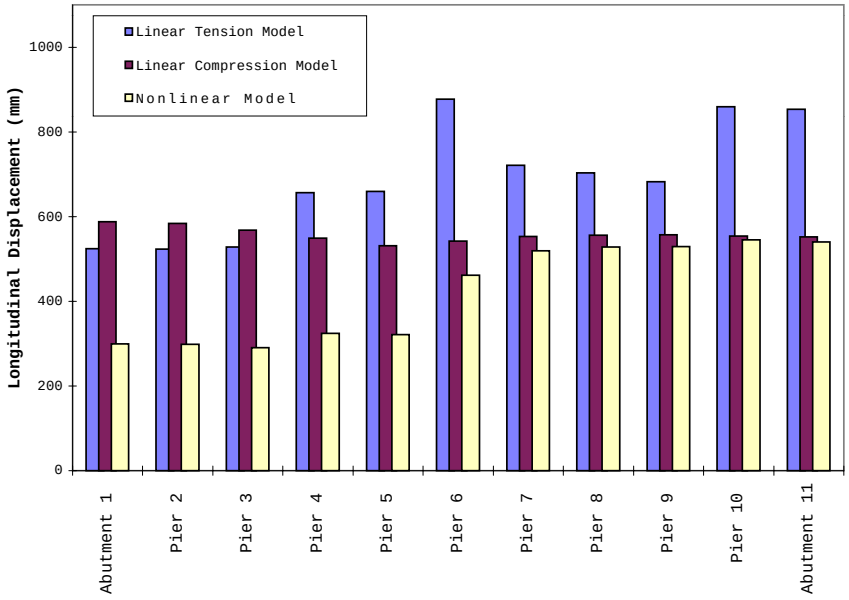

Figure 6.59: Longitudinal Displacement at Top of Piers for Hutchings et al. (1996) ICN Simulated Ground Motion

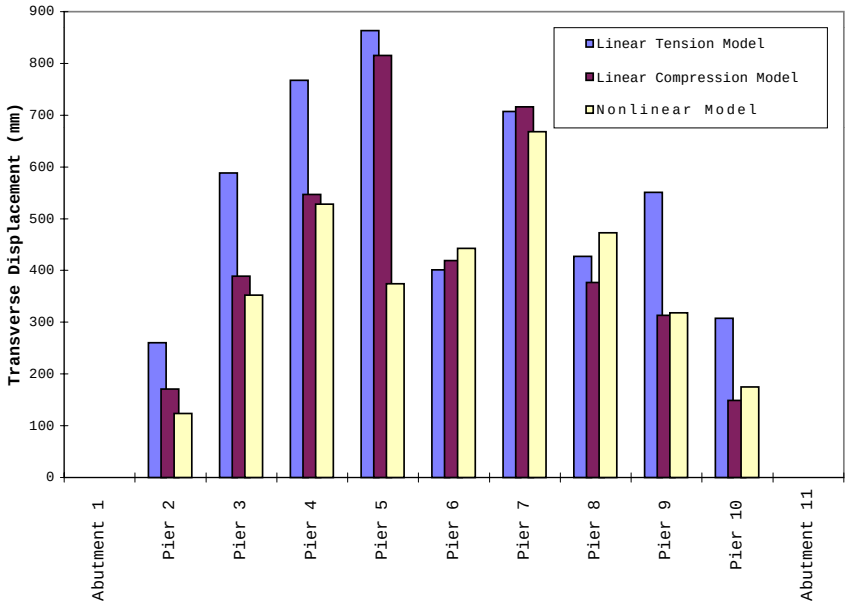

Figure 6.60: Transverse Displacement at Top of Piers for Hutchings et al. (1996) ICN Simulated Ground Motion

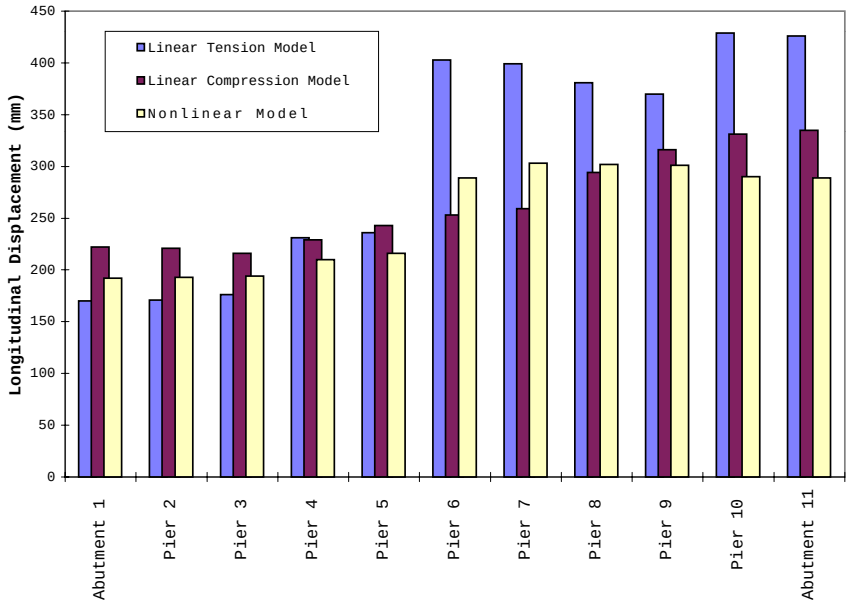

Figure 6.61: Longitudinal Displacement at Top of Piers for Jensen Ground Motion

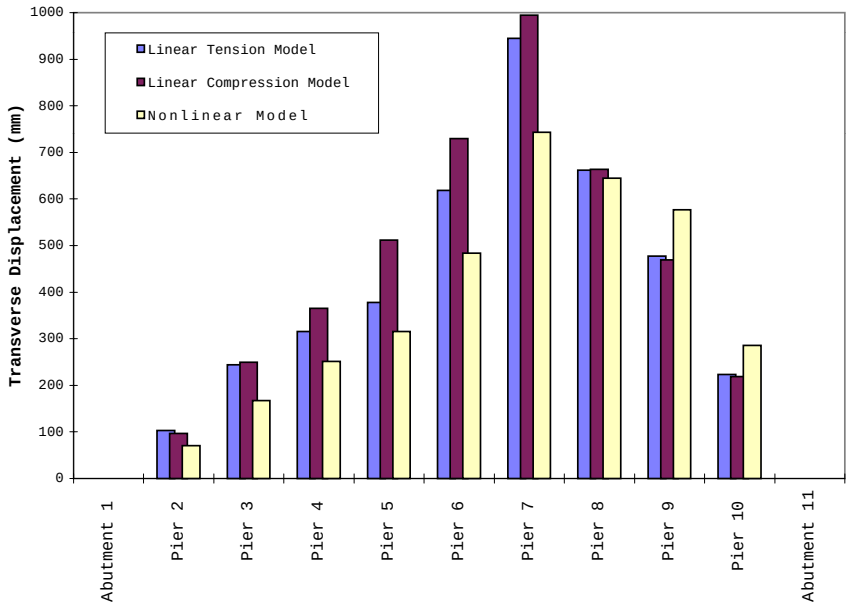

Figure 6.62: Transverse Displacement at Top of Piers for Jensen Ground Motion

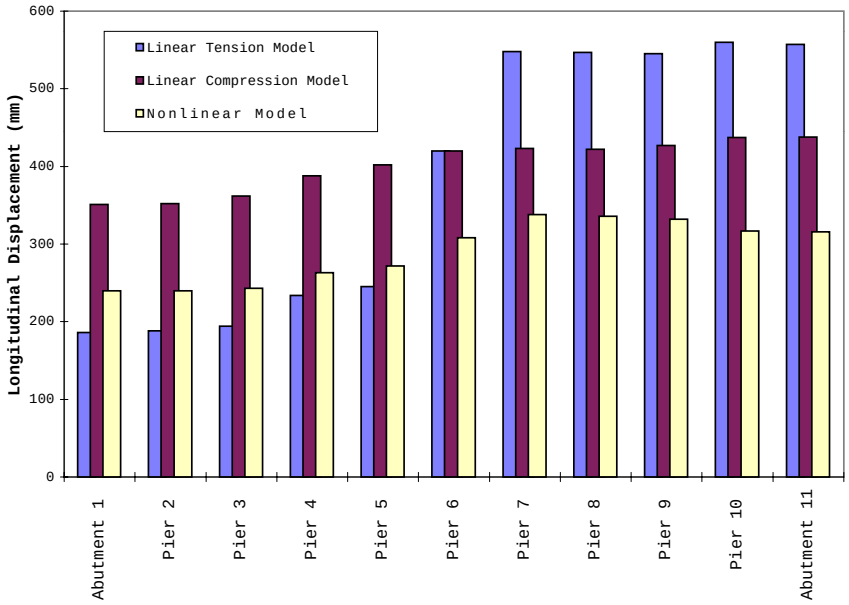

Figure 6.63: Longitudinal Displacement at Top of Piers for Newhall Ground Motion

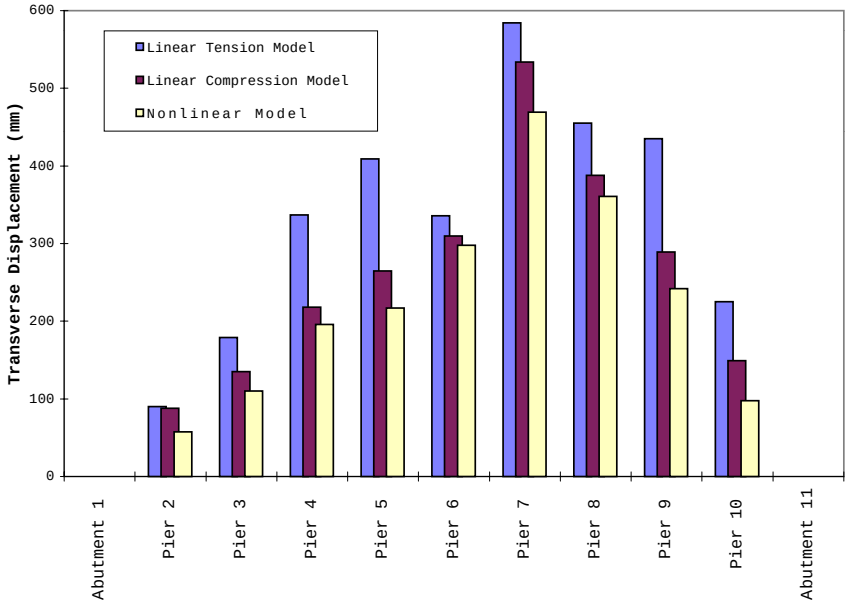

Figure 6.64: Transverse Displacement at Top of Piers for Newhall Ground Motion

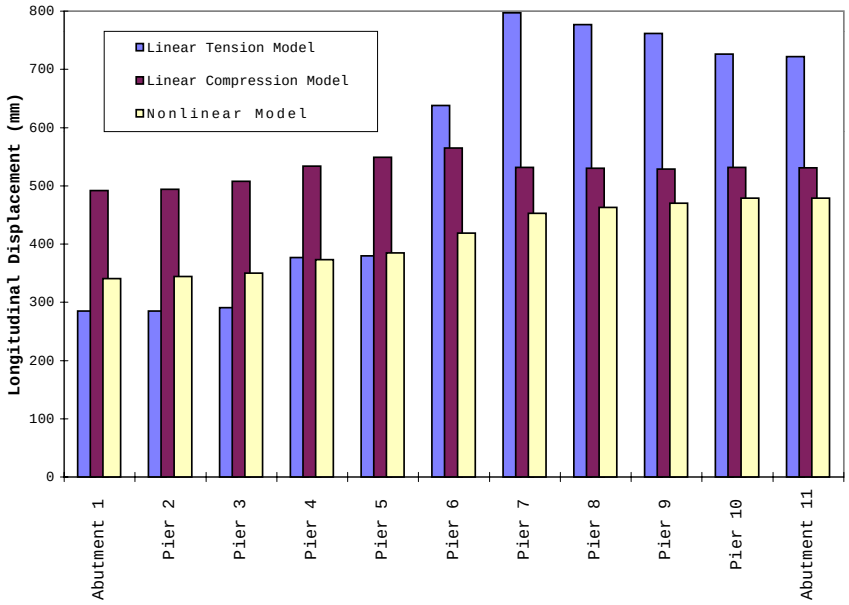

Figure 6.65: Longitudinal Displacement at Top of Piers for Sylmar Ground Motion

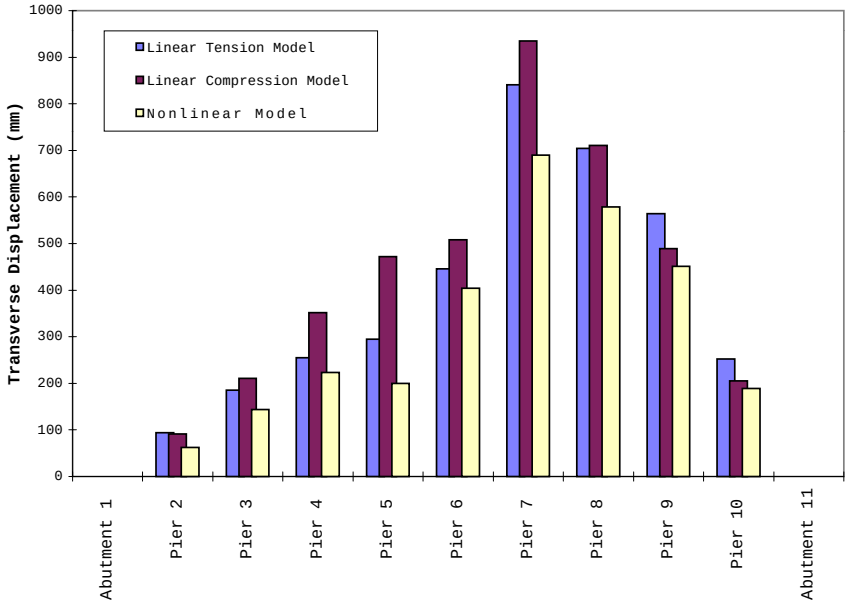

Figure 6.66: Transverse Displacement at Top of Piers for Sylmar Ground Motion

Chapter 7

Conclusions

The objective of this study was to evaluate the earthquake behavior of the Separation and Overhead bridge at the Route 14/Interstate 5 interchange in the 1994 Northridge earthquake. The partial collapse of the bridge provided a unique opportunity to learn about the behavior of an important class of highway bridges. The earthquake demands were estimated by analysis of a detailed nonlinear model of the bridge, including the inelastic flexural column behavior, inelastic soil properties, opening and closing of the intermediate hinges, and pounding and yielding of the the abutments. The ground motion at the site was estimated from four recorded stations in the epicentral region of the 1994 Northridge earthquake and two simulated ground motions established by other investigators. The free-field ground motion was assumed to be uniform over the bridge site, therefore the effects of spatial variation of ground motion were not addressed in this study.

The second objective of the study was to estimate the response of the bridge in the 1994 Northridge earthquake if it had been seismically retrofitted at the time of the earthquake. Finally, the study concludes with a discussion of earthquake analysis methods.

7.1 Postulated Failure Mechanism

From the evaluation presented in Chapter 5 the partial collapse of the Separation and Overhead bridge during the 1994 Northridge earthquake was most likely precipitated by ductile/brittle shear failure at pier 2. The modeling and simulation results indicate that the shear failure occurred at the onset of flexural yielding of pier 2 as the shear capacity decreases in the first large displacement excursion of frame 1 in the longitudinal direction away from the abutment. The analysis shows large shear force demands in pier 3 relative to its capacity, but slightly less than the demand-capacity ratio for pier 2. The remaining piers in the bridge had adequate shear capacity to withstand the forces generated by the Northridge earthquake. These conclusions are consistent with the damage observed in the bridge after the earthquake, in which pier 2 failed completely and pier 3 had significant shear cracks caused by displacement away from abutment 1. The other piers did not appear damaged.

Other failure modes not explicitly accounted for in the model were examined by a demand-capacity comparison to the time at which pier 2 reached its shear capacity. The shear capacity of the superstructure appears to have been adequate, making it unlikely that shear failure of

the box girder at pier 3 caused the collapse of the frame. The analysis, however, indicated that the box girder may have just begin to yield in the negative moment regions over piers 2 and 3. The maximum hinge displacements predicted at the time piers 2 and 3 reach shear capacity are much less than the seat width for the hinges. Unseating of hinge 4 is unlikely to have precipitated the collapse of frame 1. There may have been some yielding of the longitudinal reinforcement in a few pier shafts below the termination of the main reinforcement, but this should not have had a significant effect on the performance in the earthquake.

Although the progressive failure of the bridge was not represented in the model, the demand-capacity comparison described in the previous paragraph can it is interpreted to provide a likely sequence of failure for the bridge. Pier 2 reached its shear capacity in the first large longitudinal displacement of the bridge and was crushed under the vertical load. The box girder spanning from abutment 1 to pier 3 formed a positive flexural hinge over pier 2 after the loss of vertical load support from pier 2. The increased shear force and negative bending moment in the box girder at pier 3 quickly caused failure at that support. The box girder had nearly reached its negative flexural capacity or in fact yielded at the time that pier 2, which may explain the fracture of the unbonded tendons and extensive damage to the top of the pier 3 bent cap. Once the box girder lost support at pier 3, it was pulled off the hinge seat at hinge 4.

7.2 Hypothetical Behavior of Retrofitted Bridge

After examining the failure of the Separation and Overhead bridge in the 1994 Northridge earthquake, the model was analyzed assuming the piers had sufficient shear capacity either from a seismic retrofit or as provided for in a new design. The maximum displacements at the pier tops correspond to drift angles from 1% to 4% with approximately one-half of the displacement due to the rotation of the piers at the ground level from deformation of the pier shafts. The deformation of the shafts is sensitive to the properties of the soil and the p-y springs used to represent soil-structure interaction. The inelastic deformations in the columns generally correspond to curvature ductility demands that are less than 10, an acceptable inelastic demand for the large ground motions.

The displacement at the intermediate hinges is relatively small, although some restrainers yield for the larger ground motions. the analysis for one ground motion, the Hutchings ICN simulated record, shows that hinge unseating could been a concern for the bridge with the existing number of cable restrainers. New design procedures for intermediate hinge restrainers (DesRoches and Fenves, 1997) can be used to select restrainers required to limit hinge displacements. The response of the hypothetical retrofitted bridge shows some damage to the abutment backwall for the large ground motions (Sylmar and Hutchings, ICN). The largest abutment backwall displacement for any of the ground motions is 90 mm (3.5 in.).

The vertical component of ground motion may have a significant effect on certain response quantities. The column axial force shows little sensitivity to the vertical ground motion component for four ground motions, but the Newhall and Hutchings, ICN records have a larger effect. The Newhall ground motion has significant energy in the period range containing the vertical vibration modes of the superstructure. This leads to a large variation

of column axial forces, including net tension, which may decrease the shear capacity of the column. These results indicate that the effects of vertical motion are important to consider, especially when the spectral acceleration of the vertical motion is large in the range of the vertical vibration periods of the bridge. The influence of vertical ground motion is also noteworthy when considering the superstructure shear and flexure demands. For the Newhall and Hutchings, ICN ground motions, the superstructure demands with and without the vertical ground motion component varied by over a factor of two. The superstructure flexural capacity of bridges should be examined for ground motions expected for the effects of vertical ground motion.

7.3 Earthquake Analysis Methods

This study used state-of-the-art nonlinear analysis methods, yet the methods are currently available to design engineers. The modeling must concentrate on the most relavent aspects of earthquake behavior of a bridge. Other aspects of the complex behavior can be simplified or neglected. The model considered in this study captured the most important aspects of the seismic behavior of the bridge. In particular, the model represents intermediate hinge opening and closing, inelastic biaxial flexural response of the columns, soil structure interaction (p-y springs), and restrainer and abutment yielding. The fiber beam elements used to model the bridge piers are an accurate way to model the flexural response of the bridge columns and to account for the moment-axial force interaction. While the computation time is larger when using these types of elements compared with lumped plasticity models, they provide more accurate response data than obtainable from simpler inelastic models.

The linear design models (tension and compression) were compared with the nonlinear models. The compression model generally overestimated the maximum column displacements, but it is acceptably conservative for estimating the displacement demand. The tension model, gives excessively large column displacements and should not be used.

There is a trend in seismic design of bridges towards a two-step analysis procedure. The first step involves force-based design using a reduction factor to recognize inelastic behavior. The second step is a dispacement demand-capacity check (ATC-32, 1996). The displacement demand is obtained from a linearized analysis and the capacity is determined from a static nonlinear analsysis procedure. This study has shown that the linearized analysis, particularly with the compression model, generally gives a conservative displacement demand estimate. The static nonlinear analysis gives a pushover curve, which is a realistic estimate of the displacement capacity. A displacement check in seismic design is a useful procedure for understanding the deformations of a bridge.

REFERENCES

ACI (1992). *Building Code and Commentary for Reinforced Concrete and Commentary.* American Concrete Institute, Committee 318, Detroit, Michigan, September. ACI 318-89 and ACI 318R-89.

API (1993). *Recommended Practice for Planning, Designing and Constructing Fixed Offshore Platforms – Working Stress Design.* American Petroleum Institute, Washington, D.C., twentieth edition, July. Report Number RP 2A-WSD.

Aschheim, M. and Moehle, J. P. (1996). "Seismic Shear Strength of Reinforced Concrete Columns: Discussion," *Journal of Structural Engineering, ASCE*, Vol. 122(No. 4):pp. 461–464, April.

ATC-32 (1996). *Improved Seismic Design Criteria for California Bridges.* Applied Technology Council, Redwood City, California, June. Report Number ATC-32.

Buckle, I. G. (1994). "The Northridge, California, Earthquake of January 17, 1994: Performance of Highway Bridges," *Report No. NCEER-94-0008*, National Center for Earthquake Engineering Research, State University of New York at Buffalo, Buffalo, New York.

Caltrans (1994). "The Northridge Earthquake: Post-Earthquake Investigation Report,". Caltrans Post-Earthquake Investigation Team, January. California Department of Transportation, Division of Structures.

Clough, R. W. and Penzien, J. (1993). *Dynamics of Structures*, McGraw–Hill, Inc., New York, New York, second edition.

Darragh, R., Cao, T., Cramer, C., Graizer, V., Huang, M., and Shakal, A. (1994). "Processed CSMIP Strong-Motion Records from the Northridge, California, Earthquake of January 7, 1994," *Report No. OSMS 94-00 through OSMS 94-12*, California Department of Conservation, Division of Mines and Geology, Office of Strong-Motion Studies, Pasadena, California.

DesRoches, R. and Fenves, G. L. (1997). "New Design and Analysis Procedures for Intermediate Hinges in Multiple-Frame Bridges," *Report No. UCB/EERC-97/12*, Earthquake Engineering Research Center, University of California at Berkeley, Berkeley, California, December.

EERI (1995). "Northridge Earthquake Reconnaissance Report, Volume 1," *Earthquake Spectra*, 11:pp. 287–372. (Supplemental report to Volume 11).

Goel, R. K. and Chopra, A. K. (1997). "Evaluation of Bridge Abutment Capacity and Stiffness During Earthquakes," *Earthquake Spectra*, Vol. 13(No. 1):pp. 1–23, February.

Horton, S. P. and Barstow, N. (1995). "Simulation of Ground Motion at the I5/Route 14 Interchange Due to the 1994 Northridge, California Earthquake," *Report No. NCEER-95-XXXX*, National Center for Earthquake Engineering Research, Buffalo, New York, July. (Draft Report).

Hutchings, L. and Jarpe, S. (1996). "Ground Motion Variability at the Highway 14 and I-5 Interchange in the Northern San Fernando Valley," *Bulletin of the Seismological Society of America*, Vol. 86(No. 1B):pp. S289–S299, February.

Jennings, P. (1971). "Engineering Features of the San Fernando Earthquake of February 9, 1971," *Report No. EERL 71-02*, California Institute of Technology, Pasadena, California.

Moehle, J. (1994). "Preliminary Report on the Seismological and Engineering Aspects of the January 17, 1994, Northridge Earthquake," *Report No. UCB/EERC-94/01*, Earthquake Engineering Research Center, University of California at Berkeley, Berkeley, California.

Mylonakis, G., Simeonov, V. K., Reinhorn, A. M., and Buckle, I. G. (1997). "Implications of Spatial Variation of Ground Motion on the Collapse of SR14/I5 Southbound Separation and Overhead Bridge in the Northridge Earthquake," *ACI Special Publication*.

Naaman, A. E. (1982). *Prestressed Concrete Analysis and Design*, McGraw–Hill, Inc., New York, New York.

Papazoglou, A. and Elnashai, A. (1996). "Analytical and Field Evidence of the Damaging Effect of Vertical Earthquake Ground Motion," *Earthquake Engineering and Structural Dynamics*, Vol. 25(No. 10):pp. 1109–1137.

Park, R. and Paulay, T. (1975). *Reinforced Concrete Structures*, John Wiley and Sons, Inc., New York, New York.

Park, R., Priestley, M. J. N., and Gill, W. D. (1982). "Ductility of Square-Confined Concrete Columns," *ASCE Journal of the Structural Division*, Vol. 108(No. ST4):pp. 929–950, April.

Powell, G. and Campbell, S. (1994). "DRAIN-3DX: Element Description and User Guide for Element TYPE01, TYPE04, TYPE05, TYPE08, TYPE09, TYPE15, TYPE17," *Report No. UCB/SEMM-94/08*, University of California at Berkeley, Berkeley, California, August.

Prakash, V., Powell, G., and Campbell, S. (1994). "DRAIN-3DX: Base Program Description and User Guide," *Report No. UCB/SEMM-94/07*, University of California at Berkeley, Berkeley, California, August.

Priestley, M. N. J., Seible, F., and Uang, C.-M. (1994a). "The Northridge Earthquake of January 17, 1994: Damage Analysis of Selected Freeway Bridges," *Report No. SSRP-94/06*, Structural Systems Research Project at the University of California, San Diego, California, February.

Priestley, M. N. J., Verma, R., and Xiao, Y. (1994b). "Seismic Shear Strength of Reinforced Concrete Columns," *Journal of Structural Engineering, ASCE*, Vol. 120(No. 8):pp. 2310–2329, August.

Priestley, M. N. J., Verma, R., and Xiao, Y. (1996). "Seismic Shear Strength of Reinforced Concrete Columns: Closure by Authors," *Journal of Structural Engineering, ASCE*, Vol. 122(No. 4):pp. 464–467, April.

Reichman, Y. and Reinhorn, A. (1995). "Extending the Seismic Life Span of Bridges. Analytical Evaluation of Retrofit Measures," *Structural Engineering Review*, Vol. 7(No. 3):pp. 207–218.

Saadeghvaziri, M. A. (1996). "A Case Study from the Northridge Earthquake," In *Proceedings, Eleventh World Conference on Earthquake Engineering*, Elsevier Science Ltd. Paper No. 1890.

Somerville, P. and Abrahamson, N. (1996). "Effects of the Hanging Wall and Footwall on Ground Motions Recorded During the Northridge Earthquake," *Bulletin of the Seismological Society of America*, Vol. 86(No. 1B):pp. S93–S99, February.

Ugural, A. and Fenster, S. (1995). *Advanced Strength and Applied Elasticity*, PTR Prentice Hall, Englewood Cliffs, New Jersey, third edition.

Wald, D. and Heaton, T. (1994). "A Dislocation Model of the 1994 Northridge, California, Earthquake Determined from Strong Ground Motions,". Open File Report 94-278, United States Geological Survey.

Wallace, J. W. (1992). "BIAX: A Computer Program for the Analysis of Reinforced Concrete and Reinforced Masonry Sections," *Report No. CU/CEE-92/4*, Clarkson University, Potsdam, New York, February.